Title
Computational Study of Porous Materials for Gas Separations

Permalink
https://escholarship.org/uc/item/4f43c0tr

Author
Lin, Li-Chiang

Publication Date
2014

Peer reviewed|Thesis/dissertation

Computational Study of Porous Materials for Gas Separations

by

Li-Chiang Lin

A dissertation submitted in partial satisfaction of the
requirements for the degree of
Doctor of Philosophy

in

Chemical Engineering

in the

Graduate Division

of the

University of California, Berkeley

Committee in charge:

Prof. Berend Smit, Chair
Prof. Jeffrey Reimer
Prof. Phillip Geissler

Spring 2014

Computational Study of Porous Materials for Gas Separations

Abstract

Computational Study of Porous Materials for Gas Separations

by

Li-Chiang Lin

Doctor of Philosophy in Chemical Engineering

University of California, Berkeley

Prof. Berend Smit, Chair

Nanoporous materials such as zeolites, zeolitic imidazolate frameworks (ZIFs), and metal-organic frameworks (MOFs) are used as sorbents or membranes for gas separations such as carbon dioxide capture, methane capture, paraffin/olefin separations, etc. The total number of nanoporous materials is large; by changing the chemical composition and/or the structural topologies we can envision an infinite number of possible materials. In practice one can synthesize and fully characterize only a small subset of these materials. Hence, computational study can play an important role by utilizing various techniques in molecular simulations as well as quantum chemical calculations to accelerate the search for optimal materials for various energy-related separations.

Accordingly, several large-scale computational screenings of over one hundred thousand materials have been performed to find the best materials for carbon capture, methane capture, and ethane/ethene separation. These large-scale screenings identified a number of promising materials for different applications. Moreover, the analysis of these screening studies yielded insights into those molecular characteristics of a material that contribute to an optimal performance for a given application. These insights provided useful guidelines for future structural design and synthesis. For instance, one of the screening studies indicated that some zeolite structures can potentially reduce the energy penalty imposed on a coal-fired power plant by as much as 35% compared to the near-term MEA technology for carbon capture application. These optimal structures have topologies with a maximized density of pockets and they capture and release CO_2 molecules with an optimal energy.

These screening studies also pointed to some systems, for which conventional force fields were unable to make sufficiently reliable predictions of the adsorption isotherms of different gasses, e.g., CO_2 in MOFs with open-metal sites. For these systems, we developed a systematic, transferable, and efficient methodology to generate force fields by using high-level quantum chemical calculations for accurate predictions of properties. The method was first applied to study the adsorption of CO_2 and N_2 in Mg-MOF-74, an open-metal site MOF. Two different approaches were developed: one approach based on MP2 calculations on a representative cluster and a second approach based on DFT calculations on a fully periodic

MOF. Both approaches gave significantly better predictions of the experimental adsorption isotherms compared to conventional force fields. In addition, we extended the DFT approach to study water adsorption in these materials. Moreover, instead of deriving detailed force fields, we have also proposed an alternative method to efficiently correct initial trial force fields with little information obtained from quantum chemical calculations.

Finally, we studied the dynamics of CO_2 in Mg-MOF-74 using molecular simulations. This study addressed the dynamic behaviors of CO_2 adsorbed in Mg-MOF-74, and provided an alternative explanation to the experimentally measured chemical shifts of ^{13}C labeled CO_2 adsorbed in a powder Mg-MOF-74 sample. Our results further illustrated that subtle changes in the topology of frameworks greatly influence CO_2 dynamics.

Contents

List of Figures

List of Tables

Acknowledgements

First of all, I want to gratefully thank my advisor, Prof. Smit, for the years of great advising. Thank you for giving me such a compelling research environment to conduct advanced research. It was great to have the opportunities to participate in many projects and collaborate with other researchers. During the process of getting my doctoral degree, I have benefitted greatly from all these opportunities you provided. Additionally, I really appreciate all of your help, patience, and encouragement in the past years. Thank you.

I want to thank all the members in the Molsim group; it has been a pleasure for me to be a lab-mate (collaborator) with all of you (some of you). Thanks to Joe, Shachi, Johanna, Forrest, Fangyong, Ayelet, Roberta, Sergey, Cory, Bess, Josh, and Kyuho. Thanks to Maciek and Richard for your great help on several projects. Thanks to Prof. Gagliardi and her group members Allison, Joshua, Nora, David, and Rémi. It was great to work with all of you, and I did learn a lot during our collaboration. I also want to thank Prof. Reimer and his group member Sean as well as Prof. Long and his group members Jarad, Tom, and Eric. I did have a great time collaborating with all of you. I would like to specifically thank Jihan. You have been a great collaborator during my Ph.D. study. Without all of your support, I do not think that I could have had such a smooth graduate study. Also, congratulations on your new position at KAIST as an assistant professor.

I would also like to say think you to Jon and Kelley for keeping all the computational devices in order. Thanks also to Kristin and Cezar for helping on perfectly running the administration of the group.

I want to thank my Grandpa, Grandma, Dad, Mom, Sister, and Brother for the years of caring, encouragement, and support. Without you, I do not think that I could have gotten to this point. Thanks to all my roommates and friends. I really appreciate all your help and support. Furthermore, I want to say thank you to my wife. Thank you Szu-Chia for all your support, patience, consideration, and love. To be your husband is the best thing I have in my life.

Finally, I would like to acknowledge the financial support provided by the University of California - Berkeley, US Department of Energy's Energy Frontier Research Center (EFRC), US Department of Energy's Nanoporous Materials Genome Center (NMGC), and the Chevron fellowship.

Thank you all.

Chapter 1

Introduction[*]

1.1 Energy-related gas separations

Gas separation is a key component in many important environmental and chemical processes. Many of them are energy demanding, such as for those relying on chemical reactions or requiring cryogenic units for separations. As an example, amine scrubbing can be used to selectively separate CO_2 from flue gases, i.e., the emissions from power plants. However, the required energy for solvent regeneration is enormous. In this dissertation, I mainly focus on carbon dioxide capture but also cover methane capture and ethane/ethene separation.

1.1.1 Carbon dioxide capture

Elevated CO_2 concentration in the atmosphere is regarded as one of the largest contributing factors to global warming.[5,6] Figure 1.1 shows the monthly average CO_2 concentration that has been recorded at Mauna Loa Observatory, Hawaii, since March of 1958. It shows a continuous increase in carbon dioxide concentration. Reducing anthropogenic global CO_2 emissions is a complex issue. The scale of the problem, the costs, its interdependence with energy production, and the intrinsic uncertainties in making long-term predictions about something as complex as the climate are a few of the factors contributing to one of the biggest challenges of our time.[7] Despite advances in alternative energy, most, if not all, future energy scenarios include continuing growth in the absolute use of fossil energy.[8]

Carbon capture and sequestration (CCS), deployed at an industrial scale, is one of the few viable technologies that mitigate anthropogenic CO_2 emissions.[5,6] CCS consists of utilizing materials to capture CO_2 emissions from stationary point sources such as coal-fired power plants followed by its compression and subsequent sequestration in geological formations. CCS is very energy intensive, and capture (including the following compression) dominates both the energy consumption and the cost.[6,9] In particular, this dissertation focuses on

---

[*] Part of the material in this chapter is based on refs 1, 2, 3, and 4.

the CO_2 capture from the flue gas of coal-fired power plants, which is one of the major contributors to the total carbon dioxide emission.

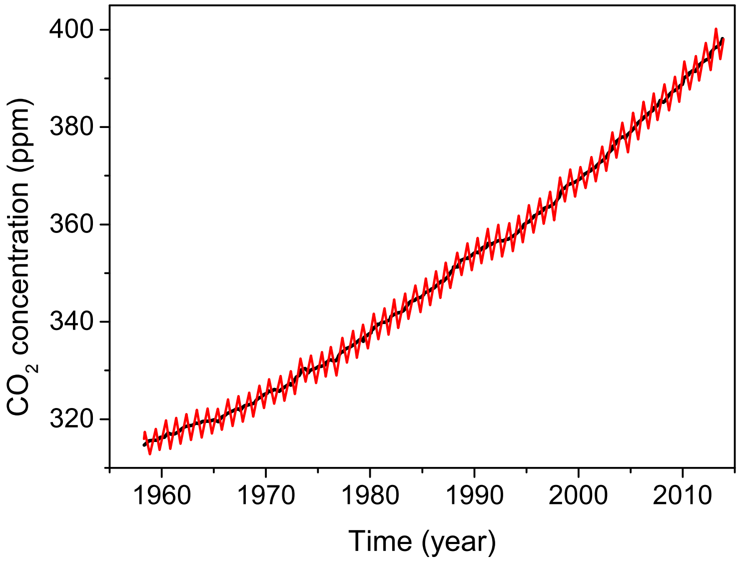

Figure 1.1: Average carbon dioxide concentration (red line) measured at Mauna Loa Observatory, Hawaii from March of 1958 to February of 2014.[10] The black curve represents the seasonally corrected data.

1.1.2 Methane capture

Methane (CH_4) is also a substantial driver of global climate change, contributing 30% of current net climate forcing.[11] In addition, concern over methane is mounting due to leaks associated with rapidly expanding unconventional oil and gas extraction and the potential for large-scale release of methane from the Arctic.[12] At the same time, methane is a growing source of energy,[13] and aggressive methane mitigation is increasingly recognized as key to avoiding dangerous levels of global warming.[14, 15]

Methane is emitted at a wide range of concentrations from a variety of sources, including natural gas systems, enteric fermentation (livestock), landfills, coal mining, manure management, wastewater treatment, rice cultivation, and a few combustion processes. We can generally group the methane concentrations of sources into three categories: high purity (>90%), medium purity (5-75%), and dilute (<5%). High-purity methane can be sold to the commodity natural gas market or converted to other chemicals (e.g, methanol and carbon black). Medium-purity methane includes landfill gas, coal-mine drainage gas, anaerobic digester gas, and low-quality gas from fossil formations. A variety of technologies have been developed for generating electricity or high-grade process heat from medium-purity methane, including technologies such as the homogeneous charge gas engine that operates just above the methane flammability limit in air (5%). Small or inconvenient flows of medium-purity methane are often simply flared.[12] Treatable dilute methane sources are some of the largest in total emissions, including coal-mine ventilation air, manure storage headspace and animal feeding house ventilation air. Some technologies have been developed for oxidizing dilute methane, such as the thermal flow-reversal reactor, but they generally yield only low-grade heat or small amounts of electricity as a co-benefit.

It is therefore highly desirable to be able to concentrate a dilute methane stream to medium purity to effectively utilize the energy, or to concentrate a medium-purity stream to high purity to convert it to a liquid or sell it directly. Conversion is especially attractive for many small or remote sources. Purification of some medium- and higher-purity natural gases is currently practiced industrially by sorption of the non-methane components (CO_2 and H_2).[16] The practice becomes uneconomic or impractical below about 40% methane.[16] For methane concentrations <40%, or for separation of methane from air rather than acid gases, we would like a sorbent that preferentially absorbs methane itself.

1.1.3 Ethane/ethene separation

Ethene is one of the largest production chemical products today due to, in large part, the demand for polyethylene. Global annual production capacity exceeds 152 million tonnes and is projected to grow by 20% over the next 5 years.[17] Large-scale production of ethene involves separating mixtures with light hydrocarbons, including methane, ethane, and propane. To achieve acceptable purity, these compounds are typically separated using a series of low-temperature distillations at high pressure.[18] The small difference in relative volatility of ethane and ethene makes the separation energy and capital intensive.

1.2 Nanoporous materials

In this dissertation, we focus on nanoporous crystalline materials. Examples of such materials include include zeolites, zeolitic imidazolate frameworks (ZIFs), and metal-organic frameworks (MOFs).[19–22]

1.2.1 Zeolites and zeolitic imidazolate frameworks (ZIFs)

Zeolites are widely used in the chemical industry as catalysts and adsorbents. Zeolites are porous aluminosilicates with pore diameters on the order of one to a few molecular diameters. These 3D crystalline solid structures are built from the building units of tetrahedral SiO_4 and AlO_4. Al has a formal charge of +3e compared to Si of +4e. To compensate for the net negative charge on the framework, aluminosilicate structures require extra framework cations, e.g, H^+, Na^+, Mg^{2+}, Ca^{2+}, etc. It should be noted that some zeolites can be made in pure-silica forms, i.e., $Si:Al = \infty$. Until now, around 200 distinct zeolite topologies have been reported.[23] Despite the relatively small number of experimentally realized zeolites structures, millions of hypothetical pure-silica zeolites have been predicted.[24] Given that each pure-silica zeolite could potentially exist with varying Si:Al ratios and different types of cations, the chemical and topological space of zeolite materials is huge.

ZIFs are, in principle, a class of metal-organic frameworks (MOFs) that have a pore topology that is isomorphic with zeolite structures.[22,25] In ZIFs the transition metal atoms (M) replace the Si atoms and imidazolates (IM) replace bridging oxides in zeolites. Given that the M-IM-M angle is similar to the Si-O-Si angle, ZIFs form 3D networks with topologies that are similar to zeolites.

1.2.2 Metal-organic frameworks (MOFs)

MOFs are a relatively new class of porous materials first synthesized about a decade ago and have become of great interest to the chemistry and material community.[26] MOFs are crystalline materials consisting of metal centers connected by organic linkers. One of the attractive features of MOFs is that they are highly tunable materials, and one can possibly synthesize an ideal framework by using exactly the right combination of metal center and organic linker for optimal performance. To date, over 20,000 MOF structures have been reported.[26] There is, however, an order of magnitude more structures, i.e., 137,953 hypothetical structures, have been predicted by enumerating existing metal clusters and organic linkers that have been used for MOFs synthesis.[27] Martin et al. further proposed an alternative approach to enumerate structures by using commercially available organic molecules.[28] Moreover, it has also been shown that MOFs can be synthesized with more than 2 different organic linkers to possess multiple functionalities, which is so-called MTV-MOFs.[29] In short, the possible number of MOF structure is close to infinite.

Importantly, there is a special subset of MOFs with so-called open-metal sites.[30] During the crystallization of such MOFs from a solution, solvent molecules can directly coordinate to the metal sites. Once the MOF crystals are formed, the material can be activated by removing these solvent molecules, leaving under-coordinated, open-metal, sites. The open-metal sites are responsible for some unique properties. For instance, M-MOF-74, also known as M-CPO-27, frameworks (e.g., M = Mg, Zn, etc.) have been demonstrated to have extraordinarily high CO_2 adsorption capacity and selectivity toward CO_2 over N_2 under flue gas conditions, highlighting them as promising candidates for CCS applications.[31–33]

1.3 Outline of dissertation

In summary, the chapters of this dissertation are organized in the following way:

Chapter 2 demonstrates the use of efficient molecular simulations which we have developed on graphic processing units (GPUs) to efficiently evaluate over one hundred thousand materials as adsorbents or membranes for carbon dioxide capture, methane capture, and ethane/ethene separation. A number of promising materials are identified to provide useful guidelines for experimental synthesis. More importantly, insightful observations regarding optimum materials are provided, which can lead to a better rational design of new materials.

Chapter 3 proposes efficient methodologies to use information from first-principles calculations to make accurate predictions. Two different methods are proposed in this chapter. First, we propose a systematic way to obtain accurate force field parameters from cluster MP2 calculations with the NEMO decomposition technique. Moreover, the methodology has been further modified to be fully compatible with periodic DFT calculations. This methodology has been proven to provide accurate predictions of CO_2, N_2, and H_2O adsorbed in open-metal site MOF materials, or even MOFs without open-metal sites. Second, we have also introduced an efficient way to make corrections to trial force fields to improve the quality of predictions with the requirement of only a few quantum chemical calculations.

Chapter 4 explains how molecular simulations are used to understand the dynamics of CO_2 adsorbed in Mg-MOF-74. An interesting hopping motion is observed, which can be used to properly explain the experimentally measured chemical shifts of ^{13}C labelled CO_2 molecules adsorbed in a powder Mg-MOF-74 sample. Additionally, a prediction for the NMR signals of CO_2 adsorbed inside Mg_2(dobpdc) is made. The prediction has been further validated by experimental measurement.

Chapter 5 concludes the dissertation.

It should be noted that this dissertation puts more emphasis on the carbon dioxide capture applications than on methane capture and ethane/ethene separation.

Chapter 2

Large-scale screenings of materials for various gas separations

Porous materials have the potential to provide a more energy-efficient means of accomplishing several gas separations. The chemical and topological space of possible materials is too large to study experimentally. For instance, around 200 distinct zeolite structures have been synthesized[23] but there are still over millions of hypothetical zeolite structures.[24] Therefore, computational approaches can play an important role in accelerating the search for optimum materials.

In this chapter, we present screening studies of over hundred thousand zeolites and zeolitic imidazolate frameworks (ZIFs) for their potential use in carbon dioxide capture, methane capture, and ethane/ethene separation through adsorption- or membrane-based processes. The organization of this chapter follows as below:

- Section 2.1 - 2.3: Carbon capture
    - Section 2.1 *In silico screening of carbon-capture materials*:[1] this section presents a large-scale screening study of zeolites and ZIFs for their performance in carbon capture and sequestration (CCS) applications through adsorption processes. A number of materials are identified that have the potential to reduce the parasitic energy of CCS by 30-40% compared to the near-term MEA technologies.
    - Section 2.2 *Predicting large CO_2 adsorption in aluminosilicate zeolites for post-combustion carbon dioxide capture*:[34] this section introduces two simple geometry descriptors in pure-silica zeolite structures for predicting aluminosilicate zeolites with high CO_2 adsorption uptake at postcombustion flue gas conditions.
    - Section 2.3 *Large-scale screening of zeolite structures for CO_2 membrane separations*:[35] this section presents a large-scale screening study of pure-silica zeolite membranes for their potential for CO_2/CH_4 and CO_2/N_2 separations.
- Section 2.4: Methane capture

  - Section 2.4 *New materials for methane capture from dilute- and medium-concentration sources*:[2] this section presents a large-scale screening of pure-silica zeolites for their potential to capture methane from low- and medium- concentration sources through adsorption processes.

- Section 2.5 : Ethane/ethene separation
  - Section 2.5 *Large-scale computational screening of zeolites for ethane/ethene separation*:[3] this section presents a large-scale screening of pure-silica zeolite adsorbents for their potential use in ethane/ethene separation.

The results obtained from these large-scale screening studies can facilitate the search for optimum materials. In addition, the insights obtained from these studies may lead to a better rational design of new materials.

2.1 *In silico* screening of carbon-capture materials*

2.1.1 Introduction

One can use simple thermodynamics to estimate the minimum energy required to separate CO_2 from flue gases (typically, 70-75% N_2, 13% CO_2, 5-7% H_2O, 3% O_2 at 40^{o}C and 1 atm) from coal-fired post-combustion power-plants. If we capture 90% of the CO_2 from a coal-fired power plant with the separation performed at 40^{o}C, the minimum energy required is of the order of 4-5% of the energy produced by the power plant.[36] Near-term capture technologies are projected to use five times the thermodynamic limit.[36] This suggests that capture processes that use less energy may be feasible. The technology for CO_2 capture considered near-term for power plants was developed as far back as the 1930s.[37,38] This technology uses aqueous solutions of amines that react with CO_2 to form carbamates and are therefore highly selective in capturing CO_2. One drawback of these amine solutions is that they contain 70% water by weight, and the regeneration cycle involves heating and evaporating large volumes of water, making the process energy intensive. Alternative separation processes that use other solvents, solid adsorbents, or membranes have the potential to require less energy.[36] One of the main challenges here is that many properties of CO_2 and N_2 are similar, and hence success of these approaches relies on the development of novel materials sensitive to these small differences. For adsorbent-based gas separations, it is important to have adsorbents with a large internal surface;[39] examples of such material include zeolites, ZIFs, and metal-organic frameworks (MOFs).[19–22] As introduced in chapter 1, the total number of possible structures of these materials is very large: hundreds of thousands of possible zeolites with different pore topologies exist in the zeolite database,[24] and a nearly infinite number of different types of MOFs can be created by changing the type of the metal and the organic linker. Therefore, we have developed a viable computational strategy to characterize large databases of carbon capture materials and identify optimal materials for CO_2 separation.

Several articles on screening for optimal separation materials have been published.[40–43] These articles consider a limited set of 10-20 different materials, which is insufficient to characterize the hundreds of thousands of different possible topologies.[24] In addition, these studies often focus on a single material property, such as selectivity or residence time, at a specific condition. However, optimizing the residence time[41] or uptake[42] in the adsorption step, for example, ignores that a material effective at adsorbing CO_2 might be difficult to regenerate. More importantly, these studies do not consider that different materials perform optimally at different conditions. In this work, we take another approach. For each material we determine the optimal process conditions by minimizing the electric load imposed on a power plant by a temperature-pressure swing capture process using that material followed by compression. This minimum load, which we call parasitic energy, is introduced as a metric

---

[*] Material in this section is based on *Nat. Mater.*, **2012**, 11, 633-641.[1]
Link: http://dx.doi.org/10.1038/nmat3336

to compare different materials.

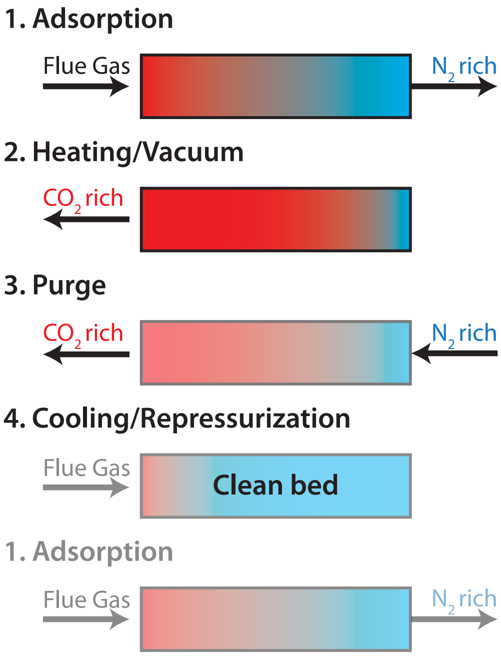

Figure 2.1: Hybrid pressure and temperature swing adsorption. In the adsorption step (1) the flue gas is brought into contact with the solid adsorbent. The material selectively adsorbs CO_2 and (nearly) pure N_2 leaves the adsorber. When the adsorber is saturated, it is regenerated (2) by heating the system and/or applying a vacuum. The purge (3) and cooling or repressurization step (4) brings the system back to its original state (1). The amount of CO_2 that is removed from the flue gas in a single cycle defines the working capacity of a material. The regenerated CO_2 is subsequently pressurized to 150 bar for geological storage.

2.1.2 Process Model

Separation of gases using microporous materials exploits the fact that at flue gas conditions CO_2 selectively adsorbs in the pores of these materials. By increasing the temperature, decreasing the pressure, or a combination of both, nearly pure CO_2 can be recovered. Figure 2.1 illustrates such a temperature-pressure swing separation process. Regardless of the regeneration method, the parasitic energy of a CCS process can be readily modeled if equilibrium adsorption and desorption are assumed. While there are many possible process configurations, they all rely on the difference between adsorption and desorption conditions to capture CO_2. The processes vary primarily in their method of gas-solid contacting and heat transfer, though neither of those factors affects performance under equilibrium assumptions. The energy required for this process has three main components: (1) energy to heat the material,

(2) energy to supply the heat of desorption (equal to the heat of adsorption), and (3) energy required to pressurize CO_2 to 150 bar, which is a standard requirement for transport and storage.[9] For a specific material and a fixed adsorption condition, we vary the desorption conditions and calculate the CO_2 and N_2 loading differential between the adsorption and desorption conditions to compute the quantity and purity of CO_2 captured. The thermal energy requirement (Q) of the process per unit mass of CO_2 captured (Δq_{CO_2}) is the sum of the sensible energy needed to heat the bed to the desorption temperature and the energy needed to supply the heat of adsorption.

$$Q = \frac{C_p m_{sorbent} \left(T_{final} - T_{flue}\right) + \left(\Delta q_{CO_2} \Delta h_{CO_2} + \Delta q_{N_2} \Delta h_{N_2}\right)}{\Delta q_{CO_2}} \tag{2.1}$$

where C_p is the specific heat capacity of the adsorbent, $m_{sorbent}$ is the mass of the adsorbent, $T_{final} - T_{flue}$ is the temperature differential between the adsorption and desorption conditions, Δq_i is the difference in loading and Δh_i is the heat of adsorption for each species. The loading at specific conditions is calculated using competitive adsorption isotherms, and the heats of adsorption are obtained directly from the molecular simulations. In a power plant, this thermal energy is supplied by diverting steam from the power cycle. Diverting steam effectively imposes a parasitic load on the power plant, which we compute as the product of the thermal energy requirement (Q), the Carnot efficiency (η) of the extracted steam, and the typical efficiency of a turbine(75%).[43] The compressor work, W_{comp}, is obtained from a multi-stage intercooled compressor model with real gas properties using NIST REFPROP[44] for fluid property data. We assume a staged compression, intercooled to 40°C, with a maximum pressure ratio of 2.5 and anisentropic efficiency of 85% below the supercritical point and 90% above it. Finally, the parasitic energy, E_{eq}, imposed on the power plant of the CCS process, is given by:

$$E_{eq} = 0.75 \eta_{T_{final}} Q + W_{comp} \tag{2.2}$$

For each material we find the optimal process conditions by minimizing this parasitic energy. Using a similar analysis, a state-of-the-art amine capture process would have a parasitic energy of 1,060 kJ/kg CO_2. A more rigorous engineering analysis of an amine process retrofitted to a coal-fired power plant which includes pressure drop through equipment, losses in heat exchangers, and other energy losses, shows a parasitic load of 1,327 kJ/kg CO_2 about 25% higher.[9] Therefore, we seek materials that exhibit a parasitic energy significantly lower than 1,060 kJ/kg CO_2 with the expectation that, similar to the amine process, a more detailed analysis of a process attached to a power plant will increase this number. We also emphasize that for the present analysis we treat the flue gas as a binary gas mixture of 14% CO_2 and 86% N_2. This assumption allows us to focus first on the energy consumption of these materials. If the energy consumption looks sufficiently attractive relative to other processes, additional criteria such as sensitivity to other flue gas components (e.g., H_2, SO_x, NO_x), as well as cost, attrition, stability, and availability can be examined.

2.1.3 Methods

We use molecular simulations to predict the adsorption properties. As input, these simulations require the crystal structure of the materials and a force field describing the interactions. In addition, by accelerating computationally expensive steps in molecular simulation using GPUs, we enable screening of materials in a high-throughput manner.

2.1.3.1 Crystal structures

For the pure-silica zeolite structures, we used the experimentally realized zeolite crystal structures from international zeolite association (IZA)[23] and the database with predicted, fully optimized zeolite crystal structures from Deem and coworkers (i.e., predicted crystallography open database (PCOD)).[24,45] This database was constructed by searching the chemical space of possible SiO_2 structures that are zeolite-like. This was done by examining all 230 space groups and a wide range of unit cell dimensions and silicon densities. Symmetry operations acting upon crystalographically unique atoms were used to generate the full unit cell structure. A Monte Carlo procedure was used to sample this vast space of possibilities giving 2.6 million topologically distinct zeolite-like structures. These structures were optimized by detailed interatomic potentials.[46,47] Depending on the force field 330,000-590,000 of these structures are thermodynamically accessible, with energies 0-30 kJ/mol-Si above α-quartz. Of these structures we only considered those with pores with a diameter sufficiently large (above 3.25 Å) for CO_2 to enter.[48] The structures in this database have topological, geometrical, and diffraction characteristics that are similar to those of known zeolites.[24,45] For the alumnosilicate structures, the location of these Al sites is known only for a limited number of structures.[49,50] A reasonable starting point is to assume a random distribution of Al over the T-sites such that Lowenstein's rule[51] is obeyed, which implies a minimum Si:Al ratio of one. For this ratio and for Si:Al equal to infinity we have one unique structure. For the other Si:Al ratios there are many different possible distributions of the Al atoms over the T sites. For these ratios we generated at least ten different Al atom distributions and the cations were subsequently added at the minimum energy positions.[52] Each distribution can have a slightly different adsorption isotherm and we averaged the parasitic energy.[50] In addition, we compared the results for systems in which the cations were fixed at the minimum energy configurations, with simulations in which the cations were free to move. For structures with a low Henry coefficient, we found a lower parasitic energy compared to a system with moving cations. For those structures with optimal Henry coefficients, these differences were negligible. For ZIFs structures used in this study, we applied the similarity between zeolite and ZIFs to the zeolite database to generate ZIFs using the ZEO++ code.[48] In the reported zinc and IM-based ZIFs with IZA zeolite topologies[25] the distance between zinc atoms and the center of IM rings is about 1.95 times larger than the Si-O distance in zeolites. A ZIF structure was generated by scaling the unit cell of the corresponding zeolite structure by the same factor and exchanging each oxygen atom with an IM group and each Si atom with a Zn atom. We have validated the resulting ZIF geometries by comparing geometries of two structures for which the experimental geometries are known: ZIF-3 (DFT) and ZIF-10 (MER). The observed differences in the geometries do not translate into significant differences in the parasitic energy.

2.1.3.2 Model and simulation details

Calero and co-workers[50, 53] have developed a force field that accurately reproduces the experimental isotherms in zeolites. For ZIFs, parameters for the framework atoms were taken from the DREIDING force field[54] and parameters for N_2 and N_2 were taken from the TraPPE force field.[55] Framework-molecule interaction parameters were calculated using the Lorentz-Berthelot mixing rules. Partial charges for ZIF framework atoms were computed using the connectivity based approach of Zhong and Xu.[56] Adsorption isotherms were calculated using grand-canonical Monte Carlo simulations (GCMC).[57] The experimental equations of state are used to convert (partial) pressures into chemical potentials.

2.1.3.3 GPU calculations

To screen a large number of zeolite and ZIF structures we developed a graphics processing unit (GPU) code to accelerate the molecular simulations. We focus on computing the Henry coefficients and the heats of adsorption in this study. The algorithm is divided into three different routines: (1) energy grid construction, (2) pocket blocking, and (3) Widom test particle insertion.

- Energy grid construction: To save computational time we construct a grid, giving the energies of the atoms at the grid positions in the unit cell of a framework.[49] The energy grid has a mesh size of 0.1 Å and the interaction between the gas molecule and all of the framework atoms is modeled by the Lennard-Jones potential and the Coulomb potential, with Ewald summations used to calculate the latter. Each of the grid points maps to a single CUDA (Compute Unified Device Architecture) thread and the pairwise potentials are computed in parallel across different CUDA blocks.[58] The positions of the framework atoms are put inside the fast constant memory in the GPU to expedite calculations. At the end of the routine, the array that contains the energy values is transferred from the GPU to the CPU as an input to the pocket blocking routine.

- Pocket blocking: In a GCMC simulation, one can insert molecules in pockets that are inaccessible from the outside.[59] The void space analysis algorithm[60] is used to detect and block these inaccessible pockets.[61] We use the values from the energy grid to determine the accessibility of a particular configuration/point in the unit cell using the (multicore) CPU, as this routine does not map well to the GPU architecture. The discrete energy grid is mapped to a binary grid of accessible/ inaccessible points based on a certain threshold value that is chosen to be large enough such that on an experimental time scale, the pocket is considered inaccessible. Finally, we utilize a parallel flood fill algorithm to segment the grid into connected, accessible regions. These regions are then classified as either channels or inaccessible pockets, and we set all grid points inside pockets to a very high-energy value.

- Widom test particle insertion: utilizing this revised energy grid, we can calculate both the Henry coefficients and the heats of adsorption using Widom insertion moves.[57] We randomly insert a guest molecule inside the simulation box and calculate both the Boltzmann factor and the energy values for the particular guest molecule configuration. We can use interpolating functions to estimate the energy values at points that are not directly on the grid. In the GPU architecture, each CUDA thread can conduct independent Widom insertion.

Overall, most of the computational wall time is spent in the GPU energy grid construction routine. In this routine, there is roughly a factor of 50 in performance improvement going to the GPU (Tesla C2050 Fermi) from the CPU (single core of a 2.4 GHz Intel 5530 Xeon).

2.1.4 Results and discussion

To determine the minimum parasitic energy of a material, the most important data are the (mixture) adsorption isotherms. As the experimental adsorption isotherms are known for only very few materials, we rely on molecular simulation to predict these isotherms for the different materials. Conventional grand-canonical Monte Carlo (GCMC) simulations allow us to predict a complete isotherm on the basis of the crystal structure of the material.[49,57] These simulations, however, require on the order of days of CPU time, which is prohibitively slow to screen hundreds of thousands of materials. To obtain adsorption isotherms in a high-throughput manner, we have developed an efficient algorithm that allows us to obtain a complete isotherm in a few seconds on a graphical processing unit (GPU). Our method relies on the observation that pure component adsorption isotherms in these materials can be accurately described using dual- or single-site Langmuir isotherms:[62]

$$q = \sum_{j=1}^{N} \frac{K_{H_{i,j}} P_i}{1 + \frac{K_{H_{i,j}}}{q_{sat_{i,j}}} P_i} \tag{2.3}$$

where q_i is the loading at the partial pressure P_i of the component i, $K_{H_{i,j}}$ is the Henry coefficient, and $q_{sat_{i,j}}$ is the saturation loading of the component i corresponding to adsorption site j. In our model, only the single-site (N equal to 1) isotherm was adopted for N_2 while either single- or dual-site (N equal to 2) isotherms were applied for CO_2. The temperature dependence of the Henry coefficients follows directly from the heats of adsorption, both of which were obtained from molecular simulations. The total saturation loading of the pure component gas was calculated using a correlation of guest molecule density in the framework to pore diameter. For CO_2 adsorption, the use of dual-site isotherms is required for structures that contain particularly strong adsorption sites; this behavior arises because

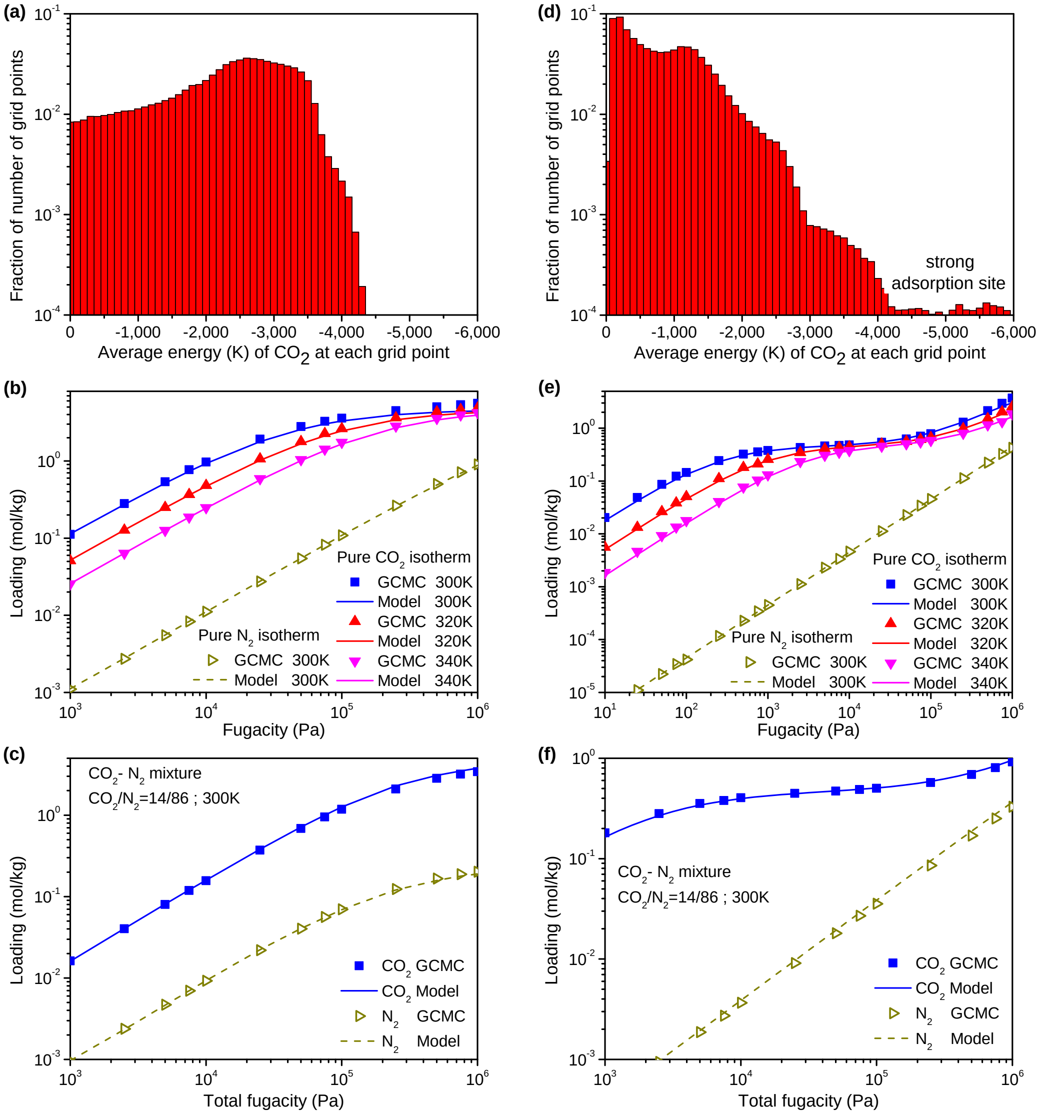

Figure 2.2: Probability distribution of the energies of a particle inserted in the pores (a,d), pure component isotherms for CO_2 and N_2 and pure CO_2 isotherms at different temperatures (b,e), and mixture isotherms (c,f) for two materials: the zeolite SIV (a-c) and the predicted zeolite PCOD8286959 (d-f). The symbols are the results from the GCMC simulations and the lines are the results of our methodology using the GPU calculations.

CO_2 first adsorbs at these sites, and only once all these positions are saturated in the rest of the material. Figures 2.2(a) and 2.2(d) illustrate the difference between materials best described by single-site and dual-site isotherms, respectively. The long tail at low energies in the energy distribution is a signature of the presence of these strong adsorption sites. If such a signature exists, we use a dual-site description; otherwise, the isotherm is described using a single-site. Figure 2.2(e) shows a typical case of such a dual site isotherm for pure CO_2. One observes a plateau in the isotherm at low pressure, which results from the saturation of the strong adsorption sites. Each strong adsorption site can generally accommodate only one CO_2 molecule, so the saturation loading for these sites is just the sum of the number of unique sites. We have developed an automated algorithm to identify the presence of these sites during molecular simulation and accordingly divide the structure into two regions, computing their own associated Henry coefficients, heats of adsorption, and saturation loadings. Figures 2.2(b) and 2.2(e) demonstrate that our model is able to predict the correct temperature dependence of the pure component isotherms.

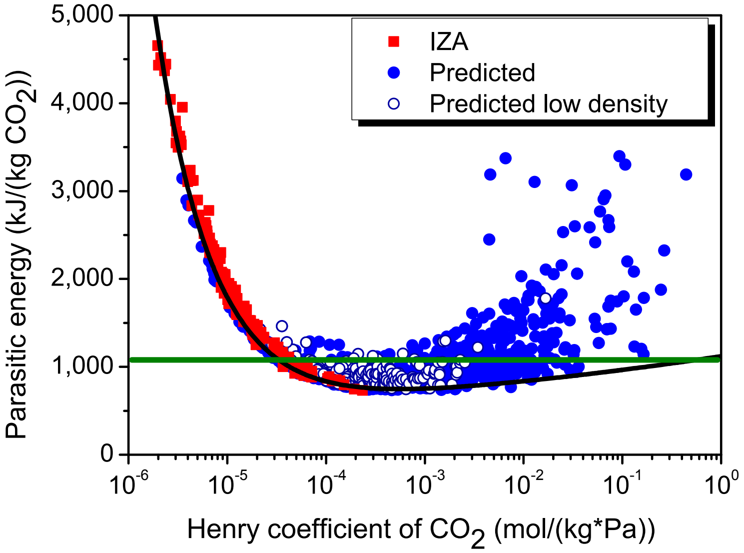

Figure 2.3: The comparison of parasitic energies between the IZA zeolite structures (red squares) with the predicted structures (blue circles). The open blue circles are computationally predicted structures near the low-density feasibility line, which are most likely to be synthesizable. The green line gives the parasitic energy of the current monoethanolamine (MEA) technology, and the black line is the minimal parasitic energy observed for a given value of the Henry coefficient in the pure-silica structures. In this graph, we plotted a representative fraction of all structures.

The most commonly used method to predict mixture adsorption isotherms is ideal adsorbed solution theory (IAST).[63] However, as carbon capture of flue gases occurs at relatively low pressure, competitive Langmuir isotherms give an equally good description. In case a dual-site model for CO_2 is used, we assume that N_2 is not able to compete with CO_2 at the stronger adsorption site, and take the saturation value for N_2 to be the same as CO_2 outside of the strong adsorption region, which is required for consistency with the assumption of the competitive adsorption isotherm.[64] To test the reliability of the competitive

Langmuir model in predicting the mixture isotherms on the basis of the pure components, we used the GCMC simulated mixture adsorption isotherms as experimental data to test whether the Langmuir model correctly predicts these mixture isotherms given the predicted pure component isotherms. We have tested over 50 different structures and for all systems, the competitive model accurately reproduces the mixture isotherms over a large range of pressures, including the partial pressures relevant for flue gas separations. Figures 2.2(c) and 2.2(f) demonstrate the performance of the competitive isotherm model with the corresponding GCMC simulations (More results for other structures can be found in supporting information of ref 1).

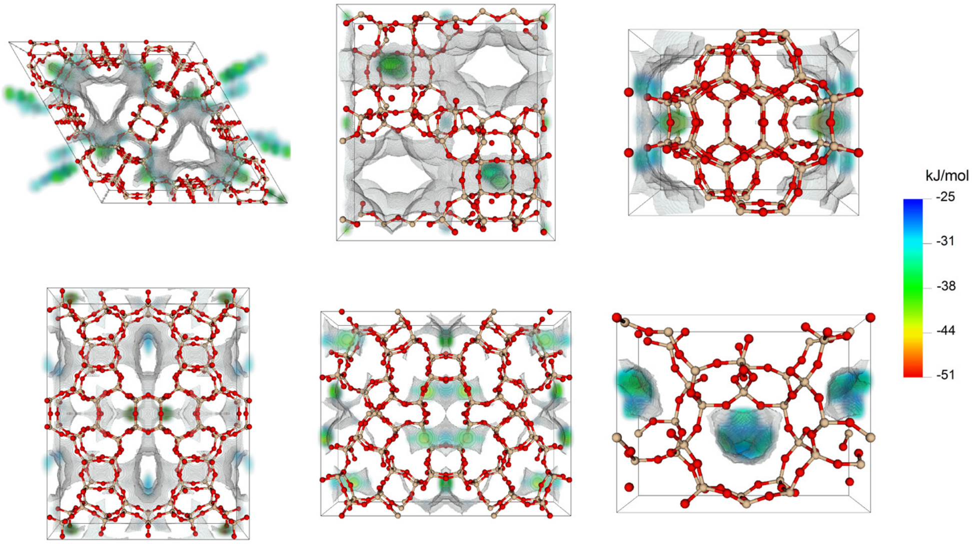

Figure 2.4: Examples of the optimal pure-silica structures. Out of the fifty top performing materials we selected the six most diverse. The figures show the atoms of materials as ball and stick (O, red; Si, tan). The surface gives the local free energies in the pores of the material, where more negative energies indicate the dominant CO_2 adsorption sites.

Figure 2.3 shows the optimized parasitic energy as a function of the CO_2 Henry coefficient for all known zeolite structures. For these materials we observe a monotonically decreasing parasitic energy as a function of the Henry coefficient. To investigate the lowest parasitic energy that can be obtained using these materials, we perform calculations on a database containing over three hundred thousand predicted zeolite structures.[24] These calculations identify predicted structures with parasitic energy that is lower than can be obtained for the known structures. Figure 2.4 shows some of the structures that have near-optimal parasitic energy. To analyze the effect of these uncertainties on the overall parasitic energies, we selected a set of materials that spanned the range of parasitic energies. To simulate the propagation of possible errors on the thermodynamic input parameters in the parasitic energy, we changed each of these values by multiplying the actual value of a parameters by

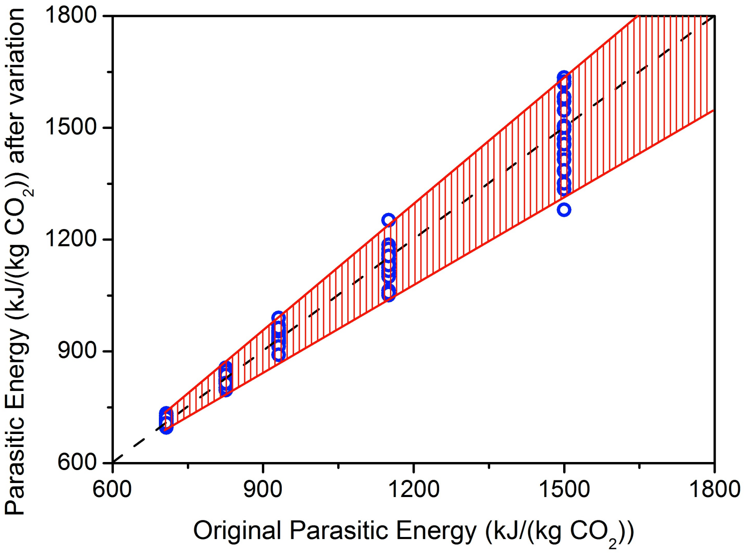

Figure 2.5: Uncertainties in the estimates of the parasitic energies. The blue dots are the 25 parameters sets for which we recalculated the parasitic energy after a change of +/- 20% of all parameters. The red line gives the upper and lower bounds of the errors in these sets.

a factor, which was randomly selected from the interval [0.8, 1.2], i.e., a maximum possible error is plus or minus 20% on each of the thermodynamic variables. In this way, we generated, for each of the selected parasitic energies, 25 different sets of parameters. Figure 2.5 shows how these uncertainties propagate for a given value of the parasitic energy. We see that for high values of the parasitic energy, the results are much more sensitive. The reason is that small changes in the Henry coefficient have a large effect on the parasitic energy. In contrast, for low values of the parasitic energy the results are robust. This is consistent with the observation that we have for these materials a very broad optimum. Hence, some variations in the parameters have little influence, as at slightly different conditions a very similar optimal parasitic energy can be found. As we are mainly interested in materials with a low parasitic energy, this analysis shows that a 20% uncertainty in the main thermodynamic parameters should not have a significant influence on our estimates of the parasitic energy.

The parasitic energy as a function of the Henry coefficient shows three regimes. The mixture isotherms in these regimes are shown schematically in Figure 2.6, 2.7, and 2.8. Adsorption of CO$_2$ takes place at flue gas conditions (1 atm and 40^{o}C). The subsequent desorption is achieved by decreasing the (partial) pressure and/or increasing the temperature. The difference in CO$_2$ concentration between adsorption and desorption defines the working capacity of a material and gives the amount of CO$_2$ that is removed in an adsorption cycle. For materials with a small Henry coefficient (see Figure 2.6), the performance is poor because the working capacity is small, yet the entire system needs to be heated to the desorption conditions, giving a high parasitic energy. In addition, the adsorption of CO$_2$ is of the same

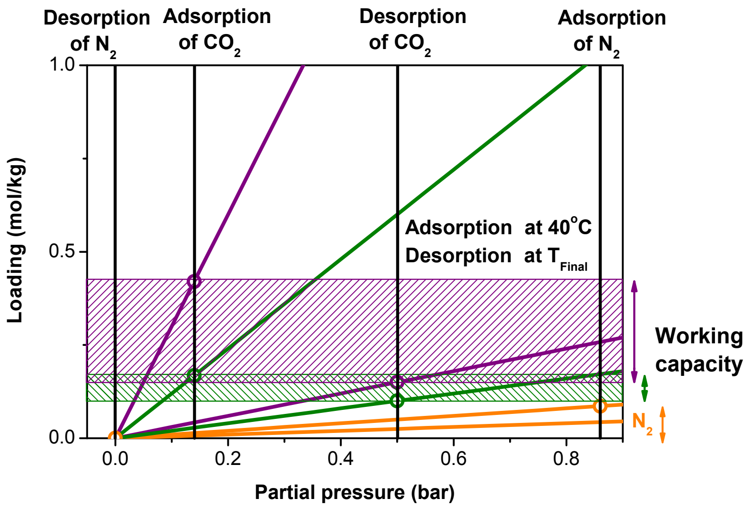

Figure 2.6: A material for which the Henry coefficient is small such that both the adsorption and desorption are in the Henry regime. A low Henry coefficient (green) gives a relatively small working capacity and purity of the product stream. Increasing the Henry coefficient (purple) gives a significant increase of the working capacity.

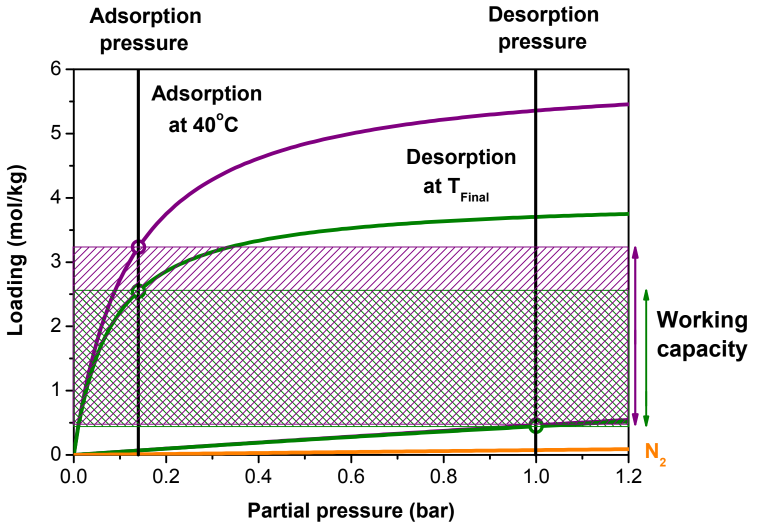

Figure 2.7: A material for which the Henry coefficient becomes much larger such that the number of adsorbed CO_2 molecules is so large that CO_2-CO_2 interactions in the materials are important at the partial pressure of CO_2 corresponding to flue gas conditions. Hence, the adsorption cannot be characterized with a Henry coefficient only.

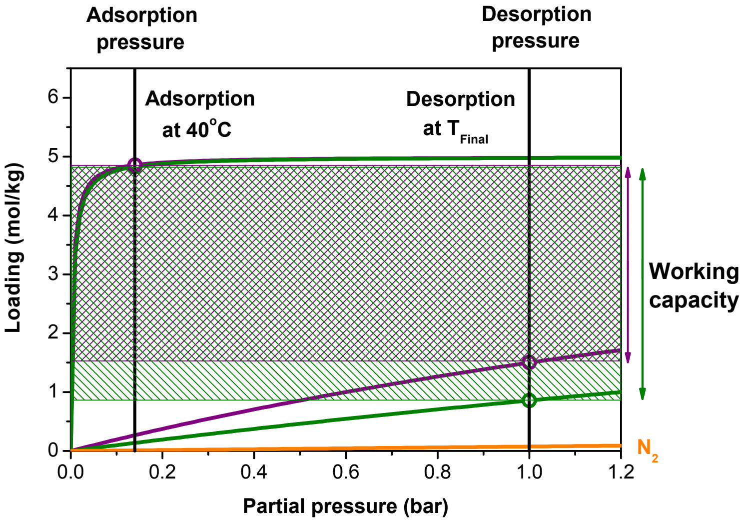

Figure 2.8: A material for which the Henry coefficient is very large such that a further increase of the Henry coefficient will have little effect on the uptake value at adsorption, as this is now dominated by the pore volume. For desorption, however, increasing the Henry coefficient will further decrease the working capacity.

order of magnitude as N_2 in these materials and hence the selectivity of such a material is unusably low. Materials with a larger Henry coefficient have a significantly larger working capacity and correspondingly lower parasitic energy. This trend continues until the Henry coefficient of the material is so large that at flue gas conditions the pressure is too high for the CO_2 adsorption to be in the linear regime. Figure 2.7 shows that at these conditions the CO_2 loading at the adsorbed state is not fully determined by the Henry coefficient anymore, and that materials with the same Henry coefficient have different working capacities depending on the pore volume. Figure 2.8 illustrates that at even larger Henry coefficients the adsorption of CO_2 becomes so strong that it becomes increasingly difficult to regenerate the material. Another important observation is that we have a broad optimum. The reason for this broad minimum is that the Henry coefficient shows a strong correlation with the heat of adsorption, and the heat of adsorption has two opposing contributions to the parasitic energy. As the temperature dependence of the Henry coefficient is proportional to the heat of adsorption, a higher heat of adsorption increases the working capacity. While this reduces the parasitic energy, it is offset by the requirement to supply more energy to desorb CO_2 which again increases the parasitic energy.

Our screening shows a large set of zeolite structures that have a parasitic energy well below the current technology (1,060 kJ/kg CO_2). Inspection of these optimal structures highlights their diversity: we find one-, two-, or three-dimensional channel structures, cage-like topologies, and more complex geometries. To illustrate this point we show in Figure 2.4 a diverse sample of structures[65] contained in the optimal zeolites. It is interesting to compare these with the optimal known zeolite structures in Figure 2.3. Several of the known zeolite structures have a sufficiently low parasitic energy, however, most of these known structures are one-dimensional channels, which may suffer from severe diffusion limitations.[24] By contrast, many of the predicted zeolite structures have adsorption sites, where CO_2 strongly adsorbs, along channels with larger diameters. Transport of CO_2 to and from the sites of adsorption occurs via the larger channels, so diffusion is not expected to be a limiting factor here. Interestingly, none of the known zeolites has this characteristic feature, and we consider this observation to be a significant discovery. This discovery was facilitated through the screening of an exhaustive number of possible topologies.

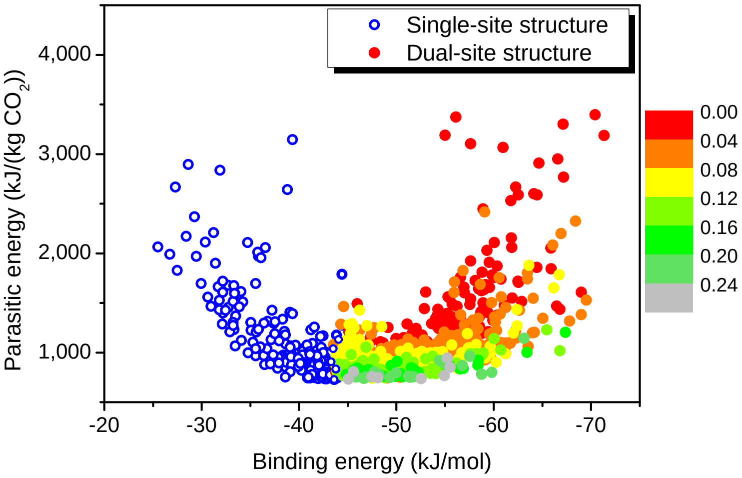

Figure 2.9: The parasitic energy as a function of the binding energy for a CO_2 molecule. The binding energy is defined as the lowest energy that can be observed in a given structure. If this binding is sufficiently strong, dual-site adsorption behavior will arise. The fraction of each materials volume which is occupied by low-energy strong adsorption sites is displayed as colored solid circles. The color bar gives the volume fraction of these low-energy regions. Structures without these specific features (that is, single site adsorption behavior) are displayed as open blue circles.

A common feature of most optimal materials is a set of local regions of the structure that bind CO_2 preferentially, leading to dual-site adsorption behavior. Figure 2.9 shows the parasitic energy as a function of the binding energy of a CO_2 molecule. To this figure we added those materials that have (near) optimal Henry coefficients, but without such dual-site behavior, which includes some of the known zeolite structures. We observe a similar correlation as for the Henry coefficient, since the binding energy dominates the Henry coefficient for structures with these preferential sites. The binding energy needs to be optimal: too low and the material adsorbs too little CO_2; too high and the material becomes too difficult to regenerate. Figure 2.9 further shows that the parasitic energy is influenced by the density of strong adsorption sites in the material; the optimal materials exhibit the largest number of strong adsorption sites per unit volume. This observation is important as it explains why these materials exhibit a lower limit for the parasitic energy. The existence of a strong adsorption site requires a minimum amount of zeolite material, which, combined with the size of a CO_2 molecule, gives an upper limit to the total number of such local regions that can exist per unit volume.

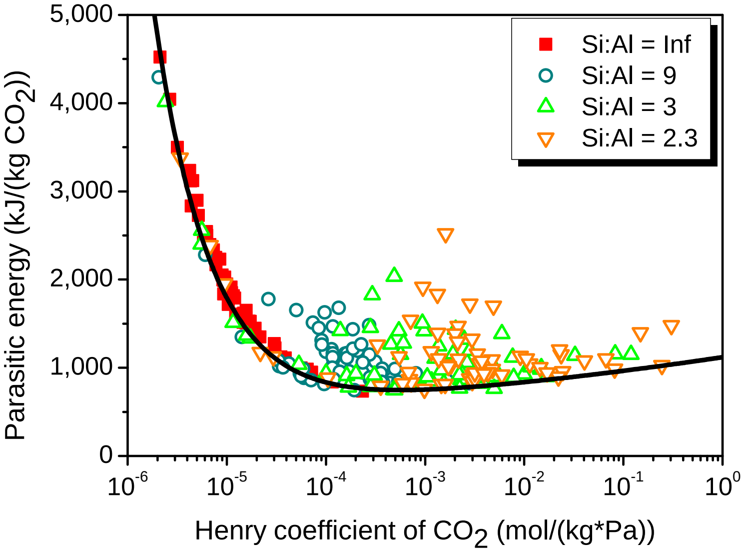

Figure 2.10: The parasitic energy as a function of the CO_2 Henry coefficient for known zeolite structures with different Si:Al ratios. In this study, we consider aluminosilicate zeolites with Na^+ cations. The pure-silica IZA structures are shown as red squares and the corresponding structures with different Si:Al ratios are labelled as indicated by open symbols.

An important practical question is whether we can synthesize these optimal materials. As the synthesis conditions of the known zeolites favor the formation of low-density structures,[45] one expects that among the predicted structures these low-density structures are the most likely ones to be synthesized. As highlighted in Figure 2.3, this subset has many structures with optimal performance indeed. Recent developments[66] in novel structure directing agents may make it possible to synthesize some of these structures. An alternative strategy to create optimal Henry coefficients is to synthesize zeolites with different Si:Al ratios. In aluminosilicate zeolites, cations are present in the pores to compensate for the charge imbalance introduced by the Al^{3+} that replaces a Si^{4+}. Figure 2.10 shows the effect of cations on the parasitic energy for the known zeolites with different Si:Al ratios (i.e., aluminosilicate zeolites with Na^+ cations). Cations create adsorption sites for CO_2 but also reduce the pore volume. The net result on the parasitic energy of these two effects depends on the particular structure. The addition of cations to low Henry coefficient structures causes a decrease in the parasitic energy due to the increased number of adsorption sites; however, additional cations eventually increases the parasitic energy as the pore volume decreases. By contrast, addition of cations to near-optimal Henry coefficient structures increases the parasitic energy since the decrease in pore volume dominates. It is important to stress that every structure has its own optimal Si:Al ratio. Comparison with the parasitic energy for the pure-silica structures shows that the addition of cations does not yield a material that has a lower parasitic energy for the same Henry coefficient. This observation is consistent with the notion that one has to create an adsorption site with exactly the right adsorption strength and that there is a limit to the maximum number of adsorption sites per unit volume.

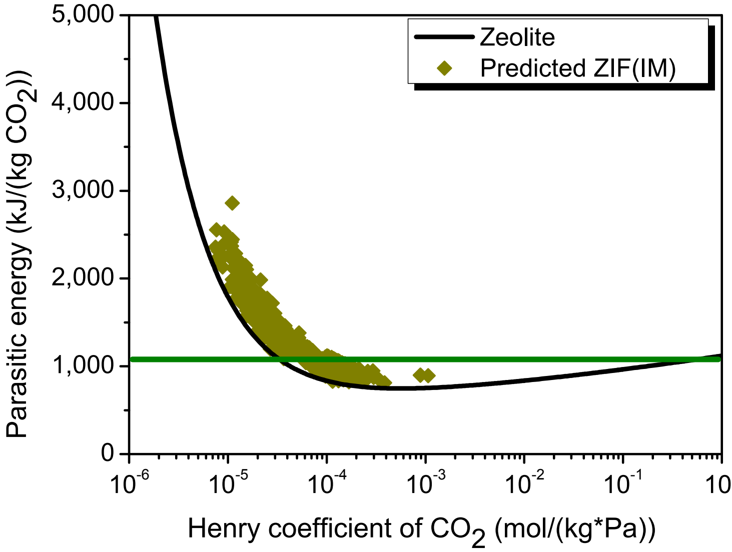

Figure 2.11: The parasitic energy as a function of the CO_2 Henry coefficient for ZIFs is shown. The green line give the parasitic energy of the current MEA technology, and the black line is the minimal parasitic energy calculated for a given value of the Henry coefficient in the pure-silica structures. In this graph, we plotted a representative fraction of all structures.

Figure 2.11 shows the parasitic energy for ZIFs. For these materials, the overall parasitic energy is higher than for zeolites. As we have focused on the simplest linker (imidazole), the selectivity towards CO_2 is rather low: linkers with higher selectivity will increase the Henry coefficient to a more optimal value and reduce the parasitic energy. Figure 2.12 gives a set of optimal ZIF structures. These structures look very different from the optimal zeolite structures; optimal ZIFs are those in which there are channels where CO_2 can access the non-hydrogen atoms of the structure.

2.1.5 Conclusions

There are important experimental consequences to our results. Our metric provides a direct insight into the overall performance of a material in an actual carbon capture process. In this

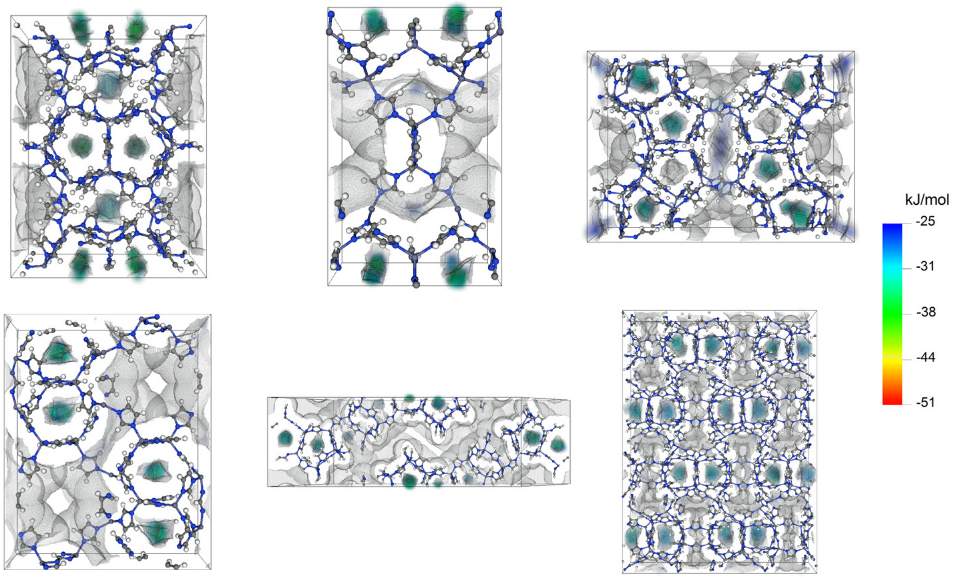

Figure 2.12: Examples of the optimal ZIF structures. Out of the fifty top performing ZIFs, we selected the six most diverse. The figures show the atoms of materials as ball and stick models (Zn, blue-grey; N, blue; H, white; C, grey). The surface gives the local free energies in the pores of the material.

context, it is instructive to compare our metric with the recently proposed alternative metric based on the adsorption breakthrough time.[41] Materials with a higher Henry coefficient, for a given saturation loading, will give a longer breakthrough time. However, as this study shows, materials with extremely high Henry coefficients perform poorly because the regeneration step cannot be ignored in a carbon capture process. This illustrates the limitation of focussing on a single material property rather than the entire process. Our screening establishes a theoretical limit for the minimal parasitic energy that can be achieved for a class of materials. Such a target will be useful to focus experimental efforts to synthesize such materials. Our screening gives for each class of material a unique structure that gives the best performance. However, from a practical point of view, 1-3% higher parasitic energies will not make the difference. To have many near optimal structures is very important as it increases the changes one of these structures can be synthesized. To facilitate this synthesis effort, all of these structures, together with all physical properties that lead to the increase in performance, are available online.[67] A specific outcome of our study is that an optimal carbon capture material has a sufficient number of adsorption sites with a binding energy that is sufficiently large to be selective, but not so large that it becomes difficult to desorb. This is a very general conclusion and explains why our parasitic energy curve holds for all materials we have studied. This parasitic energy curve can be used as a reference to benchmark other materials.

2.2 Predicting large CO_2 adsorption in aluminosilicate zeolites for postcombustion carbon dioxide capture[†]

2.2.1 Introduction

In aluminosilicate zeolites, the addition of cations changes the adsorption properties of the zeolite structure in two important ways: (1) it creates stronger adsorption sites due to the additional interactions between the CO_2 molecules and the cations, and (2) it decreases the saturation uptake of CO_2 due to the reduction in the free volume. In the adsorption isotherm, the modification is reflected as an increase in the CO_2 uptake at the low pressures and a decrease of uptake at high pressures. For the purpose of postcombustion CO_2/N_2 separation, these property changes can present a trade-off. Ideally, one would like to have as high as possible CO_2 uptake at the postcombustion flue gas condition.

There have been many experiments conducted on aluminosilicate zeolites that report significant uptake enhancement relative to the pure-silica zeolite adsorption data.[68–71] Moreover, there has been simulation work that can reproduce the experimental data on the few selected IZA zeolites with different Si:Al fractions.[1,53,72] However, to the best of our knowledge, there is no theory available that can tell us which properties of the pure-silica zeolites can lead to the best aluminosilicate zeolite structures. When referring to the best structures in this work, we use the pure component CO_2 uptake at the 0.15 bar as the quantity to be maximized as this is of interest to the postcombustion CO_2 separation community. For an aluminosilicate structure with higher CO_2 uptake at the pressure of 0.15 bar, it can potentially provide better performance in separations.

2.2.2 Methods

In our simulations, we utilize GCMC simulations to obtain the CO_2 uptake values at different pressures.[49,57,74] Same as the study presented in section 2.1, the aluminosilicate zeolite structures were generated by randomly replacing Si with Al atoms, while adhering to the Lowenstein's rule.[51] For the Na^+ cations, all of the Lennard-Jones interaction parameters and atomic charges were taken from the force field proposed by García-Sánchez et al.,[53] which has shown to be transferrable to multiple aluminosilicate zeolites at varying Si:Al ratios. For Ca^{2+}, the same Lennard-Jones force field from García-Sánchez et al. is used, but the charge is doubled. The positions of the cations were generated in two different ways: (1) fixed cations, where the cations were inserted one by one onto the unit cell at the global minimum energy configuration and (2) moving cations, where the cations were allowed to

---

[†] Material in this section is adopted with permission from *J. Am. Chem. Soc.*, **2012**, 134 (46), 18940-18943.[34] Copyright 2012 American Chemical Society.
Link: http://dx.doi.org/10.1021/ja309818u

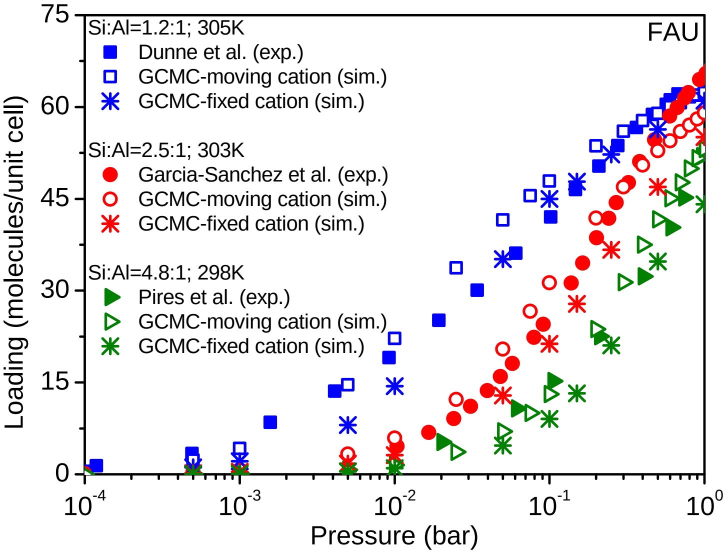

Figure 2.13: Comparison of the experimental and simulated CO_2 isotherm in aluminosilicate zeolite (Na) FAU with different Si:Al ratio. Both simulated categories: moving and fixed cation show generally good agreement with the experiment data.[53,70,73] The result with fixed cation shows lower uptake than the moving one, which provides a conservative prediction of loading in our study.

move during the GCMC simulations. Moving cations is, however, computationally expensive as it takes a very long time for the cations and adsorbates to equilibrate.[50,75,76]

Initially, the accuracy of our predictions on NaX, CaX, NaA, and CaA is checked by comparing the results with other simulation/experimental data as shown in Figures 2.13 and 2.14. Overall for NaX, there exists good agreement between our moving cations simulation data and other reported adsorption isotherm data under same conditions.[53,73] The fixed cations method generally under-predicts the CO_2 loading for most pressure values; however, there is good enough agreement that the method provides a conservative estimate of the CO_2 uptake for our screening purposes. For CaA and CaX, there is reasonable agreement between the fixed cations method and the experimental data from Bae et al.[71] although the simulation parameters of Ca^{2+} were not optimized.

To identify key structural predictors responsible for large CO_2 uptakes in aluminosilicate zeolite structures, we utilized Zeo++[48] to obtain the helium free volume (FV) and the D_i (largest included free-sphere diameter) for the 190 IZA structures and the predicted zeolite set (i.e., PCOD) of over 130,000 structures.[24] In searching for the predictors, we used the PCOD set instead of the IZA set, as having a larger number of structures at our disposal was more useful in establishing correlations. From the PCOD set, 400 zeolites were randomly selected from a FV bin size of 50 cm^3/kg. For these structures, Si:Al = 1:0 (pure-silica)

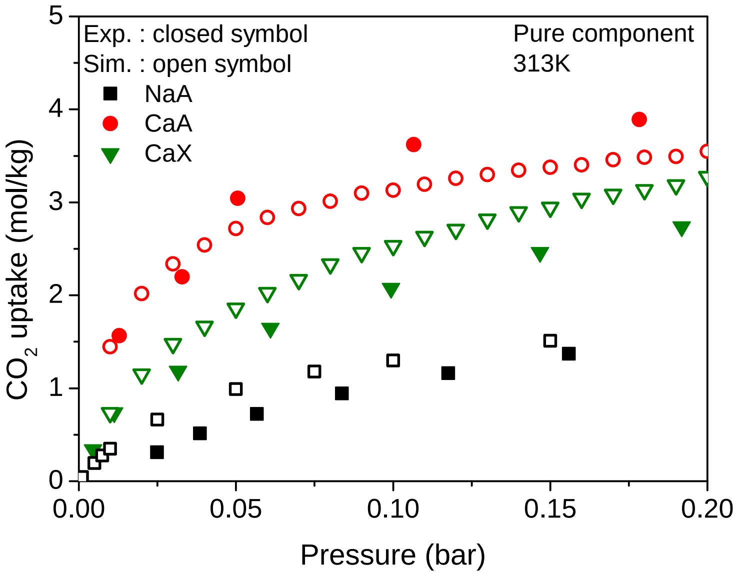

Figure 2.14: Comparison simulation isotherm with experimental data reported by Bae et al.[71] in NaA (black), CaA (LTA) (red), and CaX (FAU) (green). Calcium is further exchanged with the sodium in Si:Al = 1:1 aluminosilicate zeolite structure to obtain CaA and CaX with the exchanged ratio to be 72% and 93%, respectively. The closed symbol represents the experimental data and the open symbol shows the simulated result.

were used to generate Si:Al = 3:1 and Si:Al = 1:1 configurations along with minimum-energy fixed cation positions. In all of the structures, the adsorption properties were computed at 300K.

2.2.3 Results and discussion

Figure 2.15(a) shows the average CO_2 uptake as a function of the free volume (FV). For all pure-silica zeolites, we find that the CO_2 uptake is nearly constant. On the other hand for Si:Al = 3:1 and Si:Al = 1:1, aluminosilicate zeolite structures, the CO_2 uptake is close to zero for small FV as the cations occupy all of the free space in the structure. For larger FV, the stronger adsorption sites created by the addition of the cations coupled with the excess FV available for the CO_2 molecules enhance CO_2 adsorption in these structures. However, when the free volume becomes too large, only a small subset of the space is fully exploited, lowering its uptake. Because there are more cations present in the Si:Al = 1:1 Na^+ materials compared to Si:Al = 3:1, the CO_2 uptake for Si:Al = 1:1 is higher for zeolite structures with larger FV values and lower for smaller FV. Comparison between Ca^{2+} exchanged zeolites and Na^+ zeolites indicates that due to the larger charge on the Ca^{2+} cations coupled with reduced number of cations, the CO_2 uptake is larger at smaller FV for structures that

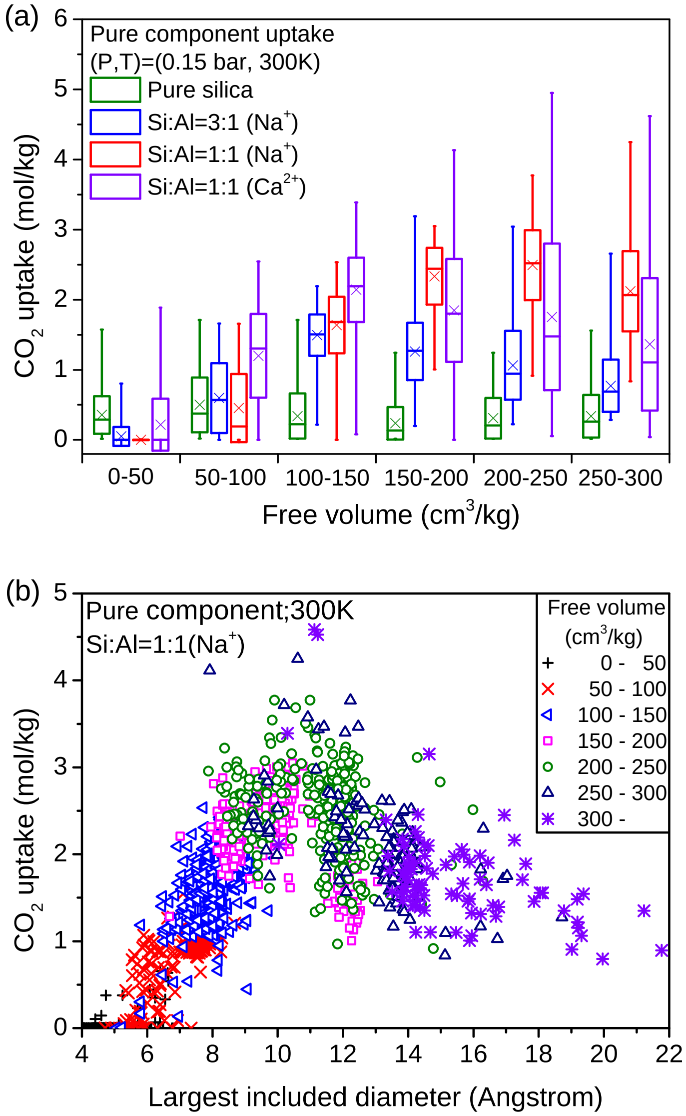

Figure 2.15: (a) Box plot of CO_2 uptake at 0.15 bar obtained from GCMC simulations for pure-silica (green), Si:Al = 3:1 (Na^+) (blue), Si:Al = 1:1 (Na^+) (red), and Si:Al = 1:1 (Ca^{2+}) (purple) as a function of free volume for six FV intervals with 400 predicted zeolite structures per interval. Each box represents from lowest to highest the minimum, average minus one standard deviation, median, average plus one standard deviation, and maximum uptake. Cross symbols represent the average CO_2 uptake values. (b) CO_2 uptake as a function of D_i for the same set of predicted zeolite structures as in (a).

contain Ca^{2+}.

The box plot in Figure 2.15(a) suggests that within the same FV bin, there are a large

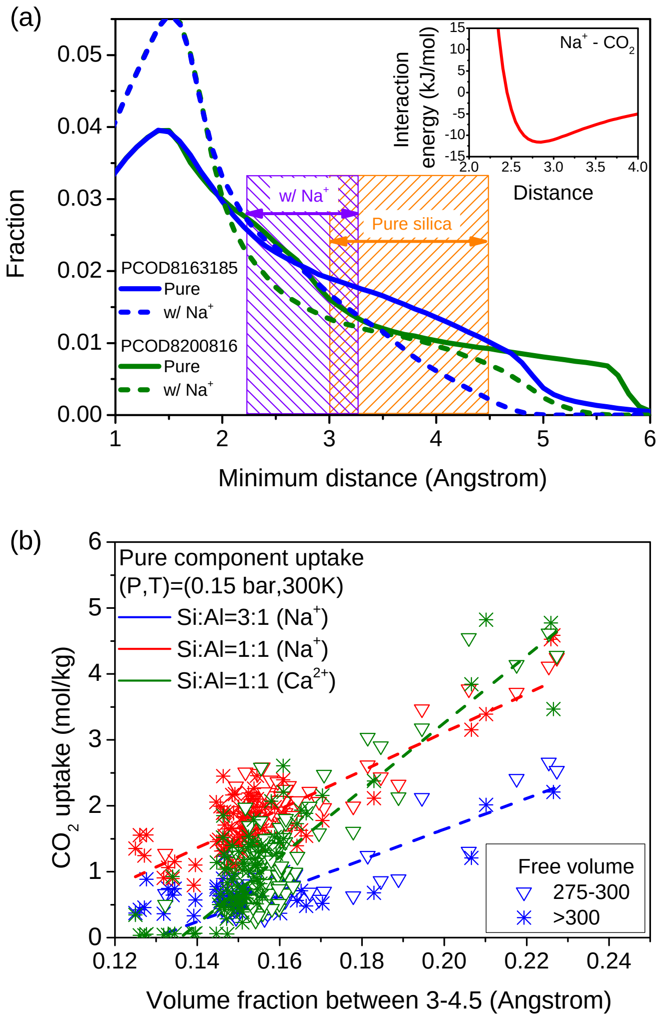

Figure 2.16: (a) Probability distribution of nearest-neighbor framework distances for the PCOD8163185 (blue) and PCOD8200816 (green) pure-silica zeolite structures (solid lines) and the structures with added Na^+ cations (dashed lines). The relative fraction of the total volume between 3 and 4.5 Å is significantly larger for PCOD8163185, leading to higher uptake (4.25 mol/kg) relative to PCOD8200816 (2.00 mol/kg) in the aluminosilicate zeolite structures. The inset shows the Na^+-CO_2 interaction energy (Lennard-Jones + Coulomb) as a function of the distance between Na^+ and the closest O (CO_2) with the CO_2 and the Na^+ aligned in a line. (b) CO_2 uptake as a function of the fraction of total volume between 3 and 4.5 Å for predicted zeolites with FV >275 cm^3/kg for Si:Al = 3:1 (Na^+) (blue), Si:Al = 1:1 (Na^+) (red), and Si:Al = 1:1 (Ca^{2+}) (green). The three dashed lines show linear fits to the data sets presented here.

number of structures with similar uptake values and a few outliers that have significantly higher uptake. These outlier optimal structures have high FV and a specific topology that allows for extraordinarily large CO_2 adsorptions. As such, these structures are not necessarily indicative of what is generally expected from the structures within the same FV bin. And overall, the CO_2 uptake predicted for the best aluminosilicate zeolite structures are much larger compared to the best pure-silica idealized IZA zeolites.

Next, the CO_2 uptake values as a function of D_i are plotted in Figure 2.15(b) for the same selected subset of the PCOD zeolite structures. Although D_i and FV are correlated, they are not exactly the same as one can observe structures with large FV yet relatively small D_i, and vice versa. Figure 2.15(b) reveals that the optimal D_i values are generally found in the range of $8 < D_i < 13$ Å. Accordingly, although the data from Figure 2.15(a) indicates that the best aluminosilicate zeolite structures are located in the bins that have the largest FV, there needs to be an upper limit restriction put on the FV in terms of D_i. In structures that possess very large D_i values, the proportion of free volume regarded as strong adsorption sites decreases, resulting in lower CO_2 uptake.

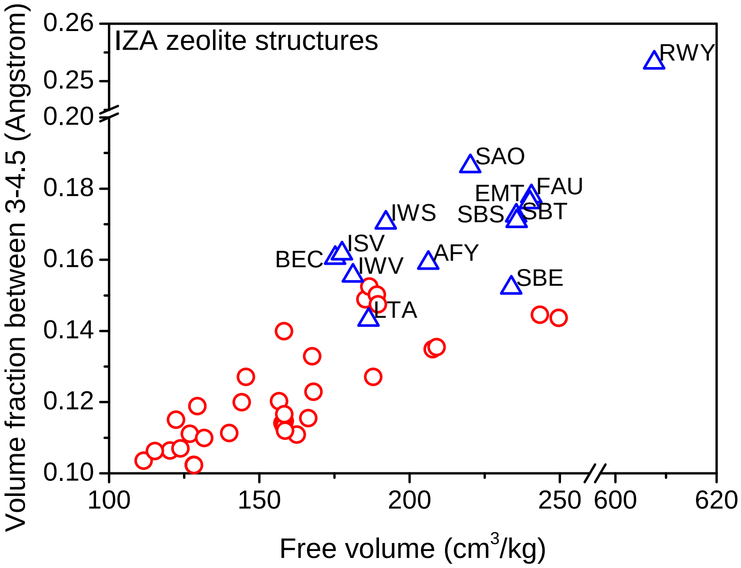

Figure 2.17: Fraction of total volume between 3 and 4.5 Å versus free volume for IZA structures with some highlighted structures in blue triangles.

Although FV and D_i are useful predictors that reduce the search space for the best zeolite structures, there are still a large number of structures that have similar FV and D_i, yet with a wide range of CO_2 loading values. For example, Figure 2.15(b) indicates that there are many structures within the optimal range of $8 < D_i < 13$ Å with very low CO_2 uptake values. Subsequently, we examined localized geometric features of each of the pure-silica zeolite structures to further filter out the unpromising structures. To help with the analysis, a three-dimensional distance grid superimposed on top of the unit cell of the pure-silica zeolite structure was constructed, with each grid point storing the distance to the nearest-neighbor framework atom (i.e., Si and O). From these values, the normalized probability distribution of all of the nearest-neighbor distances was obtained. In our analysis, two pure-silica zeolite structures (i.e., PCOD8163185 and PCOD8200816) were chosen to illustrate cases where two structures have similar FV and D_i but very dissimilar CO_2 uptake values (4.25 and 2.00 mol/kg, respectively). The solid line curves in Figure 2.16(a) demonstrates that compared to PCOD8200816, PCOD8163185 contains proportionally larger volume fraction of nearest-neighbor distances within the 3-4.5 Å range. The picture that is emerging suggests that materials need to have an ideal spot for cations to be added. This ideal spot is between 3-4.5 Å as cations placed within these distances provide optimal interactions with CO_2. This can be seen by re-plotting the probability distributions after the placement of cations in the two pure-silica structures. The new distribution curves (Figure 2.16(a) dashed lines) indicate that the disparity between the cation-added PCOD8163185 structure and the cation-added PCOD8200816 structure has now shifted towards the range between 2.25 and 3.25 Å. And this is where the strongest interaction between the Na^+ cation and the CO_2 molecule is found as shown in the inset of Figure 2.16(a). This suggests that we can quantify the quality of the material by integrating the area under the curve in the range between 3-4.5 Å, and assign it to each structure in the zeolite set. Figure 2.16(b) indicates that the largest CO_2 uptake is observed in aluminosilicate zeolite structures with high volume fraction between 3-4.5 Å in pure-silica structures for both Si:Al = 3:1 and Si:Al = 1:1 for Na^+ and Ca^{2+} cations.

Utilizing the FV and the volume fraction between 3-4.5 Å in pure-silica structure as predictors, we analyzed the IZA structures to study the use of our predictors for experimentally realized structures. According to Figure 2.17, we identify IZA structures such as SAO and RWY that may out-perform the more commonly studied structures like FAU and LTA. To facilitate the experimental efforts, we have summarized a list of promising IZA structures in Table 2.1.

2.2.4 Conclusions

We obtained adsorption data for thousands of materials using an efficient algorithm that can quickly compute the adsorption properties of aluminosilicate zeolites. Our analysis indicates that the structures with largest CO_2 uptake values possess both large free volume and specific configurations of Si/O framework atoms such that the regions with nearest-neighbor distances between 3 and 4.5 Å are maximized. From the experimental as well as the simulation point of views, this finding significantly reduces the complexity in finding the most promising structures for CO_2 capture. Accordingly, we have discovered simple predictors that can allow us to determine a priori which pure-silica zeolite structures will provide the largest CO_2 uptake values for different Si:Al ratios and for different cation types. From our study, SAO and RWY are identified as examples of promising IZA structures for aluminosilicate zeolites, and many other structures in the PCOD set are predicted to potentially possess even larger CO_2 uptake than any of the known zeolite structures. This

Structure	Free volume (cm^3/kg)	Fraction of total volume between 3.0 and 4.5 Å
BEC	175.3	0.161
ISV	177.5	0.162
IWV	181.1	0.156
DFO	185.3	0.149
LTA	186.4	0.143
MEI	186.7	0.152
RHO	188.0	0.127
AFS	189.1	0.150
BPH	189.5	0.147
IWS	192.1	0.170
AFY	206.7	0.159
VFI	207.7	0.135
OSO	209.0	0.136
SAO	220.2	0.187
SBE	233.8	0.153
SBS	235.5	0.173
SBT	235.7	0.171
EMT	240.0	0.176
FAU	240.5	0.178
OBW	243.4	0.145
TSC	249.6	0.144
RWY	607.7	0.253

Table 2.1: Top 20 free volume IZA structures and their fraction of the total volume with the min. distance from the framework atoms between 3.0 and 4.5 Å.

study allows us to systematically rank all existing and hypothetical zeolite materials. Of course, there are many factors (e.g. feasibility of forming aluminosilicate structures, costs, stability, diffusion coefficients, etc.) that determine whether a particular material will work in practice. Our ranking is useful in guiding this selection process. In the future, we hope to extend this work by considering the presence of water, as it can influence the adsorption properties.

2.3 Large-scale screening of zeolite structures for CO_2 membrane separations[‡]

2.3.1 Introduction

Recently, there have been several articles that pertain to computational screening of a large database of porous materials in search for optimal materials for CCS, including those introduced in previous sections.[1,27,34,40,74,77] However, most of these calculations focus on adsorption processes; in contrast, far less attention has been given to screening for membrane processes.[78,79] Separations using membranes,[80] also have the potential to significantly reduce the energy costs. In this study, we present a novel computational approach that allows us efficiently predict the permeation of a material for membrane separation applications. The main reason for this is that the screening of membranes requires, in addition to the adsorption properties, also information about the diffusion coefficients. However, most diffusion coefficient calculations require expensive molecular dynamics (MD) simulations, and as such, much work in the past has focused on analyzing only 10-20 structures.[40] To avoid conducting MD simulations for thousands of structures, one can apply a geometric criterion to select those materials for which one component can enter but not the other.[65,79,81] This is a very efficient method to screen materials with very high diffusive selectivity, but not necessarily for high permeability. Moreover, the geometric approach ignores the energy interactions between the guest particle and the host framework atoms, which leads to predicted diffusion properties that are independent of the specific chemistry used to functionalize a material. In this work, we demonstrate that a reliable estimate of the diffusion coefficient can be obtained from a free energy calculation. In this approach, we take full advantage of the information contained within the free energy landscape throughout the entire unit cell of the crystal structure and apply the transition-state theory (TST) to calculate the diffusion properties.[82,83] Mapping this algorithm to the high-throughput processing power of the GPUs, we have accurately characterized the adsorption and the diffusion properties of over 87,000 experimentally realized structures, i.e., IZA, and predicted pure-silica zeolite structures from Deems database.[23,24,84] For the predicted zeolite database PCOD, same as the work presented previously, a set of 330,000 structures within +30 kJ/mol Si of α-quartz was further reduced to 139,397 by removing structures with largest free-sphere diameter below 3.25 Å.[48] From the reduced set, we selected over 87,000 zeolite structures that have orthogonal unit cells to facilitate calculations. Similar work has been conducted by Haldoupis et al., but their approach was limited to computing diffusion coefficients of spherical molecules such as CH_4.[85] Our method can compute diffusion coefficients of both spherical and non-spherical molecules within a single structure in just a few seconds, providing the speed-up required to screen thousands of different structures. Moreover, our algorithm explores the entire channel

---

[‡] Material in this section is adopted with permission from *J. Am. Chem. Soc.*, **2013**, 135 (20), 7545-7552.[35] Copyright 2013 American Chemical Society.
Link: http://dx.doi.org/10.1021/ja400267g

profile and identifies multiple channels and free-energy barrier locations, which can provide a more accurate picture of diffusion in porous materials. At this point, it is important to note that zeolitic membranes have been synthesized.[86,87] However, these studies have been limited to a few pore topologies, so an important practical question we would like to address is whether these materials are close to the optimal performance, or whether significant gains can be expected if one would try to synthesize a membrane using a different zeolite topology. To illustrate how our screening can be used to find the optimal material, we use as an example the separation of CO_2 from CH_4 in natural gas reservoirs. Natural gas reservoirs may contain up to 70% CO_2, and the production of these reservoirs would require the separation of CO_2 from the natural gas and injection back into the reservoir. As CH_4/CO_2 has high pressure, membranes are ideal to carry out this separation efficiently. At this point, it is important to emphasize that the ideal material for a separation depends on the actual process requirements. We use our screening approach to illustrate this point with a simple model that mimics the separation of CH_4 from CO_2 at conditions typical of a natural gas reservoir. The increase in efficiency of our method allows us to screen many materials and identify the optimal structures for an entire class of materials. Establishing such a theoretical limit provides important guidance for future material synthesis. Our study identifies the general characteristics of the best-performing structures. It can be expected that, in other classes of materials, structures with similar characteristics will also perform very well.

2.3.2 Methods

In our calculations, we assume that the zeolites are perfect, infinitely large crystals such that the periodic boundary conditions can be used. The number of unit cells is chosen such that the simulation box extends at least twice the cutoff radius of 12 Å in all three perpendicular directions. The host framework atoms are assumed to be rigid, and the pairwise gas-gas and gas-host interactions consist of Lennard-Jones forces and electrostatic interactions. The force fields developed by García-Pérez et al. are used in this study as they have been shown to be transferrable for variety of zeolite structures.[50] The temperature is set to be 300 K in all of the work. The MD simulations were conducted utilizing the CPU cores in our own cluster while the efficient diffusion coefficient calculations and the GCMC simulations were conducted utilizing the NVIDIA Tesla C2050 GPU cards from the Dirac Cluster at the National Energy Research Supercomputing Center (NERSC). It should be noted that, although we focus mostly on zeolite structures with CO_2, N_2, and CH_4 as resident gas molecules, the techniques developed to compute the diffusion coefficients can readily extend to other gas molecules and to other materials.

- Molecular dynamics simulations: For an MD simulation, the gradient of the potential energy with respect to position is calculated for each adsorbate particle, including the van der Waals forces and Coulombic forces. This energy gradient manifests as a force which, constrained by intramolecular considerations, results in an acceleration according to Newtons second law of motion. In an MD simulation, the force on each particle is sampled periodically, allowing an update to each particles position and velocity. With sufficiently small time steps (0.5 fs) and sufficiently long simulations (>1 ns), a collection of trajectories produced from MD simulations can be analyzed to calculate the self-diffusion coefficient.[49] In this study MD simulations were carried out in the canonical ensemble, using a Nosé-Hoover thermostat.

- Efficient diffusion coefficient calculations: At the start of the simulation, an energy grid that contains detailed information about the free energy profile of the gas molecules inside the porous material is constructed and subsequently analyzed to obtain both the adsorption and the diffusion properties of the system. A sufficiently fine mesh size of 0.1 Å is chosen for all structures and the resulting grid is superimposed on top of a single unit cell, where each of the grid points represents the total pairwise free-energy summation between the gas molecule and all of the framework atoms. For gas molecules such as CO_2 and N_2, which cannot be represented as a point particle, 250 randomized center-of-mass rotations of the molecule are conducted on the grid point to obtain an average Boltzmann-weighted free energy of the gas molecule at that point. The expression for free energy, F_i, at a specific grid point is expressed as follows:

$$F_i = -k_B T log \frac{\sum_{j=1}^{N_{tot}} exp(-E_j/k_b T)}{N_{tot}} \tag{2.4}$$

where $N_{tot} = 250$ and E_j is the potential energy of CO_2 (or N_2) molecule of a given randomized j configuration. For zeolite structures, the number of energy grid points is typically on the order of 10^6 and 10^7, and the calculations only take a few seconds using our GPU code.

From the constructed energy grid, points where $F_i < 15 k_B$T are considered accessible, while the rest are inaccessible. The choice of the $15 k_B$T cutoff was made such that energy values higher would be considered inaccessible during a typical experimental time scale.[74] The binary information (i.e., accessible/inaccessible) stored in a separate grid can be used to determine both the number of the channels and the channel direction. For example, in determining the number of channels along a given spatial direction (e.g., X-direction), a two-dimensional flood fill algorithm at X = 0 along the Y-Z plane is used to combine the adjacent accessible points together. The flood fill algorithm implemented here is similar to the one we utilized to determine blocked regions in porous materials.[74] After identifying the distinct number of accessible regions at X = 0, each of these sections are analyzed separately in subsequent analysis. To analyze the entire channel, we compute the sum of Boltzmann weights along the Y-Z plane slice at a given X value for all grid points that are connected to the initial accessible region at X = 0. The algorithm continues from X = 0 to X = L_X, where L_X is the unit cell size along the X-direction. If at any point, we encounter a dead-end (i.e., Y-Z plane where sum of Boltzmann weights is zero) we conclude that the channel does not exist along this region and proceed to the next possible candidate either along the same X-direction or along Y or Z directions. Upon successful traversal to the end of the unit cell, the sum of Boltzmann weights for each value of X can be utilized to identify the peak/trough of the free energy profiles for that specific channel along the X-direction. The entire free-energy profile is utilized to compute the diffusion coefficient given that there can be multiple lattice sites along the same channel. The diffusion coefficient value of an individual channel can be obtained from the TST[88, 89] taking into account multiple hop-rates generated from the analysis assuming a random walk along the lattice sites. The total diffusion coefficient value along a given direction (e.g D_X) consists of linear combination of the channel diffusion coefficients weighted by its local Henry coefficient values. Finally, the total self-diffusion coefficient is calculated as $D_S = 1/3(D_X + D_Y + D_Z)$. Throughout this work, the effects of adsorbate concentration on the diffusion behavior were neglected in order to allow for extremely fast diffusion characterization. The sensitivity of the diffusion coefficients for different loading values will vary based on the structure topology, but is not expected to impact these results significantly. In fact, the assumption of constant diffusion coefficient is commonly used in applications.[49]

- Grand-canonical Monte Carlo simulations: GCMC simulations were utilized to obtain the gas uptake value as a function of fugacity. In GCMC, the chemical potential, volume, and temperature are kept constant throughout the simulation and random insertion, deletion, and translation moves were used to propagate the MC system from one cycle to the next. We have utilized various efficient techniques such as density biased sampling, energy grid usage, and parallelization of energy calculations to reduce the average overall wall time of a single GCMC simulation to under a minute.[90] The number of equilibration cycles and production cycles were set respectively at 250,000 and 100,000. The mixture isotherms were obtained from the computed pure isotherm data using the IAST, which has been demonstrated to be generally applicable to make good predictions about mixture behaviors for various porous materials.[63] It is important, however, to note that some particular cases may need some variant theories of IAST,[91] which is regarded to be out of the scope for this current work.

2.3.3 Results and discussion

The transport of molecules through a membrane can be characterized by its permeability. The permeability is defined as the product of the solubility and the diffusion coefficient of the gas molecules. As such, permeability is a crucial component for evaluating membrane performance,[80] and it requires computation of both adsorption and diffusion properties of the system. For the adsorption part, we use existing computational methods based on GPUs.[74] The methodology used to compute the diffusion coefficients described in the Methods section has been implemented for this work. We have selected a set of representative experimental zeolite structures from the IZA database to test our method. Figure 2.18 compares the self-diffusion coefficient (D_S) of CO_2, N_2, and CH_4 gas molecules at infinite dilution and T = 300 K for the two methods, and it shows that our method provides a reasonably accurate description of the diffusion. The discrepancies between the two methods result from a variety of different reasons such as correlated hops for large diffusion values[82] and the presence of complicated channel profiles that makes very accurate TST analysis difficult. In general, the MD simulation wall time scales with the inverse of D_S, becoming intractable in slowly diffusing systems as hops across a large barrier becomes increasingly rare. Accordingly, given that our model based on the TST uses an algorithm where the wall time remains independent of the diffusive coefficient values, an enormous speed-up (few seconds versus several weeks) can be gained compared to MD simulations in structures with small D_S.

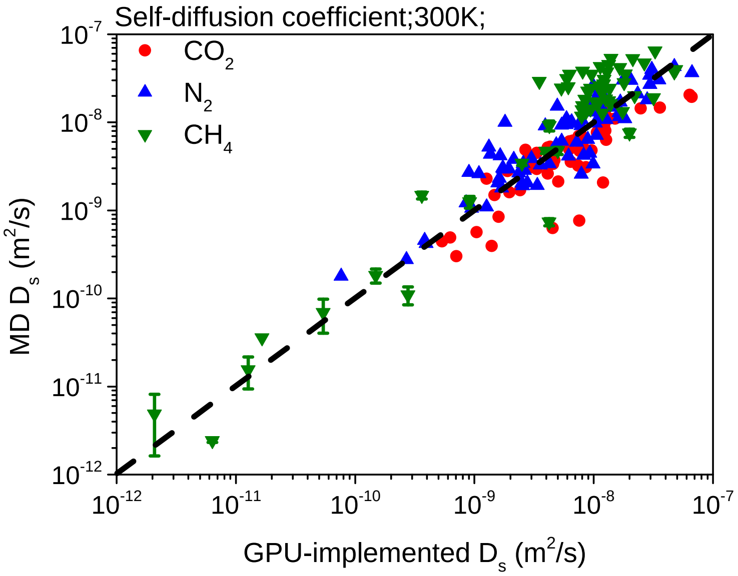

Figure 2.18: Comparison of two different methods (MD and GPU-implemented TST) to compute the self-diffusion coefficients of CO_2 (red circles), N_2 (blue up-triangles), and CH_4 (green down-triangles) molecules for IZA zeolite structures. The dashed line indicates the region of perfect agreement between the two methods. The error bars from the MD simulations are provided for only a few selected zeolite structures.

Figure 2.18 also illustrates that the zeolite data points for CO_2 and N_2 are concentrated in the highly diffusive region (i.e., D_S >10^{-9} m^2/s), whereas CH_4 data points are scattered across a wider range of D_S values. Because the kinetic diameter of CH_4 is larger than both CO_2 and N_2, there exists more structures with relatively smaller diffusion coefficients for CH_4. Also, due to the long-range electrostatic interactions present for the non-polar CO_2 and N_2 molecules with quadruple moments, the likelihood of finding structures with a relatively high energy barrier remains small as the contributions of the nonlocal interactions spread across the entire channel. On the other hand, the lack of electrostatic interactions in CH_4 molecules translates into free energy landscapes that are determined solely by short-range interactions from the neighboring framework atoms, which enhances the likelihood of finding channels with a narrow, pinched region (i.e., large energy barrier) separating the adsorption sites for certain topologies.

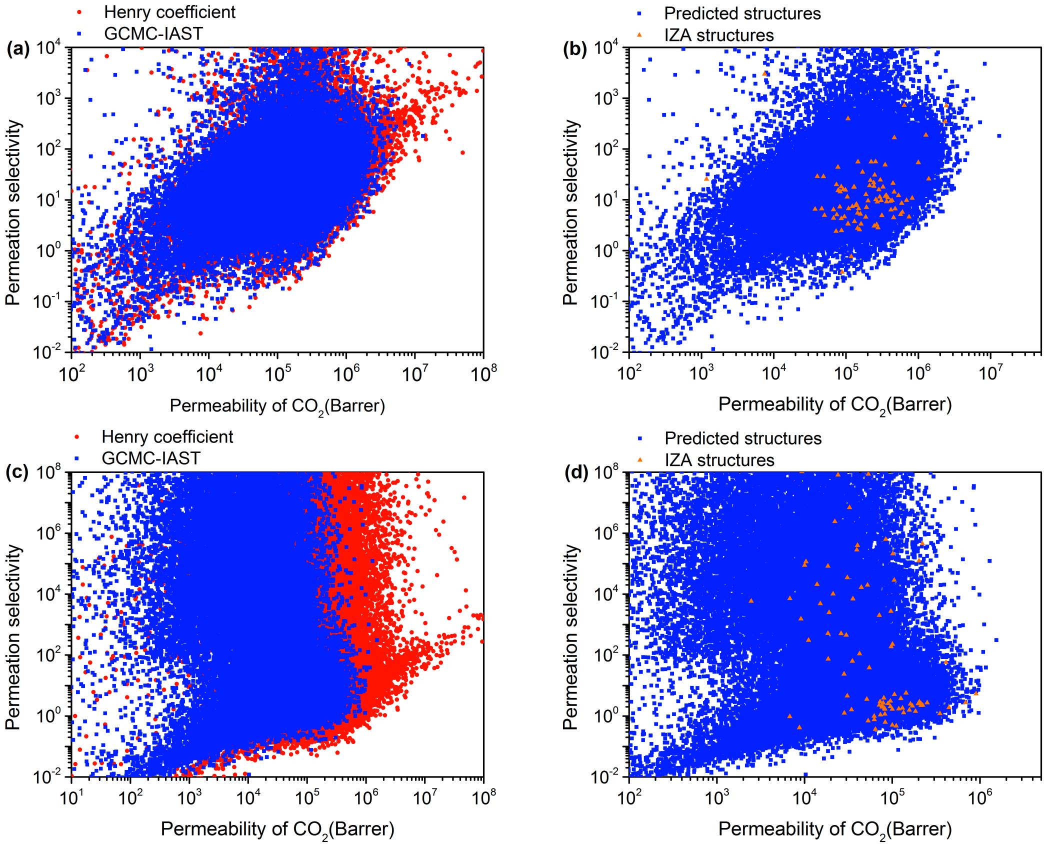

Figure 2.19: Permeation selectivity as a function of CO_2 permeability for (a) CO_2/N_2 separations (K_H, red; GCMC-IAST, blue), (b) CO_2/N_2 separations for GCMC-IAST in predicted (blue) and IZA (orange) zeolites, (c) CO_2/CH_4 separations (K_H, red; GCMC-IAST, blue), and (d) CO_2/CH_4 separations for GCMC-IAST in predicted (blue) and IZA (orange) zeolites.

Next, we explore the different characteristics between CO_2/CH_4 and CO_2/N_2 separations for the zeolite structures. For analysis, we included over 87,000 predicted zeolite structures in order to detect possible patterns that can emerge for the entire class of materials and for selected separations that might not be obvious in analyzing just a few structures. In most membrane research, the relative performance of a material is estimated from a Robeson plot, which gives the relationship between permeability and the permeation selectivity.[92] In all cases, the permeation selectivity value less than one indicates that the membrane is selective but the CO_2 ends up in the retentate. Figure 2.19(a) and (b) shows the zeolite Robeson plots for CO_2/N_2, and Figure 2.19(c) and (d) shows those for CO_2/CH_4 separations. We considered two different methods to compute the adsorption component of the permeability and permeation selectivity: (1) using the Henry coefficient, K_H, which gives an accurate description of the adsorption at low pressures and (2) using the grand-canonical Monte Carlo (GCMC) simulations for obtaining pure component isotherm and applying the ideal adsorbed solution theory (IAST) for estimating mixture adsorption at given condition.[63] In general, using K_H values overestimates the permeability, as shown in the Robeson plots in Figure 2.19(a) and (c) (red data points). Since most gas separation occurs at higher pressures, the uptake values at the actual separation pressure provides a better measure of permeability compared to K_H. For CO_2/N_2 separations the flue gas operating condition of total fugacity equal to 1 bar (14% CO_2 and 86% N_2) was used, while for CO_2/CH_4 the total fugacity of 10 bar (50% CO_2 and 50% CH_4) was used. Upon increasing the pressure, the gas uptake begins to saturate; thus, the adjusted permeability value based upon GCMC-IAST becomes smaller at pressures outside of the linear Henry regime. Because CO_2/N_2 separation occurs at a lower pressure compared to CO_2/CH_4 separation, the overall shift in the data points in the Robeson plots (indicating decrease in CO_2 permeability) in Figure 2.19(c) becomes more apparent for CO_2/CH_4.

It is instructive to compare our results with the well-known Robeson plots for polymer materials. For these materials, one typically observes a limiting behavior, the Robeson upper bound, as materials that have high selectivity have low permeability and materials with high permeability have low selectivity.[92,93] In the literature, deviations from this Robeson upper bound have been reported for nanoporous materials.[94] Figure 2.19 shows, however, that nanoporous materials have a qualitatively very different behavior, in which the concept of a Robeson upper limit has little value. The reason is that the difference in solubility of guest molecules in these materials can vary orders of magnitudes, while in the Robeson upper limit, it is assumed that all materials have a similar solubility.[93] In Figure 2.19, most of the data points in the CO_2/N_2 Robeson plot are concentrated in a narrow band of permeation selectivity values and indicates a general positive correlation between CO_2 permeability and CO_2/N_2 permeation selectivity. On the other hand, the data points for the CO_2/CH_4 Robeson plots are spread across a wider range of selectivity values with less meaningful correlations being found between permeability and selectivity. Because both CO_2 and N_2 molecules are non-polar with quadruple moments, linear, and have comparable kinetic diameters, the diffusion properties of the two gas molecules are similar. Moreover, the values of $K_H(N_2)$ of the entire database are in a much narrower range compared to the corresponding values of $K_H(CO_2)$. Accordingly, given this narrow range of $K_H(N_2)$ values and similar diffusive properties between CO_2 and N_2, the shape of the Robeson plot is dictated largely by $K_H(CO_2)$, which is positively correlated in both the permeability and the permeation selectivity. The CO_2/N_2 points located along a narrow band can be also seen in the CO_2/CH_4 Robeson plot as well. However, additional, more scattered data points exists in this Robeson plot, which is caused by the dissimilarity between the CO_2 and the CH_4 molecules. Most of these outliers correspond to zeolite structures that possess very narrow channels, leading to relatively low CH_4 diffusion coefficient values or from different

CO_2/CH_4 adsorption sites.

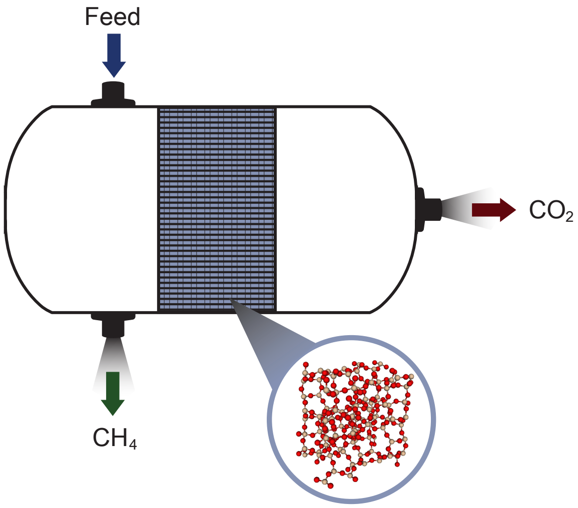

Figure 2.20: An illustration of a simplified membrane separation process with the feed (equal molar CH_4/CO_2 mixture) gas at 300K separated into CO_2 and CH_4 utilizing a membrane comprised of zeolite materials.

To identify the structures most promising for CO_2/N_2 and CO_2/CH_4 separations, a suitable metric that can quantify the material performance needs to be constructed. A diagram that illustrates the CO_2/CH_4 separation process is shown in Figure 2.20. The target for the CO_2/CH_4 separation is to obtain a high purity CH_4 stream in the retentate side. The conventional approach in identifying the top performing structures for such a membrane separation is to select those materials that have the highest permeability and selectivity. We use a simple membrane design to illustrate that from a practical point of view, this criterion does not provide us the optimal material. The argument that one needs to be in the upper right corner in the Robeson plot (i.e., high permeability and selectivity region) assumes that selectivity is equally important as permeability. Our analysis shows that for a given separation, one needs a minimum selectivity; the best material is the one with highest permeability out of all materials that satisfy this minimum selectivity criterion. Selectivity is the dominant factor only for separations that require an extremely high purity. Baker et al. reached a similar conclusion for the N_2/CO_2 separation.[80] In an ideal membrane system, the area of the membrane is assumed to be a measurement of the cost of the entire process, and this area is shown to be mainly dominated by and inversely proportional to the CO_2 permeability (detailed derivation can be found in the supporting information section 2 of ref 35). Hence, we can rank those materials that satisfy the minimum selectivity criterion based on the membrane area that is required for the separation.

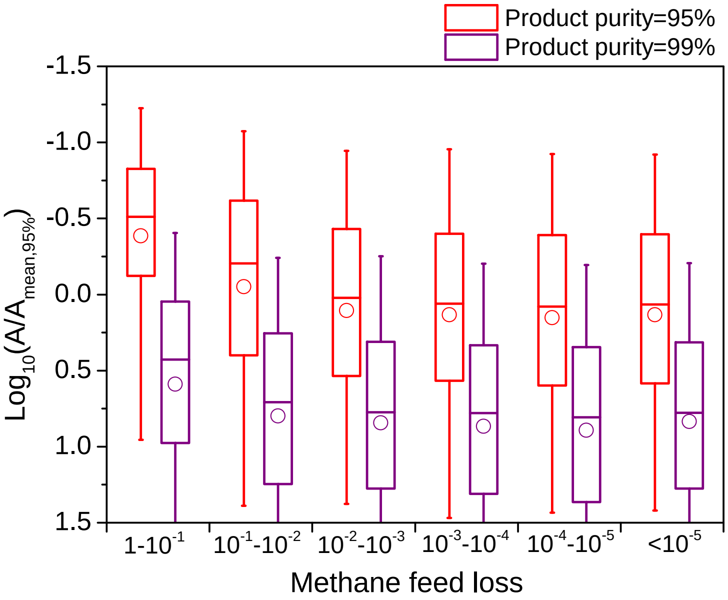

Figure 2.21: Membrane area as a function of CH_4 feed loss for zeolite structures that satisfy the minimum purity requirement of 95% (red) and 99% (purple). $A_{mean,95\%}$ is defined as the logarithm averaged area with the given 95% purity. The segments within each box from bottom to top represent the 5%, 25%, 50%, 75%, and 95% points for each bin with the circle indicating the average value for the whole bin.

With a working performance metric at hand, we plot the membrane area as a function of CH_4 feed loss (i.e., 1 - methane recovery) for materials that satisfy the methane purity criteria of 95% and 99% purities in Figure 2.21. The feed loss gives us the amount of methane that we inject with the CO_2 in the reservoir. As we are screening many materials, a clear trend emerges with some structures that have nearly ideal properties and have therefore, an exceptionally high performance. However, from a synthetic point of view, it might be very difficult to synthesize exactly these materials. In Figure 2.21, the box representation is used to indicate the exceptional materials and show the general trend: the lines above and below the boxes show the structures with good and poor performance, and the boxes show the trends as represented by a large number of structures that have the same properties. In the following, we focus on these general trends. As expected, the membrane area tends to increase for smaller membrane feed loss, indicating that if we require a higher selectivity, we will have less materials to choose from.

For a specified purity requirement, we can isolate the top structures and identify common features that separate these structures from the others. For example, we plot the CO_2 heat of adsorption as a function of the Henry coefficient, $K_H(CO_2)$, for the top 1% structures that satisfy the product purity requirement of 95%. The best structures possess Henry coefficient

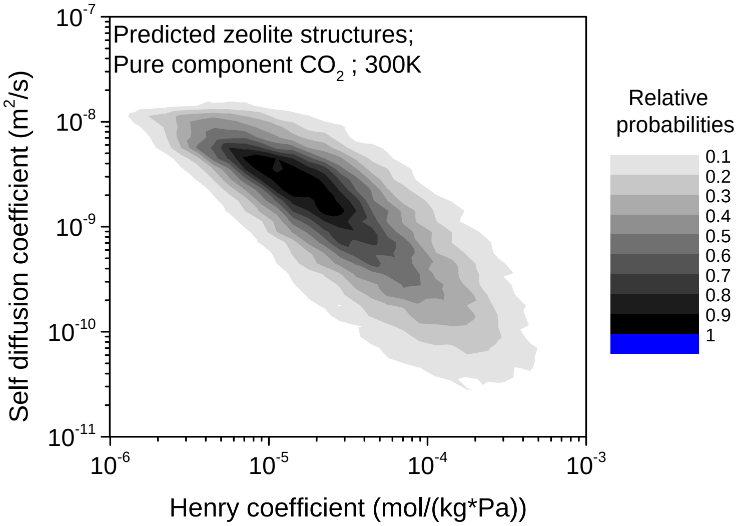

Figure 2.22: $D_S(CO_2)$ as a function of $K_H(CO_2)$ for the predicted zeolite structures. Most of the zeolite structures have the Henry coefficients and self-diffusion coefficients to be within 5x10^{-6} $<K_H<$5x10^{-5} mol/kg/Pa and $10^{-9} < D_S < 10^{-8}$ m^2/s, respectively.

that is in the intermediate range ($10^{-5} < K_H(CO_2) < 10^{-4}$ mol/(Kg-Pa)). In structures that have very small $K_H(CO_2)$, the overall CO_2 permeability and the permeation selectivity is too small, making them suboptimal for membrane separations. In structures that have too large of $K_H(CO_2)$ ($K_H(CO_2) > 10^{-3}$ mol/(Kg-Pa)), one key factor comes into play that degrade performance: there is an inverse relationship between $K_H(CO_2)$ and D_S, as can be seen from Figure 2.22. Structures with large $K_H(CO_2)$ possess strong adsorption sites that cause the diffusion rate to decrease as the effective barrier separating one adsorption site to another becomes large. Among structures that are inside the optimal Henry coefficient range, the optimal structures tend to have low heat of adsorption values (blue data points in Figure 2.23). A high heat of adsorption often corresponds to strong adsorption sites, which lead to low diffusion coefficients. At this point, it is instructive to compare our results with those from geometrical screening.[79] Geometrical screening identifies the best materials as the ones that possess pore diameter values similar to the kinetic diameter of the molecules that have to be separated. Intuitively, this makes sense as one can imagine that the separation process will be optimized when one guest molecule species is just small enough to diffuse across the channel, while the larger one being blocked. To gain insights in the differences between the two methods, we plot the CO_2 permeability as a function of the largest free sphere diameter (D_f)[48] for all structures shown in Figure 2.24. The largest free sphere diameter is a measure of the size of the molecule that can enter a particular structure. A simple geometric criterion is to select those structures that have a D_f large enough for CO_2 to enter but too small for CH_4. In our analysis, two important points emerge that cannot be deduced from a pure geometrical analysis. First, few high performing structures possess very large D_f values, which deviates from what is predicted from geometrical analysis. Because most geometrical analysis focuses on selectivities, only the structures that consists of pore diameters that are close to the size of the guest molecules are deemed interesting and worthwhile for investigation. Our energy-based method reveals that for 95% purity requirement, one can identify structures that lie outside of this region (blue data points for D_f >4 Å in Figure 2.24(a)). Once the desired purity is set to be very large at 99.9% (Figure 2.24(b)), the best-performing structures tend to be concentrated in the region D_f = 3-4 Å. For such a high purity, it is essential to have high selectivity and the geometric criterion ensures this. The second important point is that our method can readily differentiate large and small CO_2 permeability values in structures that are located within the optimal D_f values (3-4 Å) as our method can compute accurate D_S values. Accordingly, the set of potential candidates for membrane separation can be further refined using the energy-based analysis.

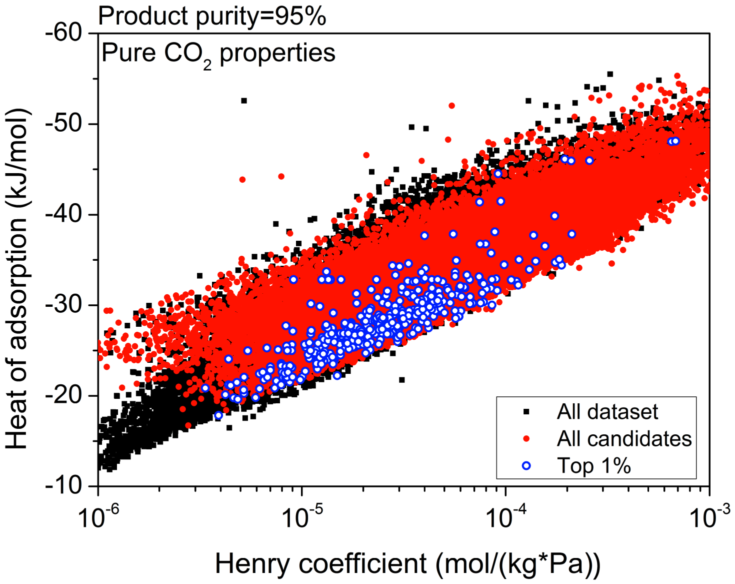

Figure 2.23: Heat of adsorption as a function of $K_H(CO_2)$ for all zeolite data sets (black), selected candidate sets that satisfy the 95% purity requirement (red), and the top 1% best-performing structures from the set of all candidate structures (blue).

Until now, we have assumed that CO_2 is the component with the highest permeation. As this is the case for most known porous materials, one normally does not consider a separation where CH_4 or N_2 is assumed to be the component with the highest permeability. Such a material, however, would be of interest as it would allow for separation in which the CO_2 is retained while preferring permeability of CH_4 or N_2. This process can be attractive since in the conventional process, the CO_2-rich stream is the low-pressure permeate and hence needs to be repressurized for transportation and storage, while in the inverse process, the CO_2-rich stream is the retentate and repressurizing is not required. Such process will be particularly attractive for those natural gas fields in which the CO_2 concentration exceeds 50%. Figure 2.25 shows the Robeson plots corresponding to this separation where the same data points from Figure 2.19 were plotted with inverted permeation selectivity values. In general, the permeability as well as the selectivity for the top performing structures are predicted to be lower as the number of structures that possess larger CH_4 and N_2 uptake values compared to the CO_2 uptake values at the interested separation process is very small. We did not identify any of the known experimental (IZA) zeolite structures that possessed CH_4/CO_2 or N_2/CO_2 permeation selectivity values >10. On the other hand, screening of the predicted zeolite structures does reveal a large number of structures that would allow for such a separation, suggesting such a separation is possible.

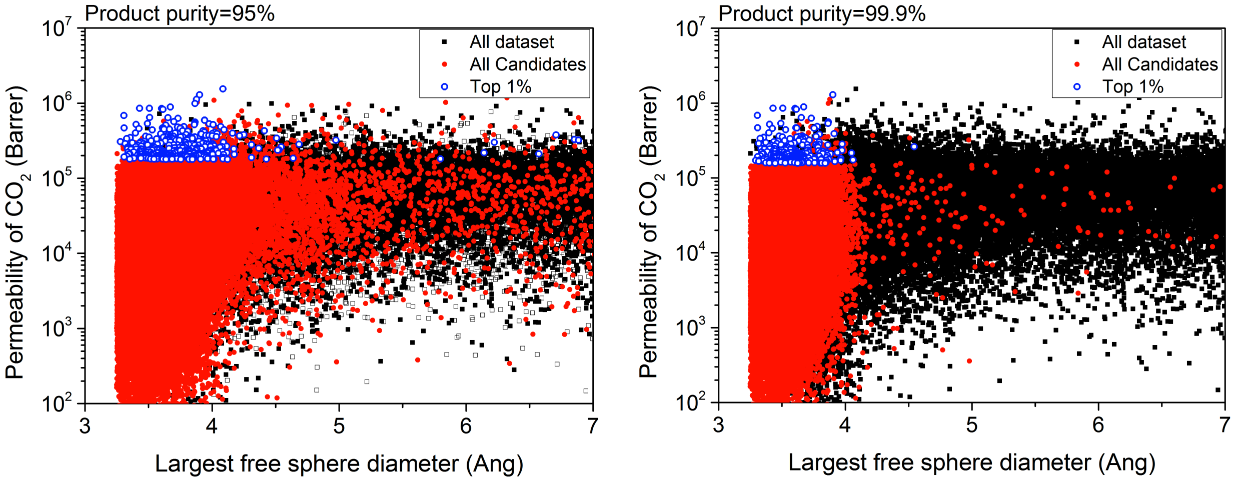

(a) (b)

Figure 2.24: CO_2 permeability as a function of largest free sphere diameter for (a) 95% CH_4 purity and (b) 99.9% CH_4 purity for all the zeolites in the data set (solid black), the candidate subsets that fulfill the purity requirement (solid red), and the top 1% structures (i.e., top 1% in area with recovery >90%) (open blue).

It is interesting to make comparisons between the best predicted zeolite structure and the best IZA structure we identified from our screening analysis. In our evaluation, the membrane area, which is dominated by and inversely proportional to the CO_2 permeability is used as a metric that needs to be minimized to have the best membrane separation performance. The ratio between the smallest membrane area found in the IZA and the PCOD structures are defined as the performance gain.[24] For CO_2/CH_4, this gain ranges from 4 to 7 for differing minimum selectivity requirements that range from 85 to 98% purity with the recovery set at 0.90. Among the IZA structures, ABW and GIS zeolite structures were identified to have the largest CO_2 permeability as both of these structures possess relatively strong CO_2

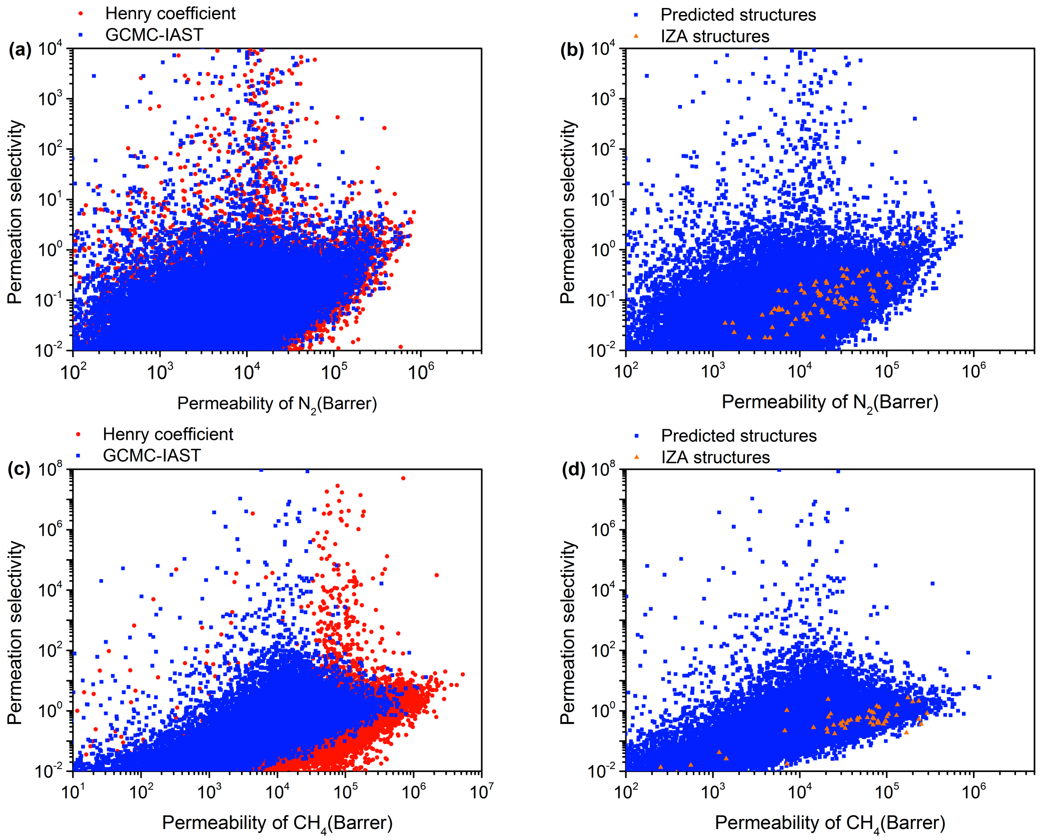

Figure 2.25: Permeation selectivity as a function of N_2 permeability for (a) CO_2/N_2 inverse separations (K_H, red; GCMC-IAST, blue) and (b) CO_2/N_2 inverse separations for GCMC-IAST in predicted (blue) and IZA (orange) zeolites. Permeation selectivity as a function of CH_4 permeability for (c) CO_2/CH_4 inverse separations (K_H, red; GCMC-IAST, blue) and (d) CO_2/CH_4 inverse separations for GCMC-IAST in predicted (blue) and IZA (orange) zeolites.

adsorption sites spread throughout the entire main channels. The $K_H(CO_2)$ values computed at T = 300 K are 5.42x10^{-5} and 1.45x10^{-4} mol/(Kg-Pa), while the D_S values are 8.01x10^{-9} and 3.51x10^{-9} m^2/s, respectively, for ABW and GIS. These values indicate that the best IZA structures do not possess exceptional adsorption or diffusive properties but are well-balanced in both. Figure 2.26(a) shows the CO_2 free energy landscape within the GIS structure where blue regions indicate relatively strong adsorption regions. The best PCOD structures for CO_2/CH_4 is identified to be PCOD8186909. Similar to ABW and GIS, the best predicted structures also show well-balanced adsorption and diffusion properties. Finally, for the structures optimal for the inverse process shown in Figure 2.25, the best structures tend to have strong CO_2 binding sites that reduce its diffusion coefficient to lower the CO_2 permeability. Concurrently, these structures possess strong enough CH_4 binding sites with

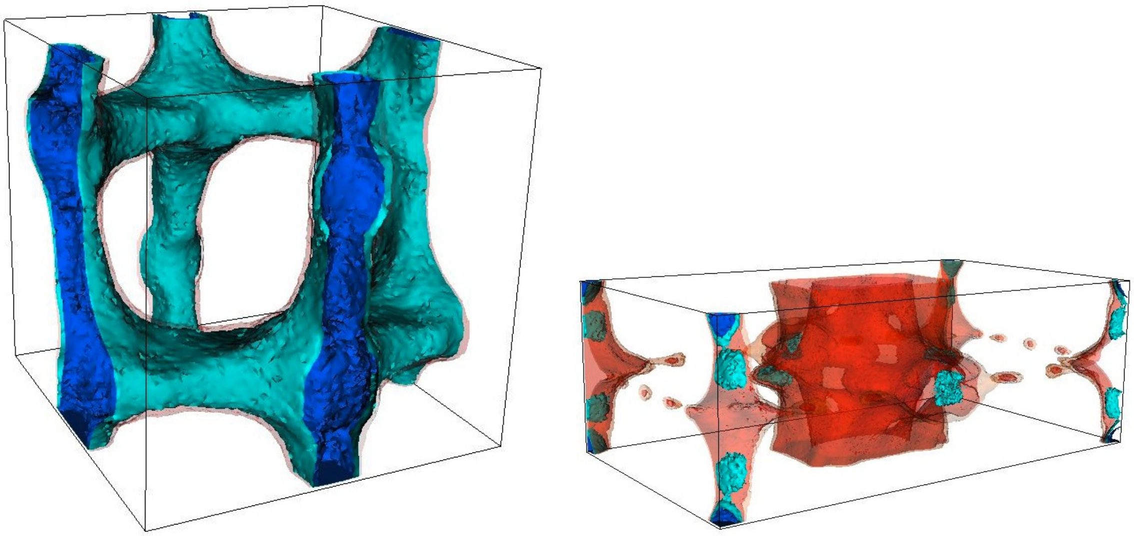

(a) (b)

Figure 2.26: (a) CO_2 free energy landscape within a unit cell of GIS structure, which is predicted to be one of the best structures for both CO_2/N_2 and CO_2/CH_4 separations. (b) CO_2 free energy landscape within a unit cell of PCOD8198030 structure, which is predicted to be one of the best structures for CH_4/CO_2 inverse separation. The blue regions indicate low-energy adsorption sites (minima values of -4,493 and -6,775 K for GIS and PCOD8198030, respectively), the red indicates relatively high energy regions while the rest represents inaccessible regions

fast enough diffusive properties for CH_4 to make them optimal for the inverse process. A sample structure (i.e., PCOD8198030) is shown in Figure 2.26(b), where a significant energy barrier exists in the main channel for CO_2 molecules with the strongest adsorption sites.

2.3.4 Conclusions

In summary, we have implemented an efficient method to determine diffusion coefficients based on the application of the transition-state theory to the energy landscape of a large collection of structures. These diffusion properties, when combined with adsorption properties, can characterize the membrane performance for a given microporous material. Applying this method to a database of over 87,000 predicted zeolite structures, we found that for CO_2/CH_4 separations, the best-performing predicted structure can improve the performance as measured by the required area of a membrane by a factor of 4-7 compared to the best known zeolite structure. Robeson plots for the CO_2/CH_4 separation reveal two distinct subclasses of structures: (1) a group with a relatively low permeation selectivity which varies in proportion to the permeability of CO_2, and (2) a group with much higher permeation selectivities which is presumed to arise mainly from diffusion selectivity, i.e., molecular sieving. These two different groups are not as clearly observed for the CO_2/N_2 separation, since the two particles have more similar dimensions, making molecular sieving less possible. The best material achieves a high selectivity without creating adsorption sites that slow down the diffusion. A simple experimental signature to recognize such a material for CO_2/CH_4 separation is a material that has intermediate range of CO_2 Henry coefficient (i.e., $10^{-5} < K_H(\mathrm{CO_2}) < 10^{-4}$ mol/(Kg-Pa)) and a relatively low heat of adsorption (i.e., -30 to -20 kJ/mol).

2.4 New materials for methane capture from dilute- and medium-concentration sources[§]

2.4.1 Introduction

It is important to explore the possibility of using a sorbent for methane purification. Accordingly, we consider the following general problems: (1) concentrating a medium-purity stream to the high-purity range and (2) concentrating a dilute stream to the medium-purity range. For purposes of analysis, our proxies for these cases are (1) a low-quality natural gas (simplified as 30% CH_4 and 70% CO_2 by mole fraction at a total pressure of 70 bar) and (2) coal-mine ventilation air (simplified as 1% CH_4, 1% CO_2 and 98% N_2 at a total pressure of 1 bar). Both of these are potential large-scale, high-impact applications for a sorbent for methane. The example cases illustrate two general characteristics of methane purification. First, because processes related to the ones that produce methane also produce CO_2, almost all natural methane streams contain significant levels of CO_2. Second, for dilute streams, N_2 is the dominant component to exclude. O_2 is also abundant, but for combustion applications, it is desirable to carry at least as much O_2 as CH_4 through the process.

For going from medium- to high-purity methane, a sorbent selectivity of CH_4 over CO_2 greater than 1 is required and generally, the higher the selectivity, the fewer absorption-desorption cycles required to reach desired purity. For going from dilute to medium purity, the selectivity of CH_4 over N_2 is more important for determining the number of cycles. The selectivity of CH_4 over CO_2 may also be important, depending on the application. For combustion at low concentrations (e.g., 5% CH_4), selectivity is not relevant. However, if the gas is to be further purified, or is to be used in an advanced (e.g., biologically based) conversion process, then selectivity close to or greater than 1 is desirable.

In this work, we carry out thorough exploration of zeolites for their effectiveness in methane capture. The systematic screening of around one hundred thousand zeolite structures has uncovered a few candidates that appear technologically promising. We use free-energy profiling and geometric analysis in these candidate zeolites to understand how the distribution and connectivity of pore structures and binding sites can lead to enhanced sorption of methane while being competitive with CO_2 sorption at the same time.

2.4.2 Methods

The Henry coefficient and the pure component adsorption isotherms for CO_2, CH_4, and N_2 gas molecules were computed using our highly efficient graphics processing unit code,[74,90] and the ideal adsorbed solution theory was then applied to estimate the mixture component uptake to reproduce the aforementioned conditions relevant to methane separations.[63] In our simulations, all interactions between gas molecules and the zeolite framework were described

---

[§] Material in this section is based on *Nat. Commun.*, **2013**, 4, 1694.[2]
Link: http://dx.doi.org/10.1038/ncomms2697

at the classical force field level with atomic partial charges (for Coulombic interactions) and 12-6 Lennard-Jones parameters (for van der Waals interactions) taken from García-Pérez et al.[50] The framework was assumed to be rigid throughout the simulations, an assumption that is considered to be reasonable in zeolite structures.[49]

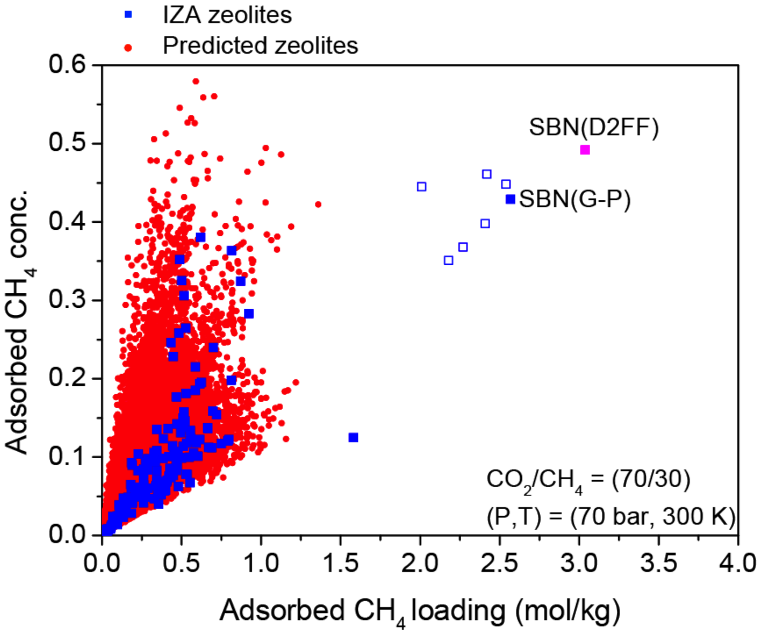

Figure 2.27: Molar concentration of CH_4 in the adsorbed phase versus CH_4 loading in zeolites. Results are shown for 190 IZA (blue) and over 87,000 predicted (red) zeolite structures with input gas-phase mixture composition of 30% CO_2 and 70% CH_4 at pressure of 70 bar and T = 300 K. The SBN that shows exceptional performance for this separation is plotted for two different force fields, García-Pérez (blue-solid) and D2FF (pink-solid). The unit cells of the SBN were changed from -3 to 3% of their original sizes, and relaxed using DFT for García-Pérez (blue-no fill).

2.4.3 Results and discussion

In this study, we analyzed 190 experimentally realized IZA structures and over 87,000 PCOD structures from Deems hypothetical zeolite database[24] to search for materials suitable for methane capture. Because of the quadruple moment of CO_2, the interaction between the CO_2 molecules and the framework atoms are generally much stronger than for the CH_4 molecules. Accordingly, finding zeolite structures that simultaneously lead to a large adsorbed CH_4 concentration (relative to adsorbed CO_2) and high CH_4 loading poses a significant challenge even with the large number of diverse zeolite structures at our disposal. For mixtures that contain methane at relatively low pressure, the binding energy of methane is the primary factor that determines the performance of the structure. On the other hand, for separations that occur at higher pressures, the CH_4-CH_4 interaction could also play a significant role. Thus, we expect that the total pressure of the initial mixture gas will largely dictate the type of materials optimal for methane capture.

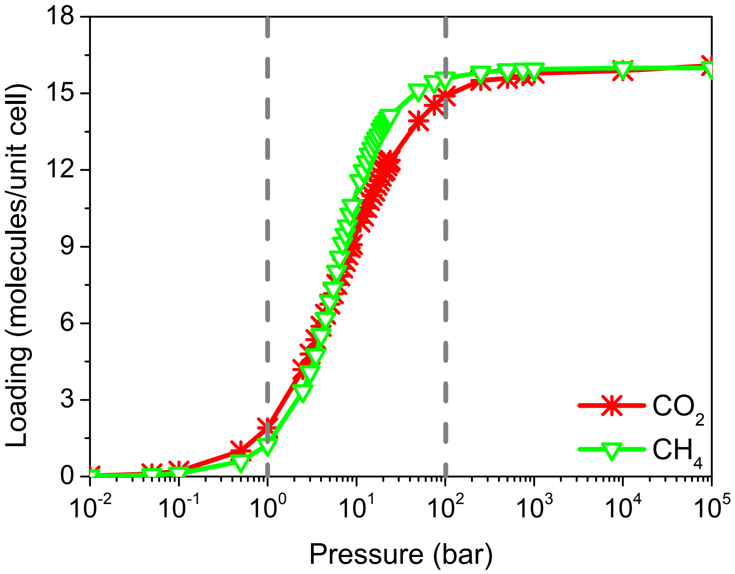

Figure 2.28: Zeolite SBN CO_2/CH_4 adsorption isotherm. CO_2 (red) and CH_4 (green) adsorption isotherm data at T = 300 K where the two curves intersect one another at P = 5 bar and P = 105 bar. The dashed lines divide the isotherms into three important regions: (1) Henry regime, (2) strong CH_4-CH_4 interaction regime and (3) saturation regime.

First, we performed the zeolite screening for the application involving a low-quality natural gas mixture feed consisting of 30% CH_4 and 70% CO_2 (in mole fraction) at 70 bar and 300 K. Figure 2.27 indicates the adsorbed CH_4 concentration (mole fraction) in the adsorbed gas mixture as a function of the adsorbed amount of CH_4 (that is, CH_4 loading) for all of the IZA and the predicted zeolite structures. The results immediately reveal an IZA structure, SBN, that stands out in its performance-roughly 2.75 (mol/kg) adsorbed CH_4 and 45% adsorbed CH_4 concentration. We also utilized the recently published force field D2FF, which is developed based on dispersion-corrected density functional theory (DFT), from Sholl and coworkers[95] to compute the SBN CO_2 adsorption isotherms. Adsorption isotherms calculated via D2FF have been shown to accurately reproduce the experimental isotherms for CHA, MFI and DDR silicate zeolite structures.[95] In this study, the SBN CO_2 isotherms obtained from D2FF predict even better overall performance (see Figure 2.27) with reduced CO_2 uptake for all of the pressure values. To further test the robustness of our finding, sensitivity analysis was conducted by changing (in steps of 1%) the SBN lattice parameters from -3 to +3% of the original optimized value of a = 14.374 Å, b = 12.448 Å, and c = 13.846 Å. For each perturbed structure, the lattice constants were kept fixed while the atomic coordinates were optimized using DFT with the quantum code SIESTA.[96] As shown in Figure 2.27, all of the perturbed SBN data points are close to the original SBN data, indicating that in spite of a small dependence of its performance on force field parameters and lattice constant, SBN is clearly one of the best structures for methane capture.

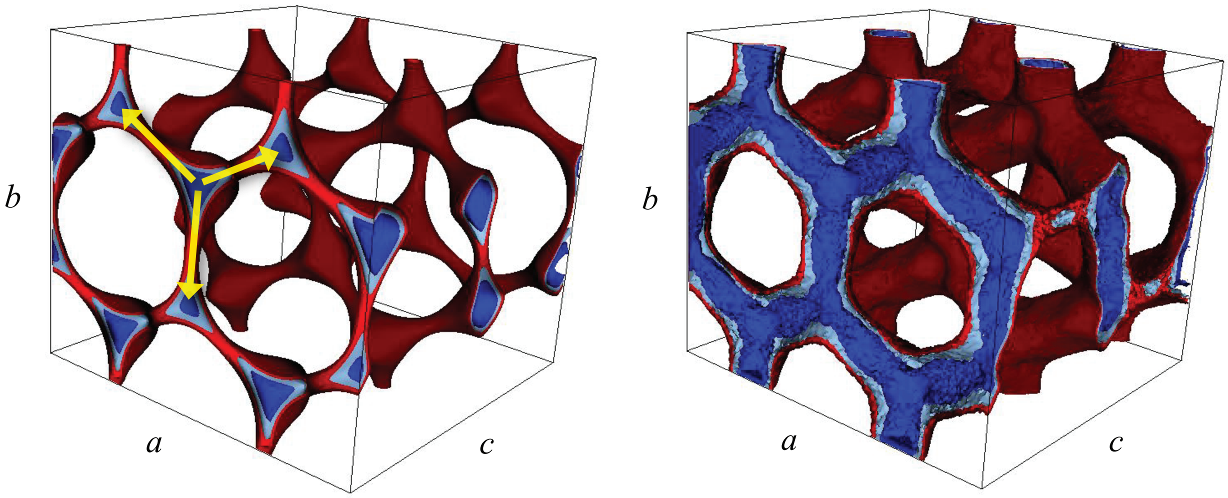

(a) (b)

Figure 2.29: Free-energy landscape inside SBN unit cell for (a) CH_4 and (b) CO_2 molecule with lattice parameters a = 14.374 Å, b = 12.448 Å, and c = 13.846 Å. Dark blue represents low-energy strong binding sites, and red represents high energies. The three yellow arrows separate one binding site to another, and the distance values range from 4 to 4.6 Å.

To further explore the reason behind the exceptional performance of SBN, we plot in Figure 2.28 and 2.29 the simulated adsorption isotherm curves and the free-energy landscapes, respectively, in this zeolite for both CO_2 and CH_4. Within the idealized SBN structure, blue represents low-energy regions and red represents high-energy regions, with the rest indicating inaccessible regions. To help with the analysis, the adsorption isotherm curves are divided into three regimes based on the total pressure (that is, P <1 bar, 1 bar <P <100 bar and P >100 bar), representing the Henry regime, strong CH_4-CH_4 interaction regime and saturation regime, respectively (see Figure 2.28). In the Henry regime (P <1 bar), the guest particle-framework interaction dominates the adsorption properties where the Henry coefficient $K_H = 0.86$ and 0.52 (mol/kg/bar) for CO_2 and CH_4, respectively, leading to higher uptake of CO_2 in this region. The difference can be explained by comparing the binding energy values (CH_4 : -22.09 (kJ/mol) and CO_2: -28.57 (kJ/mol)) of the two molecules. At P closes to 5 bar, the two isotherm curves intersect each other, beyond which the CH_4 uptake becomes larger. To understand the increased uptake of CH_4 in SBN at P >5 bar, we analyze in Figure 2.29 the free-energy profiles of CO_2 and CH_4. We find that the CH_4 adsorption sites are highly localized with each site connected to three nearest-neighbor adsorption sites (indicated by yellow arrows in Figure 2.29(a)) with a separation barrier. The distances between these adsorption sites range from 4 to 4.6 Å with the average being at around 4.33 Å. Such separation values align closely with the minimum energy distance of two centre-of-mass CH_4 molecules, about 4.2 Å. On the other hand, the adsorption sites for CO_2 are less distinct from one another, and do not in general correspond to optimal CO_2-CO_2 distances (see Figure 2.29(b)). As a result, the CH_4 uptake in SBN is higher than that of CO_2 uptake for P up to a few thousand bars, well above the pressures considered for low-quality natural gas separations. At P equal or larger than 100 bar, the CH_4 loading saturates to 16 molecules per unit cell, equal to the number of distinct CH_4 adsorption sites that can be counted from the free-energy profile in Figure 2.29(a).

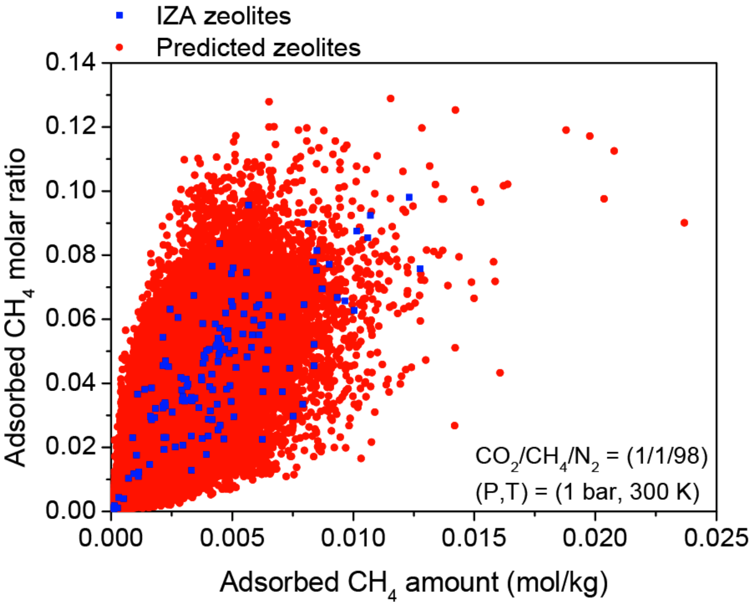

Figure 2.30: CH_4 capture using zeolites for coal-mine ventilated air. Adsorbed CH_4 concentration versus CH_4 loading for IZA (blue) and predicted (PCOD) (red) structures.

For coal-mine ventilation air comprised of 1% CH_4, 1% CO_2, and 98% N_2 at a total pressure of 1 bar, similar analysis was conducted to evaluate structures suitable for this separation. The three-component ideal adsorbed solution theory was utilized to obtain the mixture loading values from the pure component isotherms. Figure 2.30 shows the results for the IZA and the predicted zeolite structures. At this condition, the uptake values of these three gases tend to lie within the linear region in the pure component isotherms for most zeolite structures, and accordingly, a strong correlation exists between Henry coefficient and uptake values at this pressure. Thus, it is not surprising that in our analysis, we found that the top 20 structures (where the metric was taken to be simply the product of the solubility and selectivity) in the predicted zeolite database possess a CH_4 Henry coefficient >1.36 (mol/kg/bar) at 300 K, which puts them within the top 0.1% of the largest K_H in the database. Zeolite SBN, which has a relatively smaller K_H = 0.52 (mol/kg/bar), is predicted to have poor performance for this separation. The analysis of the free-energy landscape reveals that most of the top structures are comprised of one-dimensional channels for the CH_4 molecules. In addition, geometry analysis utilizing Zeo++[48] indicates that the maximum included sphere along these free paths has diameters between 5-6 Å. Thus, these channels can be characterized as narrow and not cage-like. In general, the zeolite structures with narrow channels can form strong CH_4 binding sites as the number of framework oxygen atoms located within close (i.e., 3-4 Å) vicinity to the centre of the binding sites can be maximized within this topology. On the other hand, a cage-like environment tends to provide fewer framework oxygen atoms at optimum distances from the CH_4, and thereby leads to low Henry coefficient values.

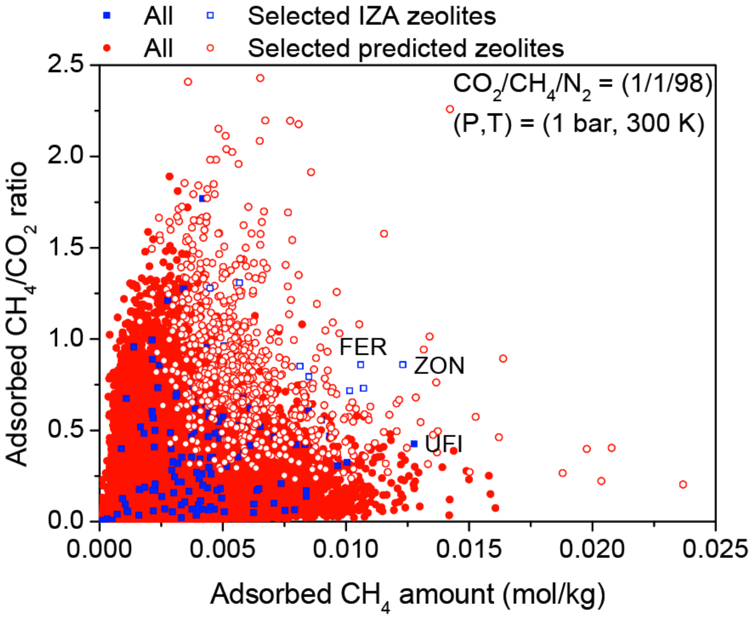

Figure 2.31: The same data points demonstrated in Figure 2.30 are plotted with adsorbed CH_4/CO_2 ratio as a function of adsorbed CH_4 amount. The no fill data points represent zeolite structures from a that have adsorbed CH_4 molar ratio >0.08. Thus, the best structures are structures within the set of no fill data points that also have large adsorbed CH_4 amount and large CH_4/CO_2 ratio values.

In this separation, we further focused on zeolite structures that also possess high adsorbed CH_4/CO_2 ratio. For this low-pressure condition, the adsorbed CH_4/CO_2 ratio can be regarded as the previously defined selectivity as the ratio of Henry coefficients. Figure 2.31 shows the CH_4/CO_2 selectivity of all structures plotted in Figure 2.30 as a function of adsorbed CH_4 amount, with open symbols indicating the structures with adsorbed CH_4 molar ratio >0.08 in Figure 2.30. The IZA structures with the largest adsorbed CH_4/CO_2 ratio were identified to be ZON and FER, with $K_H(CH_4) = 1.29$ and 1.12 (mol/kg/bar), respectively. Moreover, we have identified many PCOD structures that have a very large adsorbed CH_4/CO_2 ratio (>2.00), which can be promising for the separation (e.g., PCOD8301873 and PCOD8307399). Although IZA structures such as UFI have even larger $K_H(CH_4) = 1.39$ (mol/kg/bar) than what is computed for ZON and FER, the CH_4/CO_2 selectivity is only 0.44, which is much smaller compared to ZON (0.85) and FER (0.94). Analysis of these three structures based on the free-energy profiles reveals that the number of low-energy adsorption sites for CO_2 is larger compared with CH_4, which might partially be responsible for the relatively low CH_4/CO_2 selectivity value in UFI. In general, it is difficult to find common characteristics among zeolite structures that possess both large $K_H(CH_4)$ and large CH_4/CO_2 selectivity as intricate and subtle differences in the framework composition seem to make large contributions.

Besides pure-silica zeolite structures, we have also conducted large-scale screening on aluminosilicate zeolite structures in which some of the silicon atoms are substituted with aluminum atoms with the addition of cations to ensure charge neutrality. Similar work has been conducted in the past to analyze CO_2 adsorption in aluminosilicate zeolite structures.[34] In our analysis, we found aluminosilicate zeolite structures to be, in general, sub-optimal for methane reduction; the presence of cations creates strong binding sites for the CO_2 molecule, and subsequently leads to inferior CH_4/CO_2 selectivity values. However, more in-depth study needs to be conducted to determine whether we can completely rule out aluminosilicate zeolites as a viable class of materials for methane capture. One can also attempt to screen a large database of porous materials such as MOFs, ZIFs or covalent organic frameworks (COFs)[97] to identify structures optimal for methane capture. Unfortunately, many of the synthesized structures possess strong interactions between the metal atoms and the CO_2 molecules, and thus are more promising for CO_2 capture. Finally, there have been recent attempts in the literature to utilize activated carbon[98] and graphene[99] for methane capture. Activated carbon could be a good storage medium for relative pure methane,[98] but is probably not an ideal system to preferentially adsorb CH_4 over CO_2. Graphene, with proper doping and inter-layer spacing could potentially isolate CH_4,[99] but more work needs to be done to optimize such a system for selective methane capture with high loading capacity. A large-scale screening approach such as ours could be appropriate for such an exploration.

2.4.4 Conclusions

With the aim of discovering materials capable of isolating or concentrating methane at minimum energy costs, we have carried out extensive *in silico* screening of over 87,000 zeolite structures. Cutting-edge computational tools were employed, including highly efficient sorption code[74,90] for the zeolites that employs classical force fields with well-validated parameter sets. Two specific application areas were targeted, that is, concentrating methane from a medium-concentration source to a high concentration (for example, purifying a low-quality natural gas) and concentrating a very dilute methane stream into one of the moderate concentrations (for example, enabling energy production from coal-mine ventilation air). Both these applications warrant materials that need to have higher affinity to methane than to CO_2, a challenging proposition given methane's essentially non-polar character. We found that some of the zeolites show considerable promise both in terms of CH_4 uptake capacity and CH_4/CO_2 selectivity. Particularly noteworthy is the zeolite SBN, which has a large number of binding sites that are formed in such a way that maximizes the CH_4-CH_4 interactions, resulting in extraordinarily high performance for concentrating methane from a medium-concentration source to a high concentration. For dilute methane, on the other hand, there are zeolites like ZON and FER that possess large $K_H(CH_4)$ as well as high CH_4/CO_2 selectivity, making them excellent candidates for concentrating dilute methane stream into moderate concentration. For the latter separation, we have also identified other structures in the predicted zeolite database that could potentially outperform ZON and FER. All these structures consist of narrow one-dimensional channels that create strong binding sites for CH_4 by having a significant number of framework oxygen atoms at optimal distances from the CH_4 centre.

2.5 Large-scale computational screening of zeolites for ethane/ethene separation¶

2.5.1 Introduction

In addition to the widely used cryogenic processes for ethane/ethene separation, several other approaches for separating light olefins and paraffins have been proposed in the literature. These include physical and chemical absorption processes, extractive distillation, membranes, and adsorption onto porous materials.[18,100–105] The similarity of molecular sizes between ethane and ethene molecules contributes to the difficulty of the separation. Amongst these methods, adsorbent materials can potentially provide better separation of these components. By interacting more strongly with one component of the mixture, i.e., ethane/ethene mixture, an adsorbent may provide an adsorbed mixture richer in one component or limit the diffusion of one component for a kinetic separation.[100] Previous efforts with porous materials have looked into both physically adsorbing materials, such as zeolites,[104] and chemically adsorbing materials, such as MOFs with open-metal sites.[102,103] In addition, ZIF, specifically ZIF-8, has been investigated as a potential candidate for performing kinetic separation via the enhanced diffusivity of ethene compared to ethane within the material.[101] For this work, we focus on zeolite structures as possible candidates for adsorption-based separation and focus on ethane/ethene separation. In this study, we have used computational techniques to predict the thermodynamics of both ethane and ethene molecules adsorbed on these materials and conducted detailed analysis of their crystal structures. GCMC simulations were performed to obtain uptake of ethane and ethene for zeolite structures in both the IZA database[23] and Deem's hypothetical database.[24] With the development of our high-performance adsorption isotherm simulation code, we have the capability to characterize a large database of porous materials within a reasonable computing time.[74] As shown in previous sections, we have utilized this software to conduct large-scale screening simulations to identify optimal materials for carbon capture[1,34,35] and methane capture.[2] In this work, we have extended the scope of our simulation tool to explore a large database of zeolite structures for ethane/ethene separation.

2.5.2 Methods

GCMC simulations are widely used to predict the adsorption isotherms of pure and mixed gas in porous materials. At each point on the isotherm, a constant chemical potential (fugacity) of the gas, volume, and temperature are specified[57] to obtain the uptake values of ethane/ethene molecules. Molecular simulations of ethane in different zeolites have been carried out by many groups[106–111] while ethene has been studied far less.[112–114] A united-atom

---

[¶] Material in this section is adopted with permission from *Langmuir*, **2012**, 28 (32), 11914-11919.[3] Copyright 2012 American Chemical Society.
Link: http://dx.doi.org/10.1021/la302230z

force field that uses the 12-6 Lennard-Jones potential model was developed for alkanes and alkenes in the zeolites by Smit and co-workers, and it has been validated to reproduce the vapor liquid equilibrium of guest molecules.[82,115] The simulated adsorption isotherms computed using this force field show excellent agreement with the experimental data for several different known zeolite structures, and thus, we assumed the force field to be transferable to all pure-silica zeolite structures. To save computational time, a box composed of few, multiple unit cells of the material extending at least twice the distance of the cutoff radius, $R_{cut} = 12$ Å, in all directions is used for the simulation domain. All the interactions are cut off and shifted to zero at pairwise distances larger than R_{cut} without any tail corrections. The zeolite framework is regarded as being rigid, and periodic boundary conditions are applied. In the GCMC simulation, several million configurations are sampled through random insertion, deletion, and translation moves of a single guest molecule in order to obtain an accurate ensemble average. Same as previous sections, for the hypothetical zeolite database, the PCOD set of 139,397 was selected to be within +30 kJ/mol-Si of α-quartz[24] and methane accessible. We conducted GCMC simulations and characterized 30,000 randomly chosen zeolite structures from the filtered 139,397 hypothetical zeolite set in order to further reduce computational cost while still exploring a significant portion of the filtered zeolite set. Because we consider zeolite structures with the same chemistry (i.e., silicon and oxygen) and assumed the rigidity of the framework, the structure's geometry is the main factor that determines the material's separation performance. Given that small changes in the geometry lead to varying adsorption properties, a very large number of zeolite structures need to be examined in the screening process to find those suitable for ethane/ethene separation. To perform large scale screening for ethane/ethene separation, we utilized various techniques to accelerate the GCMC simulations.[90] Prior to the MC moves, energy grids with a spacing of 0.1 Å are computed and stored for all interactions between the framework and the guest atoms. Density-biased sampling techniques are utilized to make biased insertion moves into low energy regions within the simulation volume to speed up the MC equilibration process. Finally, we utilize the thousands of GPU threads within the GPU hardware to efficiently allocate threads to workload during the GCMC simulations.[58,74] With all of these optimization techniques in place, it takes only a few minutes of total wall time to obtain a complete pure component isotherm up to 100 bar (fugacity of the gas).

2.5.3 Results and discussion

Mixture isotherms are the most essential information used to evaluate the separation performance of a multicomponent system. However, direct mixture isotherm calculations can be inefficient given that the composition of a mixture input stream of process might also be a variable, and recalculations of the isotherms would be required for different ratios of the mixture. Subsequently, in the context of our large-scale screening, while the performance of a zeolite structure was still measured from the mixture isotherms, predictions were made from the IAST with the pure component isotherms calculations[63] instead. The IAST theory is a widely used method to predict the mixture isotherm and has been validated in many adsorption systems.[49]

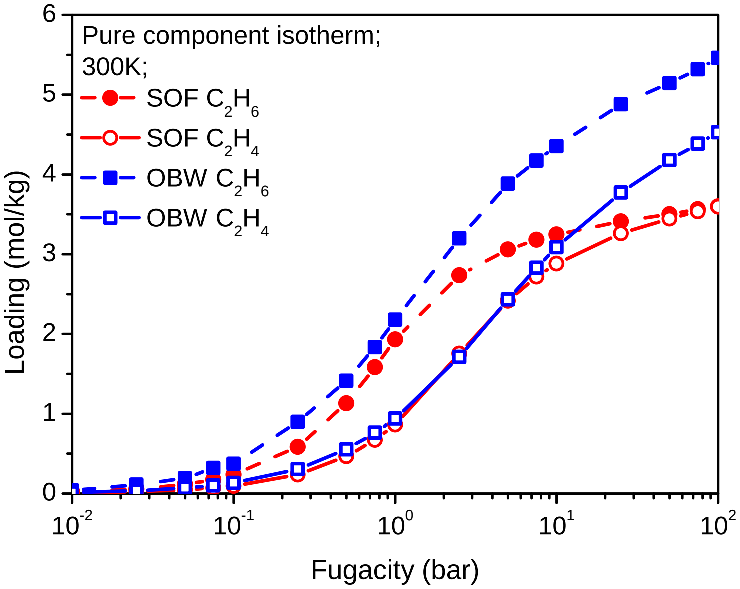

Figure 2.32: Ethane (dashed line) and ethene (solid line) adsorption isotherms in OBW (blue) and SOF (red) at 300 K from GCMC simulations.

2.5.3.1 Pure component isotherms

The pure component isotherms for both ethane and ethene molecules inside zeolite structures were obtained through GCMC simulations over a wide range of fugacity. It is interesting to note that two different types of isotherms emerged from our large-scale adsorption isotherm calculations. Figure 2.32 shows the pure component isotherms of zeolites OBW and SOF, which were chosen as IZA structures representing these two distinct classes of isotherms. Comparisons at high fugacity (i.e., between 1 and 100 bar) indicates that, for OBW, the loading difference between ethane and ethene remains relatively constant throughout this pressure range, while, in SOF, the difference becomes smaller as the uptake values of ethane and ethene converge to the same saturation point of around 3.5 mol/kg at very high fugacity of gas. As will be shown later, the difference in saturation behavior between the pure component isotherms serves as an important indicator that determines the separation characteristics of the zeolite materials.

In order to explain the different isotherm behaviors between OBW and SOF, we utilized the GPU code to generate the energy profiles of ethane and ethene inside the two structures. Figure 2.33 shows the energy contour profiles, representing the sum of the potential energies between the ethane/ethene molecules and all of the framework atoms within the unit cell of

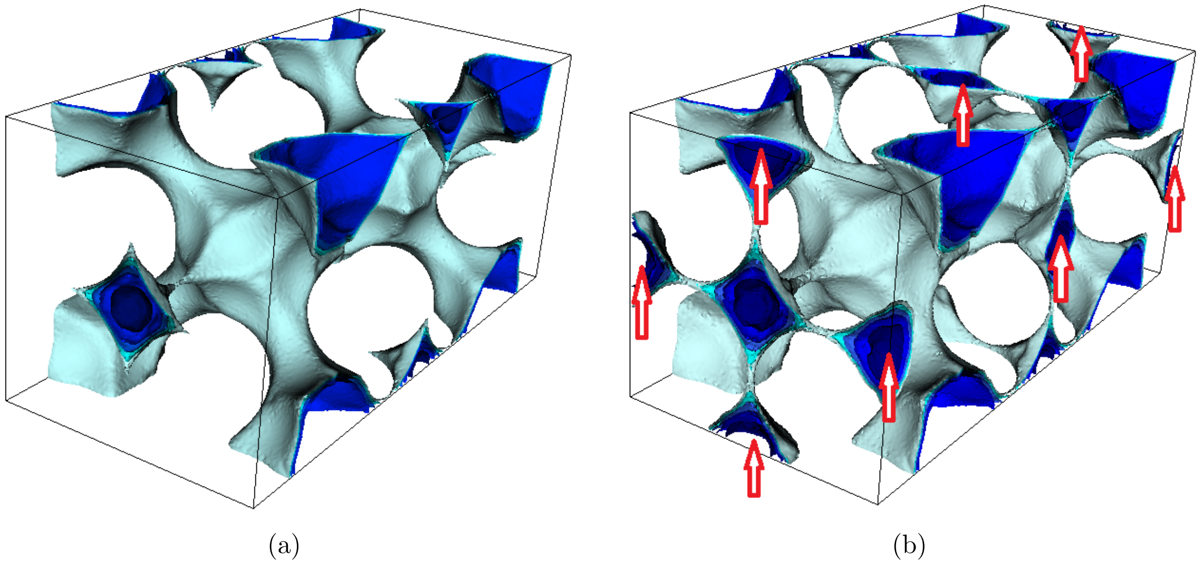
(a) (b)

Figure 2.33: OBW unit cell energy contour plots for (a) ethene and (b) ethane molecules. The blue colored part indicates low energy adsorption regions within the OBW structure. The red arrows point to low energy regions that are present for ethane but absent for ethene.

OBW, with the blue regions indicating low energy adsorption sites. Because both ethane and ethene are represented as polyatomic molecules in our simulations, the average energy of the molecule at each grid point was obtained via conducting 100 center-of-mass test rotations and collecting the Boltzmann-weighted average energy for all of the random rotation moves. Comparison between the ethene (Figure 2.33(a)) and the ethane (Figure 2.33(b)) energy contour plots reveals that the ethane molecule occupies additional regions within the unit cell that are energetically forbidden to the ethene molecule. These extra ethane adsorption sites are separated from the main channel by a relatively large energy barrier. We impose a cutoff energy value, $E_{cut} = 15k_BT$ (with T = 300 K), where an adsorption site surrounded in all spatial directions by an energy barrier higher than E_{cut} is deemed to be inaccessible. In our code, we have implemented a blocking routine that allows for automatic identification of inaccessible regions via the flood fill algorithm.[60,61,116] The value of E_{cut} was chosen to be sufficiently large such that diffusion across this barrier is not expected within the experimental time scale.[60,61,116] It turns out that, in OBW, the energy barrier separating the extra adsorption sites from the main channel is high enough to block diffusion of ethene while low enough to allow diffusion of ethane molecules as can be seen from Figure 2.33. Thus, changing E_{cut} in our simulations can alter the diffusion properties in such a way that the adsorption properties for ethane and ethene become similar to one another. In our large-scale screening process, we have identified many zeolite structures similar to OBW, where the energy cutoff criterion imposed to enable/disable diffusion into localized regions led to extra adsorption sites for ethane. In reality, we expect the diffusion properties of ethane and ethene to be similar enough to one another in these types of zeolite structures such that the two gas molecules will either both diffuse into all of the same localized regions if the experimental time scale is long enough or be forbidden to access the same localized regions if the time scale is short enough. Although a non-equilibrium separation based on membranes, for example, can exploit these properties if the diffusion coefficients of the two molecules are sufficiently different from one another, in this study we focus on equilibrium separations and consider structures similar to OBW as being suboptimal.

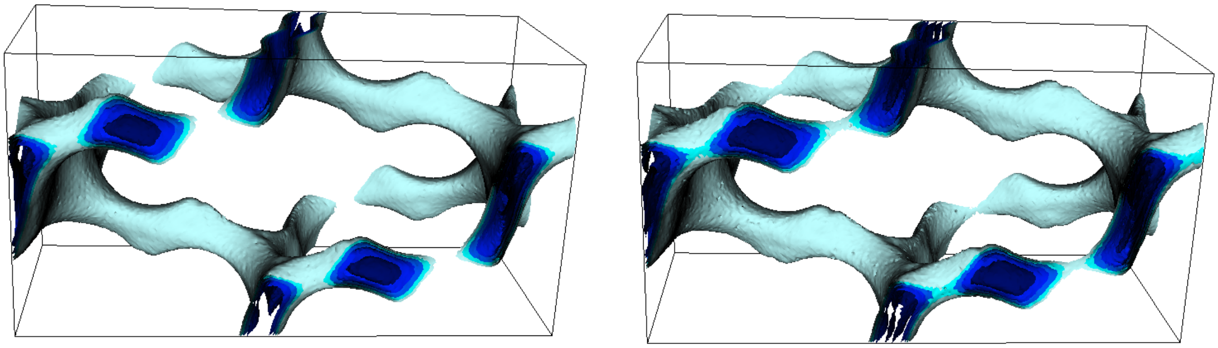

(a) (b)

Figure 2.34: SOF unit cell energy contour plots for (a) ethene and (b) ethane molecules. Similar to Figure 2.33, blue indicates low energy adsorption regions, which happens to be in similar locations for both ethane and ethene in the case of SOF.

On the other hand, the ethane/ethene energy contour plots for zeolite SOF (Figure 2.34) reveal that the low energy regions for the two molecules are same for both gas molecules. Because ethane and ethene share the same adsorption sites, it is not surprising that the uptake of two molecules converges to the same value at high pressure as seen from Figure 2.32. In the rest of this study, we concentrate on zeolite structures similar to SOF, where high working capacity and high selectivity for separation cannot be simply explained from differing diffusion behaviors (as was the case in OBW).

2.5.3.2 Mixture isotherms

Although IAST has been validated for a variety of systems, it remains important to test its applicability in the ethene/ethane system. The SOF mixture isotherm computed using GCMC simulations was treated as a benchmark case used to determine the accuracy of IAST. The simulated adsorption isotherm curves seen in Figure 2.35 demonstrate that the mixture isotherm data produced from pure component isotherms via IAST are in excellent

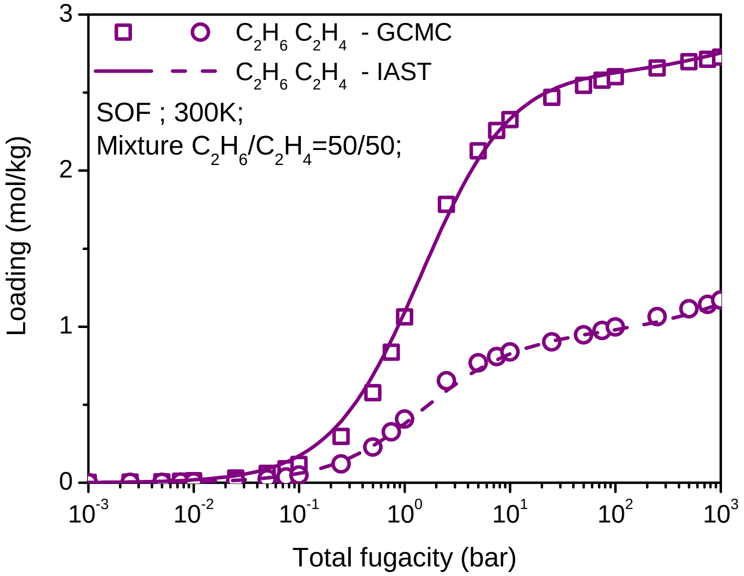

Figure 2.35: Comparison of the IAST-predicted and GCMC-computed mixture isotherms in zeolite SOF. Open symbols show the GCMC-computed ethane-ethene (1:1) mixture isotherm in SOF at 300 K as a function of total fugacity. The lines show the predicted mixture isotherm by IAST.

agreement with the mixture isotherm data obtained from the GCMC simulations over a very wide range of fugacity. We have also tested IAST on the zeolite OBW, and the result is shown in Figure 2.36. The mixture isotherm for OBW clearly shows that IAST cannot be applied to predict the mixture isotherm accurately. The main difference between these two structures comes from the similarity of the surface area of the material accessible to each component in the mixture. As shown in Figure 2.33 and Figure 2.34, the accessible surface area of each component is nearly identical in SOF but not in OBW. More detailed information, such as identifying accessible regions for each component from molecular simulation prior to applying IAST, will improve the prediction of the mixture isotherms in materials like OBW. A detailed evaluation of IAST is out of the scope of this work and will be studied as a separate topic. In conclusion, for those structures similar to SOF studied in this study, IAST can be used to predict the mixture behavior with high accuracy.

2.5.3.3 Screening

In order to find optimal zeolite structures that can be best utilized for ethane/ethene separation, we need to construct a criterion that separates high performance structures from the poor performing ones. In this study, we assume that a pressure swing process for an equimolar mixture of ethane/ethene input stream was applied for the separation. Additionally,

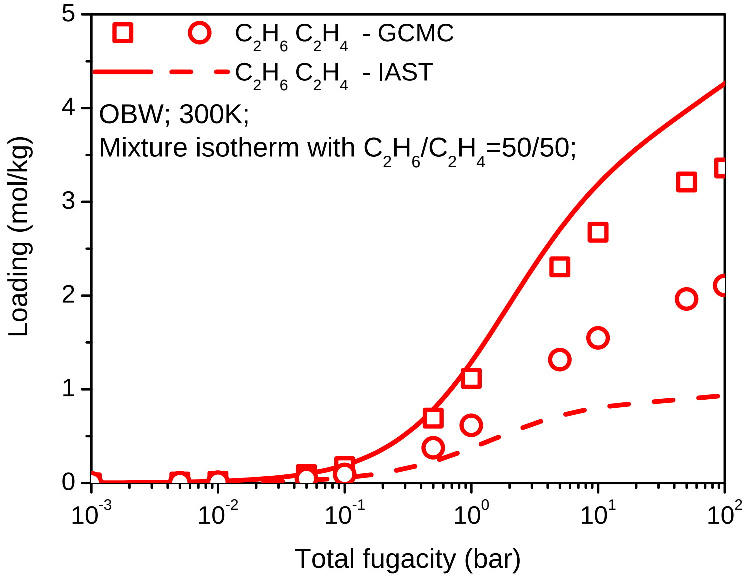

Figure 2.36: Comparison of the IAST-predicted and GCMC-computed mixture isotherms in zeolite OBW. Open symbols show the GCMC-computed ethane-ethene (1:1) mixture isotherm in OBW at 300K as a function of total fugacity of the mixture while the lines show the IAST-predicted mixture isotherm.

we assume that the adsorption stage is carried out at 1 bar and 300 K, and the desorption stage is set to be simply vacuum. Both the selectivity (i.e., S, ratio of ethane/ethene molecules) and ethane working capacities (L) are treated as the two most important quantities that determine the efficiency of the ethane/ethene separation process since it would be ideal to both minimize the number of cycles needed to separate the input stream to a given purity and maximize the working capacities of ethane (i.e., loading of ethane at the adsorption stage) molecules to minimize the overall cost. Given their importance, it would seem intuitive to search for structures that maximize the product of the two aforementioned quantities (i.e., S x L). Therefore, we chose S x L as a metric that indicates the performance of a given structure.

Figure 2.37 shows the two-dimensional ethane/ethene separation performance plot for 171 IZA structures as well as 30,000 hypothetical zeolite structures from Deem's database. Most of the data points (99.8%) fall below the reference performance curve of S x L = 3, which we utilized to separate high and low performance regions within the zeolite search space. At this point, we would like to stress that the choice of 3 here is intuitively arbitrary. The purpose of providing a reference line is to qualitatively define a number of promising materials. It is not surprising that most of the structures perform poorly given that ethane and ethene molecules are very similar to one another, resulting in similar adsorption properties for a given structure. From the top structures, we have identified that 7 out of 171

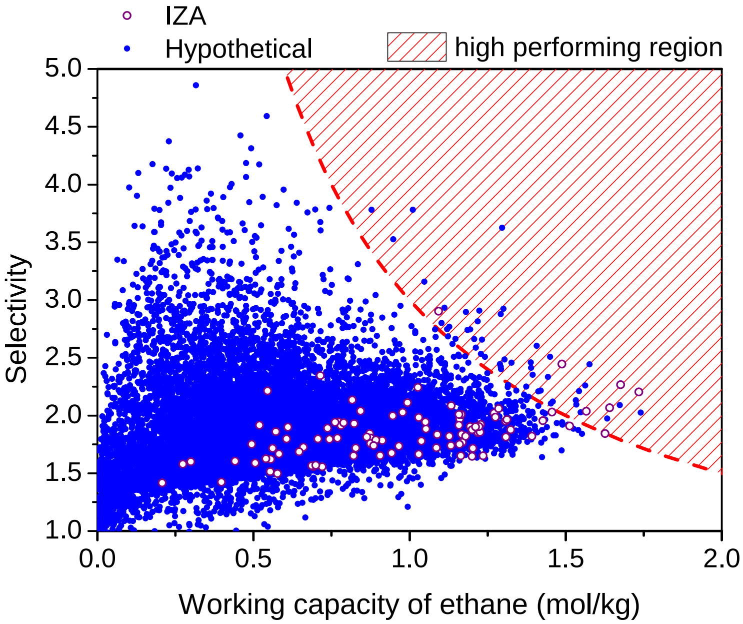

Figure 2.37: Two-dimensional ethane/ethene performance plot for 171 IZA structures (magenta, open circles) and 30,000 hypothetical zeolite structures (blue, closed circles). For each of the points both the selectivity (vertical axis) and ethane loading (horizontal axis) are obtained from the predicted mixture isotherm by using IAST. The dashed red line represents the reference performance curve of S x L = 3 and serves to separate the high (above the line) and the low (below the line) performance zeolite structures.

IZA structures (i.e., from the highest to lowest: zeolites EPI, STW, THO, EAB, PUN, SOF, and MEI) and 50 out of 30,000 hypothetical structures lie above the S x L = 3 curve. The highest performing structures in the hypothetical and the IZA databases are PCOD8156587 (S x L = 4.70) and zeolite EPI (S x L = 3.82), respectively. Included in the set of top performing structures is SOF, which possesses both high selectivity (2.9) and working capacity (1.1 mol/kg). In order to explain SOF's high performance, the pairwise interactions between the gas and the host framework atoms are studied in greater detail. Figure 2.38(a) shows the two energy curves that describe the Lennard-Jones interactions between CH_2 of ethene and CH_3 of ethane and the oxygen zeolite framework atom. In the definition of the force field, the Lennard-Jones interactions between ethane/ethene molecules and the silicon framework atoms are assumed to be zero. To obtain high selectivity and uptake of ethane molecule, there needs to be a specific localized region within the zeolite structures such that (a) the interaction between CH_3 and oxygen is maximized while the CH_2-oxygen interaction is suboptimal (leading to high selectivity) and (b) the number of such localized regions is maximized (leading to high uptake). In order to gain a large enough energy difference that translates into distinct, high-selective adsorption properties for the ethane/ethene molecules,

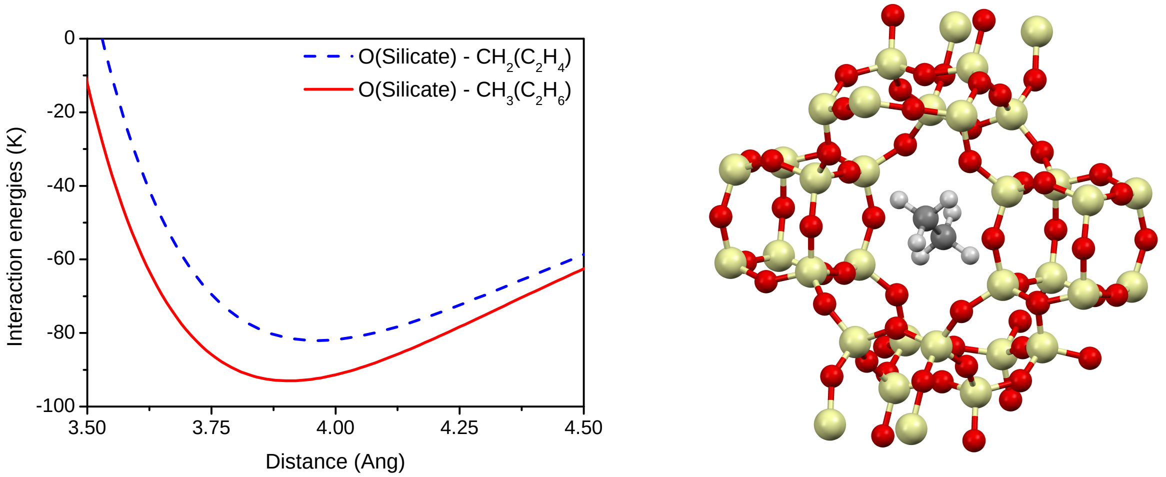

(a) (b)

Figure 2.38: (a) The CH_2-oxygen and CH_3-oxygen Lennard-Jones interaction as a function of distance. The minimum interaction energy for CH_2-oxygen (CH_3-oxygen) occurs at a distance of 3.96 (3.90) Å. (b) A localized region of framework atoms that lead to high performance ethane/ethene separation in SOF.

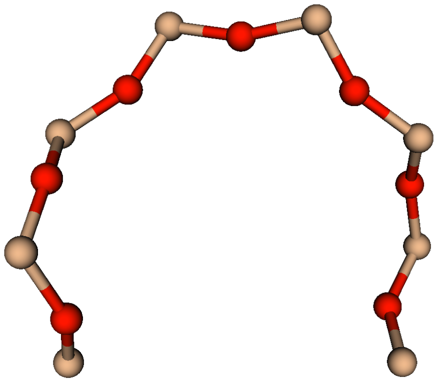

Figure 2.39: The illustrated arrangement of zeolite framework atoms was identified in the preferential ethane binding region of the best performing separation material, PCOD8156587. A pair of such framework atom arrangements, one around each CH_3 group of a guest ethane molecule, gives rise to a large number of favorable guest-host interactions, leading to preferential ethane adsorption.

the two sites within the coarse-grained guest molecule need to be surrounded by as many oxygen atoms as possible in a localized region radius of roughly 3.9 Å where the distance creates the largest binding energy difference between CH_3-oxygen and CH_2-oxygen interactions. The zeolite framework geometry depicted in Figure 2.38(b) shows a channel diameter of about 7 Å in the zeolite SOF that provides a localized region optimal for preferential adsorption of ethane over ethene. Since all structures examined in this study are pure-silica zeolites and so share the same chemical composition, framework geometry, rather than chemistry, is the main factor which determines a material's separation performance. Having determined the characteristics of preferential sites for ethane adsorption in zeolite frameworks, one can utilize cheminformatics to efficiently screen a large database of zeolite materials to identify those structures that contain this specific preferential geometry without the need to conduct molecular simulations.[117] Through inspection of the potential energy surface, we identified the specific zeolite framework geometry present in the preferential ethane binding site of the optimal separation material, PCOD8156587 (highest S x L metric); the arrangement of zeolite atoms around one CH_3 group of the guest is shown in Figure 2.39, and coordinates can be found in supporting information Table SI 1 of ref 3. Two zeolite framework atom arrangements similar to this, in close proximity in a guest-accessible channel, will give rise to strong ethane-host interaction due to the large number of framework atoms at an optimal distance from each CH_3 group of the ethane molecule. Given this understanding of the optimum framework geometry, we can identify other materials which exhibit similar framework atom arrangements, following the procedure described in ref 117. Accordingly, we find that, out of the 30 optimum separation materials with the largest S x L metric values, 27 (90%) could be identified without the need for simulation, by searching only for this preferential framework geometry.

As a result, we have illustrated that, through high-throughput simulation, structural features that dominate adsorption performance of a material can be determined. Accordingly, for hypothetical zeolite structures that have yet to be simulated, efficient prescreening of databases can identify promising candidate materials prior to molecular simulation, ensuring that the more computationally expensive techniques can be selectively applied. A greater degree of discrimination between promising candidate materials identified in this way is achievable through, for instance, consideration of the relative proportion of a framework's guest-accessible volume which is composed of such preferential framework geometries; however, these developments are beyond the scope of this work and will be described in a future study.

2.5.4 Conclusions

Utilizing a high-throughput GPU code, we have characterized adsorption properties of ethane and ethene molecules inside all of the experimentally verified IZA zeolite structures and 30,000 hypothetical zeolite structures. We have observed that, due to the similarities shared between the two gas molecules, most of the zeolite structures are not suitable for ethane/ethene separation. However, we have identified a number of optimal structures, which possess both high selectivity and high ethane working capacity. Furthermore, we have determined the structural geometry that is responsible for preferential ethane adsorption and have shown that optimum ethane/ethene separation materials can be identified by screening framework geometries using this knowledge. Although the number of high-performing structures remain very small, the insights gained from our simulation results can help identify the ideal zeolite structures for ethane/ethene separation. And we believe that the procedures outlined here can be extended to explore suitability of ethane/ethene separation in other classes of materials.

Chapter 3

Force-field development from first-principles calculations

In chapter 2, we have evaluated (pure-silica and aluminosilicate) zeolites and zeolitic imidazolate frameworks (ZIFs) for their potential use in several different gas separations. Ideally, one would like to apply a similar screening approach to study other classes of materials, in particular, metal-organic frameworks (MOFs). The chemistry of MOFs, however, is much more diverse compared to the aforementioned zeolites. Accordingly, dissimilar to zeolite and ZIF materials, a few sets of developed force fields cannot be generally applied to all MOF materials for screening purposes, which imposes a great challenge on computational studies. As an example, open-metal site materials, M-MOF-74 (also known as M-CPO-27, M = Mg, Zn, etc.), have been demonstrated to be promising candidates for CCS applications.[31–33] It has also been shown that commonly used force fields can only provide a limited description of the interaction between guest molecules (e.g., CO_2) and these open-metal sites, which therefore yields a very poor estimation in adsorption properties.[40] Herein, there is a necessity to develop different methods for such a chemically diverse class of materials to accurately characterize materials.

In this chapter, two different methods are introduced. In addition to (1) detailed derivation of force fields, (2) efficient corrections to trial force fields (potentially not accurate) is also proposed. Both of these methodologies require inputs from first-principles calculations as accurate references. The organization of this chapter follows as below:

- Section 3.1 - 3.2: Detailed derivation of force fields
  - Section 3.1 *Ab initio carbon capture in open-site metal organic frameworks*:[118] this section introduces a novel methodology to obtain accurate force fields for CO_2 and N_2 adsorbed in porous materials from high-level MP2 quantum chemical calculations with the NEMO decomposition technique on the level of cluster calculations.

  - Section 3.2 *Force-field development from electronic structure calculations with periodic boundary conditions: applications to gaseous adsorption and transport in metal-organic frameworks*:[4] this section presents a revised methodology that is built upon the one introduced previously in section 3.1. To facilitate the automation of the proposed methodology as well as reduce the limitations imposed by the cluster calculations, we further modify our method to be fully compatible with density functional theory calculations with periodic boundary calculations.

- Section 3.3: Efficient corrections on initial trial force fields
  - Section 3.3 *Efficient determination of accurate force fields for porous materials using ab initio total energy calculations*:[119] this section presents an alternative approach in which a detailed derivation of force field parameters is not required. Instead, we efficiently make corrections on trial (potentially not accurate) force fields based upon a few quantum chemical calculations, e.g., binding energy.

These two proposed approaches allow us to accurately and efficiently characterize MOFs materials or even some other classes of materials.

3.1 *Ab initio* carbon capture in open-site metal-organic frameworks[*]

3.1.1 Introduction

It is important to develop a theoretical method that supports experimental efforts to identify an ideal MOF for carbon capture. A key aspect is the ability to predict the properties of a MOF before the material is synthesized. At present it is possible to carry out accurate quantum chemical calculations on these types of systems.[120] State-of-the-art density functional theory (DFT) calculations provide important insights in the energetics and siting of CO_2 at zero Kelvin.[120] The separation of flue gas, however, requires thermodynamic information (e.g., adsorption isotherms) at flue gas conditions (40 ^{o}C and 1 atm). This type of information can be obtained from molecular simulation using classical force fields.

For some classes of MOFs these predictions still pose significant difficulties, particularly for MOFs with open-metal sites.[33, 121–127] These materials crystalize in such a way that both linkers and solvent molecules coordinate to the metal centers. The stability of the materials allows the removal of the solvent, which creates an open-metal site. This site has a very high affinity to CO_2 making the material very promising for carbon capture. Reasonable predictions on the ability of a material to adsorb CO_2 can be often made using existing generic force fields.[40, 42, 128] However, for these materials Krishna and van Baten observed that, exactly at the conditions that are important for flue gas capture, the universal force field (UFF[129]) fails to correctly describe the adsorption of CO_2.[40] The reason is that an open-metal site imposes a very different chemical environment compared with those considered in the development of these force fields.[124]

Ideally one would like to use state-of-the-art quantum chemical calculations to evaluate the energy for each state point of a grand-canonical Monte Carlo (GCMC) simulation to compute the adsorption isotherm. However, such calculations would require millions of years of CPU time. In this work, we have developed a methodology to obtain accurate force fields from quantum calculations that correctly predict the adsorption isotherms of CO_2 and N_2 on MOFs with open-metal sites. Our approach is based on the NEMO methodology,[130, 131] which decomposes the total electronic interaction energy obtained from quantum chemical calculations into the various contributions (electrostatic, repulsive, dispersion, etc.). The force field expression closely matches the functional form of the NEMO decomposition, allowing us to accurately fit the parameters of the force field to reproduce the quantum calculations. We have developed a strategy to obtain the interaction for each atom-type of the MOF with CO_2 (or N_2).

The UFF[129] or Dreiding[54] force fields are frequently used to describe the interaction of gas molecules with the atoms of the MOF.[42, 128, 132] In these force fields, the non-bonded energy is described by a Lennard-Jones potential plus Coulomb interactions. As these force

---

[*] Material in this section is based on *Nat. Chem.*, **2012**, 4, 810-816.[118]
Link: http://dx.doi.org/10.1038/nchem.1432

fields are employed for many different systems, the parameters should give a reasonable description of the interaction of CO_2 with Mg in many different chemical environments (for example, a zeolite instead of a MOF). Our quantum calculations show that, due to the open-metal site, CO_2 (and N_2) can get closer to the metal site than what predicted by the UFF/Dreiding force fields. The aim of this work is to develop a systematic methodology to obtain force fields from quantum chemical calculations that correctly describe the interaction of the guest gas with the open-metal site. To determine a complete isotherm at flue gas conditions, and this requires taking into account ensemble averages involving millions of different configurations. When developing a force field one has therefore to ensure that a large number of different configurations are described in a reasonable way, and not just the minimum energy configuration, which is usually the focus of a quantum chemical calculation.

3.1.2 Methodology

Some key steps in our methodology are discussed below. A more detailed description can be found in the supporting information of ref 118. It should be noted that, in the next section, a revised methodology built upon this work is also proposed. A complete and clear introduction and discussion of every step in our methodology can be further seen in section 3.2.

3.1.2.1 Crystal structures

Our calculations relied on an accurate representation of the crystal structure of Mg-MOF-74. Unfortunately at present, single crystals of Mg-MOF-74 have not been obtained and the structural information is therefore obtained from powder diffraction data[133–135] Detailed inspection of these experimental structures shows a significant distortion of the bridging ligand in powder diffraction data (Mg-MOF-74), which is not observed in our DFT calculations. We used PW91 (QuantumEspresso(QE)[136]) and PBE (SIESTA[96,137] and VASP[138,139]) to obtain the fully relaxed structure of the MOF. The good agreement between these two approaches confirms the validity of the localized basis set approach employed within SIESTA. The lattice parameters and the C-C bond lengths within the ligand of the relaxed geometry obtained with PW91 (QE) and PBE (SIESTA and VASP) are reported in Table 3.1. Similar results were obtained with D3LYP by Valenzano et al.[120] The fact that four different approaches predict nearly identical crystal structure gives us confidence in the reliability of the theory. It is therefore surprising that a comparison with the experimental structure show such large deviations. For example, we found a deviation of the C_a-C_b and C_d-C_b bond distances by as much as 8% and 7%, respectively. As we are interested in predicting the adsorption isotherms, we computed the adsorption isotherms of CO_2 for the experimental structure and the structures predicted by DFT (see Appendix Figure A.1). The results show that the two different DFT structures (PW91, QE) and (PBE, SIESTA) give nearly identical adsorption isotherms. But the results differ from the experimental isotherm. These differences illustrate the importance of using the correct Mg-MOF-74 structure. For Zn-MOF-74, a closely related material, it is possible to synthesize a single crystal and for this material crystal structure can be determined with higher accuracy.[134] In Table 3.1 we have compared the structural data for this material from our DFT (PW91, QE and PBE, VASP) calculations, previous calculations,[120] and experiments.[133,135] For this material our calculated lattice parameters and atomic positions are in an excellent agreement with the experimental data (the largest deviation for C_a-C_b bond length is 1.2%). Given the uncertainties with the experimental structure for Mg-MOF-74 and the excellent agreement we obtained using our DFT approach for Zn-MOF-74, we conclude that the computational structure of DFT is most likely the most reliable representation of Mg-MOF-74. Note that the optimized structures of Mg- and Zn-MOF-74 from QE are adopted while the one of Mg_2(dobpdc) obtained from VASP is used. It should be also noted that the structures obtained here are also used in the rest of sections presented in this chapter.

Metal, source	Lattice parameters		Bond lengths			
Method	a	c	C_a-C_b	C_b-C_c	C_c-C_d	C_d-C_b
Mg, this work PW91, QE	26.114	6.917	1.483	1.433	1.399	1.401
Mg, this work PBE, SIESTA	26.260	7.036	1.490	1.436	1.405	1.406
Mg, this work PBE, VASP	26.136	6.942	1.484	1.434	1.401	1.402
Mg, calc.[120] DFT-B3LYP	26.109	6.969	1.493	1.430	1.396	1.399
Mg, exp.[135]	26.026	6.759	1.540	1.314	1.430	1.509
Mg, exp.[133]	25.922	6.863	1.613	1.490	1.526	1.260
Zn, this work PW91, QE	26.095	6.888	1.482	1.430	1.397	1.400
Zn, this work PBE, VASP	26.190	6.935	1.484	1.432	1.399	1.402
Zn, exp.[134]	25.932	6.837	1.500	1.420	1.391	1.398

Table 3.1: Lattice parameters and bond distances of Mg- and Zn-MOF-74 investigated in this work from DFT calculations and experiments. All values are in the units of Å.

3.1.2.2 DFT calculations

QE calculations use Kohn-Sham orbitals and the charge distribution of the outer shell electrons are expanded in the Fourier series up to the plane-waves of the kinetic energy of 35 Rydberg and 420 Rydberg, respectively. The field exerted on the outer electronic shells C

[2s2p], O [2s2p], Mg [2p3s3p3d], Zn [4s4p3d], and H [1s] by the inner cores was described by the non-relativistic Vanderbilt ultrasoft core pseudo potentials; non-linear core correction is included in the Zn and Mg pseudo potentials. The integration over the irreducible Brillouin zone was carried out over 2x2x8, and the results were checked for convergence over 4x4x16 Monkhorst-Pack grids. Atomic positions were considered converged when the total force applied to the atoms in the unit cell is less than 0.004 Rydberg/bohr/cell.

SIESTA calculations used variationally optimized double-Z polarized basis sets implying the presence of d-orbitals for C, N and O. Non-local, norm-conserving fully separable Trouiller-Martins pseudopotentials were used. C[2s2p], O[2s2p] and Mg[2s2p3s] electrons were explicitly included in the valence. Real space integrals were performed on a mesh with a 300 Ry cutoff.

VASP calculations use projector-augmented-wave (PAW) potentials to describe the interaction between core and valence electrons. C[2s2p], O[2s2p], Mg[3s3p] and Zn[4p3d] valence electrons are explicitly included in the valence. A plane-waves kinetic energy cutoff of 500 eV is used and the integration over the irreducible Brillouin zone is carried out over a 2x2x8 Monkhorst-Pack grid. Atomic positions are relaxed until forces are lower than 0.02 eV/Å.

Interaction energies were computed using the vdW-DF functional[140, 141] as implemented in SIESTA, which was further used to compare to MP2 energies at the cluster levels and to MP2-derived force field computed energies with periodic boundary conditions. Basis-set superposition errors are counterpoise corrected.

3.1.2.3 MP2 calculations

In this work, we used second-order Møller-Plesset perturbation theory (MP2) to describe interactions of CO_2 and N_2 with MOF sites. MP2 is adequate for the treatment of electron correlation in cases where strong correlations are not present. In the Mg-MOF-74, we have defined 8 representative clusters of the MOF, which will be discussed below, to compute interactions with the guest, each cluster chosen to best represent the atom-type to be parameterized (excluding H atom-type). Within each cluster, the basis functions were chosen such that a larger contraction was used for the guest atoms, the atom-type being approached in the MOF, and its nearest neighbors, while a smaller contraction was used for all atoms father away. The interaction energies were determined by the supermolecular approach, counterpoise corrected for basis set superposition error.[142] All calculations have been performed using the MOLCAS[143] software version 7.6. Resolution of the identity (RI) and Cholesky decomposition (CD) techniques were employed to treat the two electron integrals.[144–146] The Douglas-Kroll Hess Hamiltonian[147] was used in conjunction with atomic natural orbital relativistic correlation consistent (ANO-RCC)[148, 149] type of basis functions.

3.1.2.4 NEMO decomposition

Using the MP2 interaction energies as a reference, the non-empirical model potential (NEMO)[131] decomposition was used to partition the energy into repulsion, polarization, dispersion, and electrostatic components for all clusters and paths. The electrostatic moments to second order and dipole-dipole polarizabilities were obtained using the LoProp[150] method based on the MP2 densities.[151] The terms were then grouped into repulsive, attractive, and electrostatic terms, where the charge-charge interactions and repulsion remained constant, while the polarization, dispersion, and effects of dipoles and quadrupoles were grouped into attraction terms. The importance of this decomposition is that we can fit the corresponding terms in our force field separately.

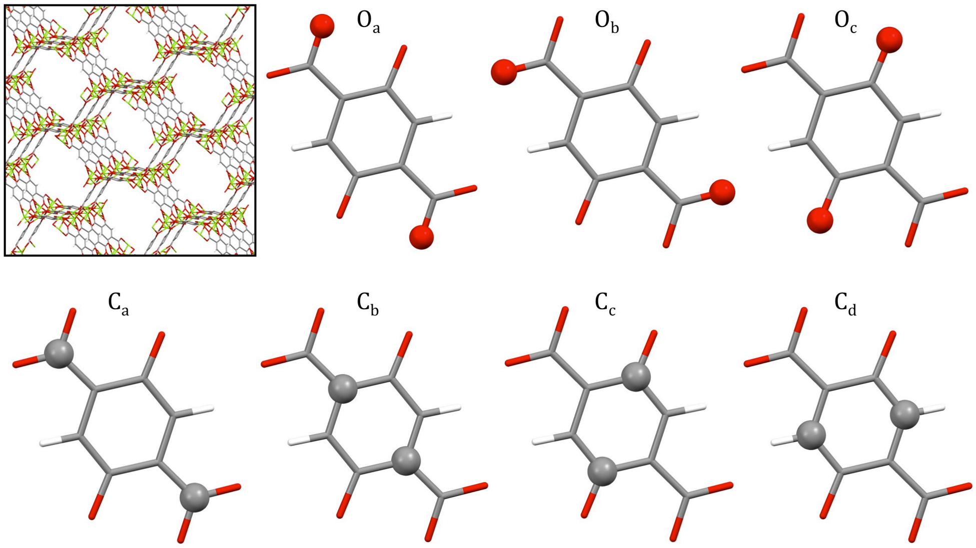

Figure 3.1: Image of Mg-MOF-74 structure (top left) where it is seen that all metal types are equivalent, and BDC linker atom-types considered in our parameterization along with the naming scheme adopted here

3.1.2.5 Force field parameterization

In our force field, the electrostatic interactions were described by charges estimated using the LoProp scheme.[150] Initial tests showed that the repulsive interactions could not be accurately described with a Lennard-Jones potential. A modified Buckingham potential was used in addition to the Coulomb interaction. The repulsive part is defined as:

$$u^{rep}(r_{ij}) = \begin{cases} \infty & r_{ij} \leq R_{min} \\ A\exp(-Br_{ij}) & r_{ij} > R_{min} \end{cases} \tag{3.1}$$

which can be fitted very accurately. For the attractive part, we used, in addition to the conventional r_{ij}^6 term, an r_{ij}^5 term to obtain a better representation of the decomposed energies:

$$u^{att}(r_{ij}) = \frac{C}{r_{ij}^5} + \frac{D}{r_{ij}^6} \tag{3.2}$$

To determine the parameters of this force field, we used the following procedure. First, we generated sets of configurations organized into paths, with one path for each type of atom in the framework, i.e., Mg, O_a, O_b, O_c, C_a, C_b, C_c, and C_d in Mg-MOF-74 (see Figure 3.1) Along each path CO_2 (or N_2) approaches a specific atom-type in such a way that for each configuration on this path the MP2 energy mainly represent the interaction of CO_2 (or N_2) with this particular atom-type. These energies should thus contribute the most to the fitting of the parameters of the force field for this particular atom-type. Namely, only the parameters for the interaction between the target atom-type and the guest molecule were adjusted to reproduce the NEMO-decomposed energy. It should be noted that, due to the NEMO decomposition technique, the decomposed energies were parameterized separately. The decomposition in electrostatic, repulsive, and attractive interactions for each path allowed us to fit this relatively large number of force field parameters efficiently and accurately.

Given that it is infeasible to carry out MP2 calculations for the full periodic MOF, we define for each atom-type (and corresponding path) a finite cluster of atoms within the MOF that should represent the electronic environment of this atom-type in the MOF. The size of the cluster is set such that the interaction of CO_2 (or N_2) with this atom-type mimics the interaction in the full MOF. For each of these paths, we selected a portion of the Mg-MOF-74 framework that is sufficiently large to accurately represent the chemical environment of the targeted atom. The size of the cluster was chosen in a compromise between accuracy and computational cost, with the size of the basis set as a constraint. Figure 3.2 shows the adopted cluster and approaching path of CO_2 and N_2 for Mg atom-type. The clusters and paths corresponding to the other 7 atom-types can be seen in Appendix A from Figure A.2 to A.8.

This mapping was carried out in two phases. We first took all atoms of a particular element and minimized the error over all paths for that element simultaneously. This adjustment was done moving outward from the metal, and started over interactively until converged. For the second phase, we optimized the force field parameters for each atom-type individually with an ordering based on its relative contribution to the total energy. The ratio of the energy between the target atom-type and the guest molecule to the total energy was computed, and the paths were taken in order from the highest to lowest ratio. This procedure was repeated until all the parameters were converged.

3.1.2.6 Grand-canonical Monte Carlo simulations

Adsorption (pure and mixture) isotherms for CO_2 and N_2 in Mg-MOF-74 were predicted using the GCMC technique, where a constant chemical potential (fugacity), volume, and temperature are imposed.[57] The heat of adsorption was calculated directly using the procedure developed by Vuong and Monson.[152] The energies of guest-framework interactions were

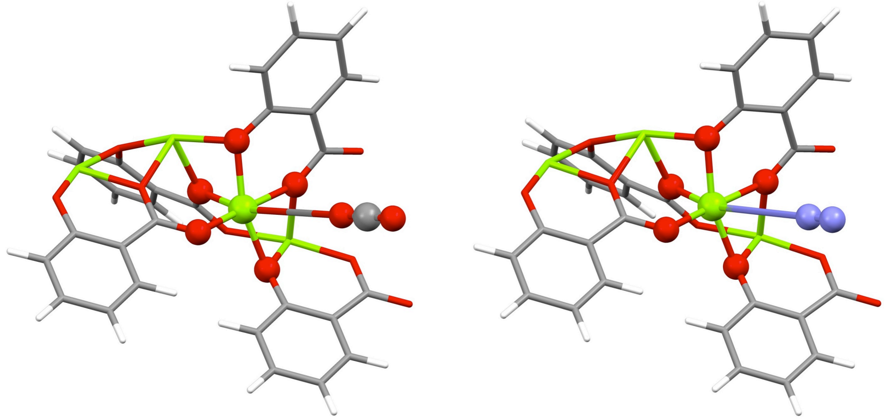

Figure 3.2: Adopted Mg atom-type cluster of Mg-MOF-74 and corresponding paths of (left) CO_2 and (right) N_2. The figures show the atoms of clusters and molecules as ball and stick (Mg, green; O, red; C, grey; H, white; N, purple)

computed using the potential model described above and guest-guest interactions were described using the TraPPE force field.[55] Electrostatic energy was computed using the Ewald summation technique. Short-range interactions were cut off and shifted to zero at a distance of 12.8 Å, and the simulation box extended at least twice this distance in all orthogonal directions. No tail correction was used. To accelerate the calculation of molecule-framework interaction energies, the short-range part of the interaction was stored in a pre-computed grid with a spacing of 0.10 Å and linearly interpolated between grid points. Trajectories were equilibrated for at least 20 million configurations before taking averages over a further 4 million configurations.

3.1.3 Results and discussion

Figures 3.3(a) and 3.3(b) show a typical outcome of the NEMO decomposition of the total MP2 energies of the Mg atom-CO_2 interaction into a repulsive and an attractive contribution, respectively, together with the fitted force fields. The electrostatic (charge-charge) contribution is identical to the leading term of the grouped-term NEMO decomposition, so no fitting is required. This figure illustrates that indeed the interaction of CO_2 with Mg dominates the total energy along this path. The repulsive interactions on this path are accurately described with our force field. Since the attractive interaction contains many different contributions and the functional form of the attractive interaction in our model only approximates the corresponding MP2 interactions, the fit of the attractive part is less accurate than the one of the repulsive part. Similar results have been obtained for the other paths. Figure 3.3(c) and 3.3(d) show that our force field can reproduce the total MP2 energies for all paths within 1-2 kJ/mol.

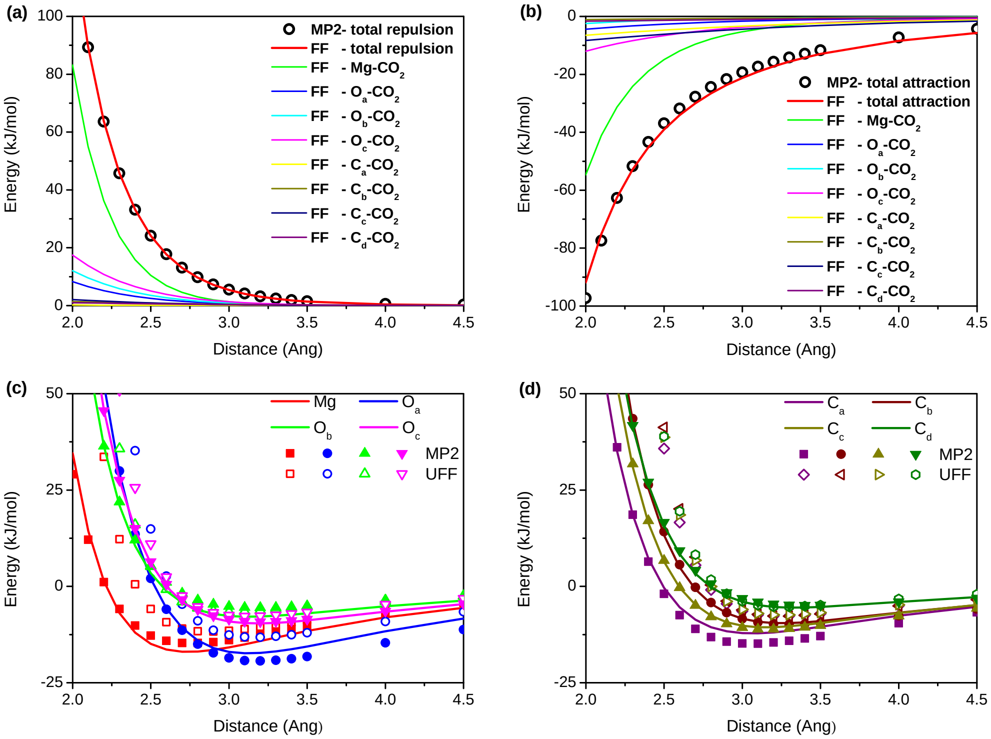

Figure 3.3: Interaction energy comparison of force field with decomposed MP2 and UFF (a) and (b): NEMO decomposition of the MP2 energies on the Mg path into (a) repulsive and (b) attractive interactions. The black circles are the MP2 results and the solid lines the fitted force fields for the various atoms. The red line gives the contribution of Mg. (c) and (d): comparison of the MP2 repulsive plus attractive energies for the eight different paths (given by closed symbols) with the results from the force field (solid lines). For comparison, we have added the predictions from the UFF force field (open symbols).

To further validate our procedure, we compared the energies obtained from our force field with those obtained from DFT calculations on the fully periodic framework for two different paths. These DFT calculations include dispersive interactions as implemented in vdW-DF and the computed CO_2-MOF binding energies and geometries are similar to those reported by Valenzano et al.[120] Figure 3.4 shows that our results are in good agreement with the DFT results. It is important to note that the path shown in Figure 3.4(a) includes the minimum energy configurations, a feature which is reproduced well by our force field. The detailed force fields for the interactions of CO_2 and N_2 with Mg-MOF-74 are reported in supporting information Tables SI 4-13 of ref 118.

It is instructive to compare our force field with the universal force fields. In Figures 3.3(c) and 3.3(d) we compare the UFF predictions of the total energies on the eight different paths. For the Mg path, we observed that the UFF force field does not allow the CO_2 molecule

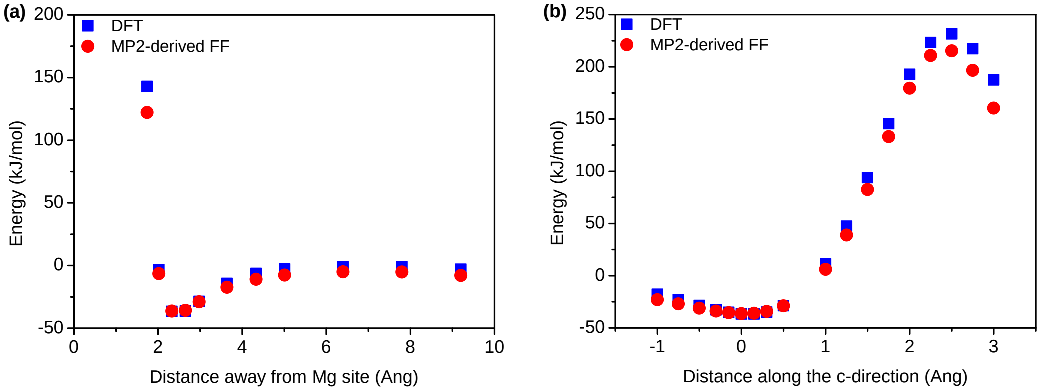

Figure 3.4: Interaction energy comparison of force field with periodic DFT. The MOF-CO_2 interaction energy is plotted along two different paths crossing the minimum energy configuration of CO_2 in Mg-MOF-74. (a) path of CO_2 approaching the open-metal site from the center of the pore, and (b) path of CO2 approaching the open-metal site in the c-direction. Blue curves are DFT calculations including van der Waals interactions and red curves are obtained from our force field. Both paths are computed in the periodic system.

to approach the Mg atom as close as the MP2 calculations predict. As a consequence, the electrostatic and dispersive interactions are underestimated significantly. The fact that we can incorporate these chemical differences in our force field is essential for a correct description of these systems; otherwise, it would not possible to reproduce the results of the quantum calculations.

3.1.3.1 Predictions from simulations utilizing new force field

As a first test of our force field we computed the heat of adsorption and compared it with the experimental values obtained by Simmons et al.,[153] Dietzel et al.,[33] and Mason et al.[123] (Figure 3.5). Our simulations quantitatively reproduce the observed dependence of the heat of adsorption as a function of loading. We predict an inflection at exactly one CO_2 molecule per Mg. The experiments show this inflection at slightly lower loadings (near 0.8 CO_2 molecule per Mg). In our simulation we assumed a perfect crystalline material in which every Mg atom is activated. As all Mg atoms are equivalent, one would expect this inflection to occur at exactly one CO_2 molecule per Mg. These observations support the conclusion of Dietzel et al.[33] According to their work, not all Mg sites are accessible in the real system. Our simulations, in agreement with the experimental data of Dietzel et al.[33] and Simmons et al.,[153] show an increase of the heat of adsorption as a function of the loading. Mason et al.[123] did not report such an increase. They obtained the heat of adsorption from a fitting procedure to a dual-site Langmuir isotherm. This procedure imposes a monotonic decrease of the heat of adsorption as a function of loading. In this study we computed the

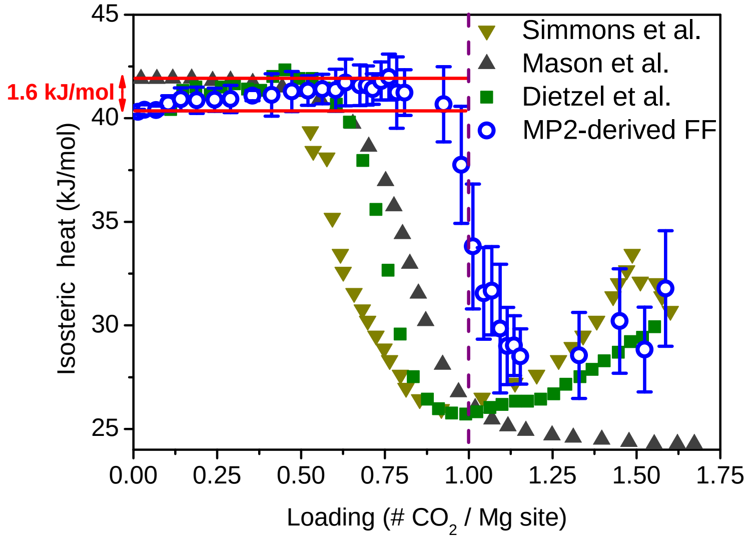

Figure 3.5: Comparison of the experimental and simulated isosteric heats of adsorptions as a function of loading. The loading is plotted as the number of CO_2 per open-metal site. For an ideal material, for which all metal sites are active, the molecular simulations predict (blue symbols) that one CO_2 binds to one open-metal site. The black, green, and olive symbols give the reported experimental data in the literature by Mason et al.,[123] Dietzel et al.,[33] and Simmons et al.,[153] respectively. Red lines indicate the enhancement of CO_2 heat of adsorption due to cooperative effects that has been predicted from the molecular simulations.

experimental heat of adsorption directly from our simulations,[152] and hence our results are independent of the interpretation of the isotherms.

In Figure 3.6 we compare the predicted adsorption isotherms with the experimental isotherms for CO_2 and N_2 in Mg-MOF-74.[123,154] We obtain excellent agreement with experimental data, and the agreement is best when we take into account that not all Mg sites are accessible in the experiments. Comparison with the simulation using the UFF force field illustrates the significant improvement in predictions made by our force field. In the Henry regime, the conventional force field underestimates the adsorption by as much as two orders of magnitude. An interesting observation is that we are not able to describe the simulated (and experimental) adsorption isotherms for CO_2 with a dual-site Langmuir isotherm (see Figure 3.7). Langmuir isotherms assume that each adsorption site is independent. The heat of adsorption data already shown that CO_2-CO_2 interactions cannot be ignored for the CO_2 binding to the Mg sites and, because of these interactions, it becomes easier to add another CO_2 molecule in the MOF. If we have a loading of approximately 1 CO_2 per 6 Mg, we observe a significant collective effect that makes it easier to add an additional CO_2 molecule adjacent to the ones already adsorbed. Figure 3.7 shows that these relatively small energies

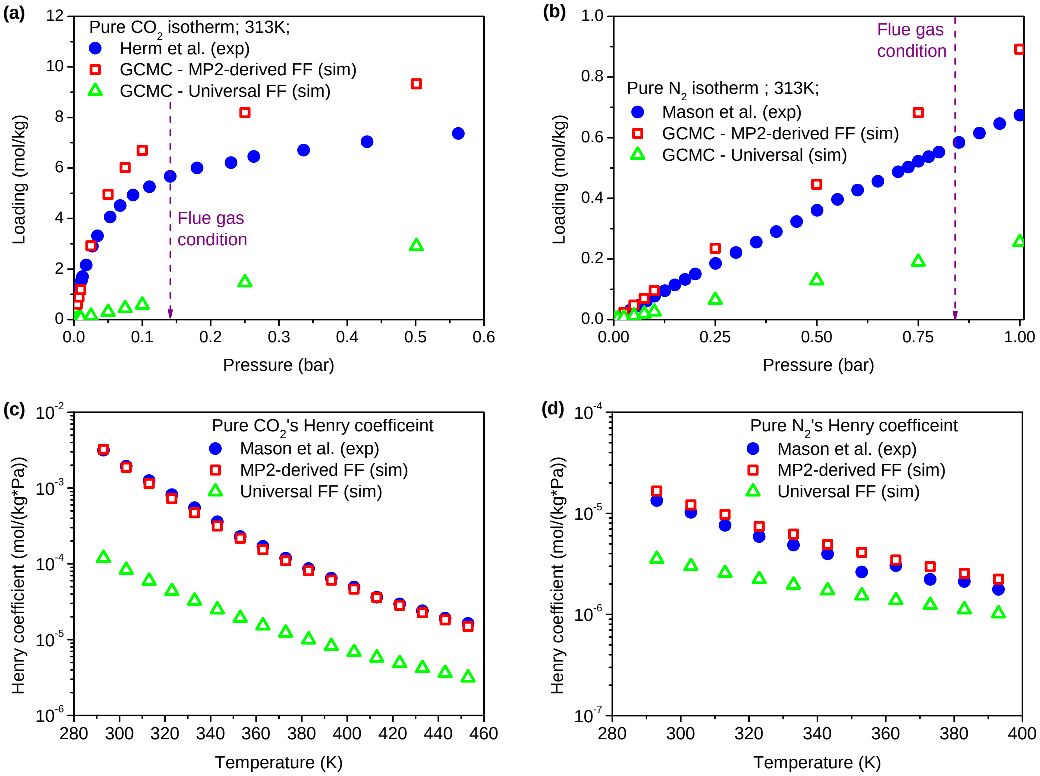

Figure 3.6: Comparison of simulated and experimental adsorption isotherms and Henry coefficients. Experimental and predicted adsorption isotherms are shows for (a) CO_2 and (b) N_2 in Mg-MOF-74. The blue circles are the experimental data of Herm et al.[154] or Mason et al.[123] The open symbols are the simulation results; the green symbols are the results of using the UFF force field and the red symbols are from the present force field. At low pressure the adsorption is linear in the pressure; the proportionality coefficient is defined as the Henry coefficient. This Henry coefficient is shown in the bottom figures as a function of the temperature for (c) CO_2 and (d) N_2.

(1.6 kJ/mol), provided from the CO_2-CO_2 interactions, essentially enhance the uptake of CO_2 up to 15% at the condition of carbon capture. This suggests that in the design of a carbon capture material one would also like to optimize these collective effects inside the material. In addition, we performed simulations to predict also the adsorption isotherms for a CO_2-N_2 mixture and the result is shown in Figure 3.8. To the best of our knowledge, mixture adsorption isotherms have not been measured for this system, yet they are essential for determining the performance of a material for carbon capture. Furthermore, we have also computed the mixture isotherms by IAST with the simulated pure component isotherms, and they are in excellent agreement with the mixture isotherms computed by GCMC simulations over a very wide range of fugacity. This result validates the applicability of IAST

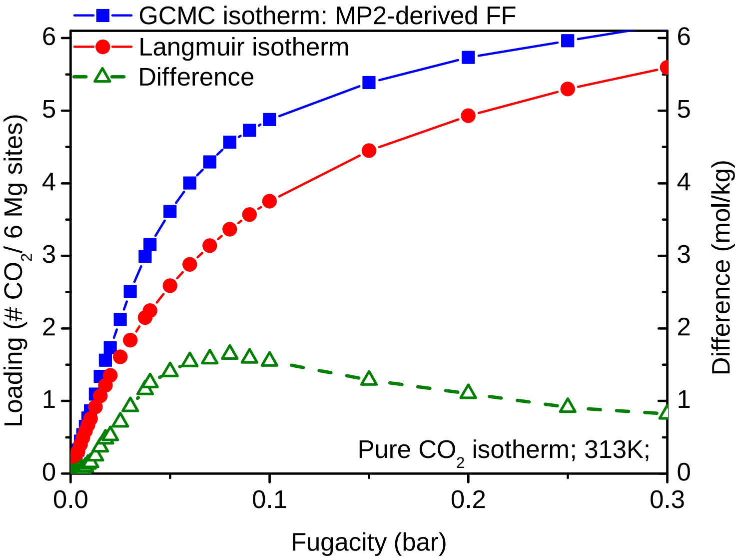

Figure 3.7: In this figure we compare a Langmuir isotherm (red) with the results from GCMC simulations (blue). The parameters of the Langmuir isotherm are obtained from the Henry coefficient from the GCMC simulations and the maximum loading of strong binding sites is set to one CO_2 per Mg site. The difference between these curves (green) indicates the enhancement induced by the presence of other CO_2 molecules.

theory for the CO_2/N_2 mixture system in Mg-MOF-74.

At this point it is instructive to compare our approach with the multi-Langmuir approach developed by Sauer and co-workers.[155] In the multi-Langmuir method, the MP2 energies at the binding sites are directly used to estimate the corresponding adsorption coefficient (or Henry coefficient) of the different adsorption sites and hence the use of force fields is avoided. The multi-Langmuir approach relies on the assumption that the isotherms can be described with a Langmuir equation and a few well-defined binding sites dominate adsorption. As for the adsorption of CO_2 in Mg-MOF-74, the use of a force field is essential to capture the enhancement at low loading and to correctly describe the adsorption at high loading.

3.1.3.2 Transferability

We should now discuss the transferability of our approach. Recently, McDonald et al.[127] synthesized Mg_2(dobpdc), a material similar to MOF-74, but with an extended linker. The structure and atom-types can be seen in Figure 3.9. Since this linker contains the same chemical groups as MOF-74, we can compute the isotherms for Mg_2(dobpdc) using the force field derived for Mg-MOF-74. Figure 3.10 shows that the predicted isotherm is in good agreement with the experimental data reported by McDonald et al.[127] We also investigated the effect of changing the metal in MOF-74. The Zn-MOF-74 isotherm can be computed by

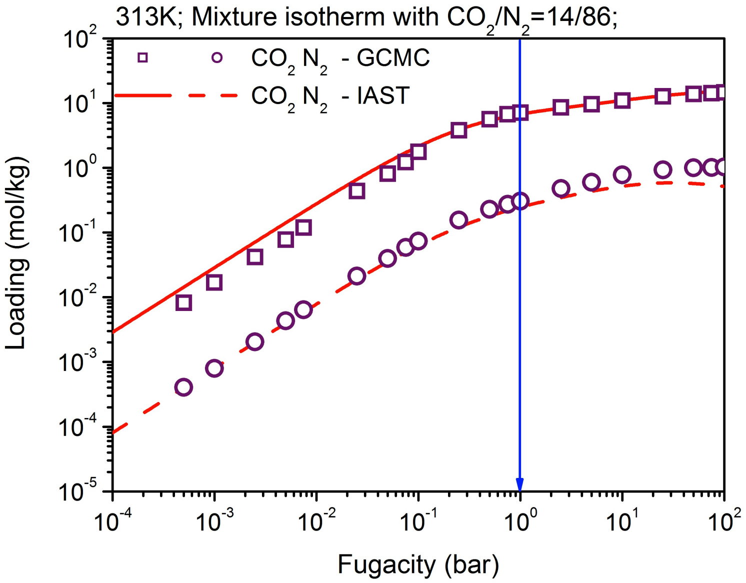

Figure 3.8: Simulated and predicted CO_2-N_2 mixture isotherm in Mg-MOF-74. Open symbol shows the predicted CO_2-N_2 (14-86) mixture isotherms in Mg-MOF-74 at 313K by using GCMC simulation with MP2-derived force field. The red line shows the mixture isotherm predicted by IAST. The blue arrow indicates the flue gas condition.

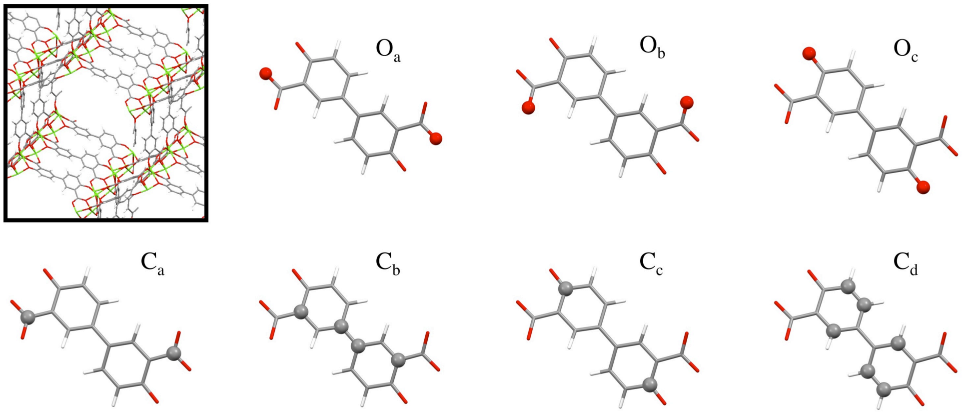

Figure 3.9: Structure and atom-types of Mg_2(dobpdc), which is an extended version of Mg-MOF-74

recalculating the force field for the CO_2 metal interactions, while keeping all other interactions the same as in Mg-MOF-74. Details can be found in supporting information section 6 of ref 118. This result is a further confirmation that our approach is transferable. In Figure

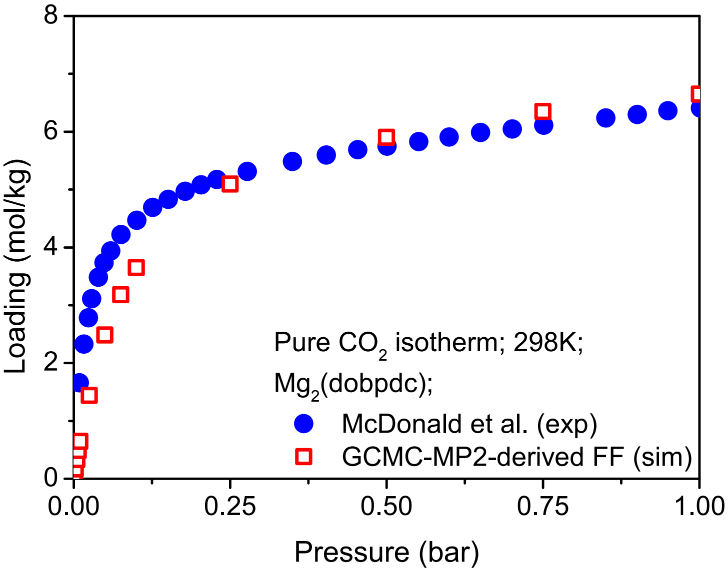

Figure 3.10: Adsorption isotherms of CO_2 in Mg_2(dobpdc), which is a material with an extended linker using the same atom-types as in the Mg-MOF-74 material. The closed and open symbols to represent the experimental and simulation adsorption isotherms, respectively

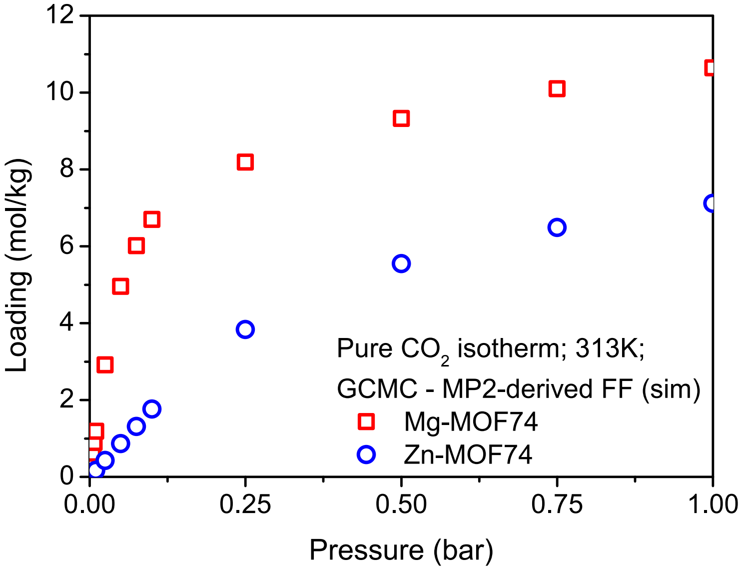

Figure 3.11: Adsorption isotherms of CO_2 in Mg-MOF-74 and Zn-MOF-74, where we test the transferability of our force field for the metal sites: replacing the Mg by the Zn force field while keeping the force field for the atoms in the linker identical.

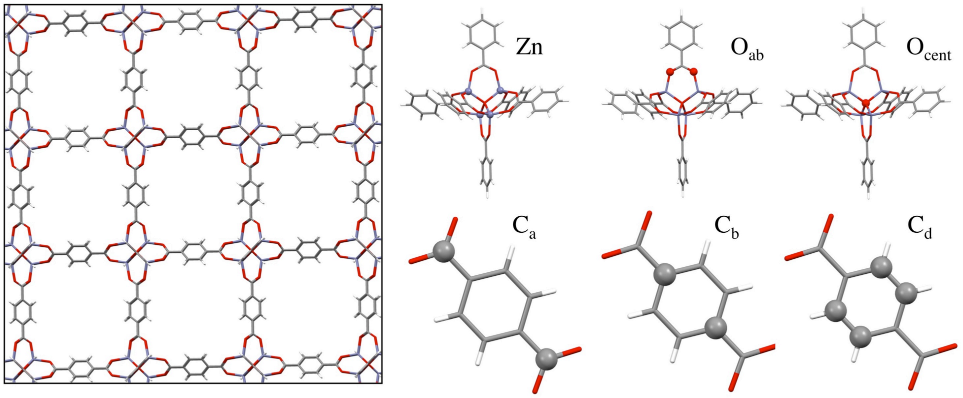

Figure 3.12: Structure and atom-types of MOF-5

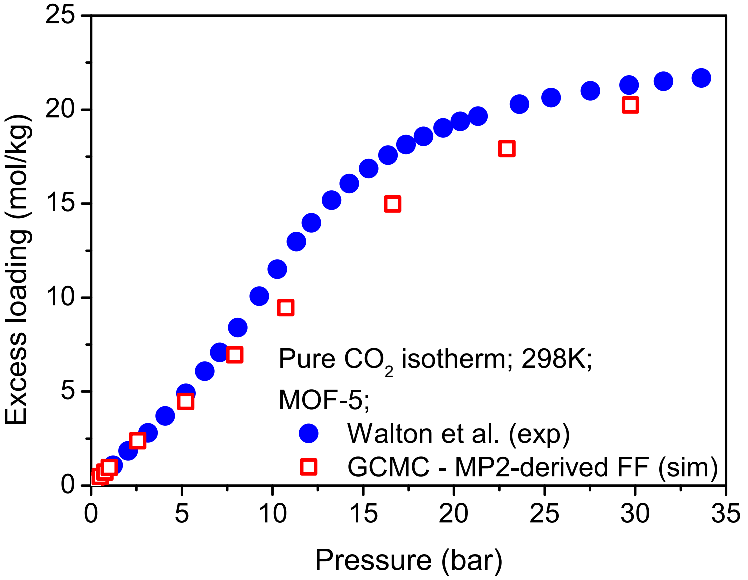

Figure 3.13: Adsorption isotherms of CO_2 in MOF-5, a material that does not have open-metal sites. The closed and open symbols to represent the experimental and simulation adsorption isotherms, respectively

3.11 we compare the predicted isotherms for Zn-MOF-74 with the corresponding isotherm for Mg-MOF-74. Finally, we employed our approach to study CO_2 in MOF-5, which does not have open-metal sites. The structure and atom-types can be seen in Figure 3.12. Additionally, the adopted cluster and CO_2 corresponding path of each atom-type can be seen in Appendix A from Figure A.9 to A.11. Figure 3.13 shows that the CO_2 simulated isotherm is in excellent agreement with the experimental one reported by Walton et al.[156] This set of results confirms that our methodology is applicable to different types of structures.

3.1.4 Conclusions

In summary, a novel methodology that yields accurate force fields for CO_2 and N_2 in an open site MOF from high-level quantum chemical calculations has been developed. These force fields take into account the subtle changes in the chemical environment induced by the presence of open-metal sites in metal organic frameworks. Our new method allowed us to reproduce the experimental adsorption isotherms for both CO_2 and N_2 in Mg-MOF-74 and to predict the mixture isotherms at flue gas conditions. We have also shown that our methodology is transferable to systems containing different metals, linkers, and different topologies. The same approach will be used to predict properties of open-site MOFs that have not yet been synthesized.

3.2 Force-field development from electronic structure calculations with periodic boundary conditions: applications to gaseous adsorption and transport in metal-organic frameworks[†]

3.2.1 Introduction

In the previous section, we proposed a methodology to develop force fields generalizable to a broad class of MOFs including open-metal site structures, and the methodology required only a small number of single-point *ab initio* calculations.[118] This method utilized MP2 cluster calculations for each configuration along approaching paths that were designed to probe specific pair-wise interaction energies. The fitting procedure was further simplified by decomposing the MP2-calculated energies into electrostatic, repulsive, and attractive interactions using the NEMO decomposition technique.[130,131] As a result, a simple fitting algorithm (i.e., grid search method) was required as only up to two variables have to be optimized at the same time. For instance, a CO_2 force field inside Mg-MOF-74 was obtained from about one hundred designed configurations, and the predicted adsorption isotherm was found to be in excellent agreement with the experimental data.

Compared to DFT calculations with periodic boundary conditions, MP2 calculations require significantly more computational resources and are therefore limited to smaller clusters. In addition, the NEMO technique was developed for molecular systems. Consequently, the previously developed force-field parameters were based upon cluster calculations.[118] By increasing the size of these clusters, one can systematically improve the description of extended (periodic) systems. However, conventional MP2 calculations scale as N^6 and are unaffordable for large clusters (i.e., >100 atoms). This poses practical limitations on the approach. As a result, this force field could not correctly describe the binding geometry of the CO_2 molecule in Mg-MOF-74 as measured, for example, with neutron diffraction.[133] Another important conclusion of the previously proposed methodology in section 3.1 is that MP2 and van der Waals dispersion-corrected DFT (i.e., vdW-DF) give nearly identical results at the cluster level for the Mg-MOF-74 system.[118] The agreement between these two approaches is not surprising, because Mg(II) is a closed-shell system and the interaction between CO_2 and Mg is dominated by dispersion-effects. It should be noted that, if open-shell transition metals (e.g., Fe(II)) were considered, one would have to be more careful because stronger electron correlation effects may occur and have to choose an appropriate functional or use multireference wave-function based methods. Accordingly, all of above suggests that we should extend our methodology to periodic systems within the DFT framework to remove all these constrains imposed by the use of cluster calculations and develop a force field that not only correctly

---

[†] Material in this section is adopted with permission from *J. Chem. Theory Comput.*, **2014**, 10 (4), 1477-1488.[4] Copyright 2014 American Chemical Society.
Link: http://dx.doi.org/10.1021/ct500094w

predicts the adsorption isotherms but also yields accurate binding geometries. In this work, we propose a new approach for deriving force fields from periodic DFT calculations. This enables all steps of the force-field generation to be conducted within a periodic framework: from the structural optimization of the MOFs, to the force-field parameterization, to classical molecular simulations (i.e., Monte Carlo and molecular dynamics). With this newly developed methodology, the computational time required to obtain a DFT-derived force field is highly reduced, about the same order of magnitude of the cost required for periodic structure relaxation. We have used this newly developed methodology to obtain an improved force field for CO_2 in Mg-MOF-74, and our new force field can accurately predict the CO_2 binding geometry, adsorption isotherm, and dynamic property inside the material. We further demonstrate that our methodology is applicable for generating force fields for water molecules within MOFs. Water is one of the major components in the flue gases emitted from coal-fired power plants, and the presence of water can potentially degrade the CO_2 adsorption performance enormously.[157,158] In this context, it is crucial to consider the effect of water on CO_2 uptake in evaluating the performance of a given MOF. Using our new *ab initio* force fields, we have studied the performance of CO_2 adsorbed inside M-MOF-74 (M = Mg and Zn) in the presence of water vapor.

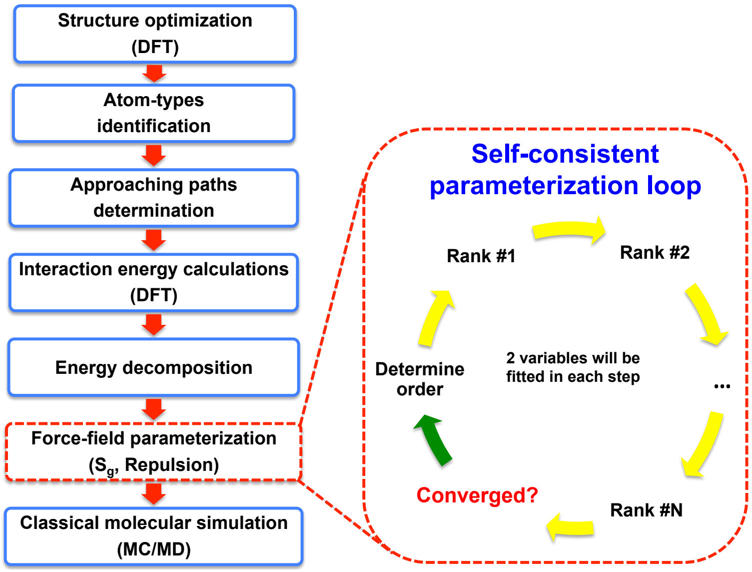

Figure 3.14: Flow diagram of the proposed method to derive force field from periodic DFT calculations.

3.2.2 Methodology

3.2.2.1 Overview

The methodology consists of the following steps (see Figure 3.14 for the flow diagram)

- Structure optimization: periodic DFT structural optimization is utilized to obtain reliable geometries, which will be used throughout the entire process.
- Atom-types identification: for a given structure, we identify different atom-types on the framework for which we need to determine the pair-wise potentials.
- Approaching paths determination: for each of the identified atom-types, we determine an approaching orientation (path) towards the atom-type and a set of configurations of the guest molecule along the orientation.
- Interaction energy calculations: for each configuration, the interaction energy between the guest molecule and the MOF is computed using DFT with an appropriate dispersion-corrected exchange-correlation functional.
- Energy decomposition: the total interaction energies are decomposed into three major contributions: long-range Coulomb interactions, short-range exchange repulsion, and dispersion interactions.
- Force-field parameterization: the force field is then parameterized with the guest-framework short-range repulsive parameters being optimized. In this step, we have introduced a self-consistently fitting loop to ensure that the force field becomes independent of the details of the energy decomposition.
- Classical molecular simulation: the obtained force field is used as the basis in classical molecular simulations for adsorptive and diffusive property predictions. These molecular simulations also require a force field for the guest-guest interactions. For these, we directly employ one of the existing models that can reproduce the experimental guest molecular properties, such as vapor-liquid equilibrium (VLE). Each step is discussed in details in the following sections. We use CO_2 adsorbed in Mg-MOF-74 as case study.

3.2.2.2 Structural optimization

For some materials, the experimental crystal structures rely on powder samples for which the accuracy of obtained atomic positions can be very limited. For instance, we have shown previously in section 3.1 that the experimentally obtained structure of Mg-MOF-74 has distorted benzene rings, and the computed CO_2 adsorption properties inside the material are very sensitive to the details of the adopted structure.[118] Accordingly, DFT, which can capture many details of the structure with good accuracy, is utilized to ensure the force fields are faithful to result from accurate crystal structures. In this study, we use the same optimized geometries as the one obtained in the previous section.[118]

3.2.2.3 Atom-types identification and approaching path determination

M-MOF-74 is composed of 4 different elements: Metal (M), O, C, and H. If one further considers the local environment of each of these elements, 9 different atom-types can be identified, denoted as M, O_a, O_b, O_c, C_a, C_b, C_c, C_d, and H (see Figure 3.1). Note that the hydrogen in this case is not considered explicitly, and thus there is no corresponding path to be considered. In our approach, the short-range repulsive forces between each non-bonding pair of framework atom-types and guest molecule are specifically probed. For each framework atom-type, the method determines an approaching orientation (path) of a given guest molecule toward the target atom-type. This approaching orientation is determined by minimizing the repulsive energy between the guest molecule and the framework atoms with other atom-types (i.e., different from the target atom-type). This procedure ensures that the pair-wise repulsive interaction between the guest molecule, particularly the closest atom, and the target atom dominates the total repulsive energy. For instance, the repulsive interaction between the $O(CO_2)$ and the Mg atom-type of the framework is designed to be the dominant component of the total repulsion along the corresponding Mg-CO_2 path. The combination, i.e., $O(CO_2)$-Mg, is the so-called approached pair along a given path. UFF force fields are used to determine these paths. For each path, near 15 configurations at different distances (i.e., with the intervals of 0.1 or 0.2 Å) from the approached atom-type are generated. Ideally, one would like to be able to generate specific paths for all atoms of the guest molecule (e.g., C and O of CO_2) with respect to all atom-types of the MOF. However, for some of the atom combinations, we cannot generate a path for which the contribution of the approached pair cannot dominate the total repulsion. We denote these atom combinations as un-approachable pairs. For MOF-74, the un-approachable pairs are those pairs that involve the carbon atom of CO_2.

3.2.2.4 Interaction energy calculations (DFT)

The interaction energies of an individual guest molecule inside the MOF (i.e., E_{int}) are defined as:

$$E_{int} = E_{MOF+guest} - (E_{MOF} + E_{guest}) \tag{3.3}$$

All the calculations are conducted in the conventional hexagonal unit cell composed of 162 atoms. We use DFT with vdW-DF2 exchange-correlation functional[140] for all total energy calculations as implemented in the Quantum Espresso code[136] with a planewave basis. We use the Troullier-Martins type norm-conserving pseudopotentials, and kinetic energy and charge density planewave cutoff are set to be 120 Rydberg and 480 Rydberg, respectively. The integration over the irreducible Brillouin zone is carried out over 2x2x4 Monkhorst-Pack grids.

3.2.2.5 Force field

We use two different types of potential forms for the short-range repulsion: the Lennard-Jones type and the Buckingham type potential as shown in Eq. 3.4 and Eq. 3.5, respectively.

$$E_{ij}(r_{ij}) = \frac{q_i q_j}{4\pi\epsilon_o r_{ij}} + 4\epsilon_{ij}[(\frac{\sigma_{ij}}{r_{ij}})^6 - (\frac{\sigma_{ij}}{r_{ij}})^6] \tag{3.4}$$

$$E_{ij}(r_{ij}) = \begin{cases} \infty & r_{ij} \leq R_{min} \\ \frac{q_i q_j}{4\pi\epsilon_o r_{ij}} + A_{ij}\exp(-B_{ij}r_{ij}) - S_g \frac{C_{ij}}{r_{ij}^6} & r_{ij} > R_{min} \end{cases} \tag{3.5}$$

where q_i and q_j are the atomic charges of atoms i and j, r_{ij} is the distance between atoms i and j, ϵ_o is the permittivity of free space, R_{min} is used to prevent the conventional Buckingham potential from going to negative infinity at short distance, ϵ_{ij} and σ_{ij} are the Lennard-Jones energy and distance parameters, respectively, (A_{ij}, B_{ij}) and C_{ij} are the conventional Buckingham parameters for repulsive and attractive contribution, respectively. In this work, we introduce a global scaling factor, S_g, for the dispersion energies. The rational for this factor will be discussed in one of the next sections.

It is well-known that the repulsive interactions can be described better with the Buckingham potential (i.e., e^{-r}) compared to the Lennard-Jones form (i.e., $1/r^{12}$) (e.g., see Dzubak et al.[118]) Therefore, we use the Buckingham potential for all approachable pairs. In the next section we discuss how we obtain the parameters of the Buckingham potential. For the pairs that are un-approachable (e.g., include $C(CO_2)$) or not considered explicitly (e.g., framework atom-type H), we keep the Lennard-Jones potential with parameters given by one of the common force fields.

3.2.2.6 Energy decomposition

The DFT-computed energies for these configurations are decomposed into long-range Coulomb interactions, short-range exchange repulsion, and dispersion interactions. The long-range Coulomb contribution is computed through the Ewald summation technique.[57] The partial atomic charges of the framework atoms are determined using the REPEAT scheme,[159] with the self-consistent DFT electrostatic potentials obtained from the DFT structural relaxation. The REPEAT scheme finds a set of atomic charges that best represents the DFT electrostatic potential surface. The charges for the guest molecules are directly taken from the guest molecule models (e.g., TraPPE[55] or EPM2[160] models for CO_2 molecules). The dispersion term is computed with C_6 dispersion coefficients that are initially taken from one of the commonly used force fields. We assume that these coefficients give reasonable relative energies but their absolute values can be off. To correct this, we introduce a global scaling factor, S_g. We can then obtain the decomposed short-range repulsion by subtracting from the total energies the sum of the dispersive and electrostatic energies. Note that without the scaling factor, this decomposition can result in negative repulsive energies (see Appendix Figure A.12). Namely, a global scaling factor is determined to ensure the decomposed repulsion energies are all positive-definite along each path.

3.2.2.7 Force-field parameterization

The methodology utilizes the short-range nature of the repulsive energies, and probes each pair-wise interaction separately (i.e., different paths for different approached pair). Given that the specific repulsion between the approached pair along a given path is designed to dominate the total repulsion, only the corresponding pair-wise repulsive parameters (i.e., 2 parameters: A_{ij} and B_{ij}) are optimized by grid search method to reproduce the total decomposed repulsion energies along the path. Further, to determine the order in which we fit these parameters of different approached pairs, we compute the ratio of the computed repulsive energy between the approached pair to the total repulsive energy for each path. The fitting of the pair-wise repulsive parameters is then performed for each path sequentially in order from the highest to lowest ratio. This procedure is repeated iteratively until all the parameters are converged (i.e., no change in parameters after a loop). With the fitted parameters of a given global scaling factor, the fitting can be further fine-tuned to obtain the optimal scaling factor by minimizing the error, i.e., difference between the energies computed by the force field and by DFT along all the paths.

3.2.2.8 Classical molecular simulations

Monte Carlo (MC) and molecular dynamics (MD) simulations are used for predicting thermodynamic and transport properties of the adsorbed gases. In these simulations, total interaction energies include the electrostatics, short-range repulsion, and dispersion energies using the force-field parameters obtained from the previous section. Non-electrostatic pair-wise potential is truncated and shifted to zero at the cutoff radius of 12.8 Å. The simulation box is composed of multiple unit cells to ensure that each distance between two successive planes of (1,0,0), (0,1,0), and (0,0,1) is at least twice the cutoff radius. Detailed information of the force-field parameters obtained in this study can be found in supporting information section 3 of ref 4. For MC simulations in the grand-canonical ensemble (i.e., GCMC simulations), several million configurations are sampled. These configurations are generated by random translation, rotation, insertion, and deletion to obtain statistically averaged loadings as a function of the fugacity with high accuracy. The MD simulations are carried out in the canonical ensemble and use the Nosé-Hoover thermostat[57] with a time step of 0.5 fs for a total simulation time of at least 10 ns.

3.2.3 Results and discussion

3.2.3.1 CO_2 adsorption and dynamics in Mg-MOF-74

To validate our approach, we first derive a force field for CO_2 adsorbed in Mg-MOF-74. The EPM2 model is adopted for CO_2 molecules while UFF force fields are used for framework atoms as a starting point. The resulting DFT-derived force field is denoted as model 1.

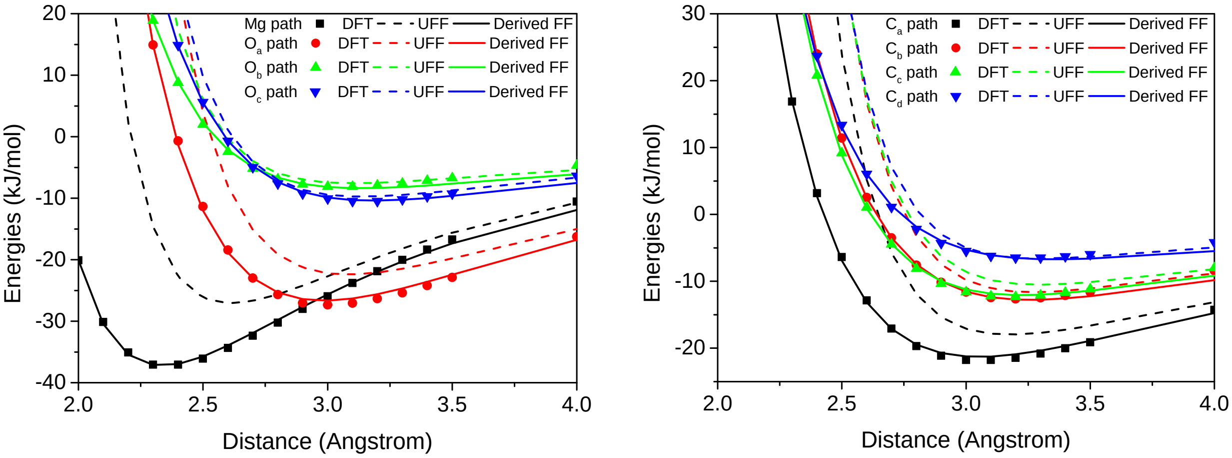

(a) (b)

Figure 3.15: Comparisons of CO_2-framework interaction energies as a function of distance inside Mg-MOF-74 obtained from the DFT calculations (closed symbols) with the ones computed from the DFT-derived force field (model 1, solid line) and the UFF (dashed line) along (a) Mg and O and (b) C paths.

Thermodynamics properties Figure 3.15 shows that the model 1 nicely reproduces the DFT energies along all the paths. Comparison with the energies computed with the original UFF force field shows that UFF overestimates the short-range repulsive energies and, therefore, underestimates the interaction energies. To further evaluate our new force field, a total of 1,200 random configurations are generated in the accessible pore volume. These points are not included in the fitting procedure. The comparison between the DFT computed energies and the force-field energies for these random configurations is given in Figure 3.16. The green-dashed line represents a perfect agreement between the DFT and force-field energies, and the energies computed by DFT-derived force field nicely lie on top of the line. In contrast, the energies computed by UFF tend to underestimate the interaction energies. To further quantify the improvement, we compute the Boltzmann-weighted mean deviation (BMD) that is defined in Eq. 3.6:

$$BMD = \frac{\sum_{i=1}^{N_S}(E_{FF,i} - E_{DFT,i})exp(-\frac{E_{DFT,i}}{k_BT})}{\sum_{i=1}^{N_S} exp(-\frac{E_{DFT,i}}{k_BT})} \tag{3.6}$$

where N_s is the total number of sampled configurations while $E_{FF,i}$ and $E_{DFT,i}$ represent the interaction energies of configuration i computed by force fields and DFT, respectively. The Boltzmann-weighted mean deviations at T = 300 K for the UFF and DFT-derived FF

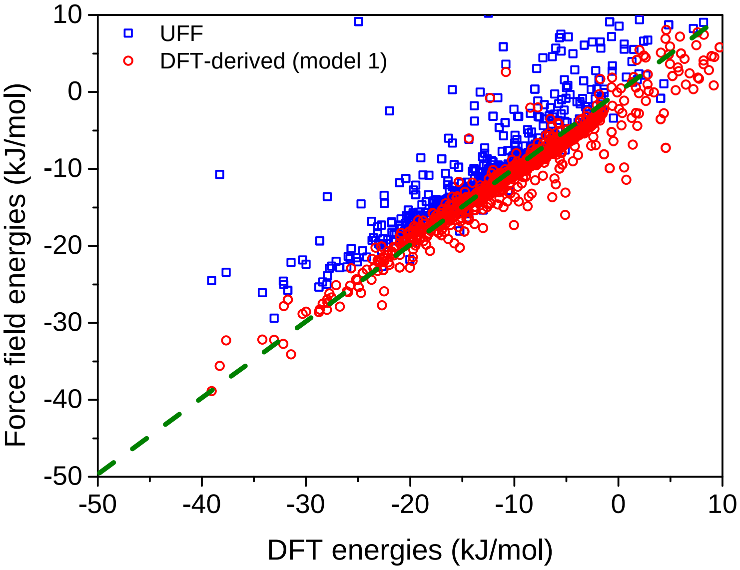

Figure 3.16: Comparison of the CO_2-framework interaction energies obtained from the DFT calculations with the ones computed from the UFF (open blue squares) and the DFT-derived force field (model 1, open red circles) for a set of 1,200 CO_2 random configurations inside the accessible pore volume of Mg-MOF-74. The green-dashed line indicates perfect agreement between the energies computed by DFT and by force fields.

(model 1) are 15.27 kJ/mol and 2.02 kJ/mol, respectively.

In Figure 3.17, we compare the adsorption isotherms of model 1 with the experimental isotherms for CO_2 inside Mg-MOF-74. Since it is well known that not all the Mg sites are accessible, we rescale the experimental isotherm by assuming 80% availability of the materials.[123] With our new DFT-derived force field, the predicted isotherm is in excellent agreement with the scaled experiment isotherm. At this point, it is instructive to compare our new force field with the one we previously derived from MP2-cluster calculations. The predicted adsorption isotherms by this MP2 force field are in good agreement with the experimental data (see Figure 3.17).[118] However, if we compare the MP2 force-field predictions for a set of random configurations with the DFT energies (see Figure 3.18), we observe that the MP2 force field cannot nicely predict the DFT-energies computed in the periodic system. The energies of CO_2 configurations located near the center of the pores are systemically overestimated. In addition, the minimum energy configuration that is predicted by this force field has a correct energy, but gives a different orientation than the one predicted by DFT. DFT predicts that the minimum energy configuration of O=C=O has an angle of near 80^o with respect to the axis parallel to the channel, whereas the corresponding angle predicted by MP2 force field is significantly smaller ($<60^o$). Predicting this angle correctly is significantly important to reproduce the NMR measured line-shape induced by CO_2 dynamics

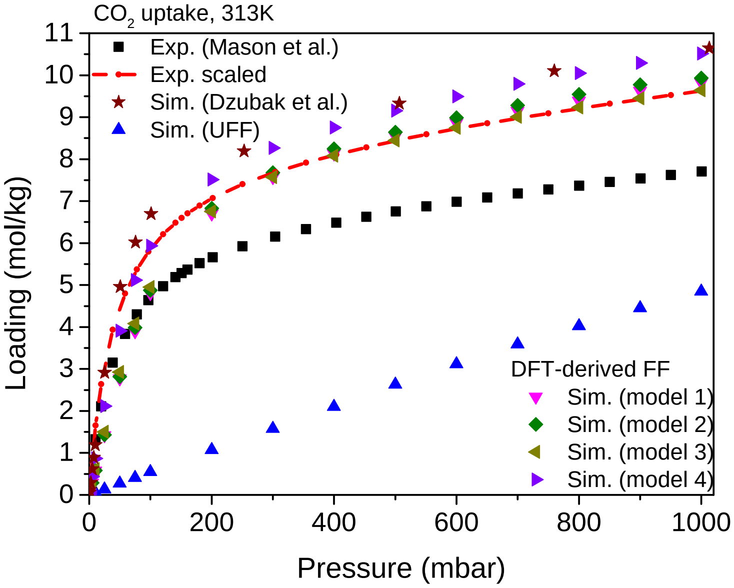

Figure 3.17: Comparison between the experimental and simulated isotherms of CO_2 inside Mg-MOF-74 at 313 K. The experimental data of Mason et al.[123] and the corresponding scaled isotherm (assume 80% of material is accessible) are shown by the closed black squares and red closed circles with dashed line, respectively. The blue closed upper-triangles show the predicted isotherm using the UFF force field while the brown closed stars show the predicted isotherm by using the MP2-derived force field of Dzubak et al.[118] The other symbols correspond to the isotherms of four different DFT-derived force fields (models 1 to 4).

(Detailed information can be found in chapter 4). These results suggest that the previously adopted clusters may have been too small to capture the range of possible interactions in the extended structure. Those not sufficiently large clusters might be the reason why an additional $1/r^5$ term in the MP2-derived force field is required to have a better fitting quality while, in this modified study, a simple $1/r^6$ in the van der Waal interaction is used. Also, the $C(CO_2)$-framework interactions are neglected, i.e., set to zero, previously but included here.

To test the robustness of our methodology, we replace the C_6 coefficients with values adopted from Grimme's DFT-D2 method[161] for the dispersive interactions between framework atoms and $O(CO_2)$ (i.e., approached pairs); the other interactions were kept the same as in model 1. This force field is denoted as model 2. Figure 3.17 shows that the predicted isotherm of this model is nearly identical to the isotherm predicted by model 1, suggesting that our methodology is not very sensitive to the choice of initial C_6 coefficients for the approached pairs. To test the sensitivity of our approach to the details of the CO_2 model, we further replace the EPM2 model by the TraPPE model for CO_2, which we refer to as

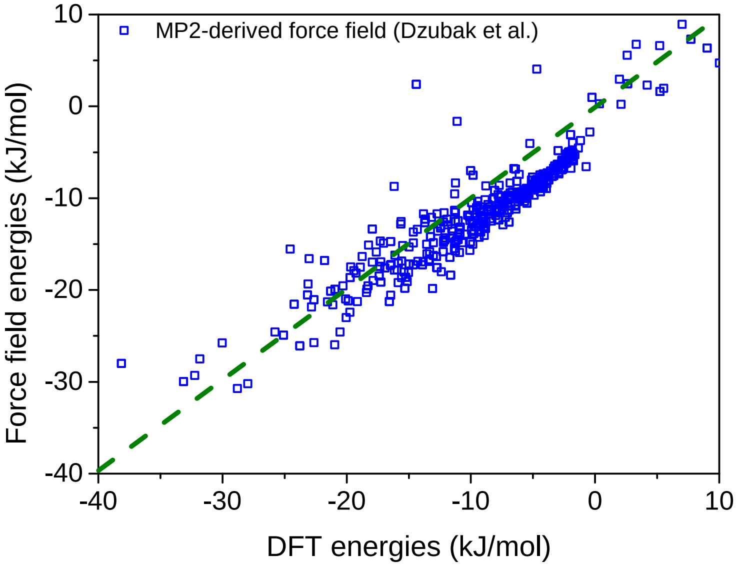

Figure 3.18: Comparison of the CO_2-framework interaction energies obtained from the DFT calculations with the one computed from the previously derived MP2 force field[118] (open blue squares) for a set of 1,200 CO_2 random configurations inside the accessible pore volume of Mg-MOF-74. The green-dashed line indicates perfect agreement between the energies computed by DFT and by force fields.

model 3. The calculated isotherm is again very similar to the ones obtained from models 1 and 2, although a slightly different loading at higher-pressure region is observed. Compared to the TraPPE model, the EPM2 has similar Lennard-Jones parameters but different partial atomic charges (i.e., -0.35e vs. -0.325e for the oxygen of CO_2, respectively). The similarity of the isotherms predicted by models 1 and 3 demonstrates that the differences in electrostatic energies can be taken into account correctly by adjusting the pair-wise repulsive energies.

Although the predicted isotherms of these three models show generally good agreement with the experimental isotherms, the calculated Henry coefficients are about 3 times smaller than the experimental values. To understand these differences, we introduce a rotational motion of CO_2 as shown in the inset of Figure 3.19. Figure 3.19 elucidates that model 1 fails to capture the DFT energy as a function of rotational angle. This model underestimates the interaction energies if CO_2 rotates toward the linker. The pair-wise parameters between $C(CO_2)$ and framework atoms are not optimized and, as these three models have similar parameters for $C(CO_2)$, similar deviations can be expected for the other models. A further improvement of the force field might be obtained by refining the parameters between $C(CO_2)$ and the framework. Unfortunately, our methodology is not applicable to the middle atom of a linear molecule (i.e., un-approachable pairs). To obtain some insights in the role of the $C(CO_2)$ interactions, we replace the parameters for the framework-$C(CO_2)$ interactions in

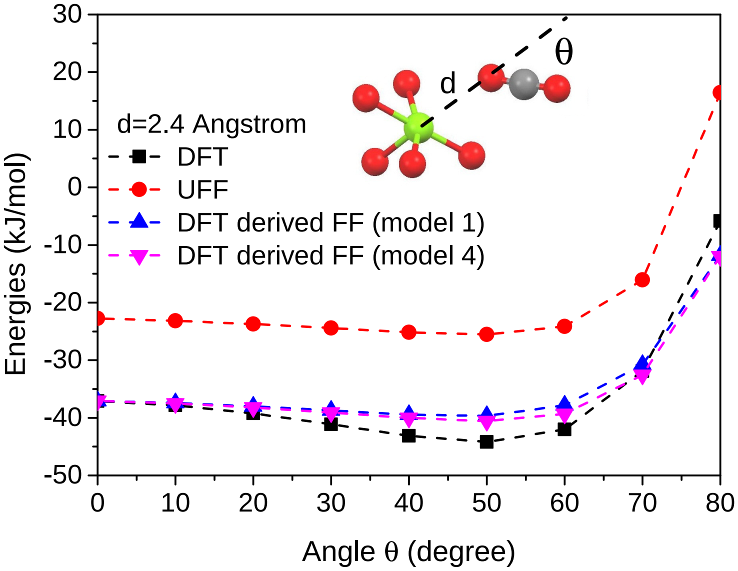

Figure 3.19: Comparison between the DFT and force-field interaction energies as a function of the angle θ. This angle gives the orientation of O=C=O with respect to the vector of Mg-CO_2 approaching path (see the inset of figure). The oxygen-Mg distance, d, is set to d = 2.4 Å. Black closed squares are the DFT reference energies and the other symbols are the corresponding energies calculated by different force fields.

model 2 with the C_6 coefficients from DFT-D2 method. As these coefficients were optimized from quantum calculations, they might give a more consistent result with the rest of the force field. Given that DFT-D2 method does not provide information on the repulsive part of the potential, we assume that the sigma parameters used in the Lennard-Jones potential has the value equal to the summation of atomic van der Waal radii. The obtained set of parameters is denoted as model 4. Figure 3.19 shows a small improvement for this model. Additionally, the Boltzmann-weighted mean deviation of model 4 for the set of 1,200 random configurations (see Appendix Figure A.13) is 0.76 kJ/mol, which is smaller than that of model 1. These improvements are also reflected in the predicted isotherm, which has better agreement with the experimental data at low-pressure region. In the high-pressure region, the loading is overestimated, which might be due to our assumptions of the repulsive parameters between framework-C(CO_2). The overestimation of the predicted energies can also be seen for a small portion of the randomly generated configurations see Appendix Figure A.13) at intermediate adsorption energies (i.e., -25 - 0 kJ/mol). It should be noted that all of these 4 models has their corresponding global scaling factor, S_g, to be further fine-tuned to minimize difference between the energies computed by the force fields and by DFT along all the paths.

Furthermore, in Figure 3.20 we compare the binding geometry computed by model 4 with the corresponding geometry obtained from DFT calculations. Table 3.2 gives a quantitative

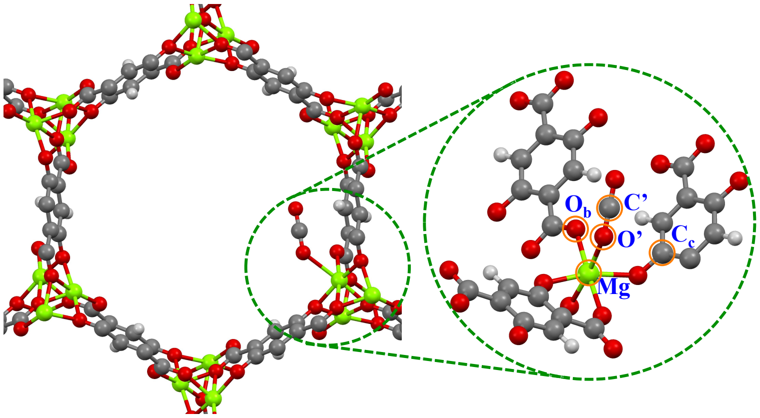

Figure 3.20: DFT Binding geometry of a single CO_2 molecule adsorbed inside Mg-MOF-74. The figure represents the material as balls and sticks (Mg, green; Oxygen, red; Carbon, grey; Hydrogen, white). The inset amplifies the binding region.

comparison of the distances between CO_2 and a few selected framework atoms. The comparison clearly demonstrates that model 4 nicely reproduces the DFT binding geometry. It is also important to note that the predicted DFT binding geometry agrees very well with the experimental binding geometry, as obtained from the neutron powder diffraction experiment at 20K by Queen et al.[133]

	Distance(Å)		
Source	O'-Mg	C'-C$_b$	C'-C$_c$
DFT	2.40	2.94	3.37
DFT-derived force field	2.42	2.94	3.25
NPD*(Queen et al.[133])	2.39	3.10	3.07

*at 20K and 0.25 CO_2/Mg

Table 3.2: Comparison of binding geometries of CO_2 in Mg-MOF-74 obtained from DFT-derived FF, DFT, and neutron power diffraction (NPD). The atomic labels used in this table can be found in Figure 3.20.

Transport properties At this point, it is instructive to apply our derived force field to study the dynamic properties of CO_2 inside Mg-MOF-74. As will be shown in chapter 4, we used the UFF force field to predict the experimentally measured ^{13}C NMR line shapes.[162] The uniaxial rotational-like NMR patterns are properly explained in terms of a hopping motion of CO_2 along the X-Y plane.[162] The UFF force field does give a reasonable prediction of the

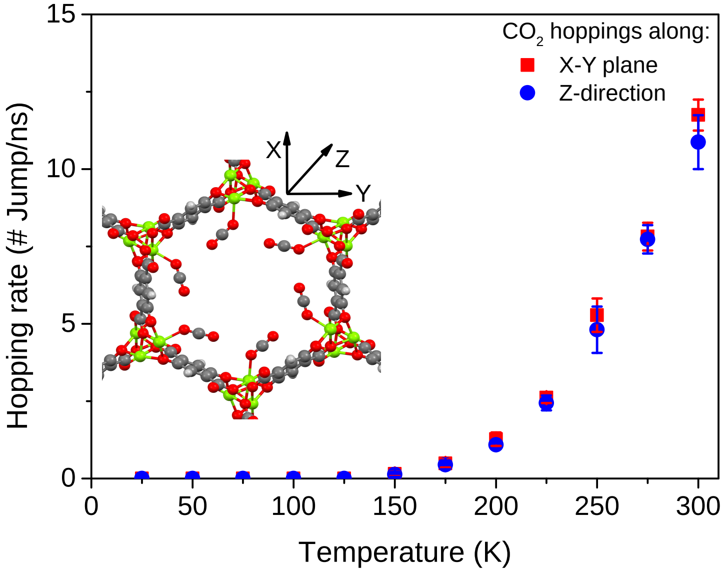

Figure 3.21: Hopping rate (number of jumps per ns) of CO_2 along the X-Y plane (red squares) and Z-direction (blue circles) as a function of temperature (K). The inset illustrates the pore topology as well as the coordinates system. The Z-direction corresponds to the crystallographic c-axis.

binding orientation and, hence, correctly predicts the equivalent rotational angle resulted from the CO_2 hopping from one metal site to another. However, as the binding energies are predicted incorrectly by UFF, we were unable to predict the correct transition temperature of experimental NMR patterns from fixation to hopping motion.[163] An important test of our new force field is whether we now can correctly predict this transition temperature. Accordingly, molecular dynamics simulations are performed with model 4, and a collection of MD trajectories is analyzed. Figure 3.21 shows that the hopping rate along the X-Y plane becomes non-zero above 150K, which is exactly the temperature where experimentally measured pattern shows the intermediate motion.[163] Furthermore, for the activation energies of the hopping motions along the X-Y plane and Z-direction, we obtain 10.7 kJ/mol and 11.4 kJ/mol, respectively, from our calculations. These activation energies are in good agreement with the experimental value, which is the average of these two activation energies (i.e., 10.0 kJ/mol). Additionally, our force field predicts a slightly higher barrier of the hopping along the Z-direction than along the X-Y plane. The result is consistent with the free energy barrier calculation performed by Canepa et al. using the *ab initio* nudged elastic band (NEB) method.[164]

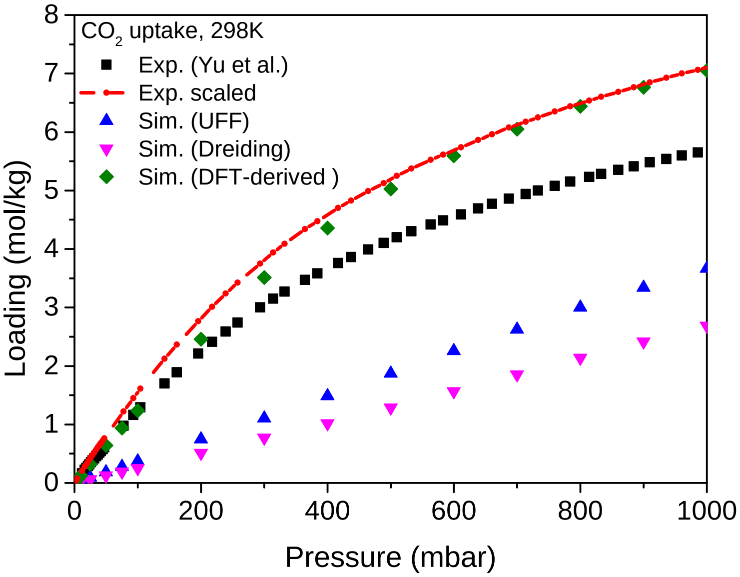

Figure 3.22: Comparison between the experimental and simulated isotherms of CO_2 inside Zn-MOF-74 at 298 K. The experimental data of Yu et al.[165] and the corresponding scaled isotherm (assume only 80% of material are accessible, which is the same value we have used for Mg-MOF-74) are shown by the closed black squares and red close circle with dashed line, respectively. The symbols are the isotherms from the GCMC simulations as predicted by the different models.

3.2.3.2 CO_2 adsorption in Zn-MOF-74

The transferability of the methodology is evaluated by studying CO_2 in Zn-MOF-74. Compared to the Mg-MOF-74 case, the main differences of the DFT energies are observed along the path towards the metal center. All other paths give very similar energies as for the Mg-MOF-74 case. In this regard, the CO_2 -Zn approaching path is the only path required to be re-optimized. We develop the force field for Zn-MOF-74 upon the model 4 for Mg-MOF-74. The obtained force fields with only the metal path to be re-parameterized can indeed reproduce the DFT energies along all other paths (i.e., O and C paths) (see Appendix Figures A.14 and A.15). Figure 3.22 shows that, for Zn-MOF-74, our predicted isotherm is also in good agreement with the experimentally scaled one.[165] Given that we can obtain such a good agreement by only re-parameterizing the metal-guest interactions, indicating that the parameters obtained in the Mg-MOF-74 are transferable to the Zn-MOF-74 as well as the method itself.

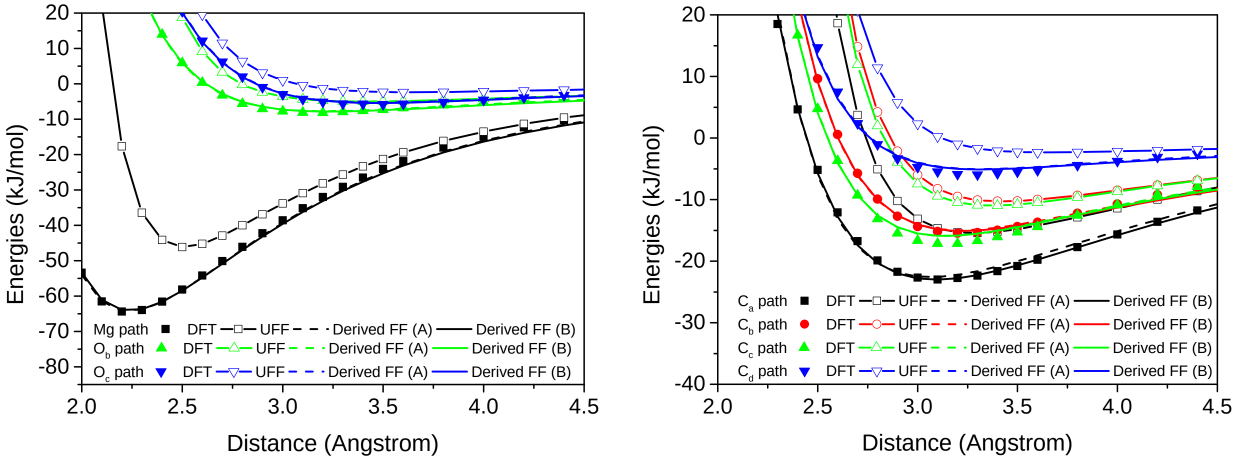

(a) (b)

Figure 3.23: Comparison of H_2O-framework interaction energies as a function of distance as obtained from the DFT calculations (closed symbols) with ones computed from the UFF (open symbols with solid lines) and the DFT-derived force field (dashed and solid lines for model A and B, respectively) along (a) Mg and O and (b) C paths.

3.2.3.3 H_2O adsorption in Mg-MOF-74

We also apply the methodology to H_2O that is a major component, next to N_2 and CO_2, of flue gases. For water we use the TIP4P-Ew model.[166] According to the TIP4P-Ew model, there is no non-electrostatic interactions between framework atoms and H(H_2O), and therefore H(H_2O) is not considered explicitly for paths determinations. Our study shows that, however, the resulting model without considering the non-electrostatic interactions between framework-H(H_2O) (model A) leads to unrealistic energies of some configurations. This problem can be further corrected by introducing H(H_2O) approaching paths explicitly into parameterization loops (model B).During the development of water models, sufficiently large global scaling factors, S_g, are chosen and have not been further optimized.

Similar to CO_2, a total of 8 paths (i.e., Mg, O_a, O_b, O_c, C_a, C_b, C_c, and C_d) are determined in which the O(H_2O) is approaching toward the different framework atom-types. We find that the path targeting the O_a atom does not give a satisfactory fitting of the DFT-energies. The O_a atom is more embedded in the framework compared to other atom-types and therefore the repulsion between the approached pair of O_a and O(H_2O) has a much smaller contribution to the net repulsion compared to the other atom-types. The reason is that the repulsion from the neighbor framework atoms prevents the O(H_2O) from probing the short-range repulsion with O_a. Accordingly, the corresponding pair-wise repulsive parameters will be far less sensitive to the DFT-decomposed repulsion, and cannot be obtained accurately. Such a poorly defined path degrades the stability of the parameterization loop. At the same time because of this effect the correction for the short-range repulsion of this pair is less important and can therefore be omitted from the optimization loop. Without the O_a path, the DFT energies along all other 7 approaching paths are nicely fitted as shown in Figure 3.23. We denote the set of parameters as model A.

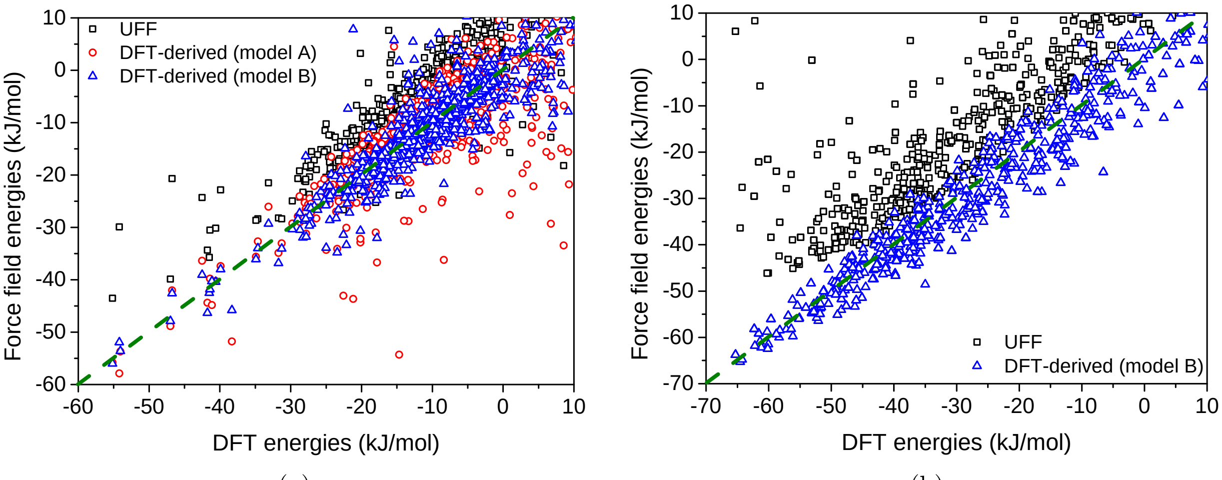

(a)

(b)

Figure 3.24: Comparison of the interaction energies obtained from the DFT calculations with the ones computed from the UFF (open black squares), the DFT-derived force field (model A, open red circles), and the DFT-derived force field (model B, open upper-triangles) for a set of randomly selected (a) 2,000 H_2O configurations in the accessible pore volume and (b) 1,000 H_2O configurations located near the open-metal sites inside Mg-MOF-74. The green-dashed line indicates the location where the energies computed by DFT and by force fields are identical.

To test the reliability of model A, we also generate a set of 2,000 random H_2O configurations in the accessible pores of this system. The comparison between the DFT and force-field energies for these configurations is shown in Figure 3.24(a). Compared to the UFF, our new force field shows a much better agreement with the DFT energies. However, model A highly overestimates the interaction energies for some configurations. For example, for one of these configurations the energy calculated from the DFT is -15 kJ/mol while model A gives -55 kJ/mol. Detailed inspection of these configurations shows that the hydrogen site in the TIP4P-Ew model causes these differences. The $H(H_2O)$ site has a positive partial charge, but the site does not include repulsive interaction, which artificially enables $H(H_2O)$ getting close to negatively charged framework atoms and thus gain favorable energies. To correct the interaction between $H(H_2O)$-framework, 2 hydrogen-approaching paths (i.e., O_b-H and C_b-H paths) are generated and included in the self-consistent parameterization loops. The fitted parameters from the O_b-H and C_b-H paths are applied to other framework atom-types with the same element type. The resulting force field is denoted as model B. Figure 3.25 compares the DFT and force-field energies along these two hydrogen paths. Model B perfectly reproduces the energies along the paths, whereas model A highly overestimates the interaction. It is intriguing to see that the UFF force field does not seriously overestimate the energies along these paths although there is no physical repulsion applied on the H(H_2O). The overestimation of the repulsive interaction between O(H_2O)-framework protects the hydrogen atoms of water and, hence, avoids this issue. Figure 3.24(a) illustrates that the energies computed by model B are in much better agreement with the DFT energies compared to the previous model. Moreover, another set of 1,000 configurations is chosen to sample the region near the open-metal sites in order to concentrate on water binding region. Figure 3.24(b) again illustrates that the model B nicely reproduces the DFT energies, and shows huge improvement compared to the UFF. Similarly, we computed the Boltzmann-weighted mean deviations at 300 K for the UFF and model B with the set of selected 1,000 configurations, and the values are 47.70 kJ/mol and 1.07 kJ/mol, respectively.

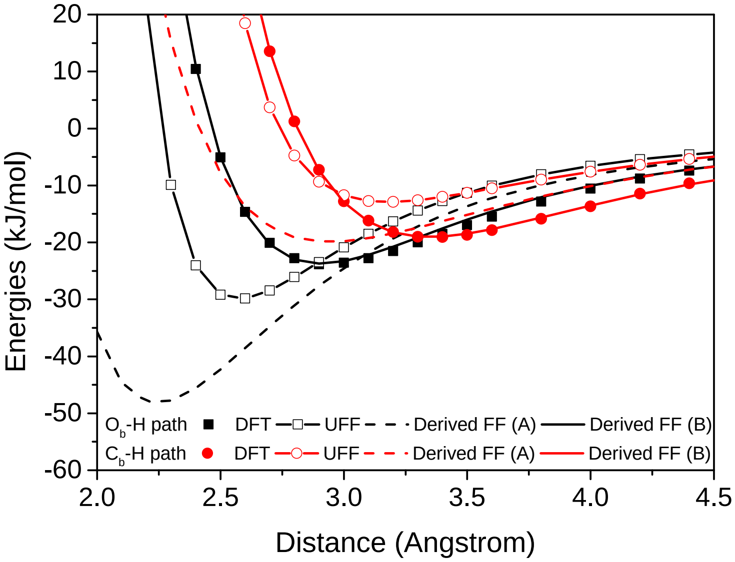

Figure 3.25: Comparison of the H_2O-framework interaction energies as a function of distance obtained from the DFT calculations (closed symbols) with ones computed from the UFF (open symbols with solid lines) and the DFT-derived force fields (dashed and solid lines for model A and B, respectively) for O_b-H (black) and C_b-H (red) paths.

In Figure 3.26(a), we compare the water isotherms predicted by the model B and the UFF with the corresponding experimental isotherms reported in the literature.[167–169] Model B isotherm agrees much better with the experimental data of Yang et al. (C)[167] compared to the UFF isotherm at the low-pressure region. At the higher-pressure region (i.e., P = 0.1-1 kPa), however, both the model B and UFF predict a much higher loading than

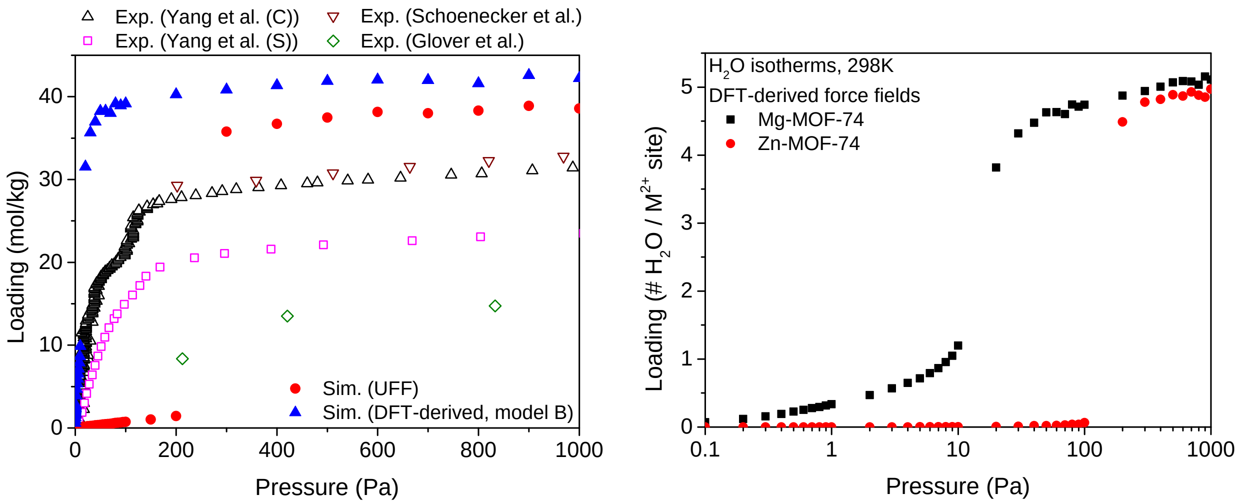

(a) (b)

Figure 3.26: (a) Comparison between the experimental and simulated isotherms for H_2O inside Mg-MOF-74 at 298 K.[167–169] The experimental isotherms are shown by the open symbols. The closed red circles and blue closed upper-triangles represent the computed isotherms with the UFF and the DFT-derived force field (model B), respectively. (b) Calculated H_2O adsorption isotherms at 298 K inside Mg-MOF-74 (closed black squares) and Zn-MOF-74 (closed red squares). In these calculations, DFT-derived force fields (model B; explicitly takes $H(H_2O)$ paths into the parameterization loops) are used.

the experimental measurement. The water adsorption isotherms in Mg-MOF-74 reported in the literature have, however, a wide range of uptake values. The experimental data of Schoenecker et al.[168] has comparable uptake at higher-pressure region with the one obtained by Yang et al. (C), whereas Glover et al.[169] obtain up to 70% lower adsorption. Moreover, Yang et al. show different adsorption behaviors with the Mg-MOF-74 samples synthesized from different methods (i.e., (C) vs. (S)). These large variations illustrate the difficulties in measuring the water uptake. These differences make it difficult to make quantitative statements on the reliability of our predicted isotherms at higher-pressure region. Same procedure (i.e., model B) is also applied to generate force field of H_2O in Zn-MOF-74, and the resulted isotherm is given in Figure 3.26(b). Interestingly, we find different adsorption mechanisms of H_2O molecules adsorbed inside Mg-and Zn-MOF-74. Zn-MOF-74 shows a much sharper transition, resembling capillary condensation, in the water adsorption isotherm as compared to Mg-MOF-74. To understand these differences, we partitioned the average energies per H_2O molecule into framework-guest and guest-guest interactions (see Figure 3.27). The results show that, because of the strong H_2O-metal interactions in Mg-MOF-74, the H_2O molecules tend to fully occupy all open-metal sites before condensation (see Figure 3.27(a)). This is consistent with the shape of H_2O isotherm in Mg-MOF-74, which has the condensation of H_2O molecules at higher loadings, i.e., beyond one H_2O molecule per metal site. In contrast, for Zn-MOF-74, the interactions between H_2O and metal sites are much weaker. As a consequence, once there is one H_2O molecule adsorbed on an open-metal site, for the next H_2O molecule it would be energetically more favorable to be adsorbed in proximity to the first H_2O molecule due to the strong H_2O-H_2O interactions. As we can clearly see from Figure 3.27(b), the strong guest-guest interactions essentially introduce a more negative average adsorption energies of H_2O molecules compared to infinite dilution conditions.

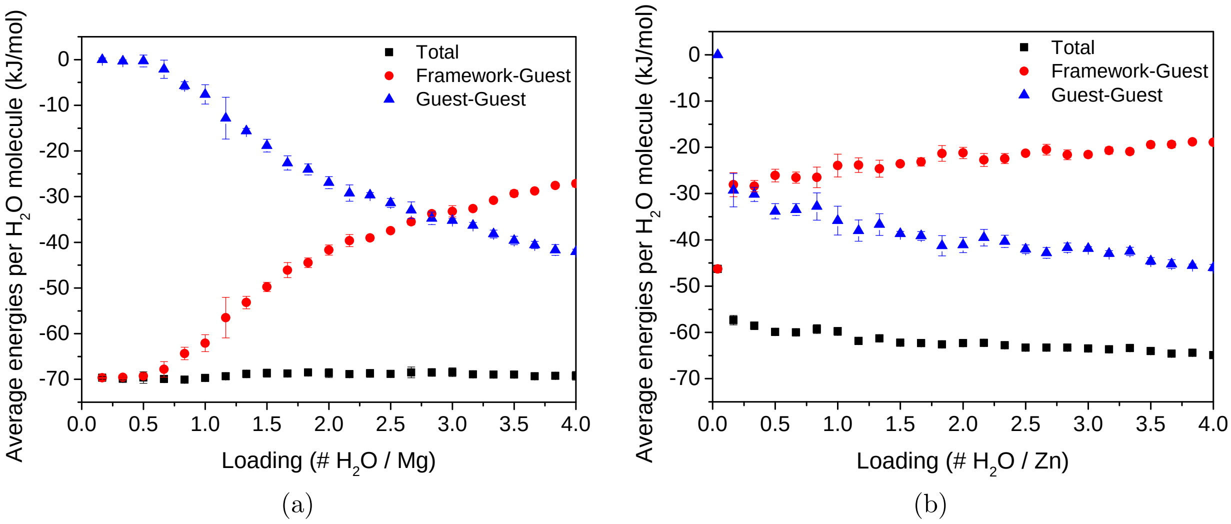

(a)

(b)

Figure 3.27: Average energies per H_2O molecule (kJ/mol) as a function of loading (number of H_2O/metal) adsorbed inside (a) Mg-MOF-74 and (b) Zn-MOF-74. To illustrate the energy contributions of framework-guest and guest-guest to the total energies, the total energies and these two components are plotted separately. In these calculations, DFT-derived force fields (model B; explicitly takes $H(H_2O)$ paths into the parameterization loops) are used.

3.2.3.4 CO_2/H_2O mixture adsorption in M-MOF-74 (M = Mg and Zn)

The presence of water has been regarded as one of the key problems for the application of MOFs with open-metal sites in CCS. With our novel force fields for CO_2 and H_2O, we are in a position to make quantitative prediction on the effect of water on the uptake of CO_2 at the typical mixture condition of flue gases for both Mg-MOF-74 and Zn-MOF-74. To the best of our knowledge, there are no experimental mixture data available on these systems. Since nitrogen has a much weaker binding strength inside M-MOF-74 compared to the other main components (i.e., CO_2 and H_2O) of the flue gases emitted from a coal-fired power plant,[170,171] we can focus on the binary mixture of CO_2 and H_2O and simply assume

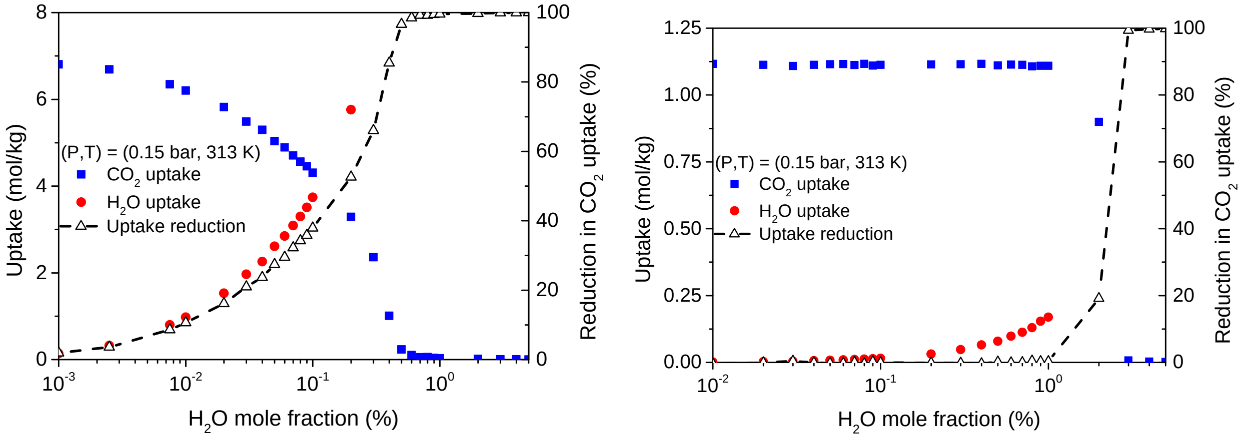

(a) (b)

Figure 3.28: Binary mixture in (a) Mg-MOF-74 and (b) Zn-MOF-74. Left y-axis: simulated binary mixture uptake of CO_2 (red closed circles) and H_2O (closed blue squares) as a function of H_2O mole fraction at total pressure of 0.15 bar and temperature of 313 K. Right y-axis: the reduction of CO_2 uptake (%) as a function of H_2O mole fraction. The definition of reduction is the ratio of CO_2 uptake under the mixture condition to the pure component CO_2 uptake at (P, T) = (0.15 bar, 313 K).

that N_2 does not adsorb at these conditions. Our simplified flue gases are at total pressure of 0.15 bar and at temperature of 313 K with a range of H_2O mole fraction varying from 0.001% to 5%. The mixture GCMC simulations are performed to predict the uptake at each specific composition. To quantify the effect of water on the CO_2 uptake performance, we introduce a reduction factor. This factor is defined as the ratio of CO_2 uptake in the presence of water vapor to pure component CO_2 uptake at (P, T) equal to (0.15 bar, 313 K). For the mixture inside Mg-MOF-74, the simulated uptake and the reduction factor as a function of H_2O composition is shown in Figure 3.28(a). Surprisingly, the result shows that the reduction of CO_2 reaches 50% in the presence of 0.2% water. At 0.5%, the CO_2 uptake is essentially equal to zero, which indicates that the material has no capability of adsorbing carbon dioxide. A detailed investigation shows that the computed binding energy of H_2O is strong (i.e., near -70 kJ/mol), and the difference in the isosteric heat of adsorption between H_2O and CO_2 is large (i.e., >20 kJ/mol). In this regard, H_2O molecules are expected to adsorb on the open-metal sites very strongly, and in a much more energetically favorable way than CO_2. Accordingly, one would need very dry flue gasses for Mg-MOF-74. Otherwise the separation performance will be degraded enormously. It is interesting to compare the effect of water on adsorption of CO_2 in Zn-MOF-74. Compared to the Mg-MOF-74, given that the binding strength of water is much weaker, Zn-MOF-74 is less sensitive to the presence of trace amounts of water vapor. Our calculations show that there is nearly no degradation in the CO_2 uptake before the occurrence of water condensation inside the Zn-MOF-74 (i.e., near 2%, see Figure 3.28(b)).

3.2.4 Conclusions

In summary, we have developed a new method to derive accurate force fields from periodic DFT calculations. The characteristic of this method is that we only calculate DFT energies on specific paths that are most sensitive to their corresponding pair-wise interactions between approached pairs. Compared to methods that use genetic algorithms, this reduces the number of required *ab initio* calculations. In addition, we use an energy decomposition scheme in combination with a self-consistent optimization loop, which allows us to fit only two parameters at the same time. Our method therefore significantly reduces the computational cost to develop *ab initio* force fields, and is relatively simple to be implemented. Part of the gain in efficiency is due to the fact that our approach uses one of the common force fields (e.g., UFF) as a starting point and aims to correct these. We have also tested the robustness of this methodology by showing that the predicted adsorption properties of the derived force fields are insensitive to the choice of the initial force field. In this work, we have demonstrated that these new force fields yield accurate estimates of the CO_2 adsorption properties inside Mg-MOF-74. We also studied the dynamics of the adsorbed CO_2 molecules in Mg-MOF-74. Both the transition temperature from fixation to hopping motion and the activation energies of CO_2 hopping motion nicely match the experimental observations. To test transferability of the resulting force fields, we have also studied CO_2 adsorbed inside Zn-MOF-74, and the predicted isotherm is in excellent agreement with the experimental data. Moreover, we have developed a force field for H_2O . This water force field gives a reasonable prediction on the water adsorption inside Mg-MOF-74 and provides significant improvements compared to the prediction made by the UFF force field. Additionally, very different H_2O adsorption mechanisms between Mg-MOF-74 and Zn-MOF-74 are found due to the difference in the H_2O-metal binding strength. Finally, with these new force fields, we make further predictions on the CO_2/H_2O mixture adsorption properties, and the results show that the performance of both Mg- and Zn-MOF-74 to uptake CO_2 can be degraded enormously by the presence of water. Compared to Mg-MOF-74, we find that Zn-MOF-74, however, can tolerate roughly four times higher in water concentration without sacrificing considerable ability of adsorbing CO_2.

3.3 Efficient determination of accurate force fields for porous materials using *ab initio* total energy calculations[‡]

3.3.1 Introduction

In order to improve computational efficiency, many efforts have focused on developing accurate force fields for porous materials. Fang et al. used hundreds of quantum chemical calculations, based on *ab initio* density functional theory and the DFT-D2 and the DFT/CC approach to compute accurate force fields for pure-silica zeolites and aluminosilicate zeolites respectively.[95,172] In their approach, two global scaling factors were added to the classical 12-6 Lennard-Jones potential, and these parameters were optimized using about one thousand single-point DFT calculations. McDaniel et al. developed force fields based on symmetry-adapted perturbation theory for CO_2 adsorption in ZIFs and demonstrated transferability for selected ZIFs.[173] Han et al. utilized high-level *ab initio* calculations to develop accurate dispersive force fields for CO_2 uptake in multivariate MOFs.[174] Chen et al. conducted similar work on the Mg-MOF-74 structure where they used a multi-objective genetic algorithm to accurately fit over a thousand of single point energies, which resulted in good agreement with the experimental isotherms as well.[99] Additionally, as shown in previous sections, we have developed a technique where single-point MP2 energy calculations were conducted along given paths that were well-designed to probe the pair-wise short range interactions to derive the force field parameters.[118] This approach yielded good agreement between the simulated and the experimental isotherm data in both open-metal site MOF structures such as Mg-MOF-74 as well as an archetypical MOF such as MOF-5. Moreover, we have modified the methodology to be fully compatible with DFT calculations. The resulted methodology is more efficient as compared to other methods.

Although the methodology we have proposed is very efficient and does not require many quantum chemical calculation, it may still imposes some difficulties while performing large-scale screening of millions of structures. Herein, in this work, we introduce an alternative method that leads to sensible prediction of adsorption properties for various porous materials in absence of a reliable fore field. Compared to the method involving detailed derivation of force field, a relatively small amount of CPU time is required to compute an adsorption isotherm using conventional grand-canonical Monte Carlo simulations. For example, using one of the generic force fields such as the UFF[129] or Dreiding,[54] we can easily compute an adsorption isotherm curve at the conditions of interest. We take advantage of the fact that although such force fields might be initially inaccurate, they lead to a qualitatively correct description about the location of the adsorption sites as well as the shape of the channels

---

[‡] Material in this section is adopted with permission from *J. Phys. Chem. C.*, **2014**, 118 (5), 2693-2701.[119] Copyright 2014 American Chemical Society.
Link: http://dx.doi.org/10.1021/jp412368m

and the pores. Consequently, one can start from an inaccurate force field and utilizing just a few quantum chemical calculations, converge to a model that leads to the correct adsorption properties. In this respect, this work is similar to the methodology proposed by Sauer and co-workers.[155] They have developed an alternative approach, in which high-level quantum chemical methods are used to obtain binding energies at a small set of pre-defined adsorption sites. This approach has been demonstrated in modeling CH_4 adsorption in Mg-MOF-74 structure.[155] Particularly, they constructed a multi-site Langmuir isotherm as an estimate of the isotherm and used quantum chemical calculations to obtain the parameters for this model. Comparatively, the advantage of our methodology is that we do not have to assume prior knowledge on the number and location of the adsorption sites and that it automatically includes guest-guest interactions.

The methodology introduced in this study will be valuable in efficiently characterizing hypothetical porous materials where reliable force fields do not exist. On top of this, the methodology remains relatively unchanged regardless of the simulated material, making it ideal for large-scale screening. In the rest of the work, the detail behind the methodology and the simulation results gathered from various different systems will be shown to demonstrate its accuracy as well as its transferability.

3.3.2 Results and discussion

3.3.2.1 CO_2 in Mg-MOF-74

To describe the methodology, we introduce a test system of CO_2 inside Mg-MOF-74, which has shown to be promising for carbon capture due to the presence of unsaturated open-metal sites.[33,121,122,124,127] The main reason for choosing this system is as follows. As shown in section 3.1, we have developed an MP2-derived force field in this same system, demonstrating excellent agreement between the simulation and the experimental data. Accordingly, for our purpose, we can assume the MP2-derived force field as providing a high-quality reference result and subsequently gather millions of single point energy values at low computational cost, which can help better illustrate our methodology. In practice, for a structure where the force field is unknown, we will not have this information at our disposal. However, this does not pose a problem as our algorithm does not rely on knowing millions of single point energy calculations prior to the simulation. All of the classical molecular simulation data obtained from this work came from our in-house developed GPU code, where the algorithm detail is described elsewhere.[74]

For the initial step, a trial force field that can reasonably describe the system of interest should be chosen. In our case, the UFF and TraPPE force field parameters are selected to model the Mg-MOF-74 framework atoms and the CO_2 molecule, respectively, as these are commonly used force fields adopted by the community.[55,129] In practice, our methodology should converge to the same model regardless of the initial force field choice. We will revisit this point later on in this section. In general, the UFF force field provides the parameters for the short-range repulsions and dispersive interactions, while the Coulomb interactions follow

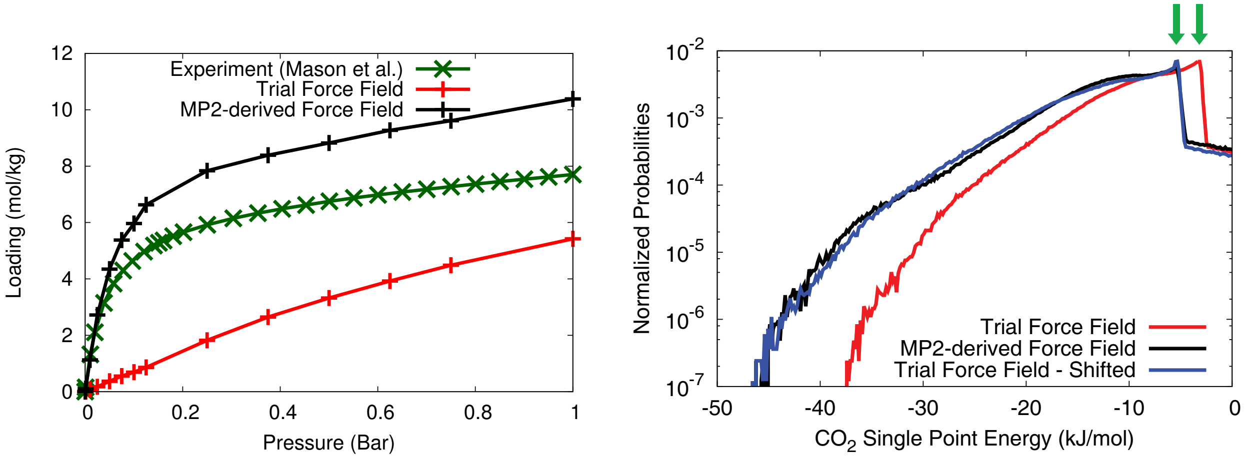

(a) (b)

Figure 3.29: (a) Experimental (green) and simulated (black: MP2-derived force field; red: UFF) adsorption isotherms for CO_2 in Mg-MOF-74 structure at T = 313 K. (b) Distribution of the CO_2 single point energy (black: MP2-derived force field; red: UFF; blue: UFF, shifted) values based on 8 million randomized insertions. The green arrows indicate the location of maximum points within the single point energy distribution, corresponding spatially to the pore centers in the Mg-MOF-74 structure.

from the charge distribution on the guest atoms and the MOFs. For the DFT-optimized Mg-MOF-74 framework, point charges are obtained from the relaxed Mg-MOF-74 *ab initio* structure using the REPEAT scheme.[159] The Mg-MOF-74 structure was taken from the one obtained in section 3.1,[118] in which the lattice vectors and atomic positions are fully relaxed using the DFT package Quantum Espresso.[136] The REPEAT scheme iteratively finds a set of framework point charges that minimizes the norm difference between the electrostatic potential of atomic charge model and the quantum chemical self-consistent electrostatic potential. Because the REPEAT scheme incurs very little computational cost compared to the entire structure relaxation procedure, it is worthwhile to obtain these accurate point charge values for our methodology since the structures need to be relaxed before the classical simulation in most cases and especially for these open-metal site structures. Subsequently, the only difference between the MP2-derived force field and the trial force field comes from the short-range repulsion and the dispersive interaction energies between the CO_2 and the framework atoms. However, this discrepancy leads to drastically different adsorption data as the two sets of force field yields K_H = 1.13x10^{-3} (mol/kg/Pa) (MP2-derived force field) and K_H = 7.2x10^{-5} (mol/kg/Pa) (UFF) at T = 313 K, resulting in two completely different adsorption isotherm curves as shown in Figure 3.29(a). Comparison between the simulated and the experimental data verifies that the MP2-derived force field leads to a better fit with the previous experiments.[123] In our calculations, we assume that all metal sites are active without any defects present in the structure. However, it has been shown experimentally that about 20% of metal sites are inaccessible, which may be due to the pore blocking or activation issue.[33] Accordingly, the MP2-derived computational model does not account for this imperfection and thus overestimates the adsorption data with the discrepancy becoming more pronounced at P $>$0.1 bar. To understand the source behind the difference between the adsorption data obtained MP2-derived force field and the trial (UFF) force field, the single point energy values are collected from random sampling. Specifically, over 8 million insertion moves are conducted on a pre-constructed grid with a mesh size of 0.1 Å, superimposed on top of the unit cell simulation volume. At each grid point, the single point energy calculation of a randomized CO_2 configuration is computed and then tabulated to obtain the normalized probability distribution shown in Figure 3.29(b). As can be seen from Figure 3.29(b), the shape of the two curves look qualitatively similar, hinting that the trial force field manages to capture the potential energy surface of the guest-framework interactions. This qualitative agreement has allowed us to understand the dynamic properties of CO_2 inside Mg-MOF-74 with the trial force field (i.e., UFF), which will be discussed in chapter 4.[162] Accordingly, minor corrections in the trial force field that artificially shift the single point curve towards the MP2-derived force field lead to the correct Henry coefficient value. The total adsorption isotherm fit outside of the Henry regime will also depend on the guest-guest (or in this case, CO_2 CO_2) interactions, which is modeled well by the TraPPE force field. The TraPPE force field has been shown to reproduce the CO_2 vapor-liquid equilibria that are dominated by inter-molecule interaction of CO_2 molecules.

In Figure 3.29(b), the minimum single point energy region corresponds to the binding energies for the two force fields. In this particular instance, the two CO_2 binding energies are $E_{reference,binding}$ = -46.22 kJ/mol (MP2-based force field) and $E_{trial,binding}$ = -37.41 kJ/mol (trial force field), leading to a difference of $\Delta E_{binding}$ = 8.81 kJ/mol (= 1059 K). Accordingly, one can shift all of the energy values obtained during the molecular simulation using the trial force field by $\Delta E_{binding}$ to obtain a better fit to the MP2-derived energy distribution near the binding energy region. Simple math indicates that $K_{H,shifted}$ = 7.2x10^{-5} x exp(1059 K/313 K) = 2.12x10^{-3} (mol/kg/Pa), moving closer to the MP2-derived K_H. In practice, the two binding energies, $E_{reference,binding}$ and $E_{trial,binding}$, can be obtained from the DFT calculations and the classical canonical Monte Carlo simulations near T = 0 K, respectively. And thus remarkably, with a single quantum chemical binding energy calculation, one can potentially obtain adsorption properties much closer to the reference result.

In principle, additional single energy calculations can be utilized from the MP2-derived force field to converge even further to the correct energy distribution curve. In practice, this would entail conducting more quantum chemical calculations, which would enhance accuracy at additional computational cost. In general, there is not a clear-cut recipe on selecting the spatial location of a guest molecule for these single point energy quantum chemical calculations. An idea suggested in this work is to sample near a local maximum region of the energy distribution curve at higher energies values and shift the trial force field to match these data points (e.g. region indicated by the two arrows in Figure 3.29(b)). This secondary shift is conducted near the local, normalized probability distribution maximum values, located between -6 to -3 kJ/mol in Figure 3.29(b). Spatially, the local maximum region corresponds to the center of the one-dimensional channel in the Mg-MOF-74 structure. The sudden drop in the curves appears for both force fields as it is not possible to move further away from the Mg metal atoms at the pore center. Unsurprisingly, $\Delta E_{center} = E_{trial,center} - E_{reference,center}$ = (-3.33) - (-5.49) = 2.16 kJ/mol $< \Delta E_{binding}$ = 8.81 kJ/mol, as the guest-host van der Waals interaction weakens further away from the open-metal sites. In other words, the trial force field does a better job of capturing the correct adsorption properties far away from the strong binding adsorption sites. In practice, one could forgo conducting additional quantum chemical calculations at the pore center and assume that $E_{reference,center} = E_{trial,center}$ = -3.33 kJ/mol in order to reduce the large computational cost incurred while retaining similar level of accuracy. Taking account these two shifts, all of the energy values less than $E_{reference,center}$ are shifted by ΔE_{center} and at the binding energy, the energy is shifted by $\Delta E_{binding}$. In between the two points, we opt for a linearized shift such that ΔE_{shift} increases linearly from $E_{trial,center}$ and $E_{trial,binding}$. The resulting shifted curve is displayed in Figure 3.29(b) in blue, and it agrees very well with the MP2-derived distribution. The resulting $K_H(\mathrm{CO_2})$ = 1.00x10^{-3} (mol/kg/Pa), which is only 13.0% less than the MP2-derived force field K_H = 1.13x10^{-3} (mol/kg/Pa). The $K_H(\mathrm{CO_2})$ was computed by shifting the energies by an appropriate amount during the Widom particle insertion moves. If we forgo the secondary shift at the pore center and assume $E_{reference,center} = E_{trial,center}$, the resulting linearized shift yields $K_H(\mathrm{CO_2})$ = 8.18x10^{-4} (mol/kg/Pa), which is 38% less than the MP2-derived force field K_H but still a reasonably good prediction. And using Grand-canonical Monte Carlo simulations, we observe that the agreement is reasonable at high pressure regions as well (1 bar: 11.27 vs 10.22 mol/kg) and (10 bar: 14.31 mol/kg vs 13.65 mol/kg), with the former being the reference result and the latter, the shifted result neglecting the secondary shift. For the purpose of illustration, the binding energy of CO_2 inside Mg-MOF-74 was computed directly from the MP2-derived force field, and the value was regarded as an exact baseline. However, the binding energy values obtained from DFT as well as other wave-function based quantum chemical methods contain several uncertainties such as the choice of functional for the dispersive energies on the DFT level and basis sets. Thus, it is important to evaluate the sensitivity of the algorithm to the binding energy values. The results can be found in the supporting information of ref 119 where computational results for both the $K_H(\mathrm{CO_2})$ and the full isotherms are reported at varying CO_2 binding energies. Overall, the stability analysis illustrates the importance of obtaining accurate quantum chemical binding energies for this system in the context of our methodology. As expected, when the binding energies become inaccurate, the adsorption properties deviate from the reference results.

Next, the effect of the initial choice in the trial force field is analyzed. An algorithm in which the final adsorption data is completely independent of the choice in the trial force field is ideal. In order to conduct the sensitivity analysis, the point charges in the CO_2 molecule were changed from their initial values of q_{C,CO_2} = +0.7e, q_{O,CO_2} = -0.35e to q_{C,CO_2} = +0.6, +0.5, +0.4, and +0.3e (with corresponding changes in q_{O,CO_2} to ensure neutrality). The resulting single point energy distributions are shown in Figure 3.30(a). The results here indicate that decreasing q_{O,CO_2} effectively reduces the energy spread (i.e., energy difference

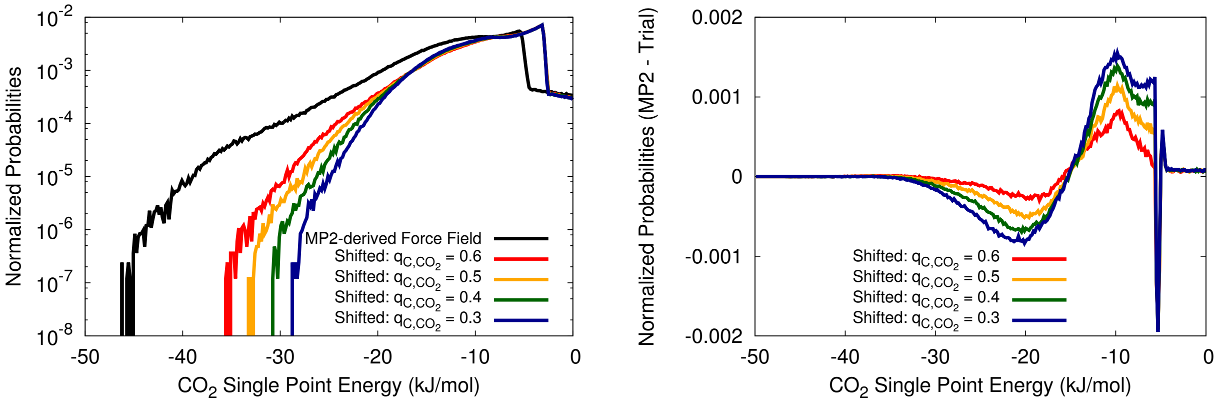

(a)

(b)

Figure 3.30: (a) CO_2 single point energy distributions for MP2-derived force field (black) and UFF for q_{C,CO_2} = +0.6, +0.5, +0.4, and +0.3e. (b) The difference between the energy distributions of MP2-derived force field (black line in (a)) and the shifted UFF (shifted lines in (a)) for q_{C,CO_2} = +0.6, +0.5, +0.4, and +0.3e.

between the minima point and the local maximum point in the curve) within the distribution. This is reasonable as imposing stronger electrostatic interactions causes sharper peaks in the minima energy. Moreover, the local peak in the distributions corresponds to the center of the pore region where the sum of the electrostatic interaction contributions is small, thus making it independent of charge. Accordingly, for smaller q_{C,CO_2} in the initial trial force field, the subsequent shift will cause a greater overestimation in the infinite dilution adsorption property as there will be proportionally more single point energies near the binding energy region when the energy spread is small. Mathematically, this effect can be visualized upon subtracting the shifted trial force energy distributions from the MP2-derived distribution (Figure 3.30(b)). As can be seen from Figure 3.30(b), for smaller q_{C,CO_2}, the overestimate from the trial force field increases between -35 and -18 kJ/mol. Since the low energy region contributes mostly to the infinite dilution adsorption properties, it is predicted that the discrepancy between the Henry coefficient values computed from the MP2-derived force field and the trial force field will increase for decreasing q_{C,CO_2}. This is supported in our calculations where for q_{C,CO_2} = +0.6, +0.5, +0.4, and +0.3e, the $K_H(\mathrm{CO_2})$ = 9.5x10^{-4}, 1.1x10^{-3}, 1.43x10^{-3}, and 1.69x10^{-3} (mol/kg/Pa), respectively. The resulting data shows that even for q_{C,CO_2} = +0.3e, which is most different from the original charge value of q_{C,CO_2} = +0.7e, the shifted correction does an accurate job of estimating the MP2-derived $K_H(\mathrm{CO_2})$ value. However, the results here underscore the importance of judicious selection of the initial force field and charge parameters. We also note from Figure 3.30(b) that there is a spike at -5 kJ/mol near E_{center} region. Upon conducting shifts, there are binning mismatches between the reference distribution and the shifted one due to a sharp discontinuity at the point, creating a numerical artifact. However, this does not affect any of the conclusions drawn from our analysis. Finally, we would like to point out that there can be other methods to correct the energy distribution instead of conducting shifts. An example of this would be to correct based on the scaling factors (e.g. ratio between the reference and the trial energies). However, in this case there can be problems where the scaling factors at the secondary sites become much larger than the one at the primary site, potentially resulting in significant over-correction. In the future, we plan to look at other methodologies that can perhaps improve upon the current methodology adopted here.

3.3.2.2 CO_2 in Fe-MOF-74 and N_2 in V- and Ti-MOF-74

The reference result that was previously used for comparison purposes was derived from classical molecular simulation data using an MP2-derived force field. However, the utility of this methodology hinges on being able to predict or to reproduce experimental data in absence of a good force field. Thus, we proceed to select two systems, (1) CO_2 in Fe-MOF-74 and (2) N_2 in V-MOF-74 and Ti-MOF-74, corresponding to cases where (1) there are experimental data in literature[175] and (2) there are neither experimental nor simulated isotherm data published anywhere.

For this analysis, the binding energies were computed using DFT with a vdW-DF2 functional[140, 176] with on-site Hubbard U corrections[177] for metal d electrons as implemented in VASP.[139] The computed binding energies for CO_2 in Fe-MOF-74, N_2 in V-MOF-74 and Ti-MOF-74 are -41, -56 kJ/mol, and -59 kJ/mol, respectively. We used a planewave energy cutoff of 1000 eV, projector augmented wave potentials, and the Brillouin zone was sampled at the Γ-point. All calculations are spin polarized. For both Fe-MOF-74 and V-MOF-74, the initial on-site magnetic moments of metal cations are set to their high-spin state according to Hund's rule in a weak-field ligand environment, and eventually converged to the same high-spin state at the end of the self-consistent electronic iteration. We obtained ferromagnetic ordering along the metal-oxide chain direction and antiferromagnetic between the chains for Fe-MOF-74, and we assumed the same ordering for V-MOF-74. For bare MOFs we used a triclinic primitive unit cell containing 54 atoms including 6 metal centers, and simultaneously optimized the lattice vectors and the atomic positions in the unit cell with variable cell dynamics with PBE+U. The calculated lattice constants of Fe-MOF-74 for the conventional hexagonal unit cell are a = b = 26.47 Å and c = 6.97 Å, which are in good agreement with experiment to within 1.7%. Then the MOF structure is assumed to be rigid while all atomic positions of the molecules in the MOF are fully relaxed by using vdW-DF2+U until the residual forces are smaller than 0.01 eV/Å. For the secondary correction at the center of the pore, we utilize the $E_{reference,center} = E_{trial,center}$ where $E_{trial,center}$ is computed from the trial force field. Given that the binding energies directly come from quantum chemical calculations with Born-Oppenheimer approximation where nuclear quantum fluctuations are not included, the zero-point energy contributions to the binding energy need to be computed and subtracted from the shift. The zero-point energy corrections computed for CO_2 in Fe-

MOF-74 and N_2 in V-MOF-74 and Ti-MOF-74 are 1.8, 4.1, and 3.9 kJ/mol respectively. The zero-point energies are calculated using DFT vibrational frequencies at the harmonic level.[178]

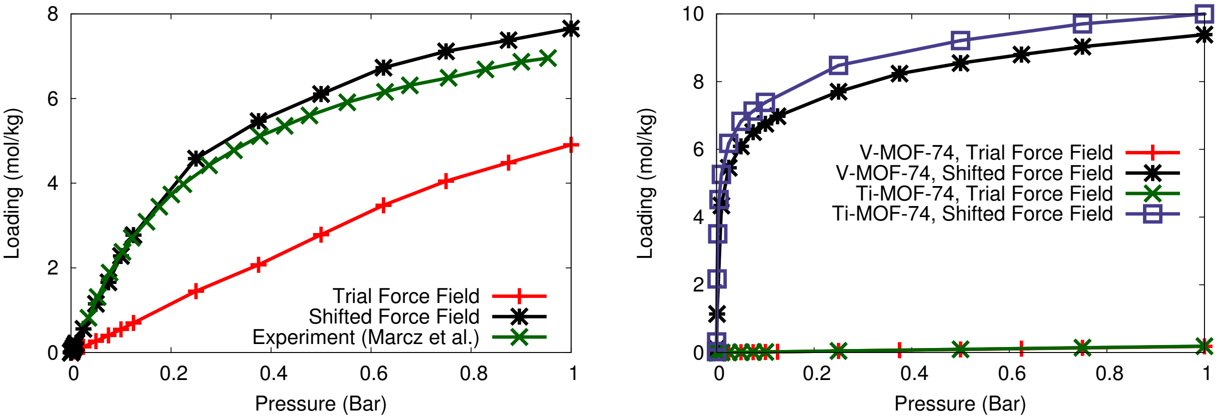

(a) (b)

Figure 3.31: Adsorption isotherm for (a) CO_2 in Fe-MOF-74 at T = 298 K and (b) N_2 in V-MOF-74 at T = 313 K. The experimental data for N_2 in V-MOF-74 do not exist and thus were excluded from the figure.

The simulated adsorption isotherm data for the two systems are shown in Figure 3.31(a) and 3.31(b). Using the UFF force field, the CO_2 TraPPE model, and the point framework charges obtained from the REPEAT scheme, the computed binding energies are -34.23, -18.58 kJ/mol, -18.7 kJ/mol for CO_2 in Fe-MOF-74 and N_2 in V-MOF-74 and Ti-MOF-74. For the secondary shift, the center of the pore energy values was assumed to be the same between the trial force field and the DFT results. Figure 3.31(a) shows very good agreement between the experimental and the simulated (shifted) isotherm data for CO_2 in Fe-MOF-74 at T = 298 K. The overestimation of CO_2 uptake at relatively high pressure values might be due to the presence of inactive metal sites in the conducted experiments. For the N_2 isotherm data, because the UFF binding energy values are very different from those computed from the DFT method, the disparity between the UFF and the shifted isotherms is significantly larger (Figure 3.31(b)) for both V-MOF-74 and Ti-MOF-74. Lee et al. have shown that this exceptionally strong binding of N_2 to V-MOF-74 is due to the subtle interplay of several interactions.[178] In practice, our methodology can be used to compute all of the isotherms for various guest molecules in the M-MOF-74 structures for different metal atoms. Conceivably, this will allow us to screen the materials and identify the optimal open-metal site MOF structures for various different applications of interest.

3.3.2.3 CH_4 and CO_2 in zeolites

In the previous systems, the adsorption is dominated by the interactions with the open-metal sites. To test our method for a system that is less dominated by strong binding sites, CH_4 and CO_2 inside zeolite structures are analyzed next. In particular, eight common pure-silica zeolite structures in the IZA database (i.e., MFI, LTA, WEI, RHO, SOD, FAU, RWY, and ABW) are chosen to demonstrate the transferability within the class of zeolite materials. The crystal structures for each of these structures can be found from an online IZA database.[23] In this analysis, the force field and charge parameter values taken from García-Pérez et al. was selected as the true, reference model as it has been demonstrated to reproduce existing experimental data for pure silica zeolite structures.[179] As a baseline, the energy distribution curves that arise from millions of CH_4 and CO_2 single point energy calculations and the CH_4 and CO_2 K_H computed from the García-Pérez force field were treated as being accurate. The CH_4 energy distributions for all eight zeolites can be found in the supporting information of ref 119. The distributions that emerge for different zeolite structures reflect the variety of pore topologies that exist within the class of zeolite materials. For example, in zeolite SOD, the single point energy has a local maximum near the binding energy region. Also, in structures like ABW, WEI, and SOD, there doesn't seem to be a distinct maximum peak that is found from the open-metal site structures. In light of this diversity, we opt to choose two different shifting strategies: (1) constant uniform energy shift, $\Delta E_{binding}$, for all single point energy values and (2) linear shift with the secondary match being set to E = 0 kJ/mol. The latter value was chosen as an adequate reference point to smooth out any over-shifting from a constant uniform energy shift.

For the two initial sets of trial force fields, the pair-wise potential depth in the Lennard-Jones parameter ϵ_{oxygen} of the zeolite framework atom is increased by 2x for and decreased by 2x for the other from its initial value, $\epsilon_{oxygen} = 89.36$ K. Effectively, the two starting force fields respectively overestimate and underestimate the correct adsorption data. In Figure 3.32, three different sets of data are plotted against the reference $K_H(CH_4)$ ((a) and (b))and $K_H(CO_2)$ ((c) and (d)) data (x-axis) at T = 313 K for the eight selected zeolite structures: (1) K_H values ('x' data points) obtained from force field with the wrong initial force field (2) K_H values ('+' data points) obtained from constant uniform shift force field and (3) K_H values ('box' data points) obtained from linear shift force field. In Figure 3.32(a) and (c) data, the starting trial force field parameter has $\epsilon_{oxygen} = 44.68$ K, while in Figure 3.32(b) and (d) the starting trial force field parameter has $\epsilon_{oxygen} = 178.72$ K. The dashed line indicates the region where the K_H values determined from the corrected force field and the reference force field are equal to one another. Figure 3.32 indicates that the wrong initial data set ('x' data points) underestimates the reference K_H result for smaller ϵ_{oxygen} (Figure 3.32(a) and (c)) and overestimates the reference K_H result for larger ϵ_{oxygen} (Figure 3.32(b) and (d)), which is reasonable given that ϵ_{oxygen} has positive correlation with binding energy values. The data points generated from using a constant, uniform shift force field is shown as '+' data points in Figure 3.32. In general, because all of the energy curves are shifted by the same amount of $\Delta E_{binding}$, there is overestimation of adsorption property with smaller ϵ_{oxygen}

(i.e., data points are above the dashed line in Figure 3.32(a) and (c)) and underestimation with larger ϵ_{oxygen} (i.e., data points are below the dashed line in Figure 3.32(b) and (d)). However, this trend does not hold for all data points as can be seen for example, in the case of zeolite RWY (Figure 3.32(c)). We attribute this to the three-site model of the CO_2 that results in less predictability compared to the case for CH_4. Overall, it can be seen that in few cases, the constant shift results in a worse fit compared to the K_H data obtained from a wrong force field. However, all of the data points tend to collectively move towards the dashed line for the shift.

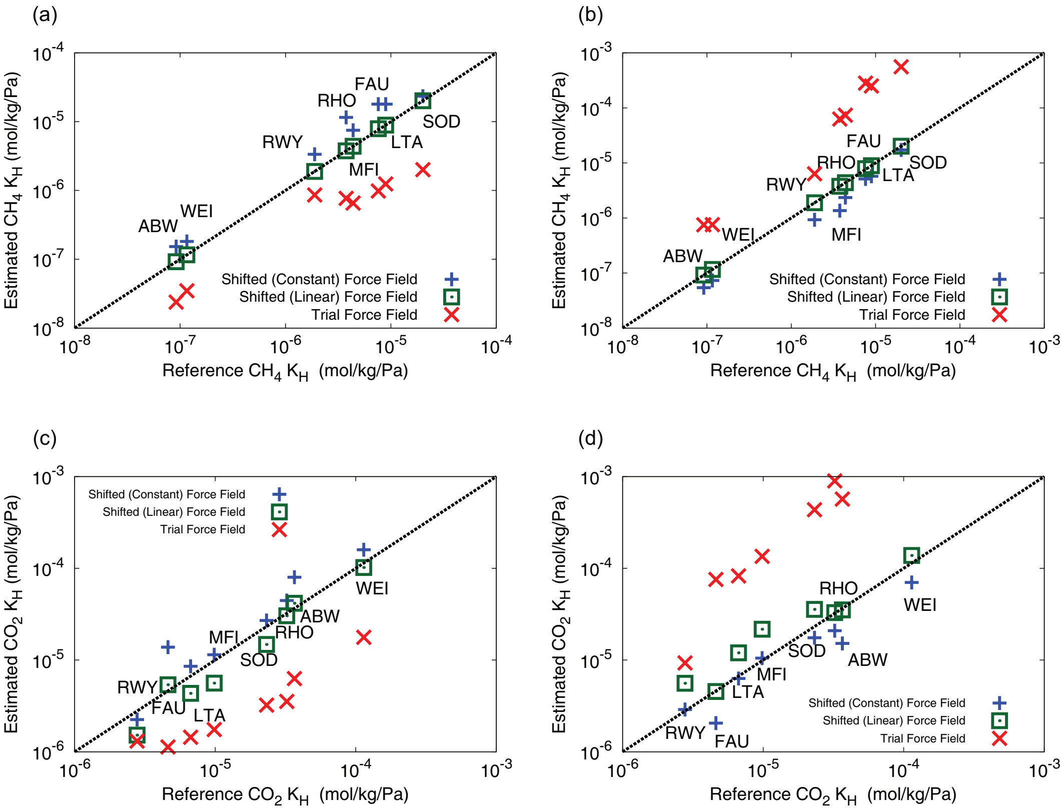

Figure 3.32: Estimated and the reference CH_4 (a, b) and CO_2 (c, d) K_H for zeolites MFI, LTA, WEI, RHO, SOD, FAU, RWY, and ABW. The dashed line is where the predicted and the reference data are equal to one another. The Lennard-Jones parameter for oxygen are (a, c) $\epsilon_{oxygen} = 44.68$ K and (b, d) $\epsilon_{oxygen} = 178.72$ K. For the constant shift, all of the energy values are shifted by a constant amount equal to the difference between the binding energies. For the linear shift, 0 kJ/mol is taken as the point for which there is zero shift for larger energy values.

Finally, the data points generated from using a linear shift are shown as ('box' data points) in Figure 3.32. For CH_4 , the linear shift results in remarkably good match between the shifted and the reference data, demonstrating the importance of simultaneously shifting to the correct binding energy while tempering the correction to avoid over-shifting. For CO_2, it becomes less clear on whether the linear shift does a better job compared to the constant shift, which is not surprising given the presence of larger degree of freedom found for the CO_2 molecule compared to CH_4. Overall, the results here seem to indicate that the methodology does a very good job of retrieving the correct adsorption data in cases where the initial force field and reference force field differ only by the pair-wise potential depth (i.e., ϵ) in the Lennard-Jones parameter. Next, we move on to a case where the initial force field has a different σ value in the Lennard-Jones parameters, where σ is the distance at which the inter-particle interaction goes to zero. Specifically, the σ_{oxygen} was decreased from σ_{oxygen} = 3.21 to 2.568 Å (i.e., 20% reduction) in the trial force field parameter. The resulting data are shown in Figure 3.33 with the symbols corresponding to the same force fields as in Figure 3.32. Overall, for both CH_4 and CO_2, the agreement between the predicted and the reference results are worse for both set of trial force fields ('+' and 'box' data points). Because changes in σ effectively change the binding distances, an overall shift in the single point energy values lead to relatively more unpredictable behavior compared to the situation where ϵ was being changed. As a result, the selection in a trial force field that correctly matches the true σ becomes more important as opposed to one that yields correct ϵ in our methodology.

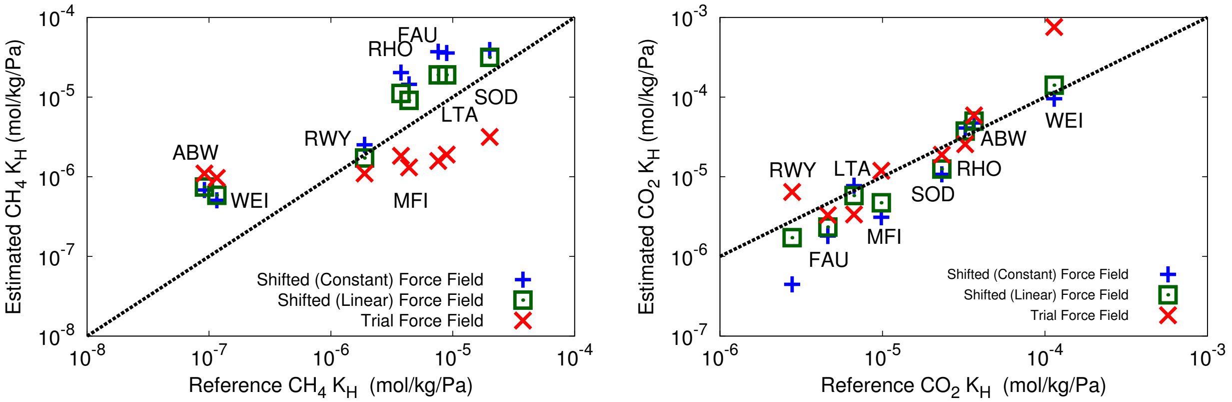

(a)

(b)

Figure 3.33: Estimated and the reference (a) CH_4 and (b) CO_2 K_H for zeolites MFI, LTA, WEI, RHO, SOD, FAU, RWY, and ABW with a trial force field with $\sigma_{oxygen} = 2.568$ Å.

The predicted (from linear shift) and the reference K_H for all eight zeolites in Table 3.3 indicate that the structures with the worst K_H predictions are ABW and WEI. Geometric analysis using Zeo++,[48] which are summarized in Table 3.3, reveal that ABW and WEI have the smallest pore limiting diameter and the smallest maximum cavity diameter, thus leading to narrow channels in these structures. Subsequently, starting with an incorrect σ

value leads to energy distribution that is completely different from the correct one as within these narrow pores. Overall, the sensitivity analysis conducted by changing σ reveals that for structures with narrow pores, it is important to choose a starting force field that models the correct distance terms in the guest-host interactions.

	K_H (mol/kg/Pa)			
	reference	linear shifted	pore limiting diameter (Å)	largest cavity diameter (Å)
MFI	4.4×10^{-6}	9.1×10^{-6}	4.64	6.30
LTA	8.9×10^{-6}	1.9×10^{-5}	4.15	10.99
WEI	1.2×10^{-7}	5.9×10^{-7}	**3.40**[a]	**4.13**[a]
RHO	3.8×10^{-6}	1.1×10^{-5}	4.00	10.37
SOD	2.0×10^{-5}	3.1×10^{-5}	2.47	6.26
FAU	7.6×10^{-6}	1.9×10^{-5}	7.29	11.18
RWY	1.9×10^{-6}	1.7×10^{-6}	6.23	14.34
ABW	9.2×10^{-8}	7.4×10^{-7}	**3.45**[a]	**4.18**[a]

[a] The boldface numbers indicate structures with small pores.

Table 3.3: Estimated and the reference $K_H(CH_4)$ for zeolites MFI, LTA, WEI, RHO, SOD, FAU, RWY, and ABW with a trial force field with $\sigma_{oxygen} = 2.568$ Å.

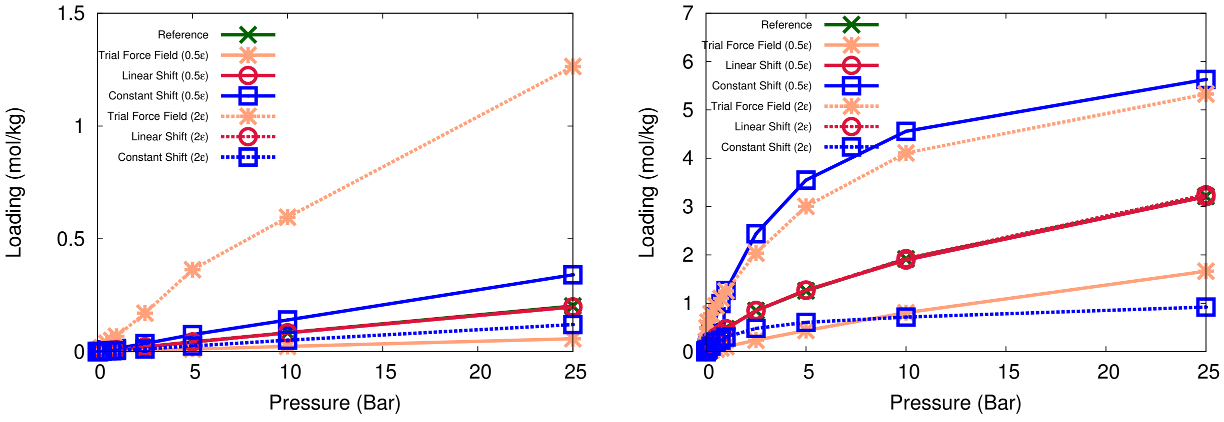

(a)

(b)

Figure 3.34: CH_4 isotherms at T = 313 K for (a) ABW and (b) FAU. The trial force field parameter uses $\epsilon_{oxygen} = 0.5\epsilon = 44.68$ K (nondashed) and $\epsilon_{oxygen} = 2\epsilon = 178.72$ K (dashed) in the Lennard-Jones potential.

Finally, the full adsorption isotherms were computed for CH_4 in ABW and FAU, and CO_2 in ABW, FAU, SOD, and RWY. ABW and FAU were chosen as representative materials

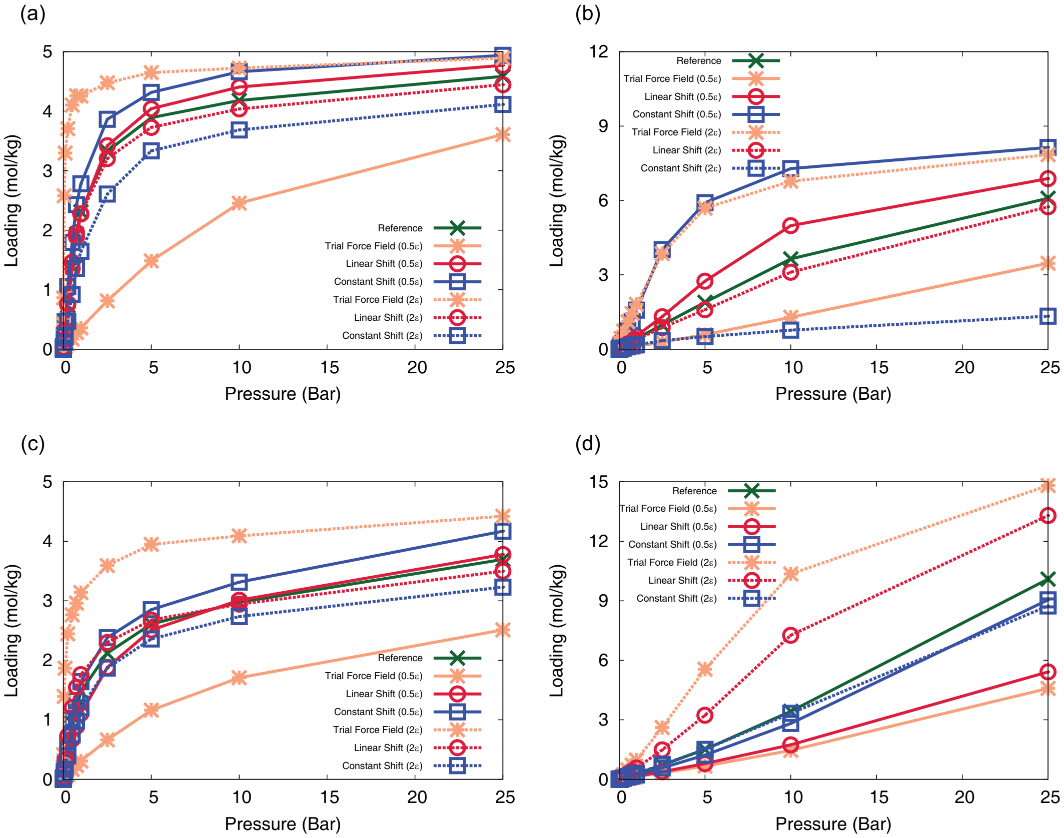

Figure 3.35: CO_2 isotherms at T = 313 K for (a) ABW, (b) FAU, (c) SOD, and (d) RWY. Similar to the case for CH_4, the trial force field parameter uses $\epsilon_{oxygen} = 0.5\epsilon = 44.68$ K (nondashed) and $\epsilon_{oxygen} = 2\epsilon = 178.72$ K (dashed) in the Lennard-Jones potential.

for small and large pore structures respectively. Two additional structures (i.e., SOD and RWY) were chosen for the CO_2 case as the constant shift method yielded more accurate $K_H(CO_2)$ in these cases. The CH_4 and CO_2 adsorption isotherms at T = 313 K are shown in Figure 3.34 and 3.35. The CH_4 isotherms (Figure 3.34) indicate that the linear shift yield isotherm data that are statistically identical to the reference data. The constant shift becomes problematic especially for zeolite FAU, where the large pore size leads to prevalence of secondary binding sites that is incorrectly shifted by the primary binding site energy difference. Accordingly, the empirical linear shift does an adequate job of tempering this effect. For the CO_2 isotherms (Figure 3.35), similar trend is observed as the zeolites with smaller pore sizes (ABW and SOD) yields good agreement with both linear and constant shifts. For zeolites with larger pores (FAU and RWY), the methodology yields inaccurate data for reasons similar to CH_4 in FAU. Unlike the case of CO_2 in M-MOF-74 structures, in these zeolites, the lack of strong primary binding sites exacerbates matter as the shift in the secondary sites are not only inaccurate but their contributions to the overall adsorption properties are larger. Accordingly, the selection of an accurate force field becomes more crucial in porous materials with weak binding sites and large pore volume when adopting our methodology.

3.3.3 Conclusions

We have developed a new methodology that allows simple and efficient, yet reasonably accurate prediction of adsorption properties in porous materials from a judicious number of *ab initio* total energy calculations. The methodology involves utilizing a trial force field to obtain reasonably accurate picture of the porous material's adsorption properties and correcting the single point energy values from the quantum chemical binding energy calculations. We have demonstrated that our methodology leads to accurate adsorption properties for a wide range of guest molecules in porous materials, including CH_4 and CO_2 inside zeolites, CO_2 in Mg-MOF-74 and Fe-MOF-74. Moreover, the predictions made for N_2 in V-MOF-74 and Ti-MOF-74 reveal significant uptake of N_2 in these two unsynthesized materials. The methodology especially works well for structures that possess strong binding sites as the adsorption properties are largely determined by the low energy regions. Also, for structures with small pores and channels, a trial force field with correct sigma values can lead to more accurate representation of the overall adsorption properties with better performance observed for linear shifts. Finally, the method does poorly for structures with large pore sizes that lack a strong adsorption sites when the trial force field is vastly different from the reference case. In this case, it is imperative to obtain an accurate force field for accurate characterization. This proposed methodology, however, can generally provide better predictions in adsorption properties compared to initial trial force fields, e.g., commonly used force fields, although the accuracy of predictions is subject to the quality of trial force fields.

Chapter 4

Understanding CO_2 dynamics in metal-organic frameworks with open-metal sites*

4.1 Introduction

Open-metal site MOFs[30] such as Mg_2(dobdc) (dobdc^{4-} = 2,5-dioxido-1,4- benzenedicarboxylate; Mg-MOF-74) possess strong CO_2 binding sites leading to large experimental CO_2 uptake values. Recently, a number of research papers devoted specifically to this structure and its variants have been published.[31–33, 123, 134, 153, 180] Most of the past research on open-metal site structures, however, has focused on the equilibrium properties of the CO_2 rather than its dynamics. The dynamics of CO_2 molecules within these structures is an important topic that can lead to better designs for open-metal site MOF structures, while exposing possible diffusion limitations. A recent study presented ^{13}C NMR spectra and relaxation times for CO_2 adsorbed inside Mg-MOF-74.[163] The observed CO_2 chemical shift anisotropy (CSA) patterns "flipped" at temperatures above 150 K, yielding CSA patterns consistent with simple uniaxial rotation of the O=C=O molecule about a fixed rotational angle. At a CO_2 loading of 0.3 CO_2/Mg^{2+}, a second motion-averaged powder pattern was observed at temperatures above 350 K. The uniaxial rotational model, when applied to the flipped CSA patterns, yielded a rotational angle that varied from 59^o (0.5 CO_2/Mg^{2+}, 300 K) to 69^o (0.3 CO_2/Mg^{2+}, 210 K). Spin-lattice relaxation times for 0.5 CO_2/Mg^{2+} in the temperature range 12 K-200 K were fit to a BPP-type relaxation mechanism governed by two different exponentially activated motions. These authors did not provide any details as to why such processes would be occurring within the Mg-MOF-74 framework. In a further study visual inspection of molecular dynamics trajectories was made to conclude that the high binding

---

*Material in this chapter is adopted with permission from *Angew. Chem. Int. Ed.*, **2013**, 52 (16), 4410-4413.[162]
Link: http://dx.doi.org/10.1002/anie.201300446

strength between CO_2 and open-metal sites, as well as the presence of the rotational motion, reduce the transversal mobility of CO_2 along the channels and thereby reduce diffusivity.[181] From a structural and thermodynamic point of view, the presence of uniaxial rotation of CO_2 in Mg-MOF-74 is not intuitive. Both density functional theory (DFT)[141,171,182] and neutron powder diffraction data at 20 K[133] illustrate that the angle θ, shown in Figure 4.1(a), between the minimum energy CO_2 configuration and the Mg-O(CO_2) vector is in the range of 50-60^o, consistent with the angle extracted from the experimental CSA pattern fit to uniaxial rotation. It seems clear, though that the chemical environment near a metal site is not perfectly symmetric with respect to the Mg-O(CO_2) vector, implying that the CO_2 is unlikely to possess a uniform free energy surface (that is, the ”cone” for uniaxial rotation is not of constant free energy). More vexing is the fact that fitting the CSA patterns to a simple uniaxial rotation yields a decreasing CO_2 rotational angle with increasing temperature.[163] At higher temperatures, one would expect CO_2 to explore a larger portion of phase space, which would correspond to an increase in the rotational angle. However, the experiments were interpreted as a decrease in the angle, suggesting a counter-intuitive reduction in entropy.

4.2 Methods

In light of these observations, we utilized molecular simulations to arrive at a different explanation for the experimental results. Canonical Monte Carlo simulations[57] were carried out at various loadings (infinite dilution, 0.3 CO_2/Mg, and 0.5 CO_2/Mg) to probe the free energy landscape of CO_2 molecules in Mg-MOF-74 at temperatures ranging from 100 K to 375 K.[74] In these simulations, both dispersive and electrostatic energies were included to model the guest-framework and the guest-guest interactions. Similar to previous studies in this dissertation, we assumed the framework to be rigid and used the DFT relaxed structure for our calculations.[118] The Lennard-Jones potential was adopted to describe the dispersion interaction, in which we used the universal force field (UFF)[129] for the framework atoms and TraPPE model[55] for the CO_2 molecule. Finally, the atomic partial charges of the framework atoms were computed using the REPEAT algorithm.[159] Detailed parameters used in this study can be found in supporting information of ref 162.

4.3 Results and discussion

In carrying out the Monte Carlo simulations, we are probing equilibrium configurations. In order to make meaningful comparisons with the NMR experiments, these equilibrium configurations must be carefully interpreted in the context of CO_2 dynamics. Figure 4.2 and Figure 4.3 provide orthographic views along the Z-direction of the possible CO_2 configurations obtained from the NVT simulation at different temperatures, 50 K and 250 K, respectively, in Mg-MOF-74 structure. From these configurations, we observe two types of

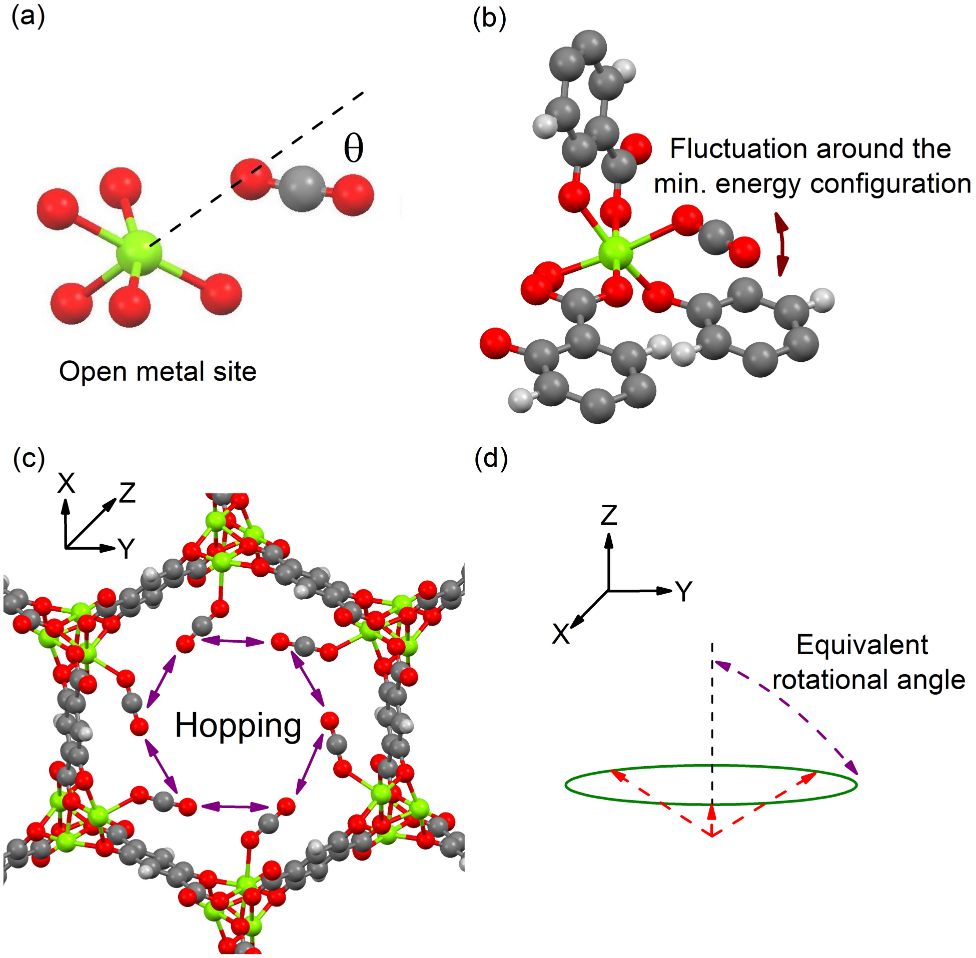

Figure 4.1: Schematic view of CO_2 binding in Mg-MOF-74 and its dynamics. (a) Orientation of CO_2 (C, grey; O, red) at the minimum-energy location near a metal site (Mg, green), (b) localized CO_2 fluctuation motion in which the oxygen atom of the CO_2 remains bound to the same metal site, and (c)non-localized hopping motion. The Z-axis in the plot corresponds to the crystallographic c-axis. (d) From an NMR point of view, the hopping of a CO_2 molecule between different metal sites in the X-Y plane (see (c)) is equivalent to a rotation around an axis parallel to the Z-axis with an angle referred as the equivalent rotational angle in this work. The CO_2 molecules (in (c)) in this illustration are assumed to be located at their minimum-energy configuration, and are represented by the dashed red lines.

motion of the CO_2 molecules: (1) fluctuation of the CO_2 molecule near the minimum energy configuration (illustrated in Figure 4.1(b)) and (2) hops between different metal sites (Figure 4.1(c)). Accordingly, in our analysis we compute the CSA patterns[183] for these two different cases (More details can be found in supporting information section 2-VI of ref 162).

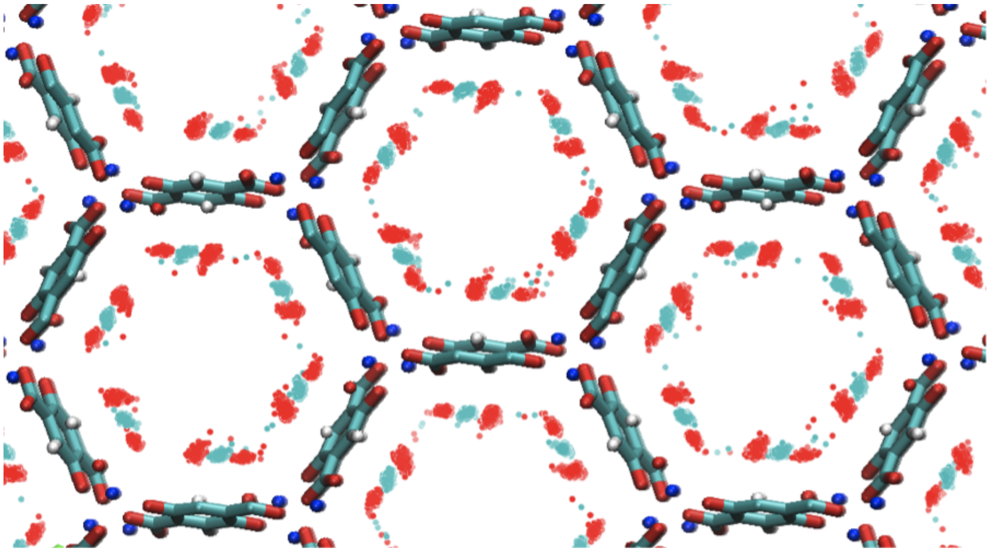

Figure 4.2: Orthographic view along the Z-direction of the CO_2 configurations obtained from the NVT simulation at 50 K in Mg-MOF-74 structure. The CO_2 molecule is represented as closed dots with C (cyan) and O (red). The framework is represented as spheres and bonds with Mg (blue), C (cyan), O (red), and H (white).

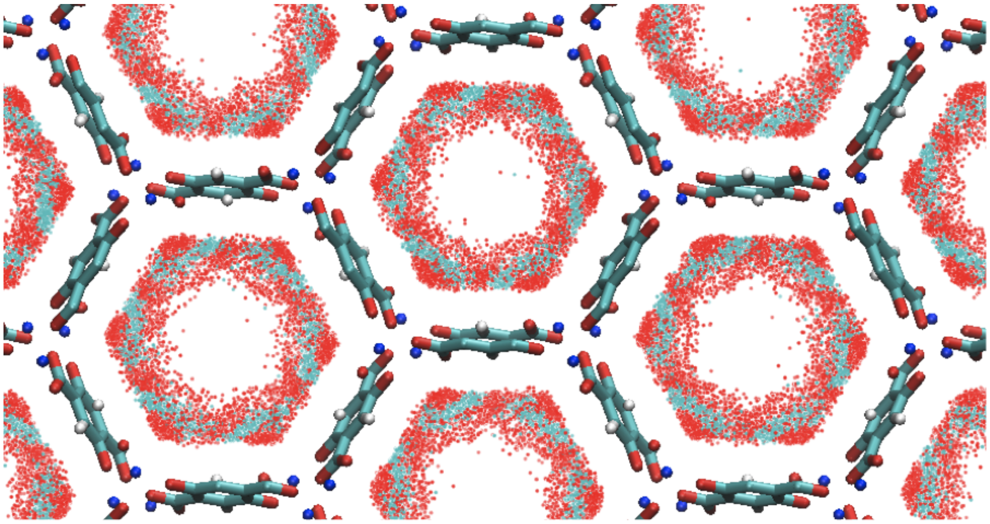

Figure 4.3: Orthographic view along the Z-direction of the CO_2 configurations obtained from the NVT simulation at 50 K in Mg-MOF-74 structure. The CO_2 molecule is represented as closed dots with C (cyan) and O (red). The framework is represented as spheres and bonds with Mg (blue), C (cyan), O (red), and H (white).

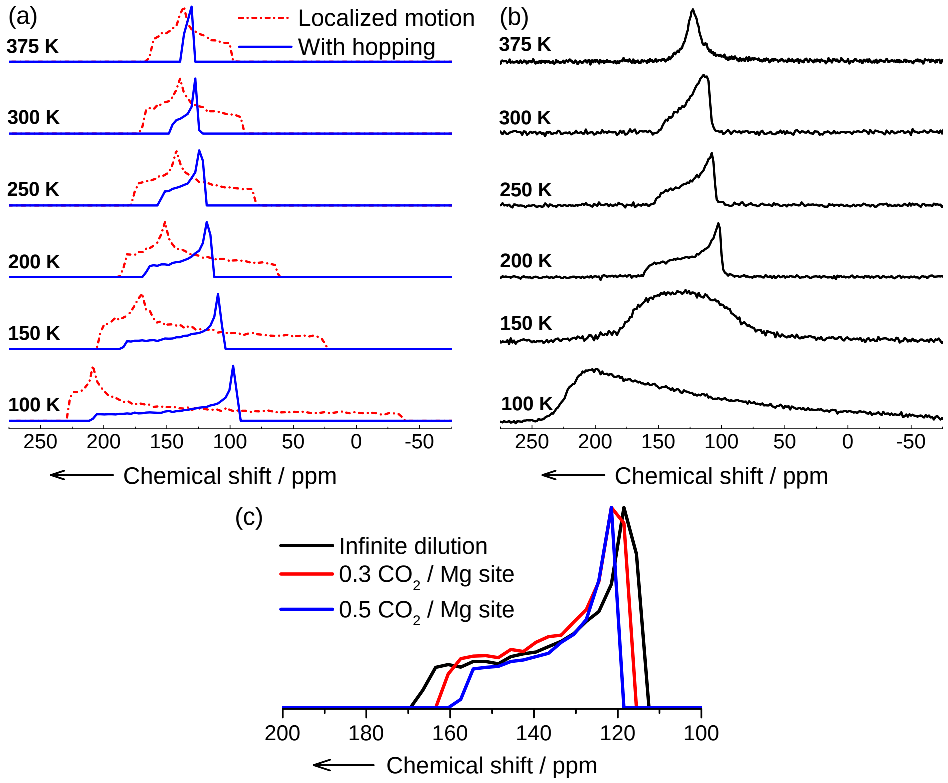

Figure 4.4: Comparison between simulated and experimental CSA patterns and the effect of CO_2 loading on the CSA patterns in Mg-MOF-74. (a) Simulated patterns with CSA tensor values of $\sigma_\perp$ = 245ppm and $\sigma_\parallel$ = -90ppm[183] at infinite dilution for localized fluctuation motions (red dashed line) and including non-localized hopping motions (blue line). (b) Experimental patterns at 0.5 CO_2/Mg site.[163] (c) Simulated CSA patterns at 200K with different loadings: infinite dilution (black), 0.3 CO_2/Mg site (red), and 0.5 CO_2/Mg site (blue).

At sufficiently low temperatures, we expect CO_2 to be localized near a single metal site with minimal motion. With the onset of motion, localized fluctuations and non-localized hops are expected to contribute differently to the motion-averaged NMR CSA pattern. Comparison of the NMR data and our simulation at T = 100 K shows that the simulated pattern corresponding to the localized fluctuations (Figure 4.4(a), dashed red line) agrees with the experimental spectrum (Figure 4.4(b)), while the simulated pattern including hopping between metal sites (Figure 4.4(a), blue lines) has a qualitatively different CSA pattern. The slight asymmetry of the CSA pattern calculated by the localized fluctuations (Figure 4.4(a), dashed red line) reflects the asymmetry of the motion (see Appendix A Figure A.16, A.17, and A.18, the 2-D projected plots demonstrate the asymmetric free energy surface near a metal site). This small asymmetry is not apparent in the experimental data owing to dipolar

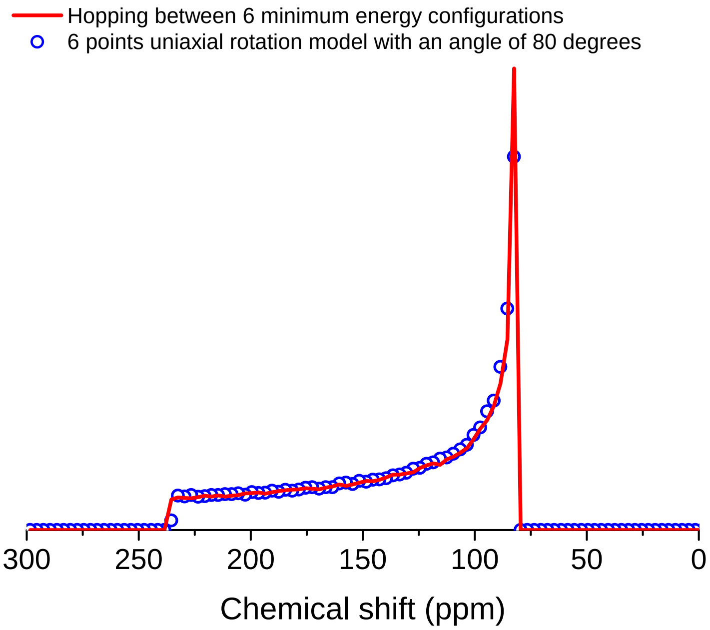

Figure 4.5: Comparison of the computed CSA patterns between the hopping motion between the 6 minimum energies configurations with equal probabilities (solid red line) and the 6 points uniaxial rotation model (equal probabilities) with a fixed angle of 80^o (open blue circles). From the comparison, it clearly indicates that the hopping motion between these minimum energies configurations has an equivalent rotational angle of 80^o.

broadening from nearby linker protons.[163] Upon increasing temperature, the experimental patterns, which show uniaxial rotational motions, clearly deviate from those simulated patterns of the fluctuation motions (Figure 4.4(a), dashed red line)

To properly account for the experimental NMR data at higher temperatures, we consider hopping motions of CO_2 between different metal sites in the X-Y plane (Figure 4.1(c)). It is important to realize that NMR only measures the relative orientation of the CO_2 molecule with respect to the applied magnetic field. Figure 4.1(c) shows the 6 minimum energy configurations obtained from DFT calculations.[118] If a CO_2 molecule hops between these configurations, the observed NMR signal is equivalent to a uniaxial rotation. This is best imagined by defining a common origin at the oxygen atom of the CO_2 that is bound to the metal site. Because of the symmetry of the crystal, these minimum energy configurations are related through a uniaxial rotation of 80^o (see Figure 4.5), with a fixed angle, which we define as the equivalent rotational angle (see Figure 4.1(d)). Hence, from an NMR point of view, hopping between these sites creates a CSA pattern that is identical to that predicted from uniaxial rotation about this equivalent angle. With the hopping motions, the simulated pattern at 100 K has an equivalent rotation angle of 71^o. However, the temperature is too low here to observe hopping, which becomes possible above 200 K.

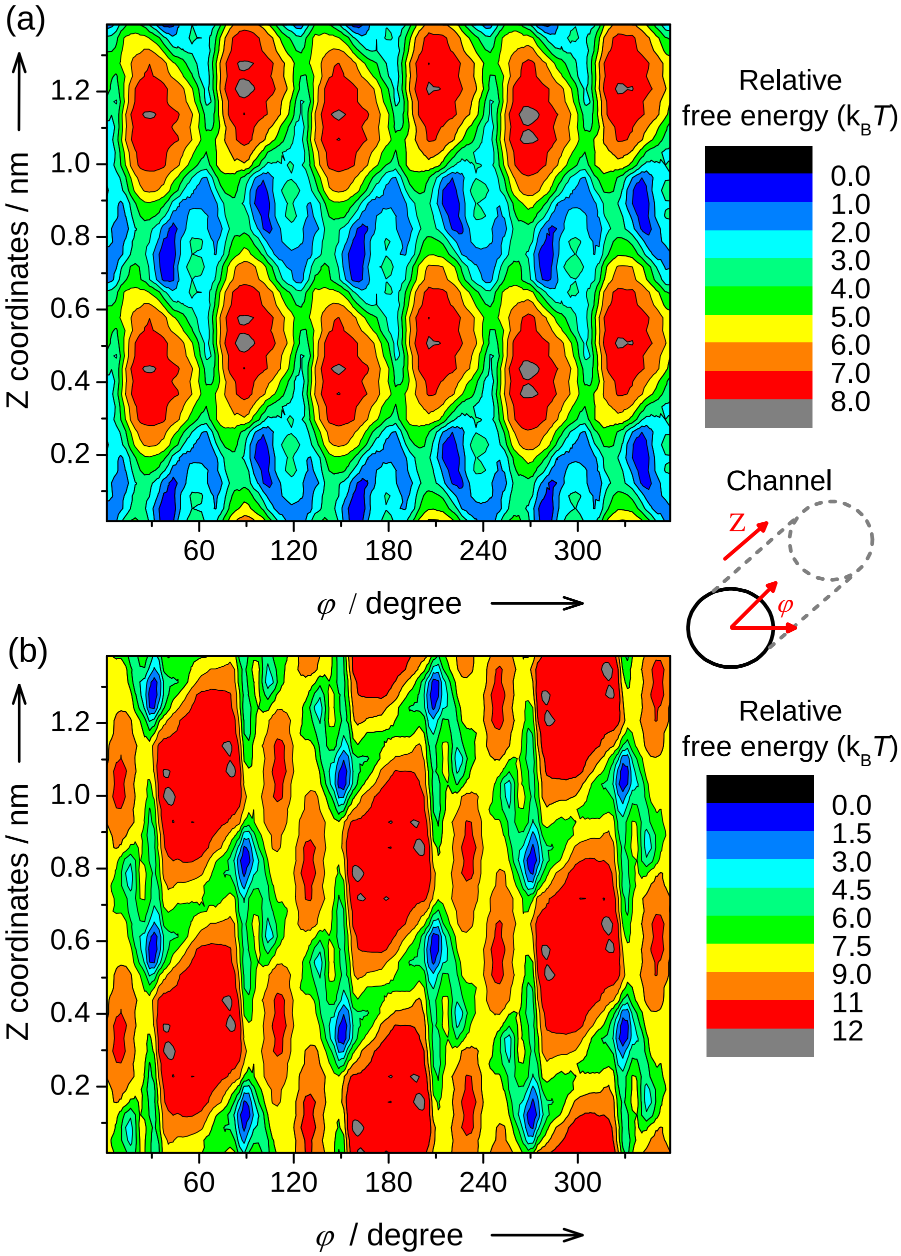

Figure 4.6: Free energy map of a cylinder-like channel in (a) Mg-MOF-74 and in (b) Mg_2(dobpdc) at 200 K is shown as a function of the angular angle φ of the channel opening and the position of the channel along the Z-direction. The minimum free energy binding site near an open-metal site was set to be zero k_BT in this illustration.

At T >200 K, the experimental pattern is equivalent to a near 60^o uniaxial rotation,[163] which is the equivalent rotational angle we calculate by including hopping between sites. Moreover, our simulations show that the equivalent rotational angle decreases with increasing temperature, which have values of 61^o and 57^o at the temperatures of 200 K and 300 K, respectively. The apparent decrease in equivalent rotational angle with increasing temperature is seen as a manifestation of thermally activated motion along the Z-direction (i.e., the changes of the $C(CO_2)$ position along the Z-direction shown in Figure A.17 and Figure A.18). Enhanced motion along the Z-direction results in a larger tilted angle of the CO_2 molecules with respect to the X-Y plane, which is the effect that decreases the equivalent rotational angle. The experimental CSA pattern at 150 K (Figure 4.4(b)) reveals a transition behavior that mixes both the localized and the non-localized CO_2 movements. We expect that this temperature is just high enough to allow the CO_2 molecules to hop between the different metal sites, but at the same time low enough to categorize hopping as a rare event. This transition temperature is an exquisite probe of the energetics of CO_2 hopping. Figure 4.4(c) shows the effect of changing CO_2 loading on the simulated CSA pattern. The results indicate that there is a shift in the pattern for larger loading values, which leads to smaller equivalent rotation angles (i.e., 60^o and 59^o at the loadings of 0.3 CO_2/Mg site and 0.5 CO_2/Mg site, respectively). This shift to smaller rotational angles is also what is observed experimentally. As the number of CO_2 molecules inside the structure increases, the repulsive forces between CO_2 molecules cause them to stay apart along the channel (Z-direction) from each other, enlarging the angle of CO_2 that adsorbed at open-metal sites with respect to the X-Y plane.

We can use the knowledge gained from this study to make a prediction regarding the CSA pattern of CO_2 in a similar structure: Mg_2(dobpdc) (dobpdc^{4-} = 4,4$'$-dioxido-3,3$'$-biphenyldicarboxylate), which is an expanded MOF-74 structure owing to an extended organic linker.[127] In this structure, the smallest Mg-Mg separations within a channel are 10.82 Å in the X-Y plane, while the corresponding separations in Mg-MOF-74 are 8.22 Å. (see Figures 3.1 and 3.9 for visualizing the structures). The local dynamics of adsorbed CO_2 are expected to be similar to those for Mg-MOF-74. The difference between these two structures is that the longer ligand might make it more difficult for a CO_2 molecule to hop between metal sites. Figure 4.6 illustrates the CO_2 free energy map[57] within a cylinder-like channel for these two structures at 200 K. The angular angle of the channel opening and the position along the direction of the channel (i.e., Z-direction) were utilized to map the entire channel profile. These maps show that a CO_2 molecule can hop to the two neighboring sites in the X-Y plane and along the Mg-O-Mg backbone in the Z-direction. It is important to note that hops along the Z-direction do not change the orientation of the molecules. Although these hops are important for the diffusion, they are not probed by the NMR methods reported previously.[163] The maps show that the free energy barrier for hopping between two adjacent sites along the X-Y plane in the expanded structure is two times larger than what is computed for in Mg-MOF-74. Given that the uniaxial rotation-like CSA pattern originates from CO_2 hops between different metal sites, the jumps should occur less frequently within the pores of the expanded structure. As a result, we predict a higher transition temperature for the expanded Mg-MOF-74 structure in which the purely localized motions become

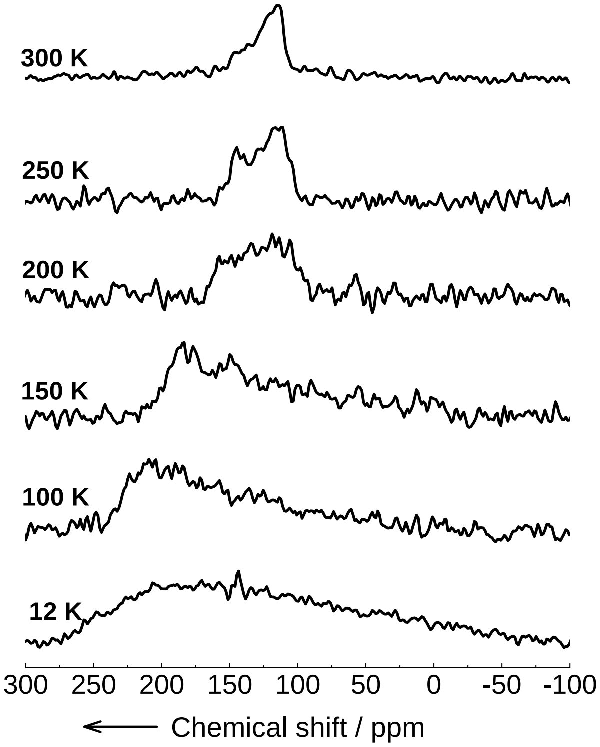

Figure 4.7: Experimental CSA patterns for Mg_2(dobpdc), an expanded variant of Mg-MOF-74, at a loading of 0.4 CO_2/Mg site and at various temperatures from 12 K to 300 K.

mixed with the hopping motions. Figure 4.7 further shows the experimental CSA pattern obtained for Mg_2(dobpdc). Comparison between Mg-MOF-74 (Figure 4.4(b)) and the expanded structure (Figure 4.7) indicates that the pattern that matches the signature of the hopping motions indeed shifts to higher temperatures, T = 150-200 K in Mg-MOF-74 and T approximates to 250 K in Mg_2(dobpdc). It would be interesting to investigate how this change in the dynamics depends on the length of the linkers.[184]

4.4 Conclusions

This work has proposed a dynamic mechanism that provides an alternative explanation for the experimental CSA pattern than the one put forward in the article of Kong et al.[163] We argue that the more proper interpretation of the NMR signal is not a uniaxial rotation at the open-metal site, but a signature of the hopping motions between different metal sites.

As mentioned in ref 163, we re-emphasize that obtaining detailed information regarding the CO_2 dynamics is important and this work illustrates that the dynamics is much richer than initially expected.

Chapter 5

Outlook

Nanoporous materials including zeolites, zeolitic imidazolate frameworks (ZIFs), metal-organic frameworks (MOFs), etc. have become of great interest to the scientific community. The use of these materials as adsorbents and/or membranes has the potential to provide a more energy-efficient means of achieving various separations. The number of possible porous materials one can envision is extremely large, therefore purely experimental approaches only can study a very limited number of candidates. To accelerate the search of promising materials, computational approaches utilizing various techniques in molecular simulation and quantum chemical calculations can play an important role. In this dissertation, several important aspects in the computational approaches were discussed. Large-scale screenings of a large number of materials for carbon capture, methane capture, and ethane/ethene separations were conducted to identify promising materials and, moreover, obtain insights into structure-property relationships. All of these findings may be used as useful guidelines for future synthesis. Additionally, novel methodologies were proposed to derive force fields or make corrections on initial trial force fields for use in molecular simulations to yield accurate estimates of properties. Furthermore, molecular simulations were used to obtain fundamental understandings of experimentally observed phenomena at molecular levels.

Based upon the current studies, three future directions are proposed. First, it is important to evaluate other classes of materials for the aforementioned separations. In the previous studies, our screenings mainly focused on zeolite materials due to their chemical simplicity. However, materials like MOFs can be more promising due to their higher chemical diversity. It is instructive to point out that some of the insights obtained from the previous screenings of zeolites can be potentially very helpful not only for future synthesis but also for future computational studies. For instance, as discussed in section 2.4 for CH_4/CO_2 separations, enhanced methane-methane interactions are essential for preferential adsorption of CH_4 over CO_2 at high pressure region (i.e., >10 bar). To ensure enhanced gas-gas interactions, structures that have individual methane binding sites separated by about 4.5 Å are required. In this respect, in future computational screenings of materials for CH_4/CO_2 and even CH_4/N_2 separations, one can specifically focus on a subset of materials that have such a desired feature. Next, it is imperative to extend the scope of considered separations to explore more possibilities. The tunability of porous materials can also make them promising for other separations. Far less attention, however, has been paid to applications other than carbon capture and natural gas purifications. One of the interesting studies in the future will be the separations of harmful gases (e.g., H_2S, SO_x, and NO_x), which are crucial to petroleum and environmental processes. Traditional liquid solvents are commonly used for these separations and the required energy for solvent regeneration is enormous. Finally, more studies are required to make the proposed methodologies for making accurate predictions of properties generally applicable to varying systems. The robustnesses of these methods on diverse structures in terms of both chemistry and topology need to be investigated. In addition, other guest molecules such as those harmful gases need to be included in the methods. Moreover, the methods need to be implemented in an automated manner for large-scale screening purposes and made available as a tool to other researchers.

In summary, we anticipate that the computational screenings of materials for various applications, advanced methodologies for making accurate predictions, and detailed understanding of adsorption phenomena at molecular levels presented in this dissertation can synergistically facilitate the discovery of new materials.

References

[1] Lin, L.-C.; Berger, A. H.; Martin, R. L.; Kim, J.; Swisher, J. A.; Jariwala, K.; Rycroft, C. H.; Bhown, A. S.; Deem, M. W.; Haranczyk, M.; Smit, B. *Nat. Mater.* **2012**, *11*, 633–641.

[2] Kim, J.; Maiti, A.; Lin, L.-C.; Stolaroff, J. K.; Smit, B.; Aines, R. D. *Nat. Commun.* **2013**, *4*, 1694.

[3] Kim, J.; Lin, L.-C.; Martin, R. L.; Swisher, J. A.; Haranczyk, M.; Smit, B. *Langmuir* **2012**, *28*, 11914–11919.

[4] Lin, L.-C.; Lee, K.; Gagliardi, L.; Neaton, J. B.; Smit, B. *J. Chem. Theory Comput.* **2014**, *10*, 1477–1488.

[5] Smit, B.; Reimer, J. R.; Oldenburg, C. M.; Bourg, I. C. *Introduction to Carbon Capture and Sequestration*, Imperial College Press, London, 2014.

[6] Metz, B.; Davidson, O.; deConinck, H.; Loos, M.; Meyer, L. *IPCC Special Report on Carbon Dioxide Capture and Storage*, Intergovernmental Panel on Climate Change (Cambridge Univ. Press, 2005).

[7] Chu, S. *Science* **2009**, *325*, 1599–1599.

[8] Pacala, S.; Socolow, R. *Science* **2004**, *305*, 968–972.

[9] Ramezan, M.; Skone, T. J.; ya Nsakala, N.; Liljedahl, G. N. *Carbon Dioxide Capture from Existing Coal-Fired Power Plants*, Report No. DOE/NETL–401/110907 (National Energy Technology Laboratory, US Department of Energy, 2007).

[10] *http://www.esrl.noaa.gov/gmd/ccgg/trends/index.html.*

[11] *Climate Change 2007: Mitigation. Contribution of Working Group III to the Fourth Assessment Report of the Intergovernmental Panel on Climate Change*, Cambridge University Press: UK, (2007).

[12] Stolaroff, J. K.; Bhattacharyya, S.; Smith, C. A.; Bourcier, W. L.; Cameron-Smith, P. J.; Aines, R. D. *Environ. Sci. Technol.* **2012**, *46*, 6455–6469.

[13] *Annual Energy Outlook 2011: With Projections to 2035, #DOE/EIA-0383.*, U.S. Energy Information Administration: Washington, DC, (2011).

[14] Shindell, D.; et al. *Science* **2012**, *335*, 183–189.

[15] *Near-term Climate Protection and Clean Air Benefits: Actions for Controlling Short-Lived Climate Forcers*, United Nations Environment Programme (UNEP): Nairobi, Kenya, (2011).

[16] Su, S.; Beath, A.; Guo, H.; Mallett, C. *Prog. Energy Combust. Sci.* **2005**, *31*, 123–170.

[17] *U.S. Petrochem. Rep.* **2012**, *2*, 8–18.

[18] Eldridge, R. B. *Ind. Eng. Chem. Res.* **1993**, *32*, 2208–2212.

[19] Férey, G. *Chem. Soc. Rev.* **2007**, *37*, 191–214.

[20] Yaghi, O. M.; O'Keeffe, M.; Ockwig, N. W.; Chae, H. K.; Eddaoudi, M.; Kim, J. *Nature* **2003**, *423*, 705–714.

[21] D'Alessandro, D. M.; Smit, B.; Long, J. R. *Angew. Chem. Int. Ed.* **2010**, *49*, 6058–6082.

[22] Banerjee, R.; Phan, A.; Wang, B.; Knobler, C.; Furukawa, H.; O'Keeffe, M.; Yaghi, O. M. *Science* **2008**, *319*, 939–943.

[23] *http://www.iza-structure.org/databases/.*

[24] Pophale, R.; Cheeseman, P. A.; Deem, M. W. *Phys. Chem. Chem. Phys.* **2011**, *13*, 12407–12412.

[25] Park, K. S.; Ni, Z.; Ct, A. P.; Choi, J. Y.; Huang, R.; Uribe-Romo, F. J.; Chae, H. K.; O'Keeffe, M.; Yaghi, O. M. *Proc. Natl. Acad. Sci. U.S.A.* **2006**, *103*, 10186–10191.

[26] Furukawa, H.; Cordova, K. E.; O'Keeffe, M.; Yaghi, O. M. *Science* **2013**, *341*, 1230444.

[27] Wilmer, C. E.; Leaf, M.; Lee, C. Y.; Farha, O. K.; Hauser, B. G.; Hupp, J. T.; Snurr, R. Q. *Nat. Chem.* **2012**, *4*, 83–89.

[28] Martin, R. L.; Lin, L.-C.; Jariwala, K.; Smit, B.; Haranczyk, M. *The Journal of Physical Chemistry C* **2013**, *117*, 12159–12167.

[29] Deng, H.; Doonan, C. J.; Furukawa, H.; Ferreira, R. B.; Towne, J.; Knobler, C. B.; Wang, B.; Yaghi, O. M. *Science* **2010**, *327*, 846–850.

[30] Dinca, M.; Long, J. R. *Angew. Chem. Int. Ed.* **2008**, *47*, 6766–6779.

[31] Caskey, S. R.; Wong-Foy, A. G.; Matzger, A. J. *J. Am. Chem. Soc.* **2008**, *130*, 10870–10871.

[32] Britt, D.; Furukawa, H.; Wang, B.; Glover, T. G.; Yaghi, O. M. *Proc. Natl. Acad. Sci. U.S.A.* **2009**, *106*, 20637–20640.

[33] Dietzel, P. D. C.; Besikiotis, V.; Blom, R. *J. Mater. Chem.* **2009**, *19*, 7362–7370.

[34] Kim, J.; Lin, L.-C.; Swisher, J. A.; Haranczyk, M.; Smit, B. *J. Am. Chem. Soc.* **2012**, *134*, 18940–18943.

[35] Kim, J.; Abouelnasr, M.; Lin, L.-C.; Smit, B. *J. Am. Chem. Soc.* **2013**, *135*, 7545–7552.

[36] Bhown, A. S.; Freeman, B. C. *Environ. Sci. Technol.* **2011**, *45*, 8624–8632.

[37] Bottoms, R. *US Patent 1*, 783,901 (1930).

[38] Rochelle, G. T. *Science* **2009**, *325*, 1652–1654.

[39] Ciferno, J. P.; Marano, J. J.; Munson, R. K. *Chem. Eng. Prog.* **2011**, *107*, 34–44.

[40] Krishna, R.; Baten, J. M. v. *Phys. Chem. Chem. Phys.* **2011**, *13*, 10593–10616.

[41] Krishna, R.; Long, J. R. *J. Phys. Chem. C* **2011**, *115*, 12941–12950.

[42] Yazaydn, A. .; Snurr, R. Q.; Park, T.-H.; Koh, K.; Liu, J.; LeVan, M. D.; Benin, A. I.; Jakubczak, P.; Lanuza, M.; Galloway, D. B.; Low, J. J.; Willis, R. R. *J. Am. Chem. Soc.* **2009**, *131*, 18198–18199.

[43] Freeman, S. A.; Dugas, R.; Van Wagener, D.; Nguyen, T.; Rochelle, G. T. *Energy Procedia* **2009**, *1*, 1489–1496.

[44] Lemmon, E. W.; Huber, M. L.; McLinden, M. O., NIST Reference Fluid Thermodynamic and Transport Properties Database (REFPROP): Version 9.0. (NIST, 2010).

[45] Deem, M. W.; Pophale, R.; Cheeseman, P. A.; Earl, D. J. *J. Phys. Chem. C* **2009**, *113*, 21353–21360.

[46] Sanders, M. J.; Leslie, M.; Catlow, C. R. A. *J. Chem. Soc., Chem. Commun.* **1984**, 1271–1273.

[47] van Beest, B. W. H.; Kramer, G. J.; van Santen, R. A. *Phys. Rev. Lett.* **1990**, *64*, 1955–1958.

[48] Willems, T. F.; Rycroft, C. H.; Kazi, M.; Meza, J. C.; Haranczyk, M. *Microporous Mesoporous Mater.* **2012**, *149*, 134–141.

[49] Smit, B.; Maesen, T. L. M. *Chem. Rev* **2008**, *108*, 4125–4184.

[50] García-Pérez, E.; Dubbeldam, D.; Liu, B.; Smit, B.; Calero, S. *Angew. Chem. Int. Ed.* **2007**, *46*, 276–278.

[51] Lowenstein, W. *Am. Mineral.* **1954**, *39*, 92–96.

[52] Calero, S.; Dubbeldam, D.; Krishna, R.; Smit, B.; Vlugt, T. J. H.; Denayer, J. F. M.; Martens, J. A.; Maesen, T. L. M. *J. Am. Chem. Soc.* **2004**, *126*, 11377–11386.

[53] García-Sánchez, A.; Ania, C. O.; Parra, J. B.; Dubbeldam, D.; Vlugt, T. J. H.; Krishna, R.; Calero, S. *J. Phys. Chem. C* **2009**, *113*, 8814–8820.

[54] Mayo, S. L.; Olafson, B. D.; Goddard, W. A. *J. Phys. Chem.* **1990**, *94*, 8897–8909.

[55] Potoff, J. J.; Siepmann, J. I. *AIChE J.* **2001**, *47*, 16761682.

[56] Xu, Q.; Zhong, C. *J. Phys. Chem. C* **2010**, *114*, 5035–5042.

[57] Frenkel, D.; Smit, B. *Understanding molecular simulation from algorithms to applications*, 2nd edn (Academic Press, 2002).

[58] Kim, J.; Rodgers, J. M.; Athnes, M.; Smit, B. *J. Chem. Theory Comput.* **2011**, *7*, 3208–3222.

[59] Bates, S. P.; van Well, W. J. M.; van Santen, R. A.; Smit, B. *J. Am. Chem. Soc.* **1996**, *118*, 6753–6759.

[60] Haranczyk, M.; Sethian, J. A. *Proc. Natl. Acad. Sci. U.S.A.* **2009**, *106*, 21472–21477.

[61] Haranczyk, M.; Sethian, J. A. *J. Chem. Theory Comput.* **2010**, *6*, 3472–3480.

[62] Krishna, R.; Calero, S.; Smit, B. *Chem. Eng. J.* **2002**, *88*, 81–94.

[63] Myers, A. L.; Prausnitz, J. M. *AIChE J.* **1965**, *11*, 121–127.

[64] Rao, M. B.; Sircar, S. *Langmuir* **1999**, *15*, 7258–7267.

[65] Martin, R. L.; Smit, B.; Haranczyk, M. *J. Chem. Inf. Model.* **2012**, *52*, 308–318.

[66] Simancas, R.; Dari, D.; Velamazn, N.; Navarro, M. T.; Cantn, A.; Jord, J. L.; Sastre, G.; Corma, A.; Rey, F. *Science* **2010**, *330*, 1219–1222.

[67] Jariwala, K.; Haranczyk, M. *http://www.carboncapturematerials.org/.*

[68] Hudson, M. R.; Queen, W. L.; Mason, J. A.; Fickel, D. W.; Lobo, R. F.; Brown, C. M. *J. Am. Chem. Soc.* **2012**, *134*, 1970–1973.

[69] Zhang, J.; Singh, R.; Webley, P. A. *Microporous Mesoporous Mater.* **2008**, *111*, 478–487.

[70] Pires, J.; de Carvalho, M. B.; Ribeiro, F. R.; Derouane, E. G. *J. Mol. Catal.* **1993**, *85*, 295–303.

[71] Bae, T.-H.; Hudson, M. R.; Mason, J. A.; Queen, W. L.; Dutton, J. J.; Sumida, K.; Micklash, K. J.; Kaye, S. S.; Brown, C. M.; Long, J. R. *Energy Environ. Sci.* **2012**, *6*, 128–138.

[72] García-Sánchez, A.; van den Bergh, J.; Castillo, J. M.; Calero, S.; Kapteijn, F.; Vlugt, T. J. H. *Microporous Mesoporous Mater.* **2012**, *158*, 64–76.

[73] Dunne, J. A.; Rao, M.; Sircar, S.; Gorte, R. J.; Myers, A. L. *Langmuir* **1996**, *12*, 5896–5904.

[74] Kim, J.; Martin, R. L.; Rbel, O.; Haranczyk, M.; Smit, B. *J. Chem. Theory Comput.* **2012**, *8*, 1684–1693.

[75] Mellot-Draznieks, C.; Buttefey, S.; Boutin, A.; Fuchs, A. H. *Chem. Commun.* **2001**, 2200–2201.

[76] Buttefey, S.; Boutin, A.; Mellot-Draznieks, C.; Fuchs, A. H. *J. Phys. Chem. B* **2001**, *105*, 9569–9575.

[77] Wilmer, C. E.; Farha, O. K.; Bae, Y.-S.; Hupp, J. T.; Snurr, R. Q. *Energy Environ. Sci.* **2012**, *5*, 9849–9856.

[78] Kusakabe, K.; Kuroda, T.; Morooka, S. *J. Membr. Sci.* **1998**, *148*, 13–23.

[79] Haldoupis, E.; Nair, S.; Sholl, D. S. *Phys. Chem. Chem. Phys.* **2011**, *13*, 5053–5060.

[80] Merkel, T. C.; Lin, H.; Wei, X.; Baker, R. *J. Membr. Sci.* **2010**, *359*, 126–139.

[81] First, E. L.; Gounaris, C. E.; Wei, J.; Floudas, C. A. *Phys. Chem. Chem. Phys.* **2011**, *13*, 17339–17358.

[82] Dubbeldam, D.; Beerdsen, E.; Vlugt, T. J. H.; Smit, B. *J. Chem. Phys* **2005**, *122*, 224712.

[83] Abouelnasr, M. K. F.; Smit, B. *Phys. Chem. Chem. Phys.* **2012**, *14*, 11600–11609.

[84] Baerlocher, C.; McCusker, L. B.; Olson, D. H. In *Atlas of Zeolite Framework Types (Sixth Edition)*; Baerlocher, C.; McCusker, L. B.; Olson, D. H., Eds.; Elsevier Science B.V.: Amsterdam, 2007; pp 72–73.

[85] Haldoupis, E.; Nair, S.; Sholl, D. S. *J. Am. Chem. Soc.* **2010**, *132*, 7528–7539.

[86] Tsapatsis, M. *Science* **2011**, *334*, 767–768.

[87] Snyder, M. A.; Tsapatsis, M. *Angew. Chem. Int. Ed.* **2007**, *46*, 7560–7573.

[88] Ruthven, D. M.; Derrah, R. I. *J. Chem. Soc., Faraday Trans. 1* **1972**, *68*, 2332–2343.

[89] June, R. L.; Bell, A. T.; Theodorou, D. N. *J. Phys. Chem.* **1991**, *95*, 8866–8878.

[90] Kim, J.; Smit, B. *J. Chem. Theory Comput.* **2012**, *8*, 2336–2343.

[91] Swisher, J. A.; Lin, L.-C.; Kim, J.; Smit, B. *AIChE J.* **2013**, *59*, 3054–3064.

[92] Robeson, L. M. *J. Membr. Sci.* **1991**, *62*, 165–185.

[93] Freeman, B. D. *Macromolecules* **1999**, *32*, 375–380.

[94] Krishna, R.; van Baten, J. M. *J. Membr. Sci.* **2010**, *360*, 323–333.

[95] Fang, H.; Kamakoti, P.; Zang, J.; Cundy, S.; Paur, C.; Ravikovitch, P. I.; Sholl, D. S. *J. Phys. Chem. C* **2012**, *116*, 10692–10701.

[96] Soler, J. M.; Artacho, E.; Gale, J. D.; García, A.; Junquera, J.; Ordejón, P.; Snchez-Portal, D. *J. Phys.: Condens. Matter* **2002**, *14*, 2745.

[97] Dawson, R.; Cooper, A. I.; Adams, D. J. *Prog. Polym. Sci.* **2012**, *37*, 530–563.

[98] Bagheri, N.; Abedi, J. *Chem. Eng. Res. Des.* **2011**, *89*, 2038–2043.

[99] Chen, J.-J.; Li, W.-W.; Li, X.-L.; Yu, H.-Q. *Environ. Sci. Technol.* **2012**, *46*, 10341–10348.

[100] Rege, S. U.; Padin, J.; Yang, R. T. *AIChE J.* **1998**, *44*, 799809.

[101] Bux, H.; Chmelik, C.; Krishna, R.; Caro, J. *J. Membr. Sci.* **2011**, *369*, 284–289.

[102] Bloch, E. D.; Queen, W. L.; Krishna, R.; Zadrozny, J. M.; Brown, C. M.; Long, J. R. *Science* **2012**, *335*, 1606–1610.

[103] Bao, Z.; Yu, L.; Ren, Q.; Lu, X.; Deng, S. *J. Colloid Interface Sci.* **2011**, *353*, 549–556.

[104] Hosseinpour, S.; Fatemi, S.; Mortazavi, Y.; Gholamhoseini, M.; Ravanchi, M. T. *Sep. Sci. Technol.* **2010**, *46*, 349–355.

[105] Shi, M.; Avila, A. M.; Yang, F.; Kuznicki, T. M.; Kuznicki, S. M. *Chem. Eng. Sci.* **2011**, *66*, 2817–2822.

[106] Nowak, A. K.; Den Ouden, C. J. J.; Pickett, S. D.; Smit, B.; Cheetham, A. K.; Post, M. F. M.; Thomas, J. M. *J. Phys. Chem.* **1991**, *95*, 848–854.

[107] Gupta, V.; Nivarthi, S. S.; McCormick, A. V.; Ted Davis, H. *Chemical Physics Letters* **1995**, *247*, 596–600.

[108] Smit, B. *J. Phys. Chem.* **1995**, *99*, 5597–5603.

[109] Macedonia, M. D.; Moore, D. D.; Maginn, E. J.; Olken, M. M. *Langmuir* **2000**, *16*, 3823–3834.

[110] Demontis, P.; Guln González, J.; Suffritti, G. B.; Tilocca, A. *J. Am. Chem. Soc.* **2001**, *123*, 5069–5074.

[111] Krishna, R.; van Baten, J. M. *Chem. Eng. Technol.* **2006**, *29*, 1429–1437.

[112] Pascual, P.; Ungerer, P.; Tavitian, B.; Boutin, A. *J. Phys. Chem. B* **2004**, *108*, 393–398.

[113] Jianfen, F.; Qiuxia, W.; Xuedong, G.; Heming, X. *J. Mol. Struct.* **2003**, *638*, 129–134.

[114] Jakobtorweihen, S.; Hansen, N.; Keil, F. J. *Mol. Phys.* **2005**, *103*, 471–489.

[115] Liu, B.; Smit, B.; Rey, F.; Valencia, S.; Calero, S. *J. Phys. Chem. C* **2008**, *112*, 2492–2498.

[116] Martin, R. L.; Prabhat; Donofrio, D. D.; Sethian, J. A.; Haranczyk, M. *Int. J. High Perform. Comput.* **2012**, *26*, 347–357.

[117] Martin, R. L.; Willems, T. F.; Lin, L.-C.; Kim, J.; Swisher, J. A.; Smit, B.; Haranczyk, M. *ChemPhysChem* **2012**, *13*, 3595–3597.

[118] Dzubak, A. L.; Lin, L.-C.; Kim, J.; Swisher, J. A.; Poloni, R.; Maximoff, S. N.; Smit, B.; Gagliardi, L. *Nat. Chem.* **2012**, *4*, 810–816.

[119] Kim, J.; Lin, L.-C.; Lee, K.; Neaton, J. B.; Smit, B. *J. Phys. Chem. C* **2014**, *118*, 2693–2701.

[120] Valenzano, L.; Civalleri, B.; Sillar, K.; Sauer, J. *J. Phys. Chem. C* **2011**, *115*, 21777–21784.

[121] Chui, S. S.-Y.; Lo, S. M.-F.; Charmant, J. P. H.; Orpen, A. G.; Williams, I. D. *Science* **1999**, *283*, 1148–1150.

[122] Millward, A. R.; Yaghi, O. M. *J. Am. Chem. Soc.* **2005**, *127*, 17998–17999.

[123] Mason, J. A.; Sumida, K.; Herm, Z. R.; Krishna, R.; Long, J. R. *Energy Environ. Sci.* **2011**, *4*, 3030–3040.

[124] Grajciar, L.; Bludský, O.; Nachtigall, P. *J. Phys. Chem. Lett.* **2010**, *1*, 3354–3359.

[125] Getman, R. B.; Bae, Y.-S.; Wilmer, C. E.; Snurr, R. Q. *Chem. Rev* **2012**, *112*, 703–723.

[126] Wu, H.; Zhou, W.; Yildirim, T. *J. Am. Chem. Soc.* **2009**, *131*, 4995–5000.

[127] McDonald, T. M.; Lee, W. R.; Mason, J. A.; Wiers, B. M.; Hong, C. S.; Long, J. R. *J. Am. Chem. Soc.* **2012**, *134*, 7056–7065.

[128] Liu, B.; Smit, B. *Langmuir* **2009**, *25*, 5918–5926.

[129] Rappe, A. K.; Casewit, C. J.; Colwell, K. S.; Goddard, W. A.; Skiff, W. M. *J. Am. Chem. Soc.* **1992**, *114*, 10024–10035.

[130] Hagberg, D.; Karlstrm, G.; Roos, B. O.; Gagliardi, L. *J. Am. Chem. Soc.* **2005**, *127*, 14250–14256.

[131] Engkvist, O.; strand, P.-O.; Karlstrm, G. *Chem. Rev* **2000**, *100*, 4087–4108.

[132] Krishna, R.; van Baten, J. M. *J. Membr. Sci.* **2011**, *377*, 249–260.

[133] Queen, W. L.; Brown, C. M.; Britt, D. K.; Zajdel, P.; Hudson, M. R.; Yaghi, O. M. *J. Phys. Chem. C* **2011**, *115*, 24915–24919.

[134] Rosi, N. L.; Kim, J.; Eddaoudi, M.; Chen, B.; O'Keeffe, M.; Yaghi, O. M. *J. Am. Chem. Soc.* **2005**, *127*, 1504–1518.

[135] Dietzel, P. D. C.; Blom, R.; Fjellvg, H. *Eur. J. Inorg. Chem.* **2008**, *2008*, 3624–3632.

[136] Giannozzi, P.; et al. *J. Phys.: Condens. Matter* **2009**, *21*, 395502.

[137] Román-Pérez, G.; Soler, J. M. *Phys. Rev. Lett.* **2009**, *103*, 096102.

[138] Kresse, G.; Furthmller, J. *Comput. Mater. Sci.* **1996**, *6*, 15–50.

[139] Kresse, G.; Furthmller, J. *Phys. Rev. B* **1996**, *54*, 11169–11186.

[140] Lee, K.; Murray, . D.; Kong, L.; Lundqvist, B. I.; Langreth, D. C. *Phys. Rev. B* **2010**, *82*, 081101.

[141] Poloni, R.; Smit, B.; Neaton, J. B. *J. Phys. Chem. A* **2012**, *116*, 4957–4964.

[142] Boys, S.; Bernardi, F. *Mol. Phys.* **1970**, *19*, 553–566.

[143] Karlstrm, G.; Lindh, R.; ke Malmqvist, P.; Roos, B. O.; Ryde, U.; Veryazov, V.; Widmark, P.-O.; Cossi, M.; Schimmelpfennig, B.; Neogrady, P.; Seijo, L. *Comput. Mater. Sci.* **2003**, *28*, 222 – 239.

[144] Aquilante, F.; Pedersen, T. B.; Lindh, R. *J. Chem. Phys* **2007**, *126*, 194106.

[145] Aquilante, F.; Malmqvist, P.-.; Pedersen, T. B.; Ghosh, A.; Roos, B. O. *J. Chem. Theory Comput.* **2008**, *4*, 694–702.

[146] Aquilante, F.; Pedersen, T. B.; Lindh, R.; Roos, B. O.; Merás, A. S. d.; Koch, H. *J. Chem. Phys* **2008**, *129*, 024113.

[147] Hess, B. A. *Phys. Rev. A* **1986**, *33*, 3742–3748.

[148] Roos, B. O.; Lindh, R.; Malmqvist, P.-.; Veryazov, V.; Widmark, P.-O. *J. Phys. Chem. A* **2004**, *108*, 2851–2858.

[149] Roos, B. O.; Lindh, R.; Malmqvist, P.-.; Veryazov, V.; Widmark, P.-O. *J. Phys. Chem. A* **2005**, *109*, 6575–6579.

[150] Gagliardi, L.; Lindh, R.; Karlstrm, G. *J. Chem. Phys* **2004**, *121*, 4494–4500.

[151] Holt, A.; Bostrm, J.; Karlstrm, G.; Lindh, R. *J. Comput. Chem.* **2010**, *31*, 1583–1591.

[152] Vuong, T.; Monson, P. A. *Langmuir* **1996**, *12*, 5425–5432.

[153] Simmons, J. M.; Wu, H.; Zhou, W.; Yildirim, T. *Energy Environ. Sci.* **2011**, *4*, 2177–2185.

[154] Herm, Z. R.; Swisher, J. A.; Smit, B.; Krishna, R.; Long, J. R. *J. Am. Chem. Soc.* **2011**, *133*, 5664–5667.

[155] Sillar, K.; Hofmann, A.; Sauer, J. *J. Am. Chem. Soc.* **2009**, *131*, 4143–4150.

[156] Walton, K. S.; Millward, A. R.; Dubbeldam, D.; Frost, H.; Low, J. J.; Yaghi, O. M.; Snurr, R. Q. *J. Am. Chem. Soc.* **2008**, *130*, 406–407.

[157] Liu, J.; Benin, A. I.; Furtado, A. M. B.; Jakubczak, P.; Willis, R. R.; LeVan, M. D. *Langmuir* **2011**, *27*, 11451–11456.

[158] Yu, J.; Balbuena, P. B. *J. Phys. Chem. C* **2013**, *117*, 3383–3388.

[159] Campaá, C.; Mussard, B.; Woo, T. K. *J. Chem. Theory Comput.* **2009**, *5*, 2866–2878.

[160] Harris, J. G.; Yung, K. H. *J. Phys. Chem.* **1995**, *99*, 12021–12024.

[161] Grimme, S. *J. Comput. Chem.* **2006**, *27*, 1787–1799.

[162] Lin, L.-C.; Kim, J.; Kong, X.; Scott, E.; McDonald, T. M.; Long, J. R.; Reimer, J. A.; Smit, B. *Angew. Chem. Int. Ed.* **2013**, *52*, 4410–4413.

[163] Kong, X.; Scott, E.; Ding, W.; Mason, J. A.; Long, J. R.; Reimer, J. A. *J. Am. Chem. Soc.* **2012**, *134*, 14341–14344.

[164] Canepa, P.; Nijem, N.; Chabal, Y. J.; Thonhauser, T. *Phys. Rev. Lett.* **2013**, *110*, 026102.

[165] Yu, D.; Yazaydin, A. O.; Lane, J. R.; Dietzel, P. D. C.; Snurr, R. Q. *Chem. Sci.* **2013**, *4*, 3544–3556.

[166] Horn, H. W.; Swope, W. C.; Pitera, J. W.; Madura, J. D.; Dick, T. J.; Hura, G. L.; Head-Gordon, T. *J. Chem. Phys.* **2004**, *120*, 9665–9678.

[167] Yang, D.-A.; Cho, H.-Y.; Kim, J.; Yang, S.-T.; Ahn, W.-S. *Energy Environ. Sci.* **2012**, *5*, 6465–6473.

[168] Schoenecker, P. M.; Carson, C. G.; Jasuja, H.; Flemming, C. J. J.; Walton, K. S. *Ind. Eng. Chem. Res.* **2012**, *51*, 6513–6519.

[169] Grant Glover, T.; Peterson, G. W.; Schindler, B. J.; Britt, D.; Yaghi, O. *Chem. Eng. Sci.* **2011**, *66*, 163–170.

[170] Canepa, P.; Arter, C. A.; Conwill, E. M.; Johnson, D. H.; Shoemaker, B. A.; Soliman, K. Z.; Thonhauser, T. *J. Mater. Chem. A* **2013**, *1*, 13597.

[171] Valenzano, L.; Civalleri, B.; Chavan, S.; Palomino, G. T.; Areán, C. O.; Bordiga, S. *J. Phys. Chem. C* **2010**, *114*, 11185–11191.

[172] Fang, H.; Kamakoti, P.; Ravikovitch, P. I.; Aronson, M.; Paur, C.; Sholl, D. S. *Phys. Chem. Chem. Phys.* **2013**, *15*, 12882–12894.

[173] McDaniel, J. G.; Yu, K.; Schmidt, J. R. *J. Phys. Chem. C* **2012**, *116*, 1892–1903.

[174] Han, S. S.; Kim, D.; Jung, D. H.; Cho, S.; Choi, S.-H.; Jung, Y. *J. Phys. Chem. C* **2012**, *116*, 20254–20261.

[175] Märcz, M.; Johnsen, R. E.; Dietzel, P. D. C.; Fjellvg, H. *Microporous Mesoporous Mater.* **2012**, *157*, 62–74.

[176] Dion, M.; Rydberg, H.; Schrder, E.; Langreth, D. C.; Lundqvist, B. I. *Phys. Rev. Lett.* **2004**, *92*, 246401.

[177] Dudarev, S. L.; Botton, G. A.; Savrasov, S. Y.; Humphreys, C. J.; Sutton, A. P. *Phys. Rev. B* **1998**, *57*, 1505–1509.

[178] Lee, K.; et al. *J. Am. Chem. Soc.* **2014**, *136*, 698–704.

[179] García-Pérez, E.; Parra, J.; Ania, C.; García-Sánchez, A.; Baten, J.; Krishna, R.; Dubbeldam, D.; Calero, S. *Adsorption* **2007**, *13*, 469–476.

[180] Bloch, E. D.; Murray, L. J.; Queen, W. L.; Chavan, S.; Maximoff, S. N.; Bigi, J. P.; Krishna, R.; Peterson, V. K.; Grandjean, F.; Long, G. J.; Smit, B.; Bordiga, S.; Brown, C. M.; Long, J. R. *J. Am. Chem. Soc.* **2011**, *133*, 14814–14822.

[181] Krishna, R.; van Baten, J. M. *J. Phys. Chem. C* **2012**, *116*, 23556–23568.

[182] Yao, Y.; Nijem, N.; Li, J.; Chabal, Y. J.; Langreth, D. C.; Thonhauser, T. *Phys. Rev. B* **2012**, *85*, 064302.

[183] Beeler, A. J.; Orendt, A. M.; Grant, D. M.; Cutts, P. W.; Michl, J.; Zilm, K. W.; Downing, J. W.; Facelli, J. C.; Schindler, M. S.; Kutzelnigg, W. *J. Am. Chem. Soc.* **1984**, *106*, 7672–7676.

[184] Deng, H.; Grunder, S.; Cordova, K. E.; Valente, C.; Furukawa, H.; Hmadeh, M.; Gndara, F.; Whalley, A. C.; Liu, Z.; Asahina, S.; Kazumori, H.; O'Keeffe, M.; Terasaki, O.; Stoddart, J. F.; Yaghi, O. M. *Science* **2012**, *336*, 1018–1023.

Appendix A

Additional figures as described in the text

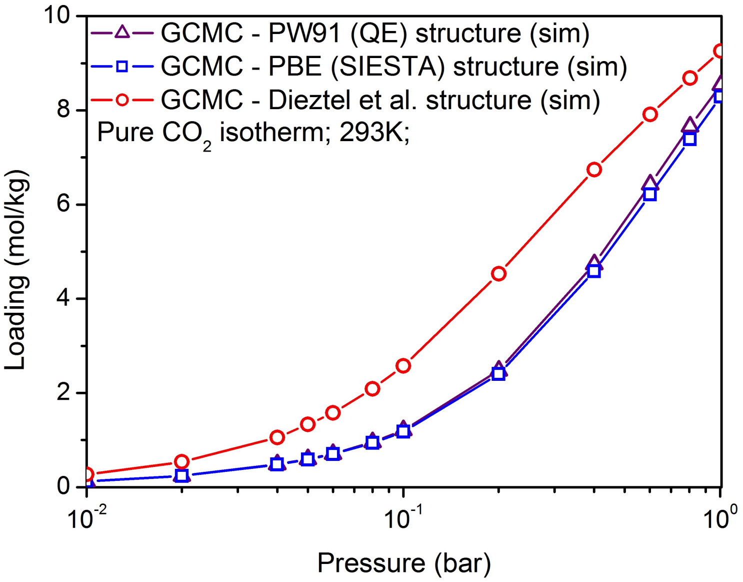

Figure A.1: Effects of the crystal structure on the adsorption isotherms for CO_2 at 293 K. This figure shows the comparison between the experimental structure of Dietzel et al.[135] and the DFT optimized structures (both QE and SIESTA). The grand-canonical Monte Carlo simulations use the UFF[129] and the TraPPE[55] force field with the Lorentz-Berthelot mixing rules to describe the CO_2-MOF and CO_2-CO_2 interactions.

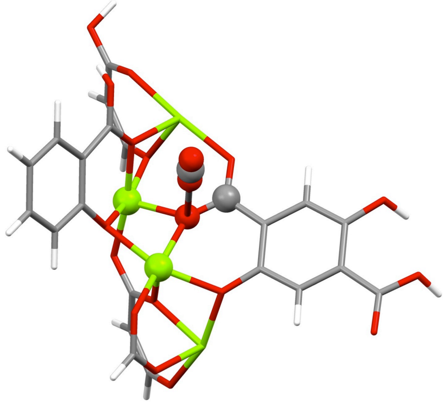

Figure A.2: Adopted O_a atom-type cluster of Mg-MOF-74 and corresponding paths of (left) CO_2 and (right) N_2. The figures show the atoms of clusters and molecules as ball and/or stick (Mg, green; O, red; C, grey; H, white; N, purple)

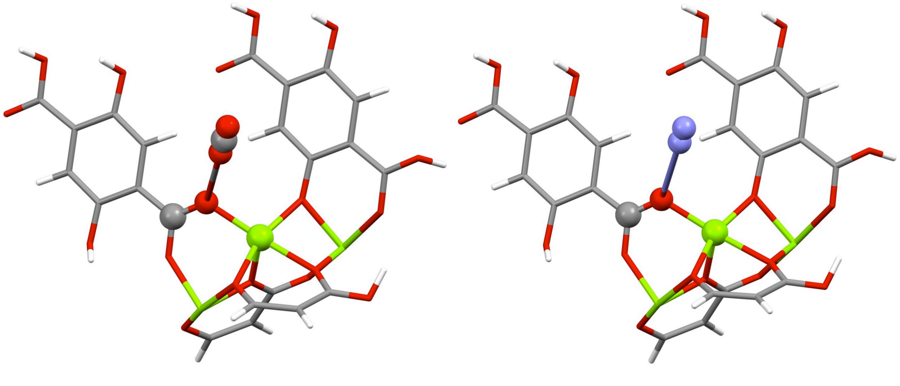

Figure A.3: Adopted O_b atom-type cluster of Mg-MOF-74 and corresponding paths of (left) CO_2 and (right) N_2. The figures show the atoms of clusters and molecules as ball and/or stick (Mg, green; O, red; C, grey; H, white; N, purple)

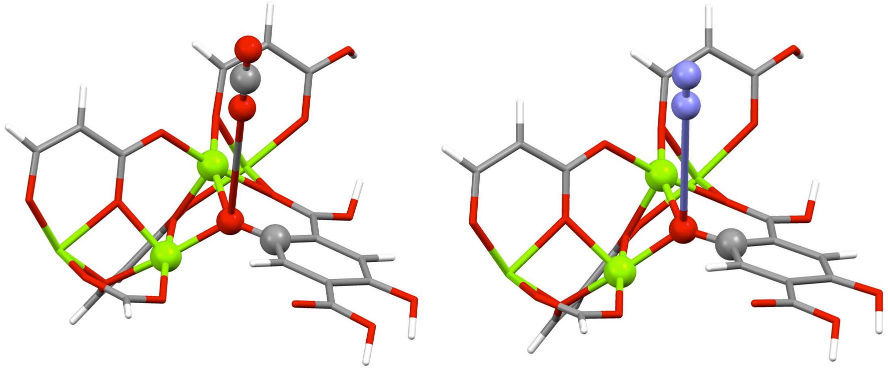

Figure A.4: Adopted O_c atom-type cluster of Mg-MOF-74 and corresponding paths of (left) CO_2 and (right) N_2. The figures show the atoms of clusters and molecules as ball and/or stick (Mg, green; O, red; C, grey; H, white; N, purple)

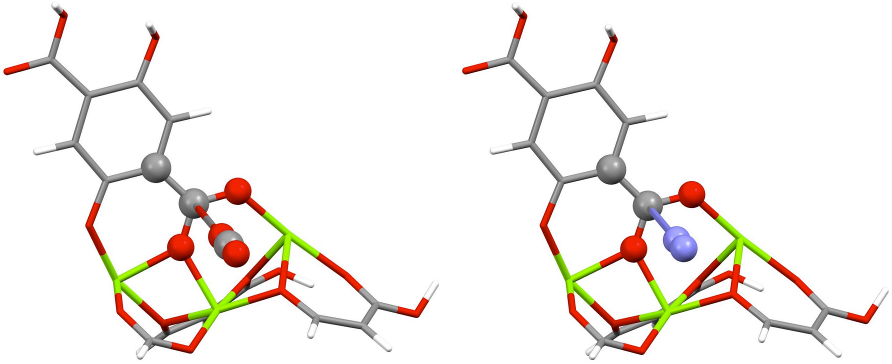

Figure A.5: Adopted C_a atom-type cluster of Mg-MOF-74 and corresponding paths of (left) CO_2 and (right) N_2. The figures show the atoms of clusters and molecules as ball and/or stick (Mg, green; O, red; C, grey; H, white; N, purple)

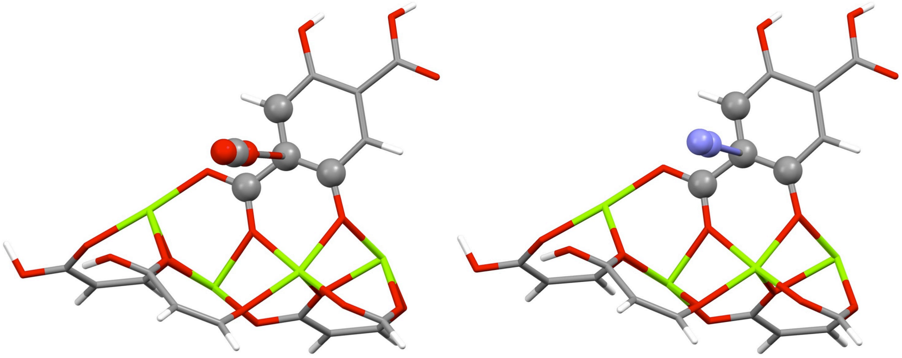

Figure A.6: Adopted C_b atom-type cluster of Mg-MOF-74 and corresponding paths of (left) CO_2 and (right) N_2. The figures show the atoms of clusters and molecules as ball and/or stick (Mg, green; O, red; C, grey; H, white; N, purple)

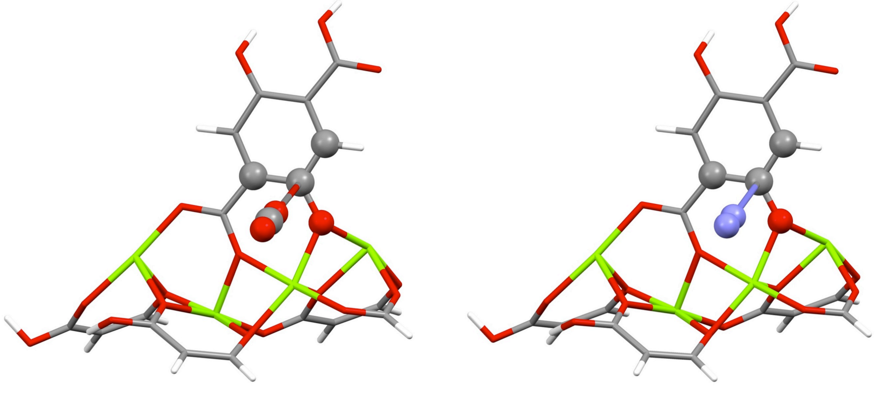

Figure A.7: Adopted C_c atom-type cluster of Mg-MOF-74 and corresponding paths of (left) CO_2 and (right) N_2. The figures show the atoms of clusters and molecules as ball and/or stick (Mg, green; O, red; C, grey; H, white; N, purple)

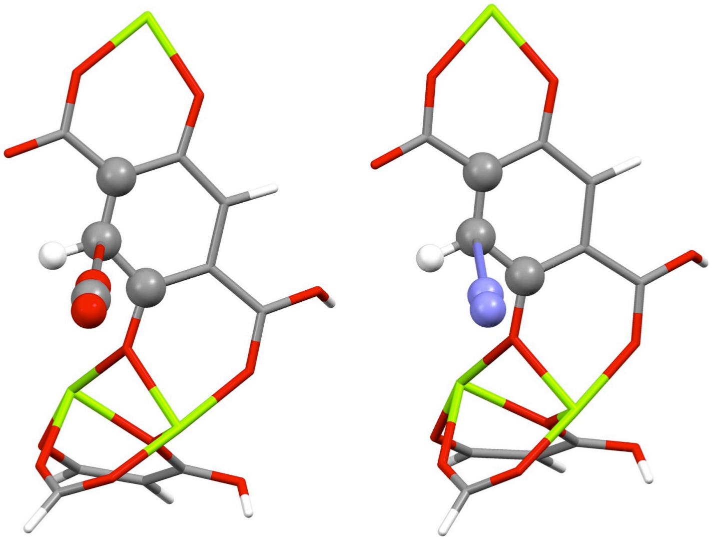

Figure A.8: Adopted C_d atom-type cluster of Mg-MOF-74 and corresponding paths of (left) CO_2 and (right) N_2. The figures show the atoms of clusters and molecules as ball and/or stick (Mg, green; O, red; C, grey; H, white; N, purple)

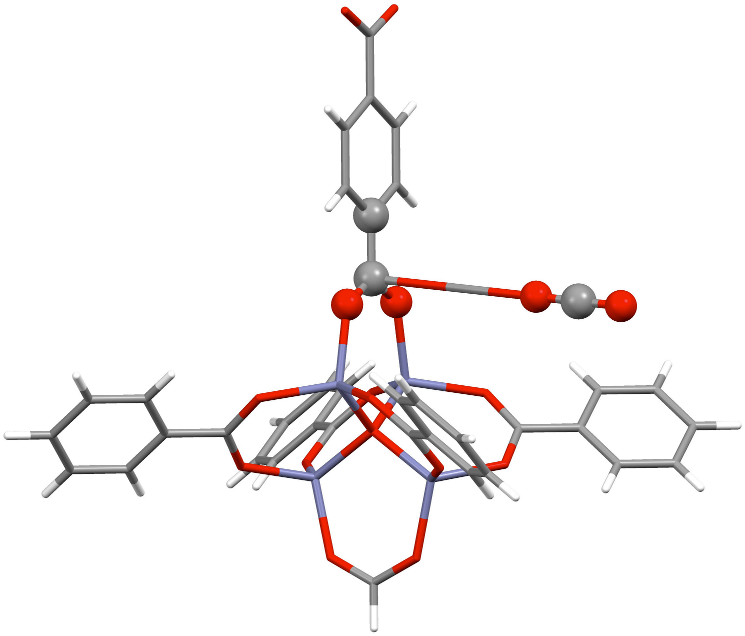

Figure A.9: Adopted C_a atom-type cluster of MOF-5 and corresponding path of CO_2. The figures show the atoms of clusters and molecules as ball and/or stick (Zn, purple; O, red; C, grey; H, white)

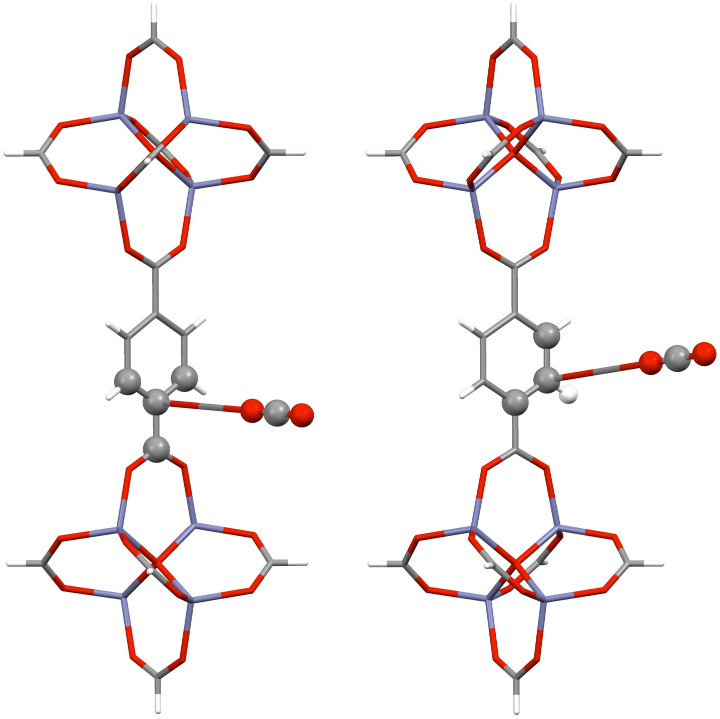

Figure A.10: Adopted (left) C_b and (right) C_d atom-type clusters of MOF-5 and corresponding path of CO_2. The figures show the atoms of clusters and molecules as ball and/or stick (Zn, purple; O, red; C, grey; H, white)

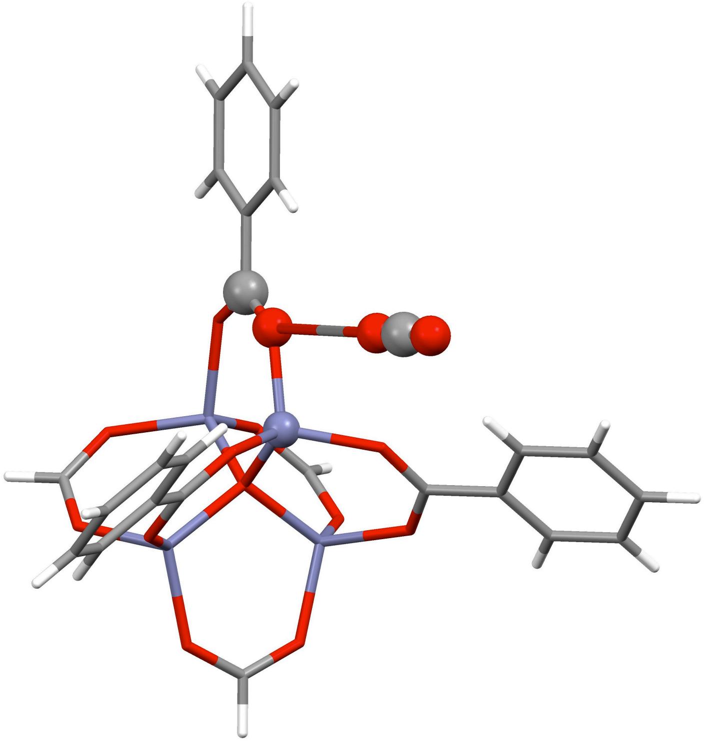

Figure A.11: Adopted O_{ab} atom-type cluster of MOF-5 and corresponding path of CO_2. The figures show the atoms of clusters and molecules as ball and/or stick (Zn, purple; O, red; C, grey; H, white)

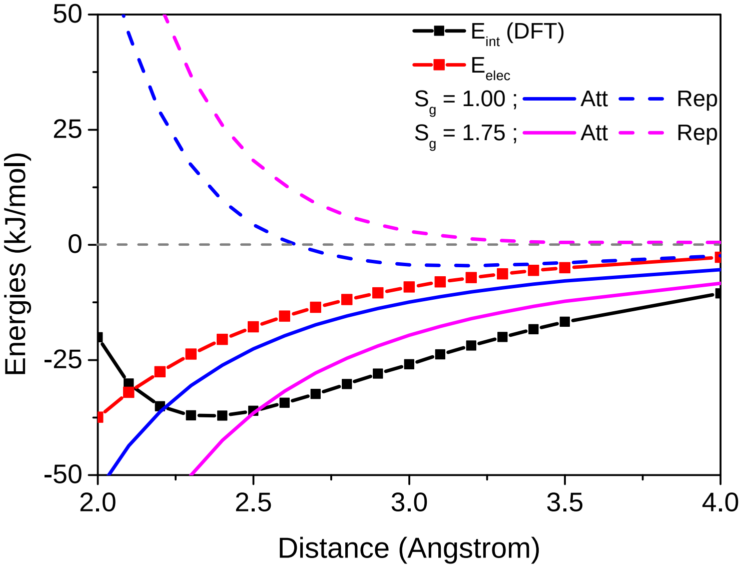

Figure A.12: Demonstration of the necessity of a global scaling factor applied in the calculated dispersion contribution while performing the energy decomposition. The black squares with solid line are the DFT total energies along a given path while the red squares with solid line are the electrostatic contributions. The solid and dashed lines represent for the calculated dispersion energies and the corresponding decomposed repulsion energies, respectively. The blue and pink colors indicate the cases of the scaling factors equal to 1 and 1.75, respectively.

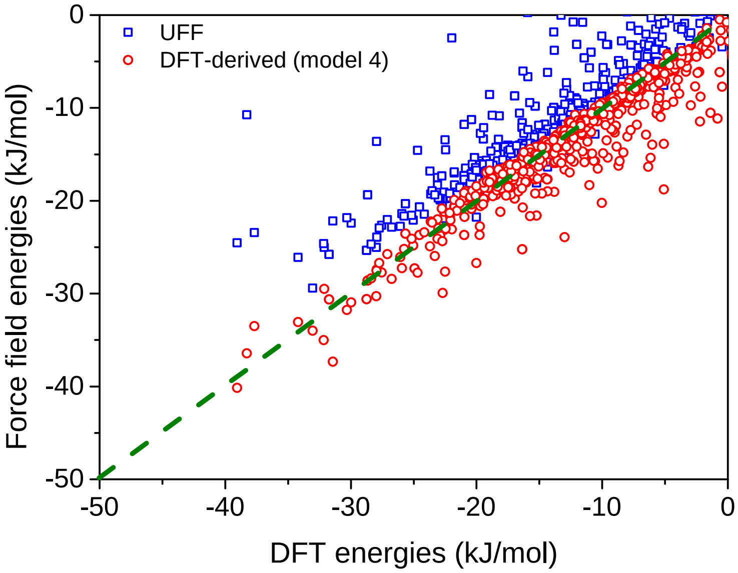

Figure A.13: Comparison of the interaction energies of CO_2-framework obtained from the DFT calculations with ones computed from the UFF (open blue squares) and the DFT-derived force field (model 4) (open red circles) for a set of 1,200 CO_2 configurations inside the accessible pore volume of Mg-MOF-74. The green-dashed line indicates perfect agreement between the energies computed by DFT and by force fields.

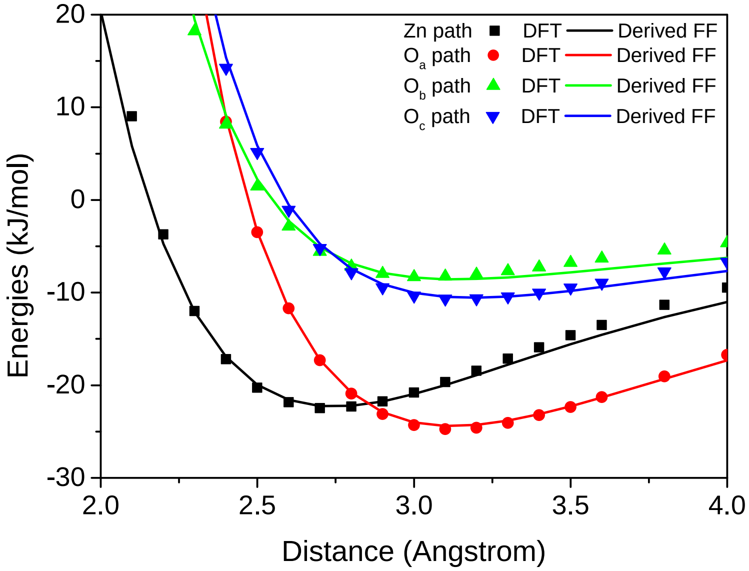

Figure A.14: Comparisons of CO_2-framework interaction energies as a function of distance inside Zn-MOF-74 obtained from the DFT calculations (closed symbol) with ones computed from the DFT-derived force field (solid line) along Mg and O paths. The DFT-derived force field demonstrated here was built upon the model 4 of CO_2 inside the Mg-MOF-74.

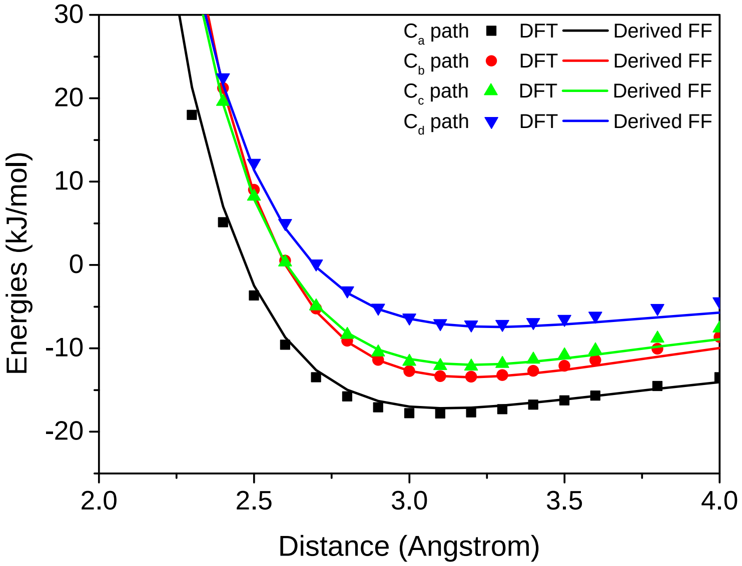

Figure A.15: Comparisons of CO_2-framework interaction energies as a function of distance inside Zn-MOF-74 obtained from the DFT calculations (closed symbol) with ones computed from the DFT-derived force field (solid line) along C paths. The DFT-derived force field demonstrated here was built upon the model 4 of CO_2 inside the Mg-MOF-74.

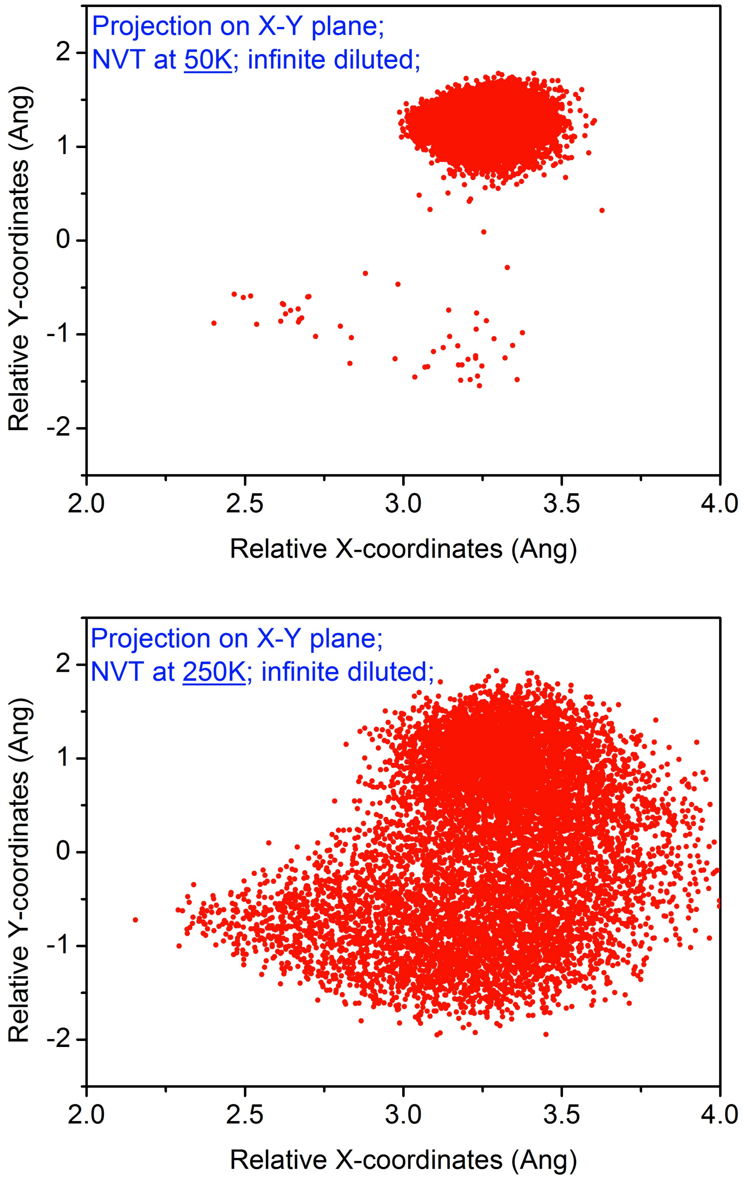

Figure A.16: Projection of the location of $C(CO_2)$ as closed dots on the X-Y plane at different temperatures of (upper) 50 K and (lower) 250 K.

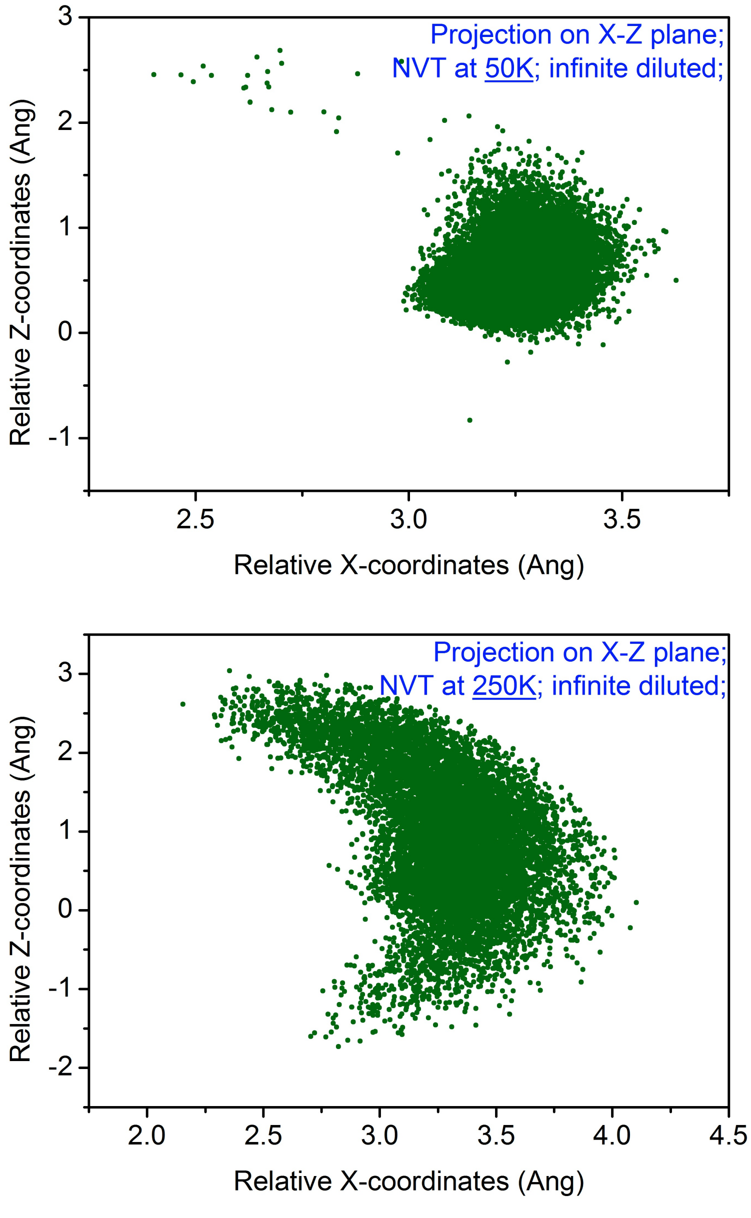

Figure A.17: Projection of the location of C(CO_2) as closed dots on the X-Z plane at different temperatures of (upper) 50 K and (lower) 250 K.

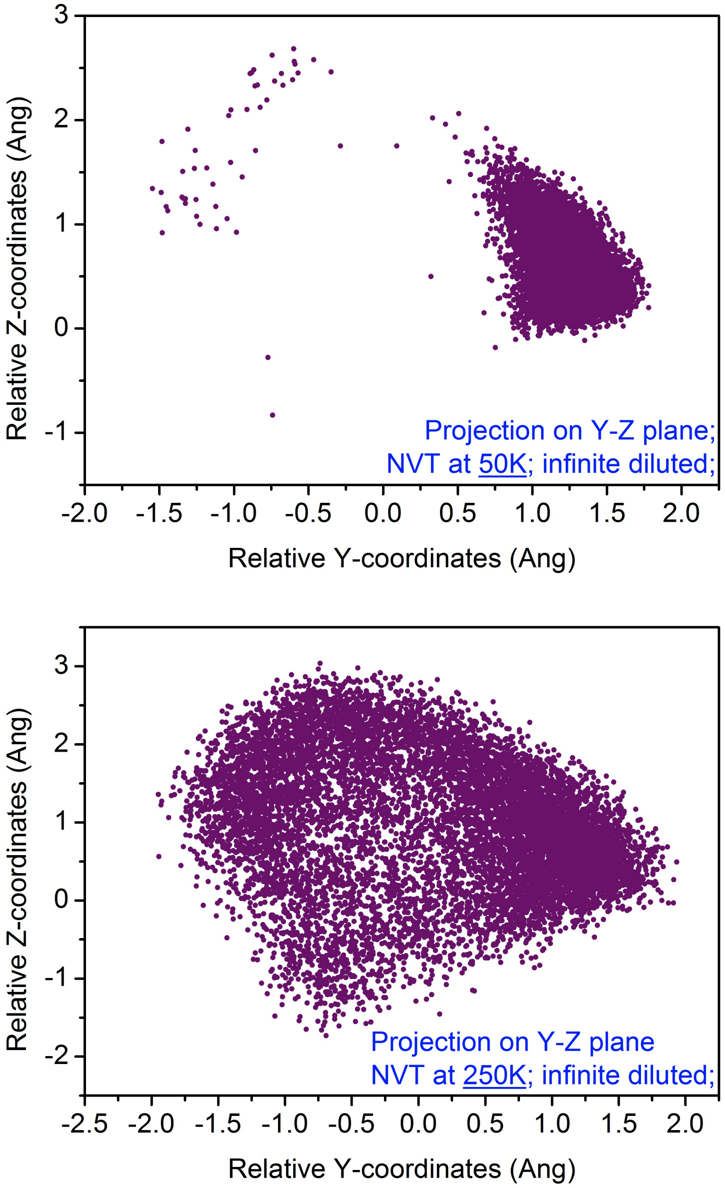

Figure A.18: Projection of the location of C(CO_2) as closed dots on the Y-Z plane at different temperatures of (upper) 50 K and (lower) 250 K.

Appendix B

Acknowledgements of each presented study

- Section 2.1 *In silico screening of carbon-capture materials*:[1] M.H., R.L.M. and C.H.R. were supported in part by the U.S. Department of Energy under contract DE-AC02-05CH11231. R.L.M and M.H. were supported jointly by DOE Office of Basic Energy Sciences and the Office of Advanced Scientific Computing Research through SciDAC project #CSNEW918 entitled "Knowledge guided screening tools for identification of porous materials for CO_2 separations". B.S. was supported as part of the Center for Gas Separations Relevant to Clean Energy Technologies, an Energy Frontier Research Center funded by the U.S. Department of Energy, Office of Science, Office of Basic Energy Sciences under Award Number DE-SC0001015. J.K. was supported by the Director, Office of Science, Advanced Scientific Computing Research, of the U.S. Department of Energy under Contract No. DE-AC02-05CH11231. M.W.D. was supported by the U.S. Department of Energy under grant DE-FG02-03ER15456. J.S. and L-C.L. were supported by the Advanced Research Projects Agency - Energy (ARPA-E), U.S. Department of Energy. K.J was supported in part by the U.S. Department of Energy under contract DE-AC02-05CH11231 through the Carbon Capture Simulation Initiative (CCSI). A.H.B. and A.S. B. were supported by Office of Innovation, Electric Power Research Institute. This research used resources of the National Energy Research Scientific Computing Center, which is supported by the Office of Science of the U.S. Department of Energy under Contract No. DE-AC02-05CH11231. All of the GPU simulations were conducted on Dirac, which is a GPU cluster at NERSC that consists of 44 Fermi Tesla C2050 cards.

- Section 2.2 *Predicting large CO_2 adsorption in aluminosilicate zeolites for postcombustion carbon dioxide capture*:[34] J.K. and M.H. were supported by the Director, Office of Science, Advanced Scientific Computing Research, U.S. Department of Energy (DOE) under Contract DE-AC02-05CH11231 and, during the final stage of this work, by DOE under Contract DE-AC02-05CH11231 through the Carbon Capture Simulation

Initiative (CCSI). M.H. was supported jointly by the DOE Office of Basic Energy Sciences (BES) and the Office of Advanced Scientific Computing Research through SciDAC Project CSNEW918 entitled Knowledge Guided Screening Tools for Identification of Porous Materials for CO_2 Separations. L.-C.L. was supported by the Deutsche Forschungsgemeinschaft (DFG) Priority Program SPP 1570. J.A.S. was supported by the DOE Advanced Research Projects Agency-Energy (ARPA-E). B.S. was supported as part of the Center for Gas Separations Relevant to Clean Energy Technologies, an Energy Frontier Research Center funded by DOE BES under Award DE-SC0001015. This research used resources of the National Energy Research Scientific Computing Center, which is supported by the DOE Office of Science under Contract DE-AC02-05CH11231.

- Section 2.3 *Large-scale screening of zeolite structures for CO_2 membrane separations*:[35] J.K. was supported by the Assistant Secretary for Fossil Energy of the U.S. Department of Energy under Contract No. DE-AC02-05CH11231. M.A. was supported by the Advanced Research Projects AgencyEnergy (ARPA-E), U.S. Department of Energy. L.-C.L. was supported by the Deutsche Forschungsgemeinschaft (DFG, priority program SPP 1570). B.S. was supported as part of the Center for Gas Separations Relevant to Clean Energy Technologies, an Energy Frontier Research Center funded by the U.S. Department of Energy, Office of Science, Office of Basic Energy Sciences, under Award No. DE-SC0001015.

- Section 2.4 *New materials for methane capture from dilute and medium-concentration sources*: J.K., R.L.M., and M.H. were supported by the Director, Office of Science, Advanced Scientific Computing Research, of the U.S. Department of Energy under Contract No. DE-AC02-05CH11231. M.H. and R.L.M were supported jointly by DOE Office of Basic Energy Sciences and the Office of Advanced Scientific Computing Research through SciDAC Project #CSNEW918 entitled Knowledge guided screening tools for identification of porous materials for CO_2 separations. B.S. was supported as part of the Center for Gas Separations Relevant to Clean Energy Technologies, an Energy Frontier Research Center funded by the U.S. Department of Energy, Office of Science, Office of Basic Energy Sciences under Award Number DE-SC0001015. J.A.S. was supported by the Advanced Research Projects Agency - Energy (ARPA-E), U.S. Department of Energy. L.-C.L. was supported by the Deutsche Forschungsgemeinschaft (DFG, priority program SPP 1570). This research used resources of the National Energy Research Scientific Computing Center, which is supported by the Office of Science of the U.S. Department of Energy under Contract No. DE-AC02-05CH11231.

- Section 2.5 *Large-scale computational screening of zeolites for ethane/ethene separation*:[3] The work at LLNL was performed under the auspices of the US Department of Energy by Lawrence Livermore National Laboratory under Contract DE-AC52-07NA27344. J.K. was supported by the U.S. Department of Energy, Office of Basic Energy Sciences, Materials Sciences and Engineering Division under Contract No. DE-

AC02-05CH11231. J.K. was also supported by the Assistant Secretary for Fossil Energy of the U.S. Department of Energy under Contract No. DE-AC02-05CH11231. The information, data, or work presented herein was funded in part by the Advanced Research Projects Agency - Energy (ARPA-E), U.S. Department of Energy. L.-C.L. was supported by the Deutsche Forschungsgemeinschaft (DFG, priority program SPP 1570). B.S. was supported as part of the Center for Gas Separations Relevant to Clean Energy Technologies, an Energy Frontier Research Center funded by the US Department of Energy, Office of Science, Office of Basic Energy Sciences under Award Number DE-SC0001015. This research used resources of the National Energy Research Scientific Computing Center, which is supported by the Office of Science of the US Department of Energy under Contract No. DE-ACO$_2$-05CH11231.

- Section 3.1 *Ab initio carbon capture in open-site metal organic frameworks*:[118] The research was supported by the U. S. Department of Energy under contracts DE-SC00015, DE-FG02-11ER16283, ARPA-E. A.L.D. and L.G. were supported by DOE Office of Basic Energy Sciences through project #DE-FG02-11ER16283. S.N.M, R.P, and B.S. was supported as part of the Center for Gas Separations Relevant to Clean Energy Technologies, an Energy Frontier Research Center funded by the U.S. Department of Energy, Office of Science, Office of Basic Energy Sciences under Award Number DE-SC0001015. Work at the Molecular Foundry was supported by the Office of Science, Office of Basic Energy Sciences, of the U.S. Department of Energy under Contract No. DE-AC02-05CH11231. J.A.S. was supported by the Advanced Research Projects Agency - Energy (ARPA-E), U.S. Department of Energy. L.-C.L. was supported by the Advanced Research Projects Agency - Energy (ARPA-E), U.S. Department of Energy during the initial stage of this project and during the final stage by the Deutsche Forschungsgemeinschaft (DFG, priority program SPP 1570). J.K. was supported in part by the U.S. Department of Energy under contract DE-AC02- 05CH11231 through the Carbon Capture Simulation Initiative (CCSI). This research used resources of the National Energy Research Scientific Computing Center, which is supported by the Office of Science of the U.S. Department of Energy under Contract No. DE-AC02-05CH11231.

- Section 3.2 *Force-field development from electronic structure calculations with periodic boundary conditions: applications to gaseous adsorption and transport in metal-organic frameworks*:[4] We gratefully thank Prof. Jihan Kim at Korea Advanced Institute of Science and Technology (KAIST) for providing helps on code modifications to facilitate the development of this methodology. This research was supported by the U.S. Department of Energy, Office of Basic Energy Sciences, Division of Chemical Sciences, Geosciences, and Biosciences under award DE-FG02-12ER16362. Work at the Molecular Foundry was supported by the Office of Science, Office of Basic Energy Sciences, of the U.S. Department of Energy under Contract No. DEAC02- 05CH11231. L.-C.L. acknowledges financial support from a Chevron Fellowship. This research used resources of the National Energy Research Scientific Computing Center (NERSC), which is supported by the Office of Science of the U.S. Department of Energy under Contract No. DE-AC02-05CH11231.

- Section 3.3 *Efficient determination of accurate force fields for porous materials using ab-initio total energy calculations*:[119] J.K. is supported by the KAIST Startup Fund (Project G04130042). B.S. and L.C.L. are supported as part of the Center for Gas Separations Relevant to Clean Energy Technologies, an Energy Frontier Research Center funded by the U.S. Department of Energy, Office of Science, Office of Basic Energy Sciences, under Award DE-SC0001015. K.L. is supported by the U.S. Department of Energy, Office of Basic Energy Sciences, Division of Chemical Sciences, Geosciences and Biosciences, under Award DE-FG02-12ER16362. Work at the Molecular Foundry is also supported by the US Department of Energy, Office of Science, and Office of BES. This research used resources of the National Energy Research Scientific Computing Center (NERSC), which is supported by the Office of Science of the U.S. Department of Energy under Contract DE-AC02-05CH11231.

- Chapter 4 *Understanding* CO_2 *dynamics in metal-organic frameworks with open metal sites*:[162] This research was supported through the Center for Gas Separations Relevant to Clean Energy Technologies, an Energy Frontier Research Center funded by the U.S. Department of Energy, Office of Science, Office of Basic Energy Sciences under award DE-SC0001015.